SCUOLA DI DOTTORATO

UNIVERSITÀ DEGLI STUDI DI MILANO-BICOCCA

Department of

Materials Science

PhD program: Materials Science and Nanotechnology Cycle XXXIII

Curriculum: *Materials Science*

Two-Dimensional Phosphorus: From the Synthesis Towards the Device Integration.

Surname: **Faraone** Name: **Gabriele**

Registration number: 833030

Tutor: Prof. Bonera Emiliano

Supervisor: Dr. Molle Alessandro

Coordinator: Prof. Bernasconi Marco

ACADEMIC YEAR 2019/2020

Abstract

Phosphorus and silicon two-dimensional (2D) allotropes have been the forerunners among the post-graphene monoelemental 2D materials. The scientific and technological advantages of these materials require the development of processing methods to guarantee their effective integration in new devices for nanoelectronics. In the present thesis work, some of the unresolved bottlenecks along the device integration path of 2D elemental phosphorus allotropes have been examined considering specifically the case of the α-P (single-layer black phosphorus or phosphorene) and β-P (blue phosphorene) 2D polymorphs.

The integration of the 2D α-P phase in devices has been the subject of extensive investigations and nowadays relies on an almost consolidated path that has led to applications spanning a wide range of fields. One of the few remaining obstacles on this path is the lack of a scalable method to produce 2D α-P layers on large areas and with accurate control of the thickness. In particular, such control is difficult to achieve in the exfoliation of layered black phosphorus (BP) crystals. In this respect, micro-Raman spectroscopy has been used both as a metrological tool to determine the thickness of the exfoliated flakes and as method to achieve their controllable thickness reduction employing the laser thinning technique. However, thickness determination methods based on the calibration of the intensity of the Raman bands have been poorly investigated in the case of multilayer BP flakes due to difficulties caused by optical interferences and anisotropy effects. In this thesis work, we have proposed a novel Raman spectroscopy approach that, carefully accounting for these effects, allowed the quick discrimination of the thickness of exfoliated BP flakes between 5 nm and 100 nm. Moreover, in order to achieve a better control of the laser thinning process down to the ultimate 2D limit, we have also investigated the effects of the substrate on the laser heating and ablation of multilayer BP flakes. Raman thermometry experiments and numerical calculations of the heat diffusion problem have elucidated that optical, thermal, and mechanical effects caused by the substrate may act differently on the laser heating and ablation of multilayer flakes depending on their thickness.

An effective device integration route for the 2D β-P phase, instead, is still missing due to more stringent requirements in the synthesis, based on epitaxial techniques, and to the instability issue outside the UHV growth environment. These obstacles are commonly shared with other members of the family of 2D epitaxial Xenes and, in this work, have been investigated considering the case of β-P epitaxially grown on Au(111)/mica substrates. The details of its atomic structure and the chemical reactivity to ex-situ and in-situ oxygen exposure have been analyzed with the aid of Scanning Tunneling Microscopy (STM) and X-Ray Photoelectron Spectroscopy (XPS). The air-instability issues have been tackled by developing an encapsulation strategy based on the in-situ growth of an Al_2O_3 capping layer that, in turn, allowed the handling of epitaxial phosphorus along the preliminary steps of a device integration process. In this respect, two novel approaches for the transfer of the epitaxial membrane from the growth substrate towards target substrates have been surveyed. Both the transfer methods can be generalized to the whole class of 2D epitaxial Xenes grown on metal/mica paving the way for the establishment of methodological standards for their manipulation. In particular, the universality of such approaches has been exploited for the successful fabrication of back-gated FET and MIM devices on Al_2O_3/multilayer silicene/Ag(111) and Al_2O_3/epitaxial phosphorus/Au(111) mica-delaminated samples, respectively. The epitaxial phosphorus MIM devices may open intriguing perspectives to study of the non-volatile resistive switching in monoelemental 2D materials.

Contents

List of Figures

List of Tables

CHAPTER 1

Introduction

1.1 Pushing forward the Moore's law boundaries

The Moore's prediction that the number of transistors in an integrated circuit doubles about every two years has led the technological and economic development of the semiconductor industry for more than 60 years. Moore's observation came from the projection of an empirical trend followed by the semiconductor industry in the early 60s so to illustrate the potential economic impact of the first silicon integrated circuits. From an economic point of view, the Moore's law illustrates that the increase in the chip integration complexity by shrinking the dimensions of the components inside it can be traded for higher manufacturing yields and hence higher revenues.[1] Indeed, in the decades following the famous Gordon Moore statement, a self-reinforcing economic cycle between the market and the semiconductor firms established and the increasing profits allowed the long-term investments in research and development.[2] Aided by this positive-feedback economic mechanism, the Moore's trajectory was continued until the first decade of the twenty-first century, practically kept on track by the scaling rules conceived by R. H. Dennard[3] in 1970 for the Metal Oxide Semiconductor Field Effect Transistor (MOSFET), i.e. the most common electronic device in integrated circuits. The forecast and the possible roadblocks along the Dennard-Moore trajectory were yearly planned in a public document known as the International Technology Roadmap for Semiconductors (ITRS). The ITRS itself contributed to transform the Moore's law from an empirical statement into a self-fulfilling prophecy.[4]

From Dennard's scaling to the equivalent scaling of the transistor dimensions

The principle of device scaling introduced by Dennard's guided the shrinking of the FET transistor dimensions until the late 1990s -early 2000s. In order to preserve the transistors performances by shrinking the lateral dimensions, the doping concentrations of the transistor channel had to scale up and simultaneously the gate oxide thickness had to scale down. However, as soon as the industry progressed toward device dimensions below 100 nm, roadblocks emerged as limiting factors to the transistor power dissipation and switching speed performances. These roadblocks were caused by a series materials' shortcomings such as the electron tunneling problem through ultrathin gate oxides, the difficulty to obtain a precise control on the distribution of dopants and the dopant clustering effects due to the use of high doping profiles in the transistor channels.[5] Therefore, in order to sustain the trends of the Moore's law in the integration density and, at the same time, circumvent the previous issues, the semiconductor industry introduced a set of materials innovations aiming to maintain equivalent performances to those obtained through the Dennard scaling rules. In the so-called "equivalent-scaling approach" the device switching speeds were increased introducing strain engineering on the silicon channels so to increase the electron and hole mobilities and the gate leakage problem through ultrathin oxides was reduced introducing high dielectric constant materials (high-K dielectrics) as gate oxides.

Unavoidable heat dissipation issues

Despite the success of these innovations, as the semiconductor companies pushed to create even denser and faster chips with smaller and smaller features, by the mid of 2000 it became clear that the power consumption as well as the heat dissipation were the main limiting factors

on the chip's performances. The reduction in the switching energy per single logical device drastically slowed down due to the constraints imposed on the heat dissipation by the MOSFET physics.[6] The most striking evidence of this problem was that the semiconductor firms stopped to increase the chips speed (or clock-rate) in order to put a limit on their ability to generate heat and, instead, opted to increase the integrated circuits performances moving towards the design of multi-core architectures. Additionally, the increasing technological challenges imposed by the equivalent scaling of smaller devices led to an increase of the expenditures associated with R&D and device manufacturing.[2] As consequence of these factors the Moore's law appeared to falter both in its technical and economic implications.

A three-trajectory strategy for the future of semiconductor industry

To face these daunting problems, after decades of progress centered on the miniaturization of the MOS transistors, the final 2016 edition of the ITRS roadmap envisaged new strategies to guide the development of the semiconductor industry and to survive at the end of the Moore's law. Specifically, three complementary approaches were outlined:

- *More Moore* that continues the historic Moore-Dennard trajectory in improvements of the transistor devices speed, area (dimensions), power (energy efficiency) and cost.
- The *More than Moore* strategy that deals with the integration of new functionalities such as sensors, radiofrequency circuits or micro-electromechanical devices in the integrated circuits tailoring them for specific applications.
- *Beyond CMOS* which includes the approaches carried out for the development of new computing architectures or entirely new computing elements based on new materials and emerging research devices as the potential successors of the silicon transistor for both logic, memory and hybrid logic/memory applications.

New device architectures and low-dimensional materials for the future of nanoelectronics

In the last decade of the twenty-first century the progress along the More Moore strategy has required both the adoption of new device geometries and the use of new materials. However, silicon still remains ubiquitous in the semiconductor industry and most of the integrated circuit todays are still based on a single transistor type, the Si-MOSFET and a single circuit technique, the Si-CMOS (complementary MOS), that employs both p-channel and n-channel MOSFETS. In order to boost the performances of conventional MOSFET based on the silicon planar CMOS technology the semiconductor foundries have adopted a progressive shift towards two alternative architectures, as illustrated in Figure 1.1. One solution relies on a thin layer of silicon on top of an insulating layer and the resulting FET device is called ultrathin body silicon-on-insulator (UTB SOI). The second possibility, instead, implies a shift from the planar structure to non-planar three-dimensional structures with the gate wrapping three sides of a vertical silicon channel region. These structures are called tri-gate transistors or FinFETs.[7] Each one of these two device architectures come with its own set of merits and drawbacks in their performances and ultimate scaling limits. However, due to the increasing technological challenges in reducing the dimensions of Si-channels, the progress along the More Moore trajectory is inexorably slowing down. Specifically, the continuous lateral scaling of the Si-channels in FinFET architectures is naturally leading towards the concept of nanowire or nanosheets transistors (see figure 1.1) as the natural options for the next generation electronic

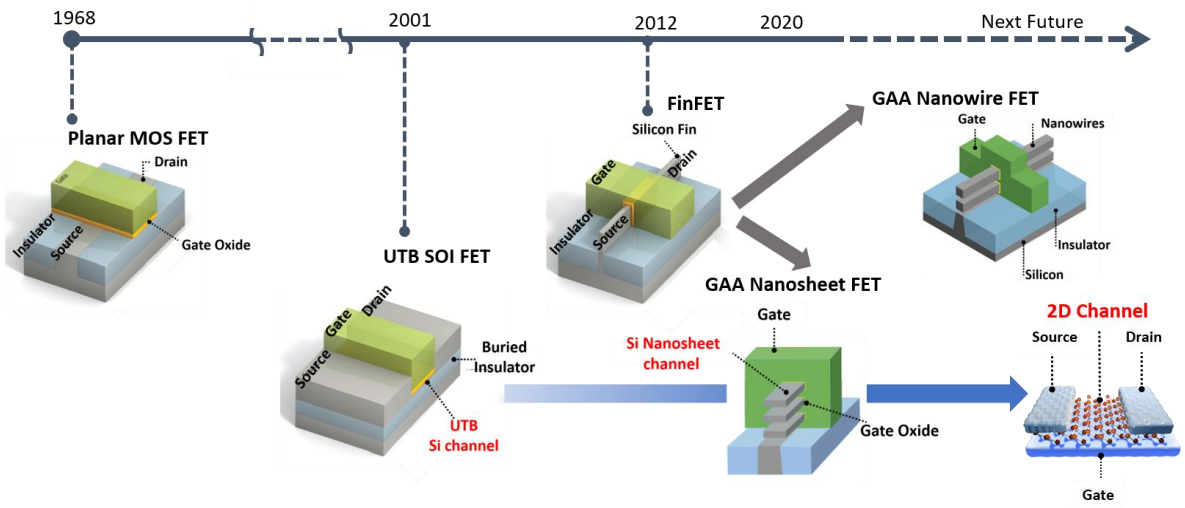

Figure 1.1 Evolution of the MOSFET transistor towards planar UTB SOI FET and 3D FinFET (or trigate transistor) architectures until the possible prototypes envisaged for next generation transistor devices: GAA (Gate All Around) Nanowires and Nanosheets FETs and 2D material channel FETs. Adapted from refs. [7][11]

devices. On the other hand, the extreme downscaling of the Si-body in UTB SOI FET envisage the use of atomically thin materials as promising candidates for the next generation devices.

In this perspective, the research on new materials that could mitigate the shortcomings of ultra-scaled silicon films is becoming a key factor to sustain the progress of the semiconductor industry in the next future. In particular, the rise on the scene of few atoms thick two-dimensional (2D) materials offers a promising alternative for a post-silicon nanoelectronics based on new devices concepts that could be eventually integrated in circuits with heterogeneous functionalities or in totally new computing architectures.

1.2 New materials for nanoelectronics: a brief journey into the 2D flatland

Since the isolation of graphene [8] by the mechanical exfoliation of graphite, the family of 2D materials has been continuously expanded to tackle not only the issues arising from an aggressive downscaling of the silicon devices (*More Moore*) but also to produce a wide range of applications that augment the potentialities of the traditional Si CMOS technology (*More than Moore*) and move it beyond the fields of digital and RF-electronics (*Beyond CMOS*).[9]–[11]

Two-dimensional (2D) materials can be generally defined as materials in which the atomic organization and bond strengths along two dimensions are similar and much stronger than the bonds along a third dimension. [12] Many of the superlative properties of these materials are consequences of the chemistry of their constituent elements, of the symmetry of their crystalline structures and, more importantly, of the strong confinement along a single direction.

Graphene

In the case of graphene (figure 1.2(a)), its honeycomb-like crystalline structure consisting of sp^2 bonded carbon atoms gives to this material a series of unprecedented properties such as an

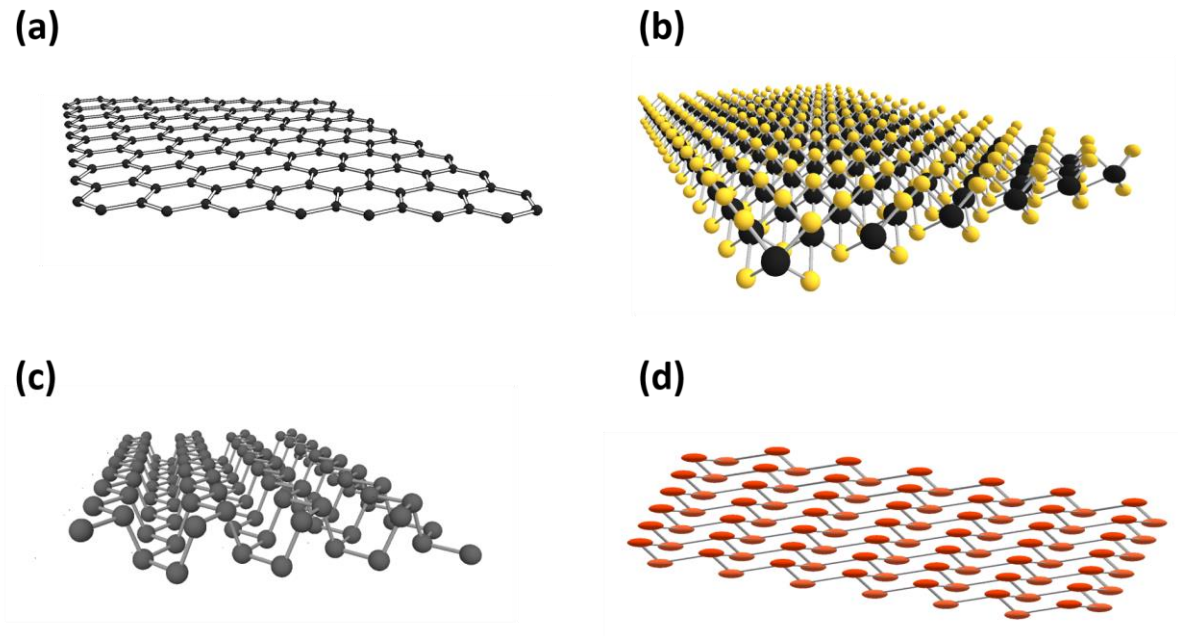

Figure 1.2 Atomic models of the crystalline structure of some representative members of the class of 2D materials: graphene **(a)**, monolayer MoS_2 **(b)**, single layer phosphorene **(c)**, and silicene **(d)**.

extremely flat and chemical inert surface, an exceptionally high electron mobility, a high thermal conductivity and a superior mechanical flexibility.[13] However, the lack of a bandgap in the electronic structure limits the use of graphene in applications where the bandgap is a fundamental requirement as, for example, in digital electronics. If this issue, on one hand, inspired considerable research efforts to open a sizable bandgap in graphene,[14] on the other hand, boosted the exploration of alternative 2D materials possessing a sizeable bandgap in their electronic structure.

2D Transition Metal dichalcogenides

Following the example of graphene, other 2D materials were discovered and isolated by exfoliation from the natural occurring bulk layered crystalline phases.[15] This was indeed the case of molybdenum disulfide (MoS_2) which belongs to the class of transition metal dichalcogenides (TMD). With a general formula MX_2 where M is a transition metal from group 4, 5 and 6 and X is a chalcogen atom, a single layer of TMD consist of three atomic planes arranged in a X-M-X form(see figure 1.2(b)). Semiconducting TMDs, such as MoS_2, WS_2, $MoSe_2$ or $MoTe_2$ have a sizable bandgap in the visible part of the spectrum that varies from indirect in the bulk to direct in the single-layer limit and lies within the 1.1 to 2.2 eV energy range making these materials the appropriate choice for digital electronics, optoelectronics and photonics applications.[16], [17] Furthermore, the family of TMD also includes many other layered compounds such as semi-metals WTe_2 and $TiSe_2$, true metals like NbS_2 and insulating TMDs like HfS_2.

Hexagonal Boron Nitride (hBN)

Another well-known member of the class of 2D materials that can be obtained by mechanical exfoliation from the corresponding layered solid is 2D hexagonal boron nitride (hBN).[18] With a bandgap value of ~6 eV and a planar crystalline structure consisting of two sublattices of

boron and nitrogen atoms arranged alternatively in a honeycomb-like lattice similar to graphene, 2D hBN has found application as substrate, gate dielectric and/or passivation and layer in van der Waals heterostructures realized with other 2D materials. [19], [20]

New 2D monoelemental materials

The simplicity of the mechanical exfoliation technique in preparing high-quality crystals fostered the research on 2D materials and, moreover, motivated the study and the discovery of new and exciting physical phenomena in these systems such as nontrivial topological properties,[21] high-temperature ballistic transport[22] and valleytronics properties.[23] However, the collection of 2D materials that can be obtained by mechanical exfoliation is rather limited since it is constrained by the relatively small number of bulk layered solids from which these materials can be isolated. The possibility to synthesize 2D materials with tailored properties according to the composition and to the growth substrate opened a completely new frontier in the 2D flatland. This was possible thanks to the introduction of chemical vapor deposition (CVD) and physical vapor deposition (PVD) techniques such as molecular beam epitaxy (MBE). These techniques, besides extending the portfolio of 2D materials, allowed also to overcome the typical limitations of the exfoliation approaches such as the small size of the 2D crystallites, the low throughput and the lack of scalability that all together are not suited for a technological exploitation of 2D materials with the current semiconductor industry standards.

In this respect, the class of 2D monoelemental materials is rather exemplificative. Mechanical exfoliation was initially used for the synthesis of the first two members of this class. In particular, soon after the discovery of graphene, phosphorene was isolated from layered bulk black phosphorus crystals. Despite being inappropriately named with the suffix *-ene*, phosphorene is not characterized by a planar crystalline structure with hexagonal symmetry similar to that of graphene but, as we will see in the next paragraph, it has a puckered lattice consisting of two parallel atomic planes (see figure 1.2(c)). However, the theoretical efforts undertaken in the prediction of stable 2D monoelemental lattices and the experimental attempts in the synthesis, carried out mainly by means of chemical or physical vapor deposition techniques, helped to considerably expand the class of available 2D monoelemental materials. Thus, to date, the existence of more than 15 new members of the class of elemental 2D materials has been experimentally and/or theoretically demonstrated.[12], [24], [25]

The Xene family

A subclass of the group of monoelemental 2D materials is the family of epitaxial 2D materials synthesized from the elements of the groups 13, 14, 15 (pnictogens) and 16 (chalcogens) of the periodic table (see figure 1.3). This class is generically termed with the name Xenes. According to this definition there are two main requisites to identify univocally any member of this family:

i) A Xene must be an atomic arrangement of atoms of a single element grown by epitaxy on a commensurate substrate.

ii) A Xenes must possess a 2D crystalline structure.

By epitaxial growth we indicate the growth of an ordered atomic layer over the surface lattice of a substrate according to a precise symmetry and commensurability relationship. By 2D crystalline structure we mean an ordered arrangement of atoms characterized by in-plane atomic bonds stronger than the out-of-plane interactions with the substrate. The latter aspect is what makes possible, in principle, the decoupling of the 2D Xene from the growth substrate and

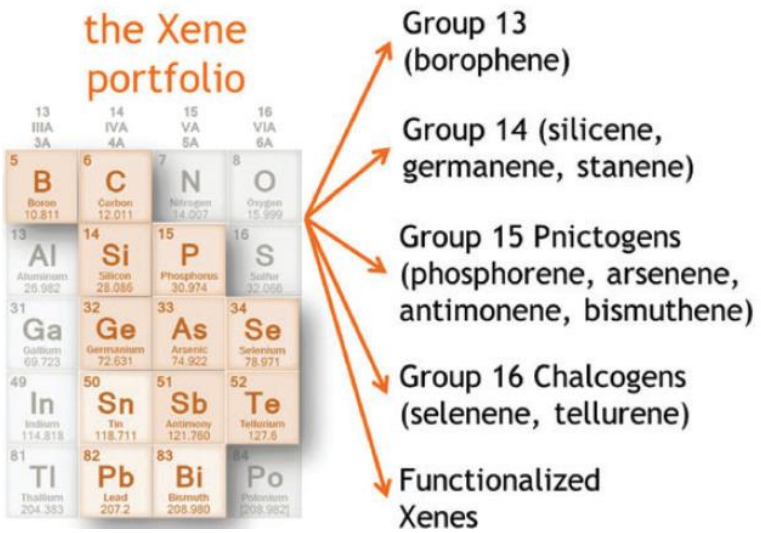

Figure 1.3 Extract from the periodic table around the elements of the group 13-16. Highlighted are the elements where the existence of a 2D epitaxial Xene form has been demonstrated. Adapted from reference [62]

differentiates it from surface alloys, surface reconstructions and subsurface precipitates that can also be obtained during an epitaxial growth process.[24]

It should be mentioned that, from a theoretical point of view, the elements of the groups 13, 14, 15 and 16 of the periodic table possess a wide variety of 2D crystalline allotropes that are energetically stable in a freestanding form.[25] Most of these 2D monoelemental lattices do not derive from naturally occurring bulk allotropes and as such they are not thermodynamically stable in ambient conditions. Their existence must be artificially forced by epitaxial growths in UHV. The resulting Xene, thus, can be considered as a metastable 2D phase that is stabilized in UHV thanks to the interaction with the substrate. However, when exposed to ambient conditions, outside the growth environment, the Xene is highly reactive needing a suitable passivation or encapsulation to protect it from the immediate degradation. This is generally true for all the Xenes apart from graphene that can be synthesized both as an epitaxial layer on a substrate [26], [27] or as a freestanding layer by mechanical exfoliation from graphite crystals. In the latter case graphene gains its chemical and thermodynamic stability in ambient conditions due to the strong bonding between the carbon atoms and also due to the small size of the exfoliated crystallites that quench the thermal fluctuations that otherwise will destroy its 2D structure.[28]

Up to now, only a limited number among the freestanding 2D allotropes of the elements of the groups 13, 14, 15 and 16 have been artificially synthesized by epitaxy and thus can be considered Xenes in the sense of the definition given above. In most of the cases the interactions between the atoms of these Xenes and those of the substrates are strong enough that the growth process is regulated by the symmetry and commensurability relationships with the substrate surface lattice. However, sometimes these interactions can cause distortions on the lattice structures of the freestanding 2D allotropes leading to epitaxial Xenes that may show a variety of surface reconstructions on a substrate, generically termed as 2D Xene phases. This is the case, for example, of silicene grown on Ag (111).[29], [30] If, instead, the interactions between the substrate and the epitaxial layer are weak the growth is nominally free from lattice matching and symmetry constraints, a situation known as van der Waals epitaxy.[31]

The 2D epitaxial lattices of the elements of the group 14: silicene[32], [29], germanene[33] and stanene[34], [35] were the first to be synthesized and belong to the so-called first generation of Xenes.[36] Silicon, germanium, and tin are isoelectronic to carbon. However, unlike the latter, where the most stable 2D allotrope, i.e. graphene, is markedly planar due to the sp^2 hybridization of the atomic orbitals, the most stable 2D allotropes of silicon, germanium and tin possess a corrugated honeycomb-like lattice due to the mixed sp^2 and sp^3 hybridization of the atomic orbitals (figure 1.2(d)). The corrugation of their atomic lattices, termed as buckling, overcomes the instability of the high-symmetry planar structures and it is an energetically favorable condition for atoms heavier than carbon and with a lower orbital overlap with respect to graphene.[37], [38] Therefore, the suffix *-ene* introduced in the name of the first generation Xenes is a reminder for the partially sp^2 hybridized alkene bonds between the atoms of the respective 2D buckled honeycomb lattices. This suffix has been later extended to denote all the remaining second generation Xenes synthetized from the elements of the group 13: Borophene[39], [40] and Gallenene[41], group 14: Plumbene [42], group15: Blue-Phosphorene[43], [44], Arsenene[45], Antimonene[46]–[48], Bismuthene[49] and group 16: Selenene[50] and Tellurene.[51]

Nowadays, however, the term Xene has assumed a much broader meaning and sometimes is interchangeably used to identify all the 2D lattices of the elements of the groups 13, 14, 15 and 16. Although the growth by epitaxy is still mandatory to qualify a 2D monoelemental lattice as a Xene, other 2D monoelemental lattices have been identified as members of this family even though not obtained by means of epitaxial growths. This is the case, for example, of borophene antimonene, arsnene and tellurene nanosheets obtained by exfoliation techniques [45], [47], [52], [53] and the case of gallenene obtained by the solid-melt exfoliation technique.[41]. According to this broader definition also 2D phosphorene crystals obtained by mechanical exfoliation from black phosphorus can be included in the family of Xenes.

Scientific and technological advantages of Xenes

The properties of the electronic band structure of the 2D monoelemental lattices make the synthesized Xenes potentially competitive with respect to other 2D materials in a wide range of applications such as flexible/low power electronics, gas/chemical sensors, spintronics and also in optoelectronics/photonics and energy applications.[25] Going from the elements of the group 13 to those of the group 16, the theoretical band structure of the 2D monoelemental lattices changes from metallic (group 13), to semimetallic with Dirac-like bands (group 14), to semiconducting with thickness dependent bandgaps (group 15 and 16). In particular, the Dirac-like conduction that characterizes the 2D silicon buckled honeycomb-like allotrope has been experimentally observed in the first FET transistor realized with Silicene on Ag(111).[54] Such findings have opened a pathway for the possible implementation of other Xenes in ultra-scaled transistors with atomically thin channels. Interestingly, the 2D allotropes of the heavier elements of the groups 14-16 (tin, bismuth, lead, selenium and tellurium) have also a band structure influenced by a strong spin orbit coupling. The spin orbit interaction in these materials is a prerequisite for the appearance of new quantum states of the matter such as the topological insulating phases. A 2D monoelemental lattice in a topological insulating phase is characterized by an insulating behavior in the bulk and by dissipationless conducting channels along the edges. These features are extremely appealing for the realization of novel beyond CMOS

devices such as FETs transistor with a 2D topological insulator channel that can be switched from the ON to the OFF state by means of a topological phase transition without dissipating energy.[38] Furthermore, the possibility to modulate the spin orbit induced band gap by strain, electric field or chemical functionalization (functionalized Xenes) paves the way for the observation of the topological insulating phases even at room temperature.

Besides the attractive scientific and technological properties predicted for the 2D monoelemental lattices, the synthesized Xenes possess also additional advantages when benchmarked against other 2D materials. For example, their inherent epitaxial nature allows to attain a precise control of the electronic structure by the substrate choice, the surface functionalization and even the degree of buckling. Furthermore, their superior crystalline quality, when attained on large areas, becomes attractive for the fabrication of 2D devices due to the homo-elemental nature of the atomic bonding that, unlike other 2D materials, inhibits the detrimental effects of crystalline defects such as grain boundaries or point defects on the electrical conductivity.

2D MXenes

The selective etching of layered precursors has been another widely used approach to synthetize 2D materials and, in particular, the members of the family of MXenes.[55] MXenes are carbides or nitrides of transition metals with a general formula $M_{n+1}X_nT_x$. Their structure usually consists of (n+1) (n=1-3) layers of a transition metal (M) such as Sc, Ti, Zr, Hf, V, Nb, Ta, Cr, Mo interleaved with n layers of Carbon or Nitrogen (X) with the outer M layers bonded to surface terminations (T) such as O, OH, F and/or Cl. The layered precursors of MXenes are the MAX phases where A is an element of the group 13 or 14 of the periodic table. The selective etching of the A-elements by acidic solutions containing fluoride ions followed by the exfoliation of the MXenes layers with the intercalation of organic molecules in polar solvents is the method that is typically used for the isolation of 2D MXenes. The hydrophilic nature of the MXenes surfaces, the high electrical conductivity and mechanical properties make these materials attractive not only for energy storage but also for catalytic and electromagnetic interference shielding applications. [56]

2D Insulating Oxides

The development of new synthesis techniques such as solution-phase solvothermal growths and the topotactic deintercalation from layered precursors,[12] additionally expanded the flatland of 2D materials. In this framework the synthesis of 2D insulating oxides such as TiO_2, MoO_3 monolayers as well as the synthesis of mica-like and perovskite-like nanosheets [57] opened new possibilities towards the realization of full-2D nanodevices.

In conclusion, the journey in the flatland of 2D materials described above, although by no means exhaustive, has illustrated the large variety of compounds that to date have been included in this group. This ensemble can be further expanded by stacking the 2D layers in van der Waals heterostructures. The latter offer the intriguing possibility to build completely new artificial materials with properties engineered for each application.[19].

1.3 The path toward the device integration of 2D materials

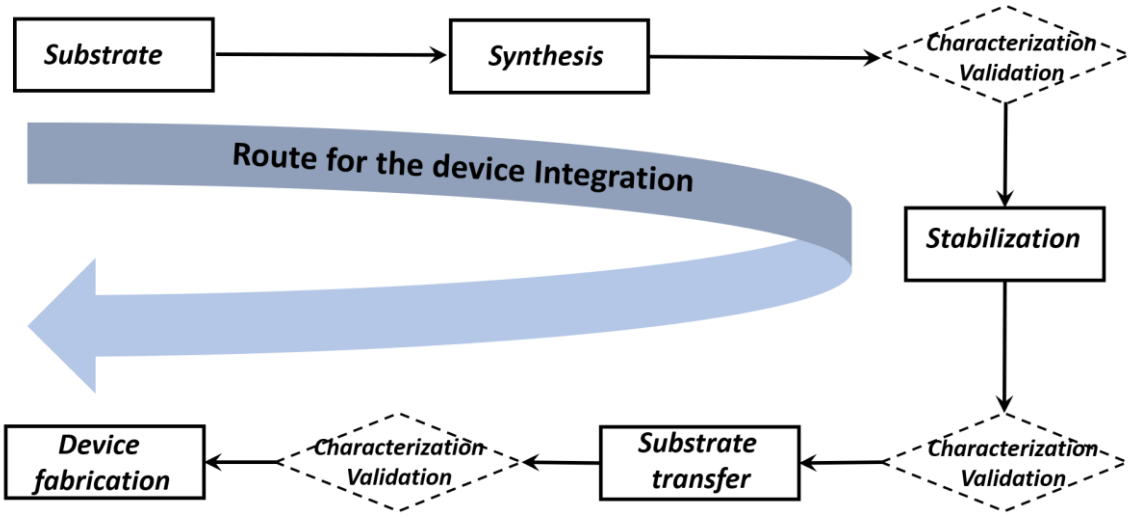

Figure 1.4 A general process flow diagram for the integration of 2D materials into devices.

Atomically thin 2D materials are among the most promising frontiers to make breakthroughs in next generation nanoelectronics. Due to the strong spatial confinement of the charge carriers within their few atom thick crystalline structures, new and exciting physical phenomena have been theoretically predicted[21], [38], [58] and experimentally proven.[59]–[61] Since the discovery of graphene, this possibility has ignited a tremendous scientific interest that has been concomitantly paralleled by the attempts to realize innovative devices.

The scientific and the technological benefits of 2D materials require the development of viable processing schemes that, on one hand, should allow an easy access to the characterization techniques used to probe their unique physical and chemical properties and, on the other, should warrant an effective exploitation in device architectures. Specifically, the following key-points can be considered as common traits of any processing method envisaged for the integration of 2D materials in functional devices.

i. The choice of an appropriate substrate that promotes the synthesis of the 2D crystalline layer permitting, at the same time, an easy decoupling from its surface.
ii. A synthesis protocol that guarantees an accurate control of the thickness and crystalline quality of the 2D material. In particular, the optimization of epitaxial synthesis techniques is a fundamental aspect to achieve a large area growth in view of the scalability requirements of the modern semiconductor industry.
iii. A stabilization strategy by encapsulation or passivation that, in the case of unstable 2D materials, can effectively prevent the air degradation problem. Furthermore, any encapsulation or passivation strategy should be designed so to allow an easy control of the stability and of the integrity of the material by means of external probes during all the subsequent processing steps.
iv. An “ad-hoc” transfer methodology from the original growth/synthesis substrate towards a target substrate. This is a critical step in all the situations where the original growth/synthesis substrate does not allow a direct exploitation of the 2D material into a device architecture.

v. Finally, the design of suitable device fabrication steps according to the chosen technological application of the 2D material.

In figure 1.4 we have sketched a simple process flow diagram that moves along the key points outlined above. In the case of air-unstable 2D materials this process flow diagram becomes often a mandatory path to achieve a reliable device implementation. This is especially true for the majority of air unstable monoelemental 2D materials and in particular for the members of the family of epitaxial Xenes.[36], [38], [62]

The device integration of epitaxial Xenes: from silicene to 2D phosphorus allotropes

Despite the potential breakthroughs that epitaxial Xenes may bring in the next generation nanoelectronics, the real applications of these materials have been hampered by the lack of viable processing standards for their synthesis and integration in device architectures. Such processing methods have to encompass a series of hurdles along the key-points highlighted above that begin from the development of epitaxial synthesis procedures on suitable substrates, then deal with the stabilization outside the growth environment and finally consider the choice of an appropriate methodology for the transfer of the epitaxial membrane from the growth substrate to new target substrates. Preliminary attempts along this direction have been carried out in the case of silicene but, in general, are completely unexplored in the case of other 2D epitaxial Xenes.[54], [62]

Aiming to expand the collection of 2D epitaxial Xenes that can be implemented in a technological platform, in this thesis work we have investigated the principal bottlenecks along the path for the integration in devices of 2D phosphorus allotropes. As we will see in the next paragraph, the interest in the synthesis and device integration of 2D phosphorus has tantalized the scientific community being motivated mainly by the early experimental and theoretical investigations on exfoliated phosphorene crystals.[63], [64] Subsequently, the experimental attempts to grow and characterize other epitaxial 2D phosphorous polymorphs [43], [44] additionally helped to ignite the scientific interest on these materials demonstrating the competitive advantages that they can bring in a post-graphene nanoelectronics.

1.4 2D Phosphorus allotropes

Elemental phosphorus exists in nature in different allotropic forms named as white, red, violet and black from their color.[65]

White, Red and Violet Phosphorus

White phosphorus (also called yellow phosphorus) is a molecular solid consisting of tetrahedral P_4 molecules that is extremely reactive, thermodynamically unstable and toxic in ambient conditions. It is the starting material to prepare all the other allotropic forms of elemental phosphorus. Red Phosphorus, for example, can be obtained by heating white phosphorus at 300°C. This allotrope is a stable amorphous solid that can be converted into a crystalline form known as violet phosphorus (or Hittorf's phosphorus) by daylong annealing at temperatures above 500°C. The structure of both red and violet phosphorus consists of polymeric phosphorus networks of different building units, typically, P_8 and P_9 cages linked together in tube-like structures (see figure 1.5).

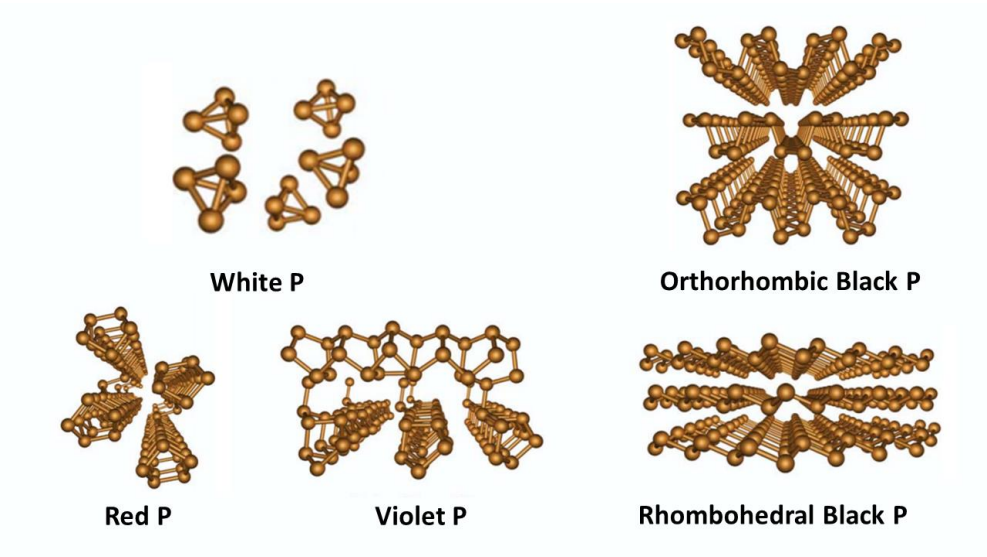

Figure 1.5 Atomic models of the principal elemental phosphorus allotropic forms.

Black Phosphorus

Black phosphorus (BP), instead, is the most stable among all the phosphorus allotropes. This allotrope was synthesized for the first time in 1914 from white phosphorus subjected to high pressures and temperatures[66] but since then various other methods have been reported for its preparation that can be achieved also at low pressures.[67] Black phosphorus is a layered van der Waals crystal with an orthorhombic crystalline structure in the D_{2h}^{18} space symmetry group that consists of parallel puckered atomic layers built of P_6 rings in a chair conformation (see figure 1.3). In each layer the phosphorus atoms are covalently bonded to three neighboring atoms with sp^3 hybrid atomic orbitals and with a lone pair of electrons protruding at ~45° out of the atomic planes. Black phosphorus crystals are characterized by a strong structural anisotropy that is reflected in electronic, optical, thermal and mechanical properties markedly different along the two principal in-plane directions, conventionally called armchair (AC) and zigzag (ZZ). In addition to the orthorhombic phase bulk BP also exhibits rhombohedral and simple cubic phases at high pressures. The rhombohedral BP phase is stable at pressures above 5.5GPa and consists of stacked honeycomb-like atomic layers (see figure 1.5) each one with a structure similar to the buckled honeycomb lattices of the 2D allotropes of silicon and germanium. The crystalline structure of the rhombohedral high-pressure phase of BP is also identical to the thermodynamically stable ambient pressure phases of the other group 15 elements: Arsenic, Antimony and Bismuth.

2D Phosphorene (or α-P)

As anticipated before, black phosphorus can be exfoliated down to a single layer to isolate a 2D crystal of phosphorus called phosphorene. The theoretical freestanding crystalline structure of this 2D allotrope of phosphorus is illustrated in figure 1.6. At variance with graphene, that is isolated from the natural occurring graphite and it is chemically and thermodynamic stable, phosphorene is not chemically stable when exposed to air but it is highly reactive and prone to an immediate degradation since it is isolated from layered BP crystals that do not exist in nature as pure elemental solids. According to the official IUPAC chemical terminology the name of phosphorene given to this 2D allotrope of phosphorus is not entirely correct. In fact, the *-ene*

suffix is assigned only to systems with double alkene bonds resulting from sp^2 hybridized (or partially hybridized) atomic orbitals, like in the case of graphene or silicene and germanene. A more appropriate name for phosphorene should be *2D-phosphane* even though the term phosphane refers to the saturated hydrides of phosphorus with general formula P_nH_{n+2}.[65] Anyway, in the following we will continue to follow the conventional (and more common) nomenclature indicating by phosphorene the 2D orthorhombic allotrope of phosphorus, that can be obtained by exfoliation from 3D BP crystals.

The scientific and technological interest in 2D phosphorene has been reawakened only in recent years mostly motivated by the exceptional properties of BP crystals. The p-type semiconducting character with a layer-dependent direct bandgap, varying from 0.3 eV in bulk to 1.52 eV in single-layer phosphorene, the extremely high charge carrier mobility, with values up to $\sim 1000\ cm^2V^{-1}s^{-1}$ in 10 nm thick samples[68] and theoretically predicted values of 10000-26000 $cm^2V^{-1}s^{-1}$ in single-layer phosphorene,[69] bridge the gap between the electronic properties of graphene and those of TMDs making few layer BP an optimal candidate for low power high-speed flexible electronic applications.[70]–[72] Furthermore, due to the tunable bandgap, ranging from infrared to visible frequencies, and thanks to the high absorption coefficient in the UV region, few layers BP finds also promising applications in photodetection. Therefore, few and multilayer BP samples have been exploited in a variety of digital/RF electronics and optoelectronics devices ranging from ultrathin field-effect transistor[68], [73] phototransistors,[74], [75] to vdW heterojunctions diode solar cells.[76] Additionally, the inherent anisotropy of its crystalline structure offers also new degree of freedoms for the orientational control of the charge carrier dynamics that can be used for high-efficiency thermoelectric devices [77] or to fabricate novel devices concepts.[78]

New two-dimensional phases of phosphorus

Besides phosphorene or α-P, elemental phosphorus possess also many other energetically stable 2D allotropes both with a honeycomb structures, β-P[79] (Blue-P), γ-P, δ-P[80], λ-P (Green-P)[81] and not-honeycomb structures ε-P, ζ-P, η-P, θ-P[82] and many other "porous" 2D phases that can be obtained through the topological assembling of phosphorus monomers, dimers, trimers, tetramers and hexamers[83] plus some special structures denoted as Ψ-P[84] and Kagome-P.[85] However, the number of experimentally synthesized 2D phases of phosphorus is fairly less if compared to the number of those that have been predicted to be stable by theoretical calculations.[86]

2D Blue phosphorene (or β-P)

In addition to phosphorene or α-P, the only other 2D phase of phosphorus that has been considered synthesized so far is the rhombohedral β-P phase known with the name of blue-phosphorene due to the theoretically predicted bandgap value above 2eV.[87]

The synthesis of blue-phosphorene (β-P) has been claimed for the first time in 2016 by Zhang et al [43] by means of epitaxial growth on the (111) oriented surface of gold. Despite there is still an ongoing debate on the true nature of this epitaxial phosphorus form [88]–[90] that prevents its complete assignment to the family of 2D crystalline Xenes (in terms of an epitaxial 2D blue-phosphorene crystal), in the following we will use the name of epitaxial phosphorus or shortly Epi-P to refer to any kind of blue-phosphorene form grown by epitaxy on substrates.

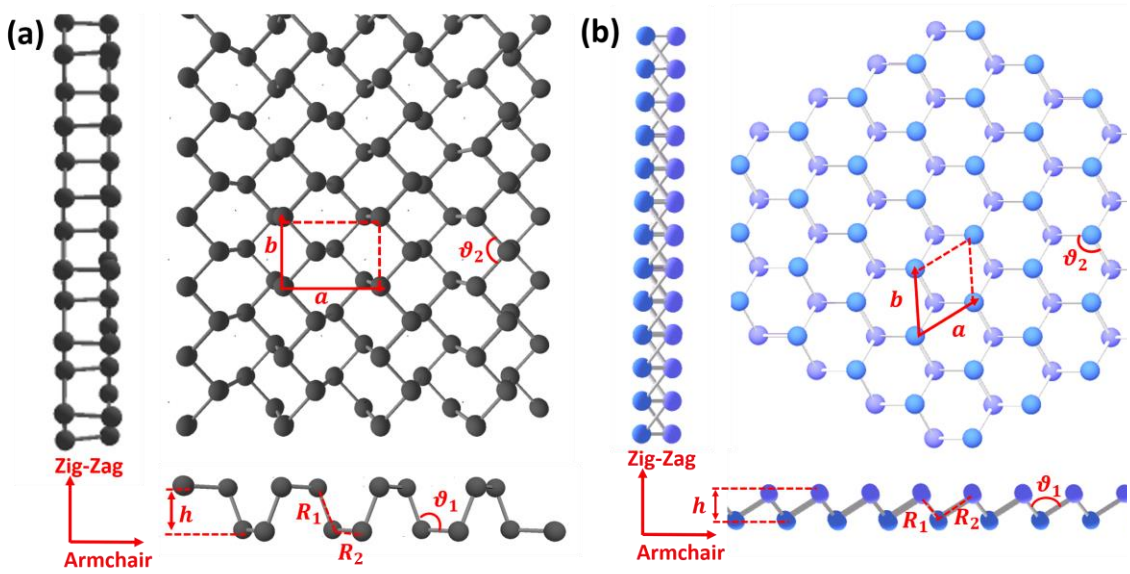

Figure 1.6 Top and side view of the crystalline structures of the freestanding 2D $\boldsymbol{\alpha}$-P or Phosphorene phase **(a)** and of 2D $\boldsymbol{\beta}$-P or Blue-Phosphorene phase**(b)**. The zigzag and armchair symmetry directions for $\boldsymbol{\alpha}$-P and $\boldsymbol{\beta}$-P are indicated on the bottom left.

Table 1.1 Geometrical parameters, bandgap and electron/hole mobilities of the 2D $\boldsymbol{\alpha}$-P and $\boldsymbol{\beta}$-P phosphorus allotropes as calculated from theory in refs.[69][77] for $\boldsymbol{\alpha}$-P and refs.[79][87][92]for $\boldsymbol{\beta}$-P.

		α-P	β-P
Symmetry/Space group		Orthorhombic/$\boldsymbol{D_{2h}^{7}}$	Rhombohedral/$\boldsymbol{D_{3d}^{5}}$
Lattice vectors	$\boldsymbol{a}$(Å)	4.58	3.33
	$\boldsymbol{b}$(Å)	3.32	$\boldsymbol{a = b}$
Buckling Parameter	$\boldsymbol{h}$(Å)	3.20	1.23
Bond Lengths	$\boldsymbol{R_1}$(Å)	2.28	2.26
	$\boldsymbol{R_2}$(Å)	2.24	$\boldsymbol{R_1 = R_2}$
Bond Angles	$\boldsymbol{\vartheta_1}$	103.51°	93.07°
	$\boldsymbol{\vartheta_2}$	96°	$\boldsymbol{\vartheta_2 = \vartheta_1}$
Bandgap Value (eV)		1.52	2.65
Electron Mobility ($10^3 cm^2 V^{-1} s^{-1}$)		$\boldsymbol{\mu_{ZZ}} \cong 0.08$ $\mu_{AC} \cong 1.10$	$\boldsymbol{\mu_{ZZ}} \cong 11.4$ $\boldsymbol{\mu_{AC}} \cong 10.3$
Hole Mobility ($10^3 cm^2 V^{-1} s^{-1}$)		$\mu_{ZZ} \cong$10-26 $\mu_{AC} \cong$ 0.64-0.70	$\boldsymbol{\mu_{ZZ}} \cong 0.33$ $\boldsymbol{\mu_{AC}} \cong 0.22$

Figure 1.4 illustrates the atomic models of the theoretical freestanding crystalline structures of α-P and β-P with the respective orthorhombic and rhombohedral unit cells. The symmetries and the theoretical geometric parameters of their crystalline structures as well as the values calculated for the bandgap and the electron mobilities are reported in Table 1. As can be seen in figure 1.3, blue phosphorene (β-P) possesses a buckled honeycomb-like lattice similar to the buckled honeycomb lattices of the 2D allotropes of silicon and germanium. The only difference with the latter is the higher value of the buckling parameter that in the case of β-P is $h = 1.23$ Å whereas for silicene is $h =$ Å 0.44 and for germanene is $h = 0.64$ Å. Unlike phosphorene (α-P), the crystalline structure of blue-P (β-P) is characterized by an evident in-plane isotropy that does not lead to significant differences in the electronic properties along the conventional zigzag and armchair directions of its lattice structure as indicated in figure 1.4.
Specifically, the value of the holes and electron mobilities of blue-P along the ZZ and the AC directions do not differ much in contrast to the case of phosphorene where these quantities are characterized by a more marked anisotropy. Theoretical calculations suggest that the n-type semiconducting character of blue-P and its high-charge carrier mobility can be exploited for the realization of high-speed field effect devices.[91], [92] Moreover, the possibility to tailor the blue-P electronic properties by surface functionalization or by the application of strain open potentialities for the observation of 2D topological insulator phases[93] as well as for the emergence of Dirac cones in its electronic structure.[94]

However, despite a plethora of theoretical studies on the possible applications of blue-P also in combination with other 2D materials to build engineered vdW heterostructures,[95]–[98] real device applications have not been reported yet. The reason for this can be found in the lack of a specific device integration method for this epitaxial material.

1.5 Motivation and outline of this thesis work

In this thesis work we examined some of the unresolved bottlenecks that prevent the establishment of a reliable route for the integration in devices of 2D phosphorus allotropes considering, in particular, the case of α (phosphorene) and β (blue-phosphorene) 2D phosphorus polymorphs.

Regarding the 2D α-P polymorph the device integration route sketched in figure 1.4 can be considered on an almost consolidated path. The reason for this can be, in part, ascribed to the existence of a layered allotrope, i.e. black phosphorus, from which the 2D α-P phase can be isolated and, in part, to the existence of substrate transfer methods and device fabrication procedures originally conceived for other 2D materials but suitably readapted in the case of 2D α-P. The only two remaining bottlenecks along the device integration path of 2D α-P can be individuated in:

(i) the air-degradation issue and,
(ii) the lack of a scalable synthesis protocol to produce 2D α-P on large areas with a high crystalline quality and a precise control of the thickness.

The air-instability issue of 2D α-P has gained a lot of scientific interest in the past and effective encapsulation methods compatible with the requirements of various device processing schemes have been successfully demonstrated.[99]–[102] The issues related to the scalability

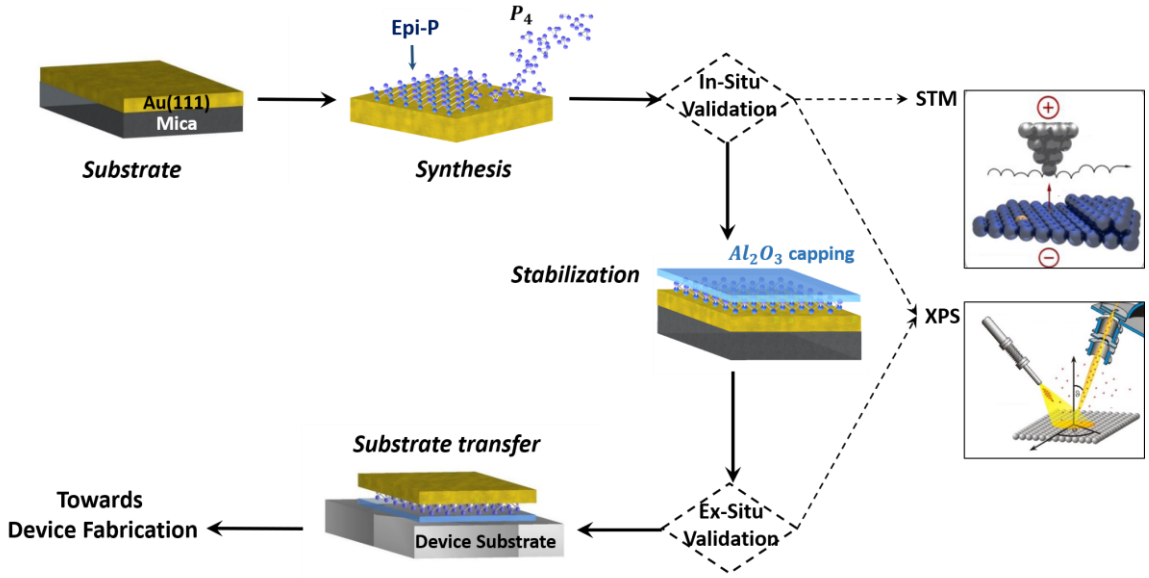

Figure 1.7 The general device integration path proposed in this thesis work for epitaxial 2D $\boldsymbol{\beta}$-phosphorene grown on Au(111)/mica substrates.

and to the lack of control on the thickness, size and crystalline quality of the samples, instead, are aspects that require further investigation in order to find better synthesis protocols for their optimization. In particular, in the case of the synthesis of 2D α-P by means of exfoliation techniques, the control of the thickness down to the extreme 2D limit is quite difficult due to the statistical nature of this kind of processes that often produce a huge amount of disperse few-layers and multilayer flakes on a substrate.

Within this context, the **Chapter 2** of the present thesis work begins by illustrating the above-mentioned problems in the top-down synthesis of α-P by exfoliation. Micro-Raman spectroscopy is, then, presented both as a tool to achieve a characterization of the thickness of exfoliated BP samples and as a methodology to investigate the thinning process of BP crystals by laser ablation. A better control on the thickness of the BP samples down to the ultimate 2D α-P limit with the laser thinning approach requires at least a preliminary knowledge of the effects introduced by the presence of the supporting substrate. Such analysis is carried out in detail in the final part of chapter 2.

Regarding the case of 2D β-P, instead, the processing methods conceived for the integration of 2D α-P in device architectures cannot be straightforwardly applied to it for two main reasons. On one hand, the synthesis of 2D β-P requires more stringent conditions, being based exclusively on bottom-up epitaxial techniques in UHV and, on the other, 2D β-P is extremely unstable outside the growth environment. Therefore, in the case of 2D β-P the device integration route has a not-well established trajectory and it is conditioned by a series of challenges related to its synthesis, to its instability outside the growth environment and to the lack of handling procedures for the substrate transfer and the device fabrication.

Figure 1.7 depicts schematically the principal steps investigated in the present thesis work to solve the above-mentioned issues and thus bring epitaxial 2D β-P towards a preliminary integration in device architectures. Each one of these steps is the object of discussion in the chapters 3, 4, 5 of the present thesis.

In detail, **Chapter 3** illustrates the problem of the choice of the substrate and the MBE growth of 2D β-P by means of Scanning Tunneling Microscopy (STM) and X-Ray Photoelectron Spectroscopy (XPS). The conditions for the growth of epitaxial phosphorus on Au(111)\mica, the models proposed for its atomic structure and the open questions on its electronic nature are analyzed in details, providing also possible perspectives for further researches.

Chapter 4 focusses on the study of the air-instability problem in 2D β-P investigating, with the aid of XPS measurement, the oxidation of epitaxial phosphorus on gold inside and outside the UHV growth environment. The results obtained have been interpreted with a critical exam of the models proposed in literature for the well-known air degradation mechanism of 2D α-P. To circumvent the air-instability problem of epitaxial phosphorus on gold an in-situ encapsulation method by means of an Al_2O_3 protective layer has been developed. The effectiveness of this encapsulation method is subsequently discussed with the aid of XPS and AFM measurements.

Chapter 5 deals with the development of methodologies for the transfer of the encapsulated epitaxial phosphorus layer from the metallic growth substrate towards target substrates for the integration into device architectures. In particular, two methods have been investigated: a *wet* or chemical approach and a *dry* or mechanical approach. Both these substrate transfer methodologies can be suitably generalized to the whole class of 2D epitaxial Xenes grown on metallic substrates and pave the way for the establishment of methodological protocols for their manipulation. In this respect, the universality of the *dry* substrate transfer method has been specifically exploited for the fabrication of two possible device architectures: a FET device based on encapsulated multilayer silicene samples grown on Ag(111)/mica and a MIM device based on encapsulated epitaxial phosphorus on Au(111)/mica. For the latter device structure, two possible microscopic mechanisms at origin of the resistive switching effect are proposed foreseeing for epitaxial phosphorus future applications in non-volatile memories.

Chapter 6 concludes the thesis work summarizing the main result achieved in the analysis of the various issues encountered along the device integration path of the α- and β- 2D phosphorus polymorphs. Moreover, the future research perspectives for the integration of 2D β-P in device architectures are also discussed.

Bibliography

[1] G. E. Moore, “Cramming more components onto integrated circuits, Reprinted from Electronics, volume 38, number 8, April 19, 1965, pp.114 ff.,” *IEEE Solid-State Circuits Soc. Newsl.*, vol. 11, no. 3, pp. 33–35, Sep. 2006, doi: 10.1109/N-SSC.2006.4785860.

[2] H. N. Khan, D. A. Hounshell, and E. R. H. Fuchs, “Science and research policy at the end of Moore’s law,” *Nat Electron*, vol. 1, no. 1, pp. 14–21, Jan. 2018, doi: 10.1038/s41928-017-0005-9.

[3] R. H. Dennard, F. H. Gaensslen, H.-N. Yu, V. L. Rideout, E. Bassous, and A. R. LeBlanc, “Design of ion-implanted MOSFET’s with very small physical dimensions,” *IEEE J. Solid-State Circuits*, vol. 9, no. 5, pp. 256–268, Oct. 1974, doi: 10.1109/JSSC.1974.1050511.

[4] M. M. Waldrop, “The chips are down for Moore’s law,” *Nature*, vol. 530, no. 7589, pp. 144–147, Feb. 2016, doi: 10.1038/530144a.

[5] P. A. Packan, “DEVICE PHYSICS:Pushing the Limits,” *Science*, vol. 285, no. 5436, pp. 2079–2081, Sep. 1999, doi: 10.1126/science.285.5436.2079.

[6] T. N. Theis and H.-S. P. Wong, "The End of Moore's Law: A New Beginning for Information Technology," *Comput. Sci. Eng.*, vol. 19, no. 2, pp. 41–50, Mar. 2017, doi: 10.1109/MCSE.2017.29.

[7] K. Ahmed and K. Schuegraf, "Transistor wars," *IEEE Spectr.*, vol. 48, no. 11, pp. 50–66, Nov. 2011, doi: 10.1109/MSPEC.2011.6056626.

[8] K. S. Novoselov, "Electric Field Effect in Atomically Thin Carbon Films," *Science*, vol. 306, no. 5696, pp. 666–669, Oct. 2004, doi: 10.1126/science.1102896.

[9] D. Akinwande, N. Petrone, and J. Hone, "Two-dimensional flexible nanoelectronics," *Nature Communications*, vol. 5, p. 5678, Dec. 2014, doi: 10.1038/ncomms6678.

[10] D. Akinwande *et al.*, "Graphene and two-dimensional materials for silicon technology," *Nature*, vol. 573, no. 7775, pp. 507–518, Sep. 2019, doi: 10.1038/s41586-019-1573-9.

[11] M. Houssa, A. Dimoulas, and A. Molle, Eds., *2D materials for nanoelectronics*. Boca Raton: CRC Press, Taylor & Francis Group, 2016.

[12] S. Z. Butler *et al.*, "Progress, Challenges, and Opportunities in Two-Dimensional Materials Beyond Graphene," *ACS Nano*, vol. 7, no. 4, pp. 2898–2926, Apr. 2013, doi: 10.1021/nn400280c.

[13] A. K. Geim and K. S. Novoselov, "The rise of graphene," *Nature Materials*, vol. 6, no. 3, pp. 183–191, Mar. 2007, doi: 10.1038/nmat1849.

[14] D. C. Elias *et al.*, "Control of Graphene's Properties by Reversible Hydrogenation: Evidence for Graphane," *Science*, vol. 323, no. 5914, pp. 610–613, Jan. 2009, doi: 10.1126/science.1167130.

[15] K. S. Novoselov *et al.*, "Two-dimensional atomic crystals," *Proceedings of the National Academy of Sciences*, vol. 102, no. 30, pp. 10451–10453, Jul. 2005, doi: 10.1073/pnas.0502848102.

[16] M. Chhowalla, H. S. Shin, G. Eda, L.-J. Li, K. P. Loh, and H. Zhang, "The chemistry of two-dimensional layered transition metal dichalcogenide nanosheets," *Nature Chemistry*, vol. 5, no. 4, pp. 263–275, Apr. 2013, doi: 10.1038/nchem.1589.

[17] Q. H. Wang, K. Kalantar-Zadeh, A. Kis, J. N. Coleman, and M. S. Strano, "Electronics and optoelectronics of two-dimensional transition metal dichalcogenides," *Nature Nanotechnology*, vol. 7, no. 11, pp. 699–712, Nov. 2012, doi: 10.1038/nnano.2012.193.

[18] D. Pacilé, J. C. Meyer, Ç. Ö. Girit, and A. Zettl, "The two-dimensional phase of boron nitride: Few-atomic-layer sheets and suspended membranes," *Appl. Phys. Lett.*, vol. 92, no. 13, p. 133107, Mar. 2008, doi: 10.1063/1.2903702.

[19] A. K. Geim and I. V. Grigorieva, "Van der Waals heterostructures," *Nature*, vol. 499, no. 7459, pp. 419–425, Jul. 2013, doi: 10.1038/nature12385.

[20] K. Zhang, Y. Feng, F. Wang, Z. Yang, and J. Wang, "Two dimensional hexagonal boron nitride (2D-hBN): synthesis, properties and applications," *J. Mater. Chem. C*, vol. 5, no. 46, pp. 11992–12022, 2017, doi: 10.1039/C7TC04300G.

[21] C. L. Kane and E. J. Mele, "Quantum Spin Hall Effect in Graphene," *Phys. Rev. Lett.*, vol. 95, no. 22, p. 226801, Nov. 2005, doi: 10.1103/PhysRevLett.95.226801.

[22] K. S. Novoselov *et al.*, "Two-dimensional gas of massless Dirac fermions in graphene," *Nature*, vol. 438, no. 7065, pp. 197–200, Nov. 2005, doi: 10.1038/nature04233.

[23] J. R. Schaibley *et al.*, "Valleytronics in 2D materials," *Nat Rev Mater*, vol. 1, no. 11, p. 16055, Nov. 2016, doi: 10.1038/natrevmats.2016.55.

[24] A. J. Mannix, B. Kiraly, M. C. Hersam, and N. P. Guisinger, "Synthesis and chemistry of elemental 2D materials," *Nat Rev Chem*, vol. 1, no. 2, p. 0014, Feb. 2017, doi: 10.1038/s41570-016-0014.

[25] N. R. Glavin *et al.*, "Emerging Applications of Elemental 2D Materials," *Adv. Mater.*, vol. 32, no. 7, p. 1904302, Feb. 2020, doi: 10.1002/adma.201904302.

[26] W. A. de Heer *et al.*, "Large area and structured epitaxial graphene produced by confinement controlled sublimation of silicon carbide," *Proceedings of the National Academy of Sciences*, vol. 108, no. 41, pp. 16900–16905, Oct. 2011, doi: 10.1073/pnas.1105113108.

[27] L. Gao, J. R. Guest, and N. P. Guisinger, "Epitaxial Graphene on Cu(111)," *Nano Lett.*, vol. 10, no. 9, pp. 3512–3516, Sep. 2010, doi: 10.1021/nl1016706.

[28] A. K. Geim, "Graphene: Status and Prospects," *Science*, vol. 324, no. 5934, pp. 1530–1534, Jun. 2009, doi: 10.1126/science.1158877.

[29] P. Vogt *et al.*, "Silicene: Compelling Experimental Evidence for Graphenelike Two-Dimensional Silicon," *Physical Review Letters*, vol. 108, no. 15, Apr. 2012, doi: 10.1103/PhysRevLett.108.155501.

[30] C. Grazianetti, E. Cinquanta, and A. Molle, "Two-dimensional silicon: the advent of silicene," *2D Materials*, vol. 3, no. 1, p. 012001, Jan. 2016, doi: 10.1088/2053-1583/3/1/012001.

[31] A. Koma, "Van der Waals epitaxy—a new epitaxial growth method for a highly lattice-mismatched system," *Thin Solid Films*, vol. 216, no. 1, pp. 72–76, Aug. 1992, doi: 10.1016/0040-6090(92)90872-9.

[32] B. Lalmi *et al.*, "Epitaxial growth of a silicene sheet," *Applied Physics Letters*, vol. 97, no. 22, p. 223109, Nov. 2010, doi: 10.1063/1.3524215.

[33] M. E. Dávila, L. Xian, S. Cahangirov, A. Rubio, and G. Le Lay, "Germanene: a novel two-dimensional germanium allotrope akin to graphene and silicene," *New Journal of Physics*, vol. 16, no. 9, p. 095002, Sep. 2014, doi: 10.1088/1367-2630/16/9/095002.

[34] F. Zhu *et al.*, "Epitaxial growth of two-dimensional stanene," *Nature Mater*, vol. 14, no. 10, pp. 1020–1025, Oct. 2015, doi: 10.1038/nmat4384.

[35] J. Yuhara *et al.*, "Large area planar stanene epitaxially grown on Ag(1 1 1)," *2D Mater.*, vol. 5, no. 2, p. 025002, Jan. 2018, doi: 10.1088/2053-1583/aa9ea0.

[36] C. Grazianetti, C. Martella, and A. Molle, "The Xenes Generations: A Taxonomy of Epitaxial Single-Element 2D Materials," *physica status solidi (RRL) – Rapid Research Letters*, p. 1900439, Oct. 2019, doi: 10.1002/pssr.201900439.

[37] S. Cahangirov, M. Topsakal, E. Aktürk, H. Şahin, and S. Ciraci, "Two- and One-Dimensional Honeycomb Structures of Silicon and Germanium," *Physical Review Letters*, vol. 102, no. 23, Jun. 2009, doi: 10.1103/PhysRevLett.102.236804.

[38] A. Molle, J. Goldberger, M. Houssa, Y. Xu, S.-C. Zhang, and D. Akinwande, "Buckled two-dimensional Xene sheets," *Nature Materials*, vol. 16, no. 2, pp. 163–169, Jan. 2017, doi: 10.1038/nmat4802.

[39] A. J. Mannix *et al.*, "Synthesis of borophenes: Anisotropic, two-dimensional boron polymorphs," *Science*, vol. 350, no. 6267, pp. 1513–1516, Dec. 2015, doi: 10.1126/science.aad1080.

[40] B. Feng *et al.*, "Experimental realization of two-dimensional boron sheets," *Nature Chem*, vol. 8, no. 6, pp. 563–568, Jun. 2016, doi: 10.1038/nchem.2491.

[41] V. Kochat *et al.*, "Atomically thin gallium layers from solid-melt exfoliation," *Sci. Adv.*, vol. 4, no. 3, p. e1701373, Mar. 2018, doi: 10.1126/sciadv.1701373.

[42] J. Yuhara, B. He, N. Matsunami, M. Nakatake, and G. Le Lay, "Graphene's Latest Cousin: Plumbene Epitaxial Growth on a 'Nano WaterCube,'" *Adv. Mater.*, vol. 31, no. 27, p. 1901017, Jul. 2019, doi: 10.1002/adma.201901017.

[43] J. L. Zhang *et al.*, "Epitaxial Growth of Single Layer Blue Phosphorus: A New Phase of Two-Dimensional Phosphorus," *Nano Letters*, vol. 16, no. 8, pp. 4903–4908, Aug. 2016, doi: 10.1021/acs.nanolett.6b01459.

[44] W. Zhang *et al.*, "Epitaxial Synthesis of Blue Phosphorene," *Small*, vol. 14, no. 51, p. 1804066, Dec. 2018, doi: 10.1002/smll.201804066.

[45] S. M. Beladi-Mousavi, A. M. Pourrahimi, Z. Sofer, and M. Pumera, "Atomically Thin 2D-Arsenene by Liquid-Phased Exfoliation: Toward Selective Vapor Sensing," *Adv. Funct. Mater.*, p. 1807004, Dec. 2018, doi: 10.1002/adfm.201807004.

[46] P. Ares *et al.*, "Mechanical Isolation of Highly Stable Antimonene under Ambient Conditions," *Advanced Materials*, vol. 28, no. 30, pp. 6332–6336, Aug. 2016, doi: 10.1002/adma.201602128.

[47] C. Gibaja *et al.*, "Few-Layer Antimonene by Liquid-Phase Exfoliation," *Angewandte Chemie International Edition*, vol. 55, no. 46, pp. 14345–14349, Nov. 2016, doi: 10.1002/anie.201605298.

[48] X. Wu *et al.*, "Epitaxial Growth and Air-Stability of Monolayer Antimonene on $PdTe_2$," *Advanced Materials*, vol. 29, no. 11, p. 1605407, Mar. 2017, doi: 10.1002/adma.201605407.

[49] F. Reis *et al.*, "Bismuthene on a SiC substrate: A candidate for a high-temperature quantum spin Hall material," *Science*, vol. 357, no. 6348, pp. 287–290, Jul. 2017, doi: 10.1126/science.aai8142.

[50] J. Qin *et al.*, "Controlled Growth of a Large-Size 2D Selenium Nanosheet and Its Electronic and Optoelectronic Applications," *ACS Nano*, vol. 11, no. 10, pp. 10222–10229, Oct. 2017, doi: 10.1021/acsnano.7b04786.

[51] Q. Wang, M. Safdar, K. Xu, M. Mirza, Z. Wang, and J. He, "Van der Waals Epitaxy and Photoresponse of Hexagonal Tellurium Nanoplates on Flexible Mica Sheets," *ACS Nano*, vol. 8, no. 7, pp. 7497–7505, Jul. 2014, doi: 10.1021/nn5028104.

[52] P. Ranjan *et al.*, "Freestanding Borophene and Its Hybrids," *Adv. Mater.*, vol. 31, no. 27, p. 1900353, Jul. 2019, doi: 10.1002/adma.201900353.

[53] J. Guo *et al.*, "Two-dimensional tellurium–polymer membrane for ultrafast photonics," *Nanoscale*, vol. 11, no. 13, pp. 6235–6242, 2019, doi: 10.1039/C9NR00736A.

[54] L. Tao *et al.*, "Silicene field-effect transistors operating at room temperature," *Nature Nanotechnology*, vol. 10, no. 3, pp. 227–231, Feb. 2015, doi: 10.1038/nnano.2014.325.

[55] Y. Gogotsi and B. Anasori, "The Rise of MXenes," *ACS Nano*, vol. 13, no. 8, pp. 8491–8494, Aug. 2019, doi: 10.1021/acsnano.9b06394.

[56] B. Anasori, M. R. Lukatskaya, and Y. Gogotsi, "2D metal carbides and nitrides (MXenes) for energy storage," *Nat Rev Mater*, vol. 2, no. 2, p. 16098, Feb. 2017, doi: 10.1038/natrevmats.2016.98.

[57] M. Osada and T. Sasaki, "Two-Dimensional Dielectric Nanosheets: Novel Nanoelectronics From Nanocrystal Building Blocks," *Adv. Mater.*, vol. 24, no. 2, pp. 210–228, Jan. 2012, doi: 10.1002/adma.201103241.

[58] X. Qian, J. Liu, L. Fu, and J. Li, "Quantum spin Hall effect in two-dimensional transition metal dichalcogenides," *Science*, vol. 346, no. 6215, pp. 1344–1347, Dec. 2014, doi: 10.1126/science.1256815.

[59] A. S. Mayorov *et al.*, "Micrometer-Scale Ballistic Transport in Encapsulated Graphene at Room Temperature," *Nano Letters*, vol. 11, no. 6, pp. 2396–2399, Jun. 2011, doi: 10.1021/nl200758b.

[60] Y. Cao *et al.*, "Unconventional superconductivity in magic-angle graphene superlattices," *Nature*, vol. 556, no. 7699, pp. 43–50, Apr. 2018, doi: 10.1038/nature26160.

[61] V. Fatemi *et al.*, "Electrically tunable low-density superconductivity in a monolayer topological insulator," *Science*, vol. 362, no. 6417, pp. 926–929, Nov. 2018, doi: 10.1126/science.aar4642.

[62] A. Molle, C. Grazianetti, L. Tao, D. Taneja, Md. H. Alam, and D. Akinwande, "Silicene, silicene derivatives, and their device applications," *Chemical Society Reviews*, vol. 47, no. 16, pp. 6370–6387, 2018, doi: 10.1039/C8CS00338F.

[63] H. Liu *et al.*, "Phosphorene: An Unexplored 2D Semiconductor with a High Hole Mobility," *ACS Nano*, vol. 8, no. 4, pp. 4033–4041, Apr. 2014, doi: 10.1021/nn501226z.

[64] A. Castellanos-Gomez *et al.*, "Isolation and characterization of few-layer black phosphorus," *2D Materials*, vol. 1, no. 2, p. 025001, Jun. 2014, doi: 10.1088/2053-1583/1/2/025001.

[65] R. Gusmão, Z. Sofer, and M. Pumera, "Black Phosphorus Rediscovered: From Bulk Material to Monolayers," *Angew. Chem. Int. Ed.*, vol. 56, no. 28, pp. 8052–8072, Jul. 2017, doi: 10.1002/anie.201610512.

[66] P. W. Bridgman, "TWO NEW MODIFICATIONS OF PHOSPHORUS.," *J. Am. Chem. Soc.*, vol. 36, no. 7, pp. 1344–1363, Jul. 1914, doi: 10.1021/ja02184a002.

[67] A. Brown and S. Rundqvist, "Refinement of the crystal structure of black phosphorus," *Acta Cryst*, vol. 19, no. 4, pp. 684–685, Oct. 1965, doi: 10.1107/S0365110X65004140.

[68] L. Li *et al.*, "Black phosphorus field-effect transistors," *Nature Nanotechnology*, vol. 9, no. 5, pp. 372–377, Mar. 2014, doi: 10.1038/nnano.2014.35.

[69] J. Qiao, X. Kong, Z.-X. Hu, F. Yang, and W. Ji, "High-mobility transport anisotropy and linear dichroism in few-layer black phosphorus," *Nature Communications*, vol. 5, Jul. 2014, doi: 10.1038/ncomms5475.

[70] X. Ling, H. Wang, S. Huang, F. Xia, and M. S. Dresselhaus, "The renaissance of black phosphorus," *Proceedings of the National Academy of Sciences*, vol. 112, no. 15, pp. 4523–4530, Apr. 2015, doi: 10.1073/pnas.1416581112.

[71] A. Castellanos-Gomez, "Black Phosphorus: Narrow Gap, Wide Applications," *The Journal of Physical Chemistry Letters*, vol. 6, no. 21, pp. 4280–4291, Nov. 2015, doi: 10.1021/acs.jpclett.5b01686.

[72] A. Carvalho, M. Wang, X. Zhu, A. S. Rodin, H. Su, and A. H. Castro Neto, "Phosphorene: from theory to applications," *Nature Reviews Materials*, vol. 1, no. 11, p. 16061, Aug. 2016, doi: 10.1038/natrevmats.2016.61.

[73] W. Zhu *et al.*, "Flexible Black Phosphorus Ambipolar Transistors, Circuits and AM Demodulator," *Nano Letters*, vol. 15, no. 3, pp. 1883–1890, Mar. 2015, doi: 10.1021/nl5047329.

[74] M. Buscema, D. J. Groenendijk, S. I. Blanter, G. A. Steele, H. S. J. van der Zant, and A. Castellanos-Gomez, "Fast and Broadband Photoresponse of Few-Layer Black Phosphorus Field-Effect Transistors," *Nano Letters*, vol. 14, no. 6, pp. 3347–3352, Jun. 2014, doi: 10.1021/nl5008085.

[75] M. Buscema, D. J. Groenendijk, G. A. Steele, H. S. J. van der Zant, and A. Castellanos-Gomez, "Photovoltaic effect in few-layer black phosphorus PN junctions defined by local electrostatic gating," *Nature Communications*, vol. 5, p. 4651, Aug. 2014, doi: 10.1038/ncomms5651.

[76] Y. Deng *et al.*, "Black Phosphorus–Monolayer MoS_2 van der Waals Heterojunction p–n Diode," *ACS Nano*, vol. 8, no. 8, pp. 8292–8299, Aug. 2014, doi: 10.1021/nn5027388.

[77] R. Fei, A. Faghaninia, R. Soklaski, J.-A. Yan, C. Lo, and L. Yang, "Enhanced Thermoelectric Efficiency via Orthogonal Electrical and Thermal Conductances in Phosphorene," *Nano Letters*, vol. 14, no. 11, pp. 6393–6399, Nov. 2014, doi: 10.1021/nl502865s.

[78] W. Xin *et al.*, "Black-Phosphorus-Based Orientation-Induced Diodes," *Advanced Materials*, p. 1704653, Nov. 2017, doi: 10.1002/adma.201704653.

[79] Z. Zhu and D. Tománek, "Semiconducting Layered Blue Phosphorus: A Computational Study," *Physical Review Letters*, vol. 112, no. 17, May 2014, doi: 10.1103/PhysRevLett.112.176802.

[80] J. Guan, Z. Zhu, and D. Tománek, "Phase Coexistence and Metal-Insulator Transition in Few-Layer Phosphorene: A Computational Study," *Physical Review Letters*, vol. 113, no. 4, Jul. 2014, doi: 10.1103/PhysRevLett.113.046804.

[81] W. H. Han, S. Kim, I.-H. Lee, and K. J. Chang, "Prediction of Green Phosphorus with Tunable Direct Band Gap and High Mobility," *J. Phys. Chem. Lett.*, vol. 8, no. 18, pp. 4627–4632, Sep. 2017, doi: 10.1021/acs.jpclett.7b02153.

[82] M. Wu, H. Fu, L. Zhou, K. Yao, and X. C. Zeng, "Nine New Phosphorene Polymorphs with Non-Honeycomb Structures: A Much Extended Family," *Nano Letters*, vol. 15, no. 5, pp. 3557–3562, May 2015, doi: 10.1021/acs.nanolett.5b01041.

[83] Z. Zhuo, X. Wu, and J. Yang, "Two-Dimensional Phosphorus Porous Polymorphs with Tunable Band Gaps," *J. Am. Chem. Soc.*, vol. 138, no. 22, pp. 7091–7098, Jun. 2016, doi: 10.1021/jacs.6b02964.

[84] H. Wang, X. Li, Z. Liu, and J. Yang, "ψ-Phosphorene: a new allotrope of phosphorene," *Phys. Chem. Chem. Phys.*, vol. 19, no. 3, pp. 2402–2408, 2017, doi: 10.1039/C6CP07944J.
[85] G. Yu, L. Jiang, and Y. Zheng, "Two-dimensional Kagome phosphorus and its edge magnetism: a density functional theory study," *J. Phys.: Condens. Matter*, vol. 27, no. 25, p. 255006, Jun. 2015, doi: 10.1088/0953-8984/27/25/255006.
[86] J. L. Zhang *et al.*, "2D Phosphorene: Epitaxial Growth and Interface Engineering for Electronic Devices," *Adv. Mater.*, vol. 30, no. 47, p. 1802207, Nov. 2018, doi: 10.1002/adma.201802207.
[87] S. Zhang *et al.*, "Semiconducting Group 15 Monolayers: A Broad Range of Band Gaps and High Carrier Mobilities," *Angewandte Chemie International Edition*, vol. 55, no. 5, pp. 1666–1669, Jan. 2016, doi: 10.1002/anie.201507568.
[88] H. Tian *et al.*, "Two-Dimensional Metal-Phosphorus Network," *Matter*, vol. 2, no. 1, pp. 111–118, Jan. 2020, doi: 10.1016/j.matt.2019.08.001.
[89] S. Zhao, J. L. Zhang, W. Chen, and Z. Li, "Structure of Blue Phosphorus Grown on Au(111) Surface Revisited," *J. Phys. Chem. C*, vol. 124, no. 3, pp. 2024–2029, Jan. 2020, doi: 10.1021/acs.jpcc.9b10511.
[90] J. L. Zhang *et al.*, "Synthesis of Monolayer Blue Phosphorus Enabled by Silicon Intercalation," *ACS Nano*, vol. 14, no. 3, pp. 3687–3695, Mar. 2020, doi: 10.1021/acsnano.0c00822.
[91] J. Wang *et al.*, "Performance of Monolayer Blue Phosphorene Double-Gate MOSFETs from the First Principles," *ACS Appl. Mater. Interfaces*, vol. 11, no. 23, pp. 20956–20964, Jun. 2019, doi: 10.1021/acsami.9b02192.
[92] J. Zhuang *et al.*, "Band Gap Modulated by Electronic Superlattice in Blue Phosphorene," *ACS Nano*, May 2018, doi: 10.1021/acsnano.8b02953.
[93] G. Yang, Z. Xu, Z. Liu, S. Jin, H. Zhang, and Z. Ding, "Strain- and Fluorination-Induced Quantum Spin Hall Insulators in Blue Phosphorene: A First-Principles Study," *J. Phys. Chem. C*, vol. 121, no. 23, pp. 12945–12952, Jun. 2017, doi: 10.1021/acs.jpcc.7b03808.
[94] Z. Deng, Z. Li, W. Wang, and J. She, "Vibrational properties and Raman spectra of pristine and fluorinated blue phosphorene," *Phys. Chem. Chem. Phys.*, vol. 21, no. 3, pp. 1059–1066, 2019, doi: 10.1039/C8CP05699D.
[95] Q. Peng, Z. Wang, B. Sa, B. Wu, and Z. Sun, "Electronic structures and enhanced optical properties of blue phosphorene/transition metal dichalcogenides van der Waals heterostructures," *Sci Rep*, vol. 6, no. 1, p. 31994, Aug. 2016, doi: 10.1038/srep31994.
[96] K. Fan, J. Tang, S. Wu, C. Yang, and J. Hao, "Adsorption and diffusion of lithium in a graphene/blue-phosphorus heterostructure and the effect of an external electric field," *Phys. Chem. Chem. Phys.*, vol. 19, no. 1, pp. 267–275, 2017, doi: 10.1039/C6CP05983J.
[97] B.-J. Wang *et al.*, "Electronic structures and enhanced photocatalytic properties of blue phosphorene/BSe van der Waals heterostructures," *J. Mater. Chem. A*, vol. 6, no. 19, pp. 8923–8929, 2018, doi: 10.1039/C8TA01019F.
[98] L. Huang and J. Li, "Tunable electronic structure of black phosphorus/blue phosphorus van der Waals p-n heterostructure," *Appl. Phys. Lett.*, vol. 108, no. 8, p. 083101, Feb. 2016, doi: 10.1063/1.4942368.
[99] J. O. Island, G. A. Steele, H. S. J. van der Zant, and A. Castellanos-Gomez, "Environmental instability of few-layer black phosphorus," *2D Materials*, vol. 2, no. 1, p. 011002, Jan. 2015, doi: 10.1088/2053-1583/2/1/011002.
[100] A. Favron *et al.*, "Photooxidation and quantum confinement effects in exfoliated black phosphorus," *Nature Materials*, vol. 14, no. 8, pp. 826–832, May 2015, doi: 10.1038/nmat4299.
[101] J. D. Wood *et al.*, "Effective Passivation of Exfoliated Black Phosphorus Transistors against Ambient Degradation," *Nano Letters*, vol. 14, no. 12, pp. 6964–6970, Dec. 2014, doi: 10.1021/nl5032293.
[102] R. A. Doganov *et al.*, "Transport properties of pristine few-layer black phosphorus by van der Waals passivation in an inert atmosphere," *Nat Commun*, vol. 6, no. 1, p. 6647, May 2015, doi: 10.1038/ncomms7647.

CHAPTER 2

Top-down synthesis of 2D phosphorus: exfoliation and thinning

2.1 Mechanical and liquid phase exfoliation

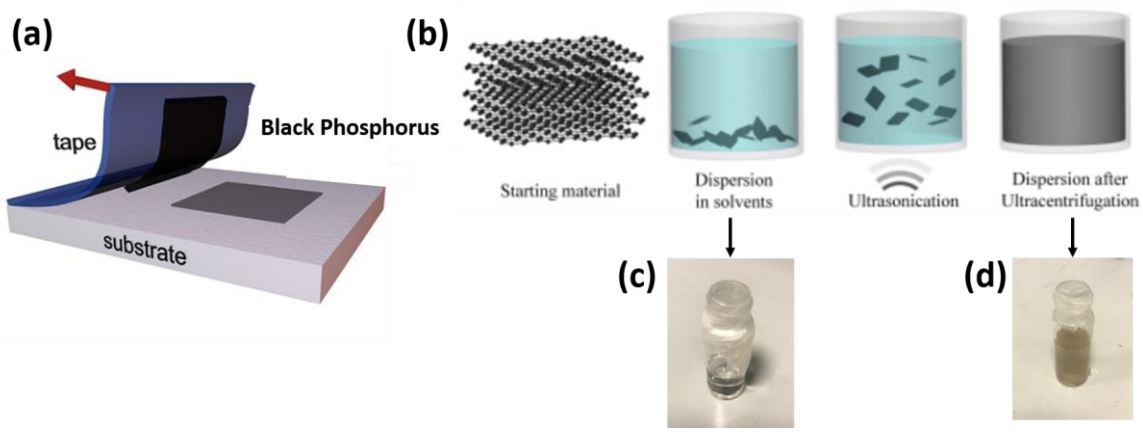

Figure 2.1 Schematic illustration of **(a)** the scotch-tape exfoliation method and **(b)** the liquid phase exfoliation method of a layered vdW material. **(c)** and **(d)** liquid phase exfoliation of black phosphorus in isopropyl alcohol before and after 3h sonication at 90W.

The top-down synthesis of 2D materials relies on the thickness reduction of layered van der Waals crystals down to the extreme 2D limit by a layer by layer removal of the topmost layers. In the case of black phosphorous the crystalline structure is characterized by anisotropic puckered layers of phosphorus atoms bonded together by weak van der Waals forces in the out-of-plane direction. Due to the high intralayer strength, the weak interlayer cohesion can be broken exerting normal and/or lateral forces that separate the topmost layers without destroying the remaining ones.

The two most common top-down synthesis techniques based on this approach are the micromechanical and the liquid phase exfoliation. Both these methods typically involve two steps: (i) the exfoliation of BP layers from the bulk crystal and (ii) the transfer of the exfoliated flakes or nanosheets onto a target substrate for their further characterization and processing [1]–[3].

Micromechanical exfoliation technique.

In the micromechanical exfoliation technique, popularly known as scotch-tape method, few layers BP flakes can be obtained by repeated peelings (mechanical-process) of bulk BP crystals using an adhesive tape (see Figure 2.1 (a)). Due to the statistical nature of the cleavage process, the exfoliation method produces hundreds of flakes with different size (usually from few µm to few millimeters), varying thickness (typically from few to hundreds of nanometers) and surface quality. The latter two aspects can only be partially controlled during the exfoliation process by choosing a tape with an optimal adhesive force. For example, Nitto brand tapes with low adhesion are commonly used in the mechanical exfoliation since they offer a good compromise between the yield of few-layers flakes and the flake surface quality leaving few glue residues on them. Once exfoliated from the bulk, the flakes can be transferred on a target substrate simply by pressing the tape carrying the exfoliated material on it and then slowly peeling it off. However, the direct tape transfer of the exfoliated flakes on a target substrate often results in low density of few layer flakes and sometimes it can leave unwanted contaminations (glue residues). An alternative method that can be exploited to avoid these problems consists, for

example, in the direct exfoliation of BP on viscoelastic polymer films (dry-transfer technique), such as poli-dimethylsiloxane (PDMS), followed by a slow release on the target substrate, as reported in Refs.[4], [5]

After the preparation, the samples need to be stored in vacuum or inert atmosphere since, differently from graphene, few layer BP quickly degrades in air due to the photo-oxidation reaction with water and oxygen[6]–[8]. To minimize this issue, a better approach consist in carrying out the exfoliation process in dark inside a nitrogen-filled glove box and then protecting the exfoliated BP flakes by spin coating on them a polymer film such as a parylene[7], poly(methyl methacrylate) (PMMA)[9], [10], or a polymer-resist[11] that prevent the reaction of the flake's surface with moisture and oxygen.

The mechanical exfoliation technique produces BP flakes with a good crystalline quality and few defects, but it is a time-consuming and low-yield process with a not-scalable production rate that is useful only for proof-of-concepts device applications. On other hand, the exfoliation of BP in liquids, results in large quantities of exfoliated material with the potentialities for a large-scale industrial production of few layer BP flakes at relatively low cost.[1], [12], [13]

Liquid Phase exfoliation technique

Generally, the preparation of few-layer flakes via liquid phase exfoliation involves three steps (see Figure 2.1(b)): (i) the dispersion of a bulk vdW crystal into a suitable solvent medium, (ii) the exfoliation via sonication and (iii) the centrifugation of the liquid suspension. The choice of the solvent medium is a key factor for the success of this technique. The exfoliation efficiency of a solvent depends on its surface tension and, moreover, an optimal solvent for the liquid phase exfoliation should be also able to easily suspend the exfoliated material. The sonication step aids the exfoliation of the dispersed material through a liquid cavitation process. Micro-jets and shockwaves caused by the cavitation bubbles exert a tensile stress on the layered crystal directed normally to the surface that peels each layer apart.[3] An effective and scalable liquid phase exfoliation process requires, beside an optimized solvent, also a proper optimization of the sonication parameters, such as the sonication time and power. The exfoliation of BP by sonication has been reported in literature using various anhydrous organic solvents such as: ethanol, isopropyl alcohol (IPA) or N-methyl-2-pyrrolidone (NMP).[14]–[17] Figures (c) and (d) show, for example, a liquid suspension of BP flakes prepared in IPA before and after the sonication. Polar solvents such as dimethyl sulfoxide (DMSO) and dimethylformamide (DMF) proved to be more effective in exfoliating atomically thin BP flakes in stable and uniform dispersions with also the additional advantage of protecting the dispersed BP nanosheets from the air-degradation[16]. However, the high boiling point and toxicity of these solvents present challenges in the post-processing. To avoid these issues, the liquid phase exfoliation of BP has been investigated also in deoxygenated water solutions obtaining excellent results[18]. Once prepared, the liquid suspensions of BP flakes are usually subjected to centrifugation in order to separate the unexfoliated BP fraction from the exfoliated material. In general, the centrifugation does not help to obtain an accurate control on the BP flake thickness and size but, varying suitably the centrifugation time and speed it is at least possible to get a liquid suspension with exfoliated BP flakes in different thickness ranges [19]. Finally, the transfer of the exfoliated material from the liquid solution on a target substrate is realized by the drop-casting method. The resulting substrate coverage and morphology of the deposited BP nanosheets film may be

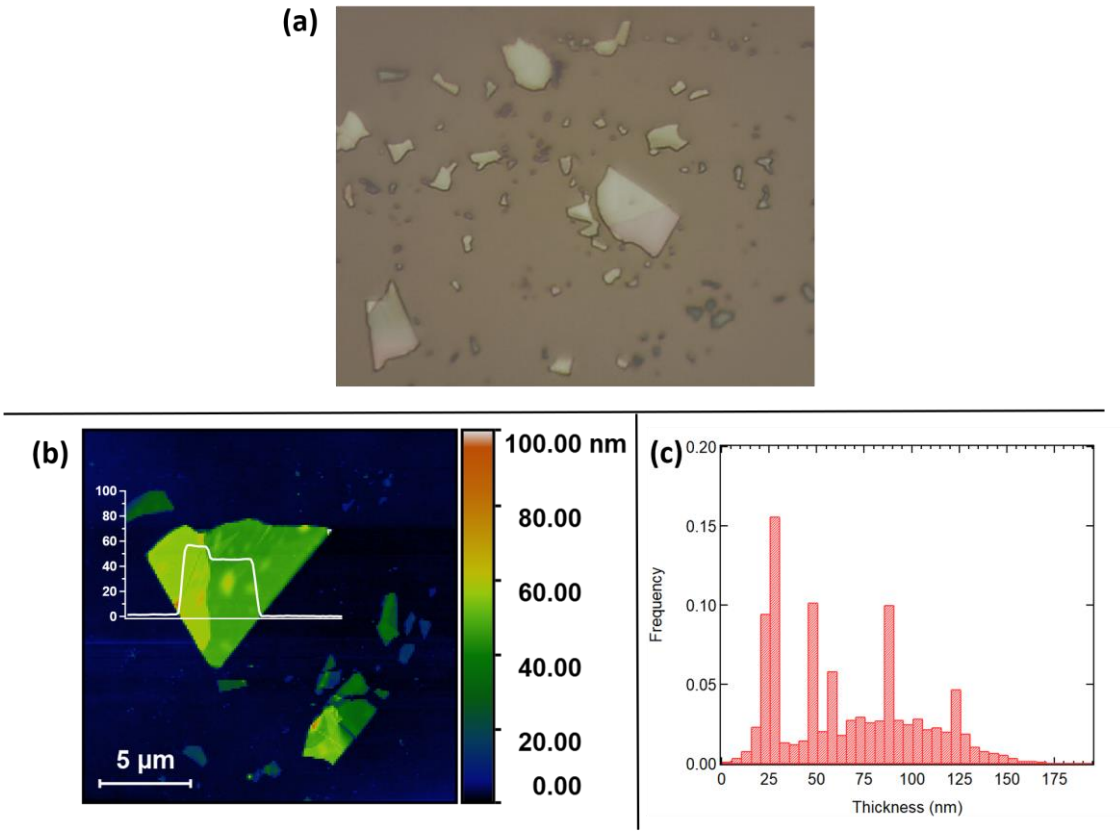

Figure 2.2 .**(a)** Optical microscope image of mechanically exfoliated BP flakes on a SiO_2(50nm)/Si substrate. A different optical contrast color with respect the substrate indicates flakes with different thickness **(b)** AFM image (20µm x 20µm) of a BP flake immediately after the exfoliation. **(c)** Distribution of the thickness of exfoliated BP flakes derived cumulating the height distributions calculated from 16 different AFM images.

highly dependent on the employed drop-casting procedure, the solvent type and eventually on the drying-up process and it also requires a preliminary optimization [20]. Compared to the mechanical exfoliation process the crystalline quality of the liquid phase exfoliated material is generally lower due to possible structural damages introduced, for example, by the prolonged sonication times. Despite this problem hinders the realization of BP electronic devices with good electrical performances, it is not high-concerning for the applications of the liquid phase exfoliated BP flakes in solution-processed nanocomposite electronic and optoelectronic devices. [15], [21], [22]

However, one of the major drawbacks of both the previously described top-down exfoliation techniques remains the lack of an accurate control on the thickness (and size) of the synthesized BP flakes. Therefore, the preliminary measurement of the flake thickness is an unavoidable step that allows any further processing of BP towards device architectures.

2.1.1 Determination of the thickness of exfoliated black phosphorus

The atomically precise way to evaluate the thickness of the exfoliated flakes is by atomic force microscopy (AFM). However, this approach becomes a challenging and time-consuming task when performed on a substrate containing hundreds of exfoliated BP flakes. As shown by the optical microscope image in Figure 2.2(a) any exfoliation procedure generates on a target

substrate a random distribution of flakes with different size and thickness. Moreover, even the thickness of a single exfoliated flake is not uniform on its surface (see the superimposed line profile in the AFM image of Figure 2.2(b)). Therefore, due to the random nature of the mechanical cleavage process, the thickness distribution calculated on the whole ensemble of the exfoliated BP flakes is always very broad. For example, in the case considered in Figure 2.2(c) this distribution varies from 5 nm to 160 nm. An additional disadvantage of the AFM approaches comes from the typical low scanning rate of this kind of measurements. Due to the quick deterioration of the thinnest BP flakes in ambient air, the AFM determination of the flake thickness may be affected by large errors. As we will see in Chapter 4 a prolonged air exposure induces the formation of bubble-like protrusions on the surface of the BP flakes. These protrusions are caused by oxidized phosphorus species (P_xO_y) and become thicker and wider upon prolonged air exposure [6]–[8], [23] increasing the flake surface roughness and, consequently, the uncertainty in the AFM determination of its thickness.

The quickest and easiest methodologies for the inspection and thickness determination of exfoliated flakes rely on optical techniques.[24] Methods based on the evaluation of the optical contrast [25]–[27] (i.e. the color of the flakes) or approaches based on optical interferometry methods [28] have been successfully applied in literature for the evaluation of the thickness of BP flakes. Usually all these optical methods are very fast, but they have the drawback to have the highest sensitivity only in the evaluation of the thickness of few layers BP flakes, i.e. below 5 nm. However, most of the exfoliated BP flakes fall inside a thickness range above 10 nm (see Figure 2.2(c)). It is therefore useful to find an optical thickness determination method that is versatile and, at the same time, suitable in the multilayer thickness regime. Micro-Raman spectroscopy turns out to be a valid alternative in this respect. To make a proper use of this technique, however, some complications arising from the anisotropy of black phosphorus, the effects of the absorption and of optical interferences need to be properly accounted. Before discussing in more detail all these aspects, we will review in the next paragraph some basic findings of the Raman spectroscopy of black phosphorus.

2.2 Raman spectroscopy of black phosphorus

In the semiclassical description, the Raman scattering of an electromagnetic wave incident on a molecule is a consequence of the light scattering from an oscillating electric dipole induced in the molecule by the not vanishing polarizability. Thus, the Raman scattered radiation results from the modulation of the frequency of the incident electromagnetic wave with the natural frequencies of vibration (normal modes) of the induced electric dipole. These natural frequencies of vibration are a feature of each molecular system and are related to its geometric and symmetry properties. The same semiclassical explanation can be extended to crystalline solids with the obvious difference that the induced dipole moment should be now replaced by an induced macroscopic polarizability vector. An external oscillating electric field with amplitude $\boldsymbol{E}(\boldsymbol{k_i}, \omega_i)$ induces a macroscopic polarizability in the crystalline solid that oscillates with an amplitude $\boldsymbol{P}(\boldsymbol{k_i}, \omega_i)$ given by:

$$\boldsymbol{P}(\boldsymbol{k_i}, \omega_i) = \overleftrightarrow{\boldsymbol{\chi}} \cdot \boldsymbol{E}(\boldsymbol{k_i}, \omega_i) \tag{2.1}$$

where $\boldsymbol{k_i}$ and ω_i are the wavevector and frequency of the incident radiation and $\overleftrightarrow{\boldsymbol{\chi}}$ is the optical susceptibility tensor (i.e. the macroscopic analogue of the molecular polarizability). The intrinsic normal modes of vibration of a solid, termed phonons, cause fluctuations in the optical susceptibility tensor that perturb the oscillating motion of the macroscopic polarizability induced by the external electric field at frequency ω_i. The fluctuations of the susceptibility tensor can be decomposed as a sum of harmonic oscillations corresponding to the normal modes of vibration, i.e. phonons at a characteristic frequency $\omega_{\boldsymbol{q}}$ and wave-vector $\boldsymbol{q}$. Therefore, as in the case of a single molecule, the Raman scattered electromagnetic wave has a frequency resulting from the modulation of the incident frequency ω_i with the frequencies $\omega_{\boldsymbol{q}}$ of the excited normal modes of vibration. In the semiclassical approximation, the intensity of the Raman scattered radiation is calculated from the intensity of the radiation emitted from a harmonic oscillating dipole. In the specific case of a crystalline solid, this means that, at the first order, the intensity of the scattered radiation can be expressed as proportional to the derivative of the susceptibility tensor with respect to the coordinates $\boldsymbol{Q}(\boldsymbol{q}, \omega_{\boldsymbol{q}})$ of an excited normal modes of vibration[29]:

$$I_s \propto \left| \hat{\boldsymbol{e}}_{\boldsymbol{i}} \cdot \frac{\partial \overleftrightarrow{\boldsymbol{\chi}}}{\partial \boldsymbol{Q}(\boldsymbol{q}, \omega_{\boldsymbol{q}})} \cdot \hat{\boldsymbol{e}}_{\boldsymbol{s}} \right|^2 \tag{2.2}$$

where $\hat{\boldsymbol{e}}_{\boldsymbol{i}}$ and $\hat{\boldsymbol{e}}_{\boldsymbol{s}}$ are the directions of polarization of the incident and scattered wave. The tensor quantity, with components:

$$R_{ij}^{\boldsymbol{q}} \equiv \frac{\partial \chi_{ij}}{\partial \boldsymbol{Q}(\boldsymbol{q}, \omega_{\boldsymbol{q}})} \tag{2.3}$$

is called the first order Raman tensor of the $(\boldsymbol{q}, \omega_{\boldsymbol{q}})$ phonon. For an incident electromagnetic wave in the visible part of the spectrum, the conservation of energy and momentum implies that only phonons with $\boldsymbol{q} \approx 0$ (zone center normal modes) can participate in a (first order) Raman scattering event. However, not all the zone center phonons of a crystal are Raman active. The zone center symmetries of the crystalline structure dictate who are the Raman active modes, the symmetries obeyed by their Raman tensors and the corresponding matrix representations determining in this way the so-called selection rules of the Raman scattering for a given scattering geometry and polarization of the incident light.

Raman scattering in Black Phosphorus

In the case of black phosphorus, the crystalline structure belongs to the orthorhombic system and therefore the zone center symmetries are described by a specific point group denoted by D_{2h}. Since the primitive cell of the BP crystal structure contains 4 atoms, the zone center phonons are 12: 3 acoustic plus 9 optical. The action of all the symmetry operations of the D_{2h} group on the atomic displacements of the zone center vibrational modes of BP determines a *reducible representation* of the zone center atomic displacements. From a group theory analysis, the reducible representation, Γ, of the atomic displacements of the zone center phonons can be always decomposed in a direct sum on the basis of the *irreducible representations* of the D_{2h} point group[30], [31]:

$$\Gamma = 2A_g \oplus B_{1g} \oplus B_{2g} \oplus 2B_{3g} \oplus A_u \oplus 2B_{1u} \oplus 2B_{2u} \oplus B_{3u} \tag{2.4}$$

Each of these irreducible representations describes how the atomic displacements of the zone center phonons transform under the symmetry operations of the D_{2h} point group. Since BP is a

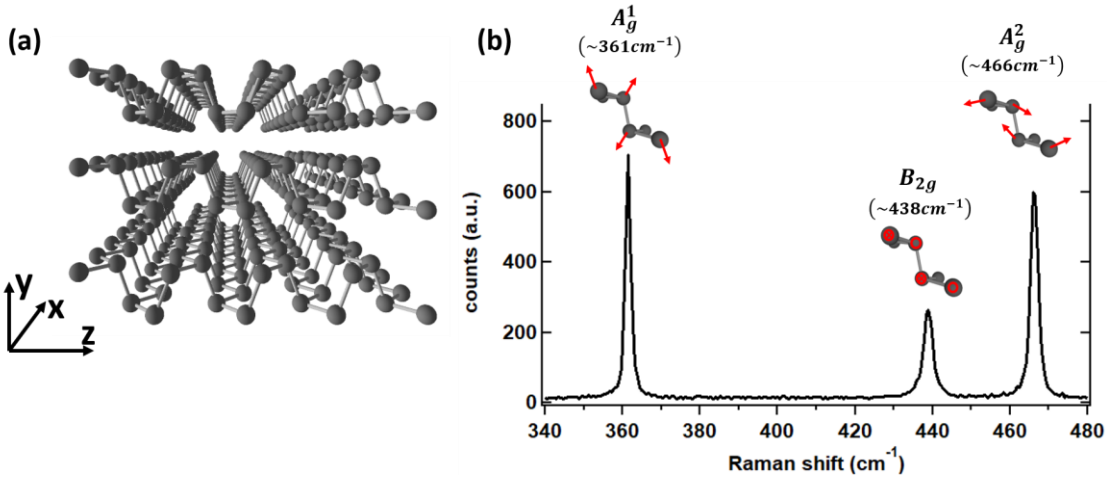

Figure 2.3 (a) Atomic model of the BP crystalline structure with the direction of the crystallographic axis indicated. **(b)** A typical Raman spectrum of a bulk BP flake with the Raman bands corresponding to the $\boldsymbol{A_g^1}$, $\boldsymbol{B_{2g}}$ and $\boldsymbol{A_g^2}$ vibrational modes. The atomic displacements of these Raman modes are indicated with red arrows in the atomic models in the insets. The red circle and circle+cross for the atomic displacements of the $\boldsymbol{B_{2g}}$ mode indicate vibrations coming out or going in the plane of the page.

centrosymmetric crystal, the Raman vibrational modes with not trivially null Raman tensors have atomic displacements invariant under an inversion symmetry operation. Therefore, the Raman active vibrational modes should possess the symmetry behavior of the irreducible representations with even parity, i.e. those denoted with a subscript *g* in (2.4). These irreducible representations are six: $2A_g$, B_{1g}, B_{2g} and $2B_{3g}$ and the corresponding Raman active modes of BP are conventionally named using the same symbols. The transformation rules imposed on the atomic displacements of the Raman active modes by the symmetry operations of the corresponding irreducible representations determine the specific matrix form of the Raman tensors.

Figure 2.3(a) illustrates a schematic model of the BP crystalline structure with the orientation conventionally adopted for the crystallographic axis. The Raman tensors of the Raman active modes in this crystallographic reference system are represented by the following matrices[30]:

$$A_g = \begin{pmatrix} a & 0 & 0 \\ 0 & b & 0 \\ 0 & 0 & c \end{pmatrix}, B_{1g} = \begin{pmatrix} 0 & d & 0 \\ d & 0 & 0 \\ 0 & 0 & 0 \end{pmatrix},$$
$$B_{2g} = \begin{pmatrix} 0 & 0 & f \\ 0 & 0 & 0 \\ f & 0 & 0 \end{pmatrix}, B_{3g} = \begin{pmatrix} 0 & 0 & 0 \\ 0 & 0 & g \\ 0 & g & 0 \end{pmatrix} \quad (2.5)$$

Most of the Raman experiments performed on exfoliated BP flakes are carried out in backscattering geometry. Since the naturally exposed surface of exfoliated BP flakes coincides with the puckered atomic planes of BP, in the backscattering geometry the electric field of the incoming and scattered light oscillates parallel to the xz-planes of BP (i.e. it has no components in the y direction). Consequently, only 3 out of the 6 previous Raman active modes can be observed: two modes with A_g symmetry, denoted A_g^2 and A_g^1, and one mode with B_{2g} symmetry. The A_g^2 (at ~470 cm^{-1}) and A_g^1 (at ~365 cm^{-1}) modes correspond, respectively, to a vibration along the armchair direction and along the out-of-plane direction (out-of-plane

stretching mode), whereas the B_{2g} ($\sim 440\ cm^{-1}$)mode corresponds to a vibration along the zig-zag direction. The atomic displacements of these modes and their Raman frequencies measured on an exfoliated bulk BP flake are illustrated in Figure 2.3(b).

The remaining 3 Raman active modes, the B_{2g} (at $\sim 197 cm^{-1}$) mode and the two B_{3g} (B_{3g}^2 $\sim 440\ cm^{-1}$ and B_{3g}^1 $\sim 230\ cm^{-1}$) modes, are forbidden in a backscattering geometry and can be only observed in bulk BP crystals when the incident light has a polarization component along the y-axis. However, these modes have been measured along the edges of exfoliated multilayer BP flakes also in absence of a y-polarized component of the excitation light and are attributed to *edge phonons* due to the rearrangement of the phosphorus atoms at the BP flake terminations[32].

Angular dependence of the Raman modes intensities

Unlike graphene and several other transition metal dichalcogenides, the intensities of the Raman spectrum of BP are strongly anisotropic when measured as function of the orientation of the BP sample. Such behavior is a consequence of the in-plane anisotropy of the BP crystalline structure and it can be fully understood in terms of the Raman scattering matrices reported in Equation (2.5). In particular, the matrix elements of the Raman scattering matrices can be measured by means of polarized Raman scattering experiments. However, since black phosphorus has a not negligible light absorption, the matrix elements of the optical susceptibility tensor χ_{ij} are complex and, therefore, the same is valid for the matrix elements of the Raman tensors. The latter can be written generally as $a = |a|e^{-i\phi_a}$. By means of polarized Raman scattering experiments it is possible to determine both the moduli and the phase factors of these complex matrix elements [33], [34].

Polarized Raman scattering experiments can be carried out in different configurations. For example, in a first configuration the sample is kept fixed and the polarization direction of the incident radiation on the BP sample surface is rotated by means of a half-wave plate. In a second possible configuration, instead, the sample is rotated with respect to the fixed polarization direction of the incident light. In both the approaches the scattered radiation can be analyzed with a polarizer placed before the Raman spectrometer. The optical axis of the collection polarizer is fixed either parallel or perpendicular to the polarization of the incident radiation. Denoting by ϑ the angle between the x crystallographic axis of BP and the polarization direction of the incident and collected Raman scattered radiation, the polarization vectors $\hat{\boldsymbol{e}}_{\boldsymbol{i}}$ and $\hat{\boldsymbol{e}}_{\boldsymbol{s}}$ can be written as: $\hat{\boldsymbol{e}}_{\boldsymbol{i}} = \hat{\boldsymbol{e}}_{\boldsymbol{s}} = (\cos\vartheta, 0, \sin\vartheta)$ for the parallel polarization configuration and $\hat{\boldsymbol{e}}_{\boldsymbol{i}} = (\cos\vartheta, 0, \sin\vartheta)$, $\hat{\boldsymbol{e}}_{\boldsymbol{s}} = (-\sin\vartheta, 0, \cos\vartheta)$ for the perpendicular polarization configuration. From equation 2.2 the intensity of the A_g and B_{2g} modes in the parallel and perpendicular collection configurations is given by[30]:

$$I_{A_g}^{\parallel} \propto (|a|\cos^2\vartheta + |c|\cos\phi_{ac}\sin^2\vartheta)^2 + |c|^2\sin^4\vartheta\sin^2\phi_{ac}$$
$$I_{A_g}^{\perp} \propto [(|a| - |c|\cos\phi_{ac})^2 + |c|^2\sin^2\phi_{ac}]\cos^2\vartheta\sin^2\vartheta \qquad (2.6.a)$$

$$I_{B_{2g}}^{\parallel} \propto (|f|\sin 2\vartheta)^2$$
$$I_{B_{2g}}^{\perp} \propto (|f|\cos 2\vartheta)^2 \qquad (2.6.b)$$

where $\phi_{ac} = \phi_a - \phi_c$ is the relative phase difference between the *a* and *c* matrix elements. The previous equations suggest that when the laser polarization is parallel to the zig-zag x-direction

the intensity of the A_g modes measured in the parallel configuration reach its maximum whereas the intensity of the B_{2g} mode reaches the minimum value. The opposite is true when the laser polarization is parallel to the armchair y-axis and the scattered radiation is measured in the orthogonal configuration.

The angular dependence of the Raman modes of BP derived from polarized Raman scattering experiments has been exploited in literature for the determination of the orientation of the crystallographic axes of exfoliated BP flakes.[28], [35]–[37] However, this approach can lead to erroneous results without a preliminary analysis of other possible polarization dependent optical effects. As we will see in the following such effects are mainly caused by optical interferences and introduce an additional wavelength and thickness dependence on the polarization behavior of the intensities of the BP Raman modes. Therefore, the determination of the crystallographic orientation of exfoliated BP samples requires always caution when performed only with the aid of polarized Raman scattering experiments. [38], [39]

2.2.1 Optical interference effects in the Raman scattering

Optical interference effects can considerably alter the intensities of the Raman bands of exfoliated BP flakes as well as those of the substrate. These effects can be understood with the same optical model developed to explain the interference enhancement of the Raman scattering from "optically thick" graphene or MoS_2 samples[40]–[42] supported on semi-infinite SiO_2/Si substrates.

Interferential modulation of the intensity of the Raman bands

In the multireflection model the excitation $|F_{ex}(y)|$ and scattered $|F_{sc}(y)|$ amplitudes of the electric field of the light at a depth y (see Figure 2.4) measured from the top surface of the sample cannot be merely calculated for each BP thickness value on the basis of the exponential light attenuation law (Beer-Lambert law). In particular, if the thickness of the sample becomes $\approx \frac{\lambda}{4n}$, where λ is the wavelength of the excitation (or scattered) light and n the refractive index of the material, constructive or destructive interference between the light rays originating from multiple reflections at the top and at the bottom interfaces of the BP sample play a dominant role and introduce an oscillating modulation on the $|F_{ex}(y)|$ and $|F_{sc}(y)|$ amplitudes as function of the y-depth. Since the light absorbed at given y-depth in the material is proportional to $|F_{ex}(y)|$, the total intensity of the Raman scattered light exiting from the SiO_2/Si supported BP sample can be calculated summing all the $|F_{ex}(y)F_{sc}(y)|^2$ contributions on the sample thickness:

$$I \propto \int_0^{d_1} |F_{ex}(y)F_{sc}(y)|^2 dy \qquad (2.7)$$

where d_1 is the thickness of the BP sample. The electric field amplitudes of the excitation $F_{ex}(y)$ and scattered $F_{sc}(y)$ electromagnetic waves at y-depth can be calculated adding all the contributions coming from the light rays reflected at the top and bottom interfaces of the sample, as performed in refs.[41], [42] obtaining the following expressions:

$$F_{ex}(y) = t_{01} \frac{\left(1 + r_{12}r_{23}e^{-2i\beta_2^{ex}}\right)e^{-i\beta_y^{ex}} + \left(r_{12} + r_{23}e^{-2i\beta_2^{ex}}\right)e^{-i\left(2\beta_1^{ex} - \beta_y^{ex}\right)}}{1 + r_{12}r_{23}e^{-2i\beta_2^{ex}} + \left(r_{12} + r_{23}e^{-2i\beta_2^{ex}}\right)r_{01}e^{-2i\beta_1^{ex}}} \qquad (2.8)$$

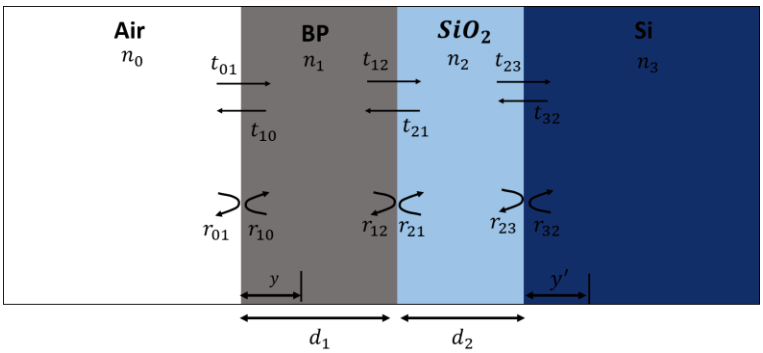

Figure 2.4 Schematics of the interfaces between air, BP, SiO_2, and Si with the notation used for the refractive indexes, reflection and transmission coefficients.

$$F_{sc}(y) = t_{10}\frac{\left(1 + r_{12}r_{23}e^{-2i\beta_2^{sc}}\right)e^{-i\beta_x^{sc}} + \left(r_{12} + r_{23}e^{-2i\beta_2^{sc}}\right)e^{-i(2\beta_1^{sc}-\beta_y^{sc})}}{1 + r_{12}r_{23}e^{-2i\beta_2^{sc}} + \left(r_{12} + r_{23}e^{-2i\beta_2^{sc}}\right)r_{01}e^{-2i\beta_1^{sc}}}$$

where the indices are assigned as in Figure 2.4 and $t_{ij} = \frac{2\tilde{n}_i}{\tilde{n}_i+\tilde{n}_j}$ and $r_{ij} = \frac{\tilde{n}_i-\tilde{n}_j}{\tilde{n}_i+\tilde{n}_j}$ are, respectively, the transmission and the reflection coefficients at the i-j interface. The phase terms are given by: $\beta_y^{sc,ex} = 2\pi y\frac{\tilde{n}_1}{\lambda_{sc,ex}}$, $\beta_i^{sc,ex} = 2\pi d_i\frac{\tilde{n}_1}{\lambda_{sc,ex}}$ with d_i the thickness of the i-th layer, λ_{ex} or λ_{sc} the laser excitation and Raman-scattered wavelength and $\tilde{n}_i = n_i - i\kappa_i$ the complex refractive index of the i-th layer.

The interference enhanced intensity for the A_g^2 Raman band at ~466 cm^{-1} calculated for a BP flake supported on a 50 nm SiO_2/Si substrate from equations 2.7 and 2.8 is illustrated in Figure 2.5(a). For this calculation we supposed that both the incident and scattered radiation are polarized along the same direction, i.e. along the zigzag or along the armchair crystallographic axis of BP. It can be noticed that the interference enhancement of the intensity of the A_g^2 mode varies strongly with the sample thickness and becomes also different, for a given thickness, changing the orientation of the sample (from zig-zag to armchair) with respect to the polarization direction of the incident light. This means that, besides the polarization dependence introduced on the intensity of the A_g^2 mode by the Raman tensor (see equation 2.6a), the effects of optical interferences cause an additional modulation of the intensity with the sample orientation that becomes different also for different BP thickness values. This result remains valid also for the polarization dependence of the A_g^1 mode, as reported in Refs. [39], [34], [38] However, unlike the A_g modes, the interference enhancement of the intensity of the B_{2g} mode at ~438 cm^{-1} depends only on the sample thickness but it is nearly independent of the sample orientation with respect to the polarization of the incident light. This result can be understood from the calculation reported in Figure 2.5(b) and remembering the polarization selection rules imposed by the B_{2g} Raman tensor (see equation (2.5)). According to these selection rules, if the incident light is polarized along the armchair (or zigzag) direction then the scattered light of the B_{2g} Raman band is polarized along the zig-zag (or armchair) direction. Therefore, as reported in Figure 2.5(b), exchanging the polarization of the incident light from armchair to zigzag does not lead to significant differences in the interference enhancement of the intensity of the B_{2g} band. Consequently, we conclude that any interference enhancement on the BP B2g band is only thickness dependent but not sample orientation dependent.

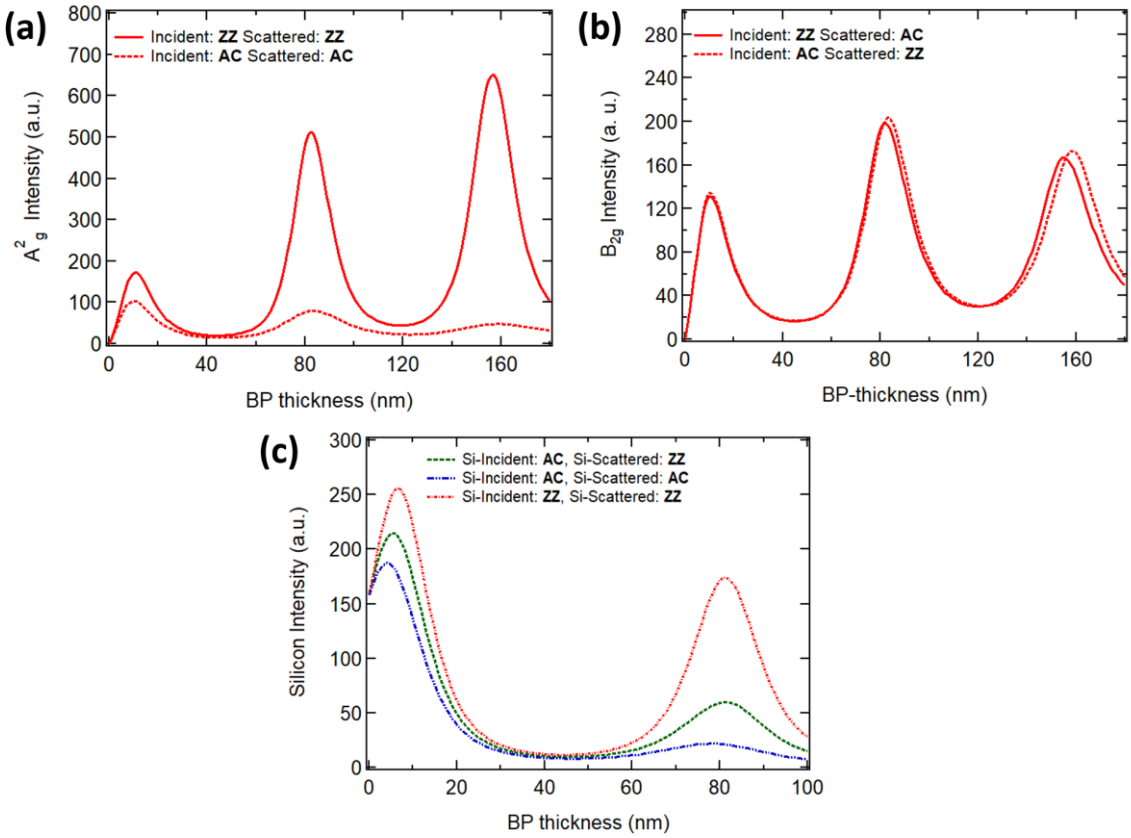

Figure 2.5 Calculated interference enhanced intensity for the $\boldsymbol{A_g^2}$ **(a)** and $\boldsymbol{B_{2g}}$ **(b)** BP Raman bands and for the silicon substrate Raman band at 520 $\boldsymbol{cm^{-1}}$ **(c)** as function of the BP thickness for different polarization directions of the excitation light. All the calculations have been performed for an excitation wavelength of 532nm and assuming a BP sample supported on a 50 nm SiO_2 on Si substrate. The values of the optical constants of BP along the armchair and the zigzag direction, of SiO_2 and of silicon are those reported in ref. [39]

Interferential modulation of the intensity of the Silicon substrate Raman band

Optical interferences can introduce also a modulation on the intensity of the silicon Raman band as function of the BP thickness when measured through BP samples thin enough to allow the collection of the Raman scattered light coming from the underlying silicon substrate. This modulation depends both on the polarization of the incident light with respect to the crystalline directions of BP and on the relative orientation between the crystallographic axes of BP and silicon. Following the approach given in Ref.[42], the amplitude of the electric field of the excitation light at depth y' in silicon (see Figure 2.4) is given by $t_{03}e^{-i\beta_{y'}^{ex}}$ whereas the amplitude of the electric field of the scattered light is: $t_{30}e^{-i\beta_{y'}^{sc}}$. Here, $\beta_{y'}^{sc,ex} = 2\pi y' \frac{\tilde{n}_3}{\lambda_{sc,ex}}$ is the phase factor for the Si-substrate and, t_{03} and t_{30}, are the transmission coefficients for the incoming and scattered light from silicon as illustrated in Figure 2.4. These transmission coefficients can be calculated adding up all the contributions from the light rays transmitted in silicon from the multiple reflections in the overlying BP/SiO_2 stack, and are given by the following expressions:

$$t_{03} = \frac{t_{01}t_{12}r_{23}e^{-i(\beta_1^{ex}+\beta_2^{ex})}}{1 + r_{01}r_{12}e^{-2i\beta_1^{ex}} + r_{12}r_{23}e^{-2i\beta_2^{ex}} + r_{01}r_{23}e^{-2i(\beta_1^{ex}+\beta_2^{ex})}} \qquad (2.9)$$

$$t_{30} = \frac{t_{32}t_{21}r_{10}e^{-i(\beta_1^{sc}+\beta_2^{sc})}}{1 + r_{32}r_{21}e^{-2i\beta_1^{sc}} + r_{21}r_{10}e^{-2i\beta_2^{sc}} + r_{32}r_{10}e^{-2i(\beta_1^{sc}+\beta_2^{sc})}}$$

As done in equation 2.7 the Raman scattered light emerging from the silicon substrate through the BP/SiO_2 stack is proportional to:

$$I_{Si} \propto \int_0^{\infty} \left| t_{03}e^{-i\beta_{y'}^{ex}} t_{30}e^{-i\beta_{y'}^{sc}} \right|^2 dy' \qquad (2.10)$$

Since BP is a linear dichroic and birefringent material, the polarization direction of the excitation light entering the silicon substrate depends on the BP thickness and on the orientation of the BP sample with respect to the polarization direction of the incoming light. The light scattered from the silicon substrate and passing through the BP/SiO_2 stack, instead, has a polarization determined by the Raman tensor of silicon and by the relative orientation between the crystallographic axis of BP and silicon. Note that silicon has a Raman scattering tensor represented in its crystallographic reference system by a matrix identical to that of the B_{2g} Raman mode of BP[43]. Therefore, assuming a (100) oriented silicon substrate with the [110] crystallographic direction at 45° with respect to the BP armchair and zig-zag axes, if the incident light is polarized along the armchair (or zig-zag) axis of BP then the scattered light exiting the silicon substrate will be polarized along the zig-zag (or armchair) direction of BP. The interferential modulation of the silicon Raman band calculated under this assumption from equations 2.9 and 2.10 is illustrated in Figure 2.5(c). As can be noticed the intensity of the silicon Raman band has an oscillating behavior with the BP thickness due to the interference effects in the overlying BP/SiO_2 stack. In general, for a randomly oriented BP flake on a SiO_2/Si substrate, the previous assumption on the relative orientation between silicon and BP is not always valid. Nevertheless, the interferential modulation of the Si band is expected to retain the maxima and minima at the same thickness values. This is proved by the calculations performed in figure 2.5(c) (blue and red dashed lines) for an excitation light polarized along the armchair (or zig-zag) direction of BP and a scattered light still polarized along the same direction outside the silicon substrate.

In conclusion we have seen that care must be taken when the A_g and B_{2g} Raman modes are used for the determination of the crystallographic axes of BP due to the presence of optical interferences. Optical interferences may affect in a non-trivial way also the intensity ratios calculated between the BP A_g or B_{2g} Raman peaks and the silicon substrate peak. Therefore, in order to avoid misleading results from any quantification carried out on such normalized intensities ratios, it is necessary to consider carefully the effects due to optical interferences.

2.3 Determination of the thickness by Raman spectroscopy

In the following paragraph we will briefly review some approaches used in literature the determination of the thickness of exfoliated BP flakes by means of Raman spectroscopy. We will firstly consider methods suited for the thickness determination in few layer flakes, i.e. with thickness below 5 nm. In the next section, instead, we will present a method that has been developed so to provide an estimation of the thickness of multilayer BP flakes in the 5 nm-100 nm range.

2.3.1 Few layers black phosphorus

In the few layers thickness regime (i.e. for BP flakes with number of layer of ~10), all the Raman methods used for the determination of the thickness should rely on features of the Raman spectrum having a sensitivity to variations of the thickness at least equal to the value of the distance between two consecutive layers in a BP crystal, i.e. of the order of ~0.525 Å. [44].

The Raman thickness determination of few layer BP flakes has been carried out in literature considering either the frequency shifts of the A_g modes, the relative intensity ratio between the A_g^1 and A_g^2 modes, or the intensity ratio between the A_g modes of BP and the Si peak of the substrate. [4], [7], [45], [46] Furthermore, the thickness of few layer BP flakes has been determined also by studying the low frequency Raman modes. [47]

Thickness determination methods based on the shift of high-frequency Raman modes

The methods relying on the frequency shifts of the A_g modes are useful for the thickness determination of few layer BP flakes (≲10-15 layers) but are not generally applicable to the thickness determination of multilayer flakes due to the lack of a sensitive thickness dependent Raman shift in this range, i.e. above ~ 5nm.[4], [7], [45] Moreover, due to the relatively small (~2 cm^{-1}) shifts of the A_g peak positions as function of the thickness of the flakes, this approach sometimes may be subjected to high inaccuracies. Additionally, this method is also complicated by the non-monotonic dependence of the frequency of the A_g modes with the layer number. The latter behavior is a consequence of the appearance of extra Raman active vibrational modes in the spectrum of few layer (≲10) BP flakes. Specifically, for few layers BP flakes (from 2 to 5 layers) the vibrational modes of two monolayer planes oscillating with different phases may combine generating new zone center vibrational modes, a phenomenon known as Davydov splitting. In bulk BP crystals these modes cannot be excited because they are not at zone center but in few layer flakes they move at the zone center due to the high number of atoms in the unit cell (*4N* atoms, where *N* is the number of layers in BP).[30] These new modes retain the same symmetry of the bulk BP vibrational modes since the zone center symmetries of few layer BP flakes continue to be represented by the D_{2h} point group. In particular, the modes resulting from the combinations of in-phase and π-phase shifted vibrations of each BP atomic plane produce an additional peak close to the A_g^2 Raman band. The presence of this additional peak is responsible of the non-monotonic frequency shift observed on the A_g modes with decreasing layer number (from 5 to 2).[7], [34]

Thickness determination based on the shift of low-frequency Raman modes

Besides the Raman modes generated by the Davydov splitting, the Raman spectra of few layer BP flakes contain additional low frequency vibrational modes. These modes are associated with layer-layer vibrations where each BP layer oscillates as a unit. Due to the weak strength of the vdW interaction, the frequencies of these vibrational modes are typically below 100 cm^{-1}, i.e. much lower than the frequencies of the intralayer A_g and B_{2g} high frequency modes. The interlayer modes can be classified as shear modes, if the atom displacements are in the plane, or as layer breathing modes when the atom displacements are perpendicular to the planes. Both shear and layer-breathing modes can be described according to the D_{2h} point group symmetries. Raman active shear-modes have B_{1g} and B_{3g} symmetries whereas the Raman active layer

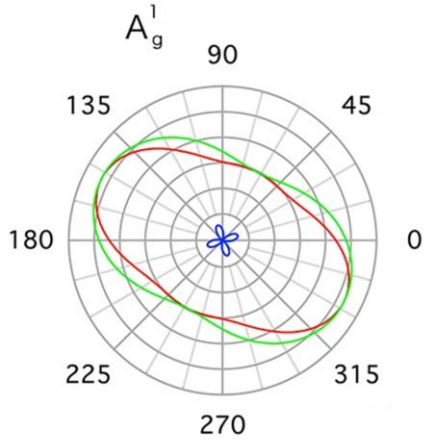

Figure 2.6 Calculation of the intensity of the $\boldsymbol{A_g^1}$ Raman band of BP as function of the orientation of the sample zigzag crystallographic axis with respect to the polarization of the incident light The intensity has been calculated for the case of parallel (red), perpendicular (blue) and unpolarized (green) detection configuration according to the equations 4.6. The values of the complex matrix elements of the Raman tensor used in the calculations are those relative to the $\boldsymbol{A_g^1}$ Raman mode as reported in ref. [39]: $\boldsymbol{a/c = 0.75}$ and $\boldsymbol{\phi_{ac} = 43°}$. Figure adapted from reference [43]

breathing modes have the A_g symmetry. According to the form of the Raman tensors reported in equation (2.5), we see that only the layer breathing modes can be observed in backscattering geometry. These low frequency modes show pronounced redshifts in the peak position by increasing the layer number due to their larger sensitivity to the interlayer coupling and, therefore, they can be used as effective and reliable thickness indicator for BP flakes with $\lesssim$10-15 layers. [47], [48] However, the measurement of the low frequency modes is challenging because the Raman peaks are usually blocked by the notch filters used to reject the excitation laser light in the Raman spectrometer. To overcome this problem, their measurement can be carried out, for example, with a Raman system equipped with triple-grating spectrometer.

Thickness determination based on the intensity ratio of Raman modes

The easiest and more immediate methods for monitoring the thickness of exfoliated BP flakes are those based on the measurement of the intensity ratios between the A_g^1 and A_g^2 Raman bands or between the A_g bands and that of the silicon substrate. These methods have been used extensively in literature for the thickness determination of both few layers BP flakes (<5 nm)[4], [7], [45], [46] and multilayer BP flakes.[49] Both the approaches, however, require attention because, as pointed out previously, the intensities of the peaks of the BP Raman spectrum are polarization dependent (i.e. sample orientation dependent) and affected by interferential effects. The sample orientation dependence of the intensity of the A_g modes calculated in absence of interferential effects is showed in Figure 2.6. These calculations have been performed using equations 2.6a for a perpendicular (blue line), parallel (red line) and unpolarized (green line) detection configuration of the scattered radiation. By unpolarized detection we mean a situation where the scattered light is not collected through a polarizer. This configuration can be also used to describe the intensity modulation obtained by ideally repeating the intensity measurements of the A_g peaks on many randomly oriented BP samples. From Figure 2.6 we

notice that the repeated measurements of the intensities of the A_g Raman band may be subjected to a modulation of more than 50% of the maximum value. In order to avoid this problem, the thickness determination of a BP flake based on the intensity measurements of the A_g peaks needs to be complemented with a previous determination of the sample orientation as well as with the evaluation of the additional polarization effects introduced by optical interferences. However, it should be mentioned that even accounting of all these effects, the intensity of the A_g Raman bands can still have a slight polarization dependence as function of the laser excitation wavelength.[39] This effect arises from the energy dependence of the matrix elements in the A_g Raman tensors and it is caused by the anisotropic quantum mechanical electron-phonon interaction in BP.[38], [39] Finally, we notice that a further complication may be introduced by the quick degradation of few layer BP flakes in ambient conditions. Due to this effect the measured relative intensity ratios of the A_g peaks do not remain constant with the time depending sensitively on the oxidation dynamic of the exfoliated BP flakes, as reported by Favron et al.[7] From the above discussion we see that the determination of the thickness of few layer BP flakes based on the relative intensity ratios of the A_g peaks can be affected by numerous source of errors despite the simplicity of the method. In the case of multilayer BP flakes in addition to all the previous difficulties another source of error arises from the saturation of the measured intensity of the A_g peaks for thickness values above 10-20 nm. In this situation the thickness determination relying on the measurement of the Raman intensities may be not conclusive at all.

2.3.2 Multilayer black phosphorus

Here we will show that a measurement of the intensity ratio between the BP B_{2g} Raman band and the silicon substrate band can be used for a quick estimation of the thickness of exfoliated multilayer BP flakes. This method becomes particularly useful in the measurement of the thickness of exfoliated BP flakes in the 5 nm-100 nm thickness range providing a thickness value with an experimental uncertainty of about 20%. Finally, we will see that a more accurate treatment that accounts also of optical interference effects does not invalidate our proposed thickness determination method at least within the measured uncertainty values.

Measurement of the B_{2g} Raman mode intensity

Figure 2.7 illustrates the angular dependence calculated for the intensity of the B_{2g} Raman band from equation (2.6.b) for a perpendicular (blue line), parallel (red line) and unpolarized (green line) detection configuration. Differently from the previous calculation performed for the A_g Raman band in Figure 2.6, we observe that the intensity of the B_{2g} band is constant for all the orientations of the sample in the unpolarized detection configuration. This means that, by ideally repeating the intensity measurements of the B_{2g} peak on many randomly oriented BP samples, the intensity of the light scattered from samples having the same thickness is not modulated by their relative (random) orientation. Moreover, we notice that even including the effects of optical interferences, the angular dependence of the intensity of the B_{2g} band does not change sensitively. As proved in figure 2.5(c), the interferential enhancement of the BP B_{2g} Raman band is nearly independent of the sample orientation with respect to the polarization of

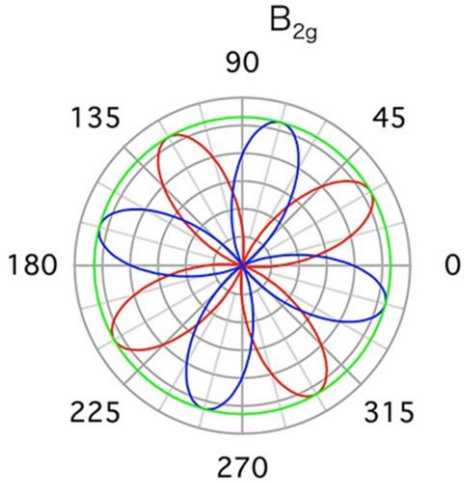

Figure 2.7 Calculation of the intensity of the $\boldsymbol{B_{2g}}$ Raman band of BP as function of the orientation of the sample zigzag crystallographic axis with respect to the polarization of the incident light The intensity has been calculated for the case of parallel (red), perpendicular (blue) and unpolarized (green) detection configuration according to the equations 2.6(b). Figure adapted from reference [43]

the incident light for a given BP thickness. Therefore, we conclude that the intensity of the BP B_{2g} Raman band is a good candidate to be used for a thickness determination method which is independent of the orientation of the BP samples.

However, in real experiments the Raman spectrometer introduces always a difference in the collection efficiency for the light scattered in two orthogonal polarizations. Due to this practical problem, the ideal situation illustrated in Figure 2.7 is never realized experimentally. In other words, since there is a difference in the collection efficiency of the light measured in parallel and orthogonal configuration, the intensity of the resulting B_{2g} band measured in an unpolarized detection configuration (green line in figure 2.7) may become angle dependent. Consequently, this effect introduces a source of error in every thickness determination method that relies on the measurement of the intensity of the B_{2g} band. A possible approach to minimize this problem is to define the measured intensity, $I(B_{2g})$, of the B_{2g} band as a weighted sum of the intensities obtained from two measurements: one with collection polarization parallel, $I^{\parallel}(B_{2g})$, and another one with collection polarization perpendicular, $I^{\perp}(B_{2g})$, to the polarization of the incident light:

$$I(B_{2g}) = I^{\parallel}(B_{2g}) + \eta I^{\perp}(B_{2g}) \qquad (2.11)$$

In equation (2.11) the weighting coefficient η is the ratio between the collection efficiency of the parallel and perpendicular configuration. The η coefficient can be determined experimentally by calculating the ratio between the maximum value of the $I^{\parallel}(B_{2g})$ and $I^{\perp}(B_{2g})$ intensities obtained in polarized Raman scattering experiments. The Raman setup used for such kind of experiments is illustrated in figure 2.8(a). The rotation of 90° of the polarization of the scattered light entering in the spectrometer was achieved by rotating of 45° the principal axes of a halfwave plate placed before the collection polarizer. The measurements of the intensity of the B_{2g} Raman band were carried out on a BP flake exfoliated on a 50 nm SiO_2/Si substrate and placed on a rotating stage. The stage was rotated in a range of 180° at steps of

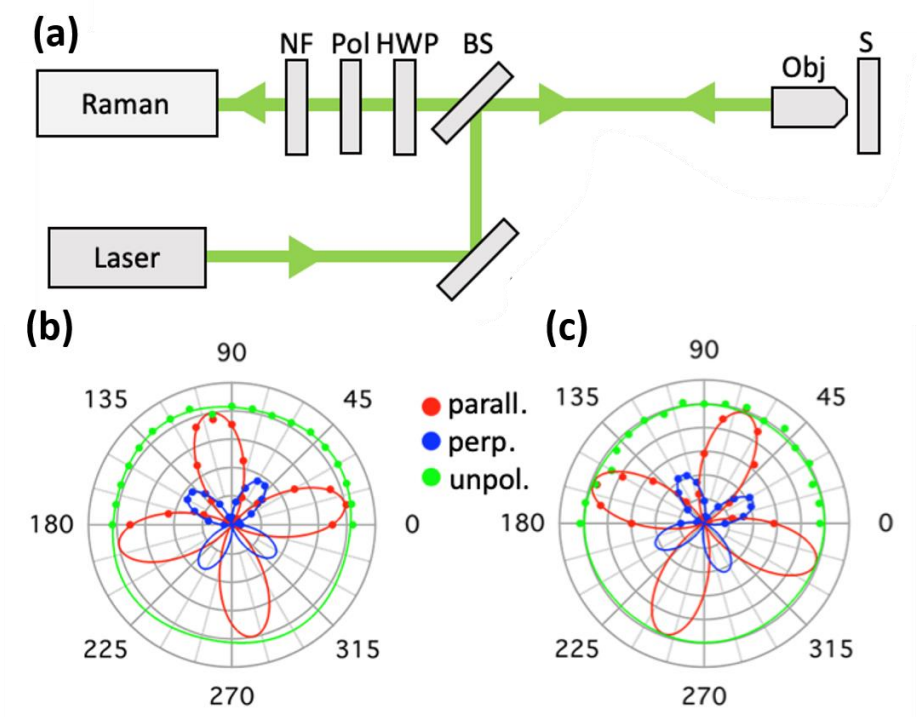

Figure 2.8 (a) Scheme of the experimental Raman setup used for the determination of the thickness of exfoliated BP flakes. NF notch filter; Pol polarizer; HWP half-wave plate; BS beam splitter; Obj objective; S sample. **(b)** Measured angular dependence of the Raman intensity of the BP $\boldsymbol{B_{2g}}$ band with the parallel (red) and perpendicular (blue) detection configurations. The green data, marked as unpolarized, are the result of the weighted sum defined in equation 2.11. **(c)** The same measurement of (b) performed on a silicon (001). Figure adapted from reference [43]

10°. The intensity values obtained from the experiments carried out in parallel and perpendicular collection configuration are reported in figure 2.8(b). It can be noticed that the response of $I^{\parallel}(B_{2g})$ and $I^{\perp}(B_{2g})$ are in good agreement with the results of the calculations showed in figure 2.7 but, as expected, they show an intensity variation for the two configurations of detection due to the polarization efficiency effect mentioned above. The experimental value for η determined from the ratio between the maxima of $I^{\parallel}(B_{2g})$ and $I^{\perp}(B_{2g})$ is ~2.[50] We see that the intensity of the B_{2g} Raman band calculated as a weighted sum of $I^{\parallel}(B_{2g})$ and $I^{\perp}(B_{2g})$ with the experimentally determined value for η is nearly independent of the sample rotation (observed the green line in figure 2.8(b)). We notice, moreover, that any other intensity measurement of the of the B_{2g} band can be quickly performed once the value of the η coefficient is known and it requires just two measurements to determine $I^{\parallel}(B_{2g})$ and $I^{\perp}(B_{2g})$ realized, for example, by rotating the axis of the halfwave plate placed before the collection polarizer.

The collection efficiency problem affects also the measurement of the intensity of the Raman band of the silicon substrate. We recall that the Raman mode of a (001) oriented silicon substrate is described by a Raman tensor identical to the Raman tensor for the B_{2g} Raman mode of BP. Therefore, ideally the same angular dependence illustrated in figure 2.7 for the intensity of the B_{2g} Raman band applies for the silicon Raman peak. To minimize the collection efficiency problem of the Silicon peak, it is possible to follow the same approach described before for the

measurement of the B_{2g} Raman band. As clearly demonstrated by figure 2.8(c) the weighted sum: $I(Si) = I^{\parallel}(Si) + \eta I^{\perp}(Si)$ is independent of the Si-substrate orientation. In our case, furthermore, the experimental value determined for the η coefficient of silicon is still ~2.[50]

Normalization of the B_{2g} Raman mode intensity and thickness determination method

We turn now to the problem of setting an appropriate thickness determination method for exfoliated BP flakes based on the measurement of the intensity of the B_{2g} Raman band. In order to get an intensity vs thickness calibration independent of the measurement parameters such as, for example, the excitation power or the defocusing of the Raman microscope objective, the intensity of the B_{2g} Raman band has to be normalized by choosing an appropriate reference. The most obvious choice for such intensity normalizations is the Raman peak of the silicon substrate on which the BP flakes are usually exfoliated.

As we have seen before, both the intensity of the B_{2g} Raman band and that of the silicon substrate are independent of the sample orientation when measured in terms of the weighted sums as defined in equation 2.11. Therefore, an intensity ratio defined by:

$$r = \frac{I(B_{2g})}{I(Si)} = \frac{I^{\parallel}(B_{2g}) + \eta I^{\perp}(B_{2g})}{I^{\parallel}(Si) + \eta I^{\perp}(Si)} \qquad (2.12)$$

is ideally independent of both the sample orientation and the experimental measurement parameters and it can be used to obtain an intensity vs thickness calibration curve. The r-values measured for different BP-flakes exfoliated on top of a 50 nm SiO_2/Si substrate as function of their AFM-measured heights are illustrated in figure 2.9. The experimental scattering of the data suggests that the measured r-values follow, in a first approximation, a monotonic exponential trend within the 25 nm-100 nm thickness range. The reproducibility of the observed trend was tested performing the same experiment with two different Raman setups named setup-1 and setup-2 in the figure. Setup-1 is a Jobin Yvon T6400 Raman spectrometer equipped with a 532 nm excitation and a 50x, 0.75 numerical aperture (NA) microscope objective; setup-2, instead, is a Renishaw InVia spectrometer equipped with a 514nm excitation and a 0.75NA microscope objective. The error reported on the measured r-values in Figure 2.9 was calculated from the standard deviation of a statistical set of measurements carried out on the same BP-flake and repeated with the two Raman setups. The errors on the BP-flakes thickness values are not related to the typical uncertainty of an AFM measurement but rather are caused by the varying height distribution of each mechanically exfoliated flake (see the AFM topography of an exfoliated BP flake reported in figure 2.2(b)).

Effects of Optical interferences on the Raman intensity normalizations

In order to validate the reliability of the exponential intensity vs thickness calibration curve suggested by the experimental data in figure 2.9, we performed additional calculations on the $I(B_{2g})/I(Si)$ intensity ratios using a more accurate model that includes the effects of optical interferences. The calculated intensity ratios were obtained using two different values for the BP complex refractive index reported in literature by Kim et al [39] (green dashed line in figure 2.9(a)) and by Mao et al [51](violet dashed line in figure 2.9(a)). As shown in the figure these calculations give quite different results and it is not clear which one should be considered as the correct model for the experimental data. However, in both the calculations we see that the calculated r-ratio increases monotonically with the BP thickness following approximately an

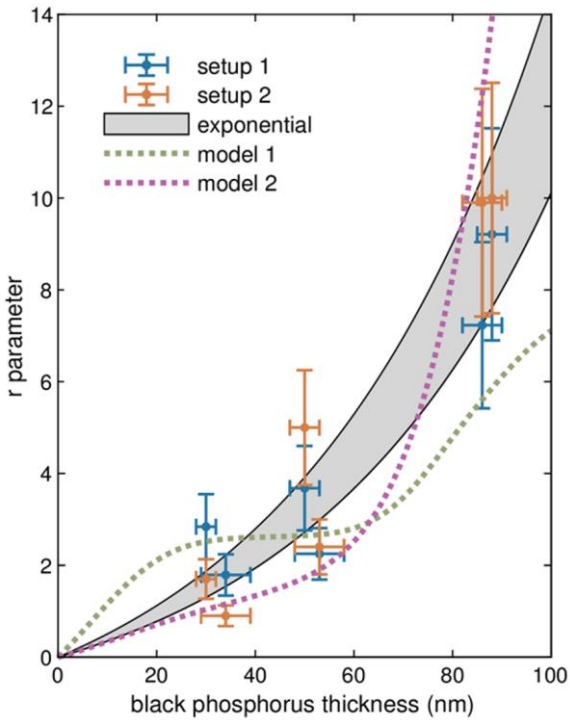

Figure 2.9 Thickness calibrations curve for BP flakes exfoliated on SiO2 \Si resulting from AFM and Raman measurements. The orange and blue point are experimental data measured with two different Raman setups. The two black solid lines are calculated with the higher and lower limits of the constant q in equation 2.13 by fitting the experimental data. The gray area between those curves is region where the thickness calibration curve may lie with a 95% of confidence. The green and violet dashed lines are the results of calculations performed accounting the effects of optical interferences and using the values of the BP complex refractive index reported in references [39](green) and [51](violet). Figure adapted from reference [43]

exponential behavior modulated by interference. Typically, the higher is the value of the extinction coefficient of BP, the smaller are the interference modulations. The reason why the $I(B_{2g})/I(Si)$ intensity ratios follow an exponential increasing behavior can be understood from the interference enhanced intensities of the BP B_{2g} and the silicon Raman bands reported in figures 2.5(b) and 2.5(c). We see that, independently of the polarization direction of the incident light or the relative orientation between the silicon substrate and the BP flake, the interference enhancement (or reduction) of the Raman signal for both the BP-B_{2g} and the Si-substrate bands occurs exactly at the same BP thicknesses. Therefore, the strong oscillations of the B_{2g} and the Si Raman band intensities as function of the BP thickness nearly cancel out when considering the ratio between them. Inspecting figure 2.9, however, we notice that the measured r-values are highly scattered between the two calculated model curves. We conclude therefore that, to a first approximation, the exponential trend observed on the measured r-values can be described using a simpler model that relies on the Beer-Lambert attenuation law for both the BP-B_{2g} and the silicon substrate Raman bands (see the gray-region in figure 2.9). Clearly this model does not account correctly for the modulation effects introduced by the optical interferences. However, considering the discrepancies between the calculations performed with different values of the BP optical constants, it can be used to satisfactorily describe the observed

data in the measured thickness range. Furthermore, within this model it is possible to obtain also an analytical expression for the thickness calibration equation:

$$r = q(e^{2\alpha_{BP}t} - 1) \qquad (2.13)$$

where α_{BP} is the absorption coefficient of BP at the excitation wavelength of 532nm, t the sample thickness and q a constant. By using the value of the BP absorption coefficient reported in literature for an unpolarized incident radiation [52], $\alpha_{BP} = 0.01\ nm^{-1}$, we obtain by fitting the value of the constant: $q = 1.9 \pm 0.3$. Therefore, knowing the q-value and by measuring experimentally the r-ratio value it is possible to obtain an estimation for the thickness of the BP flake from equation (2.13).

Source of errors and limits of validity

To conclude we will briefly examine the uncertainty and the limits of validity of the proposed Raman thickness calibration model. Regarding the uncertainty we observe that it can be determined in different ways. A first approach consists in considering the calibration curve included within the gray region between the upper and lower black solid lines in figure 2.9, which are respectively the curves calibrated with the higher and lower limits of the fitted q, as determined by imposing a 95% interval of confidence. Alternatively, the uncertainty on the thickness values determined from the calibration curve can be estimated from the root mean square error between the AFM-measured thickness values and those determined from equation (2.13). The value of this error is always about 20% of the measured thickness values and it is a consequence of more than one effect. Beside the unavoidable inhomogeneities in the thickness of the flakes, another possible source of error is related to the variation of the intensity of the Si-Raman band with the relative orientation between the BP-flake and the silicon substrate. As discussed in Section 2.2.1 the intensity of the silicon Raman band can be enhanced or reduced at a given BP thickness depending on the polarization direction of the incident and scattered light, as determined by the relative orientation between the BP crystallographic axes and the [110] direction of the silicon substrate (compare also with figure 2.5(c)). Consequently, this effect may introduce a scattering on the $I(B_{2g})/I(Si)$ intensity ratio measured on different BP flakes with the same thickness. Furthermore, the final uncertainty on the thickness values determined from the calibration curve is also affected by systematic errors. One of these errors is the position of the focal field of the Raman microscope objective. In particular, the defocusing effect on a small size flake may change the ratio between $I(B_{2g})$ and $I(Si)$. Another source of error can be possibly ascribed to the use of high NA objectives. These objectives may cause the appearance of an incident electric field having a slight polarization component in the vertical direction, introducing in this way a modification to the selection rules derived from the Raman tensors in equation (2.5). [53] In the experiments performed above and reported in figure 2.9 to get a compromise between the collection efficiency and the selectivity of the objective for a given polarization, objectives with 0.75 NA (50X) have been chosen to perform the measurements of the Raman intensities.

Regarding the validity of the experimentally determined calibration curve (2.13) we point out that it can be considered valid down to a thickness of 5nm (corresponding to 10 BP layers). This lower limit corresponds to the beginning of quantum confinement effects , which affect the electronic properties of BP and change, for example, its band-gap value.[54] Therefore, for thicknesses below 5nm the absorption coefficient of BP becomes a layer-dependent quantity

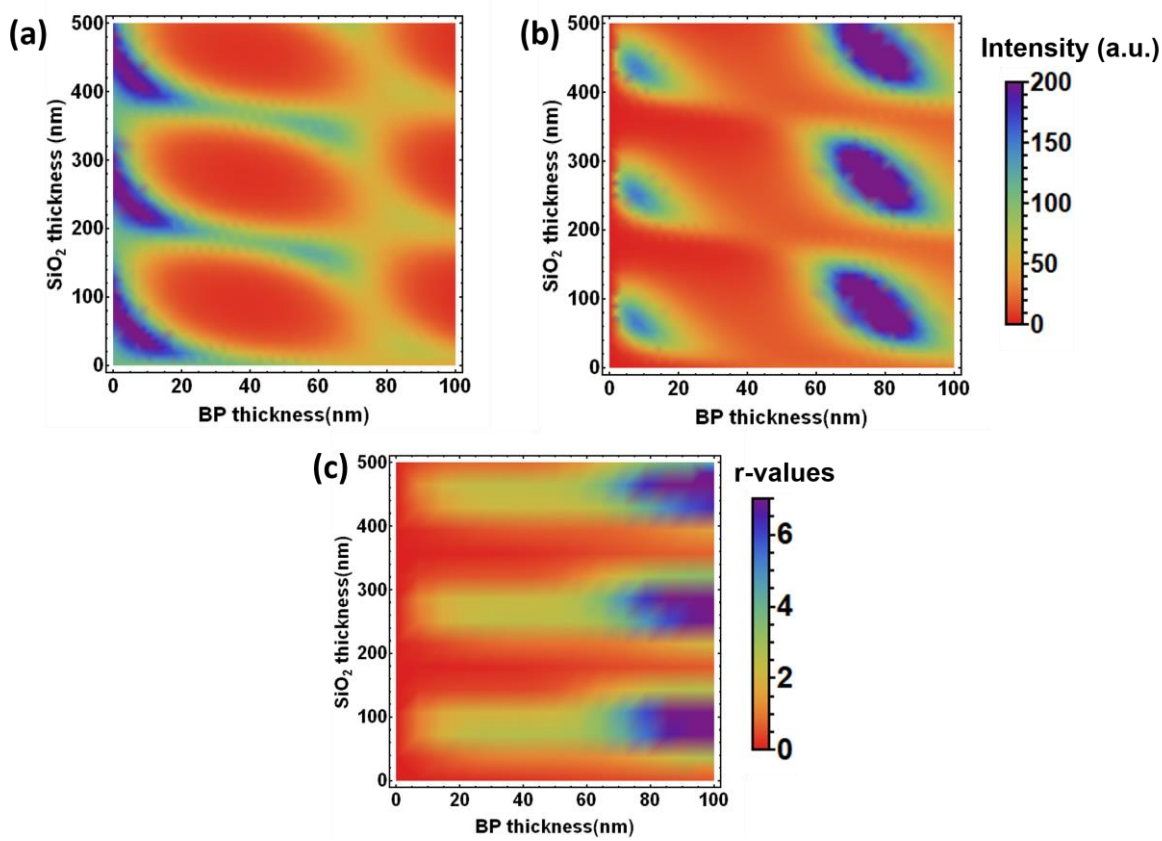

Figure 2.10 2D-plots for the interference enhanced intensity of the silicon **(a)** and BP $\boldsymbol{B_{2g}}$ **(b)** Raman bands calculated from equations (2.10) and (2.7) as function of the BP and SiO_2 thickness. **(c)** Intensity r-ratio values calculated from the contour plots in (b) and (a) according to equation (2.12). All the calculations have been performed using the BP, SiO_2 and Si complex refractive values reported in ref.[39] and assuming a 532 nm incident light polarized along the armchair direction and a scattered light polarized along the zigzag direction of BP.

and this effect may lead to significant changes in the susceptibility and, therefore, in the Raman tensors. However, as discussed previously, in the few layer-regime thickness-calibrations based on different approaches, for example by investigating the interlayer low-frequency modes[47], may work better. The tested upper limit to the validity of the thickness calibration model in equation (2.13) is 100 nm. As a final remark on the applicability of the calibration equation (2.13), we note that it can be eventually generalized to situations where the BP-flakes are exfoliated on SiO_2/Si substrates with different values of the SiO_2 thickness. This is illustrated in figure 2.10 which shows the contours 2D plots of the intensity of the BP B_{2g} Raman band, of the silicon Raman band and of the r-parameter calculated as a function of the BP and SiO_2 thickness. We note that all these quantities have a periodic behavior with the SiO_2 thickness. Specifically, the r-ratio follows a monotonic increasing trend as a function of the BP-thickness at each given SiO_2 thickness value. Clearly, for a very different SiO_2 thickness, a new calibration procedure might be required in order to determine a new value for the constant q in equation (2.13).

2.4 Thinning of black phosphorus: towards the 2D limit

Multilayer BP flakes obtained from exfoliation techniques can be either used directly in the fabrication of devices or employed for subsequent thinning steps towards the single layer limit. The controllable layer-by-layer thinning of exfoliated BP flakes has been reported in the literature with a variety of methods. Plasma etching[45], [55], [56], thermal sublimation [46], vacuum[57] and rapid thermal annealing[58] methods have all demonstrated capabilities to control the thickness of BP down to a single layer being able to preserve also the crystalline quality of the thinned flakes. Additionally, the plasma etching approach has been used to engineer the defects concentration in few layers' phosphorene flakes allowing the on-demand modulation of the optical and electronic properties.[55] The layer-by-layer thinning of multilayer BP flakes has been also investigated with scanning probe nanolithography techniques[59] and focused electron beams [60], [61]. Both these approaches have been developed to achieve an "in-situ" nanometer scale patterning of the exfoliated flakes so to reduce the air exposure problem (see Chapter 4) affecting BP in the conventional "ex-situ" device fabrication steps.

In general, however, all these thinning methods are characterized by a low throughput and do not allow for the rapid processing of large quantities of exfoliated flakes. A promising route in this respect is represented by the laser thinning technique. This thinning method is based on the thickness reduction of a layered material by means of a laser etching process and it has one of its strongest advantages in its versatility as demonstrated in the case of the thinning of graphite and multilayer MoS_2 flakes [62]–[64]. When coupled with Raman spectroscopy it can be used to obtain both a characterization and an accurate monitoring of the thickness evolution and, moreover, an in-situ optical nano-patterning of the layered vdW material.[65] Despite the fact that the laser patterned regions have their minimum size limited by optical diffraction effects and may have an high surface roughness and poor crystalline quality, an additional advantage of the laser thinning technique is the possibility of realizing a site-specific control of the physical and chemical properties of the layered material such as, for example, its local energy bandgap or crystalline phase.[66]–[68]

In the case of exfoliated multilayer BP flakes the laser etching of the atomic planes proceeds both via photochemical oxidation and sublimation processes. The laser induced photochemical oxidation of BP is caused by the photo-oxidation effect in presence of water and oxygen and it has been widely documented in the literature[7], [8] (refer to Chapter 4 for a more extensive discussion on this effect). The sublimation process, instead, involves the conversion of the absorbed light into heat via photon-phonon interactions. If the resulting lattice vibrations become strong enough, they can break the P-P bonds and ablate the material from the bulk crystal. The laser etching of BP has been achieved both using high-power ultrafast pulsed laser sources [69] [70] and low power continuous wave (CW) laser sources.[68], [71] Although most of these studies focused both on the optical characterization and on the controllable thinning/patterning of the exfoliated BP flakes, they did not addressed in detail the mechanisms affecting the laser heating and ablation of the flakes. In particular, the presence of the supporting substrate is expected to influence the heat transfer mechanism due to a not-trivial interplay between the optical and thermal properties of BP. A closer insight into these aspects is therefore

demanded in order to optimize the laser thinning process with the choice of the appropriate processing parameters, such as the laser power or the exposure time, so as to achieve a controlled layer-by-layer thinning.

In the following section we will illustrate a more in-depth analysis on the laser heating and ablation of multilayer BP flakes supported on SiO_2/Si substrates. These substrates are technologically relevant in all the devices applications of BP and therefore it is of paramount importance to achieve a more detailed understanding of the heat dissipation and ablation mechanisms of multilayer BP flakes exfoliated on them. In particular, an ineffective heat removal due to a sub-optimal heat dissipation may have dramatical effects on the performances of BP devices especially when operated in high-field conditions causing a local increase of the temperature and a subsequent chemical degradation, decomposition or unwanted thermomechanical strains which contribute to the device breakdown.[72], [73] The heat dissipation of multilayer BP flakes strongly depends on its anisotropic thermal properties and on the nature of the thermal coupling with the supporting substrate [9], [74]–[76] . Both these properties can be investigated with the aid of Raman optical thermometry techniques that make use of the heating induced by the laser optical absorption in order to give a local and contactless probe of the temperature increase in the material with a high spatial resolution and material specificity. The quantitative predictions on the thermal properties are usually extracted with the aid of numerical simulations of the heat diffusion problem and need to be always complemented by a careful inspection of the sources of errors [77]. The Raman opto-thermal method has been extensively used in the literature to study the thermal properties of suspended and supported 2D materials, i.e. their thermal conductivity and the interfacial thermal resistance with the substrate.[9],[70]–[74] Therefore, a better knowledge on the laser heating of BP, besides being useful for the optimization of the laser thinning process, can be also used to improve the interpretation of the temperature measurements obtained from Raman optical thermometry experiments so to get more accurate prediction on its thermal properties. As we will see in the following, optical, thermal and eventually mechanical strain effects caused by the supporting substrate may introduce possible sources of errors on the micro-Raman temperature measurements and, hence, affect the calculated values of the BP thermal properties.

2.4.1 Investigation of the laser heating and thinning of black phosphorus by Raman spectroscopy

Experimental methods

The laser heating/ablation experiments were carried out focusing on the surface of the BP flakes a 532 nm laser beam with a 100x 0.9 NA microscope objective and using an exposure time of 20 sec. The incident optical power was gradually increased using a series of neutral density filters (ND) at different transmission interposed on the laser beam path before the microscope objective. During the laser heating the Raman spectra of the flakes were simultaneously acquired by means of a Jobin-Yvon T6400 Raman spectrometer equipped with 1800 lines mm^{-1} grating and a liquid-nitrogen cooled CCD detector. The value of the incident laser power on the surface of the flakes was determined using a photodiode power-meter. The laser power measurements were performed after the microscope objective in order to consider the additional light attenuation caused by the optical elements on the excitation/collection laser

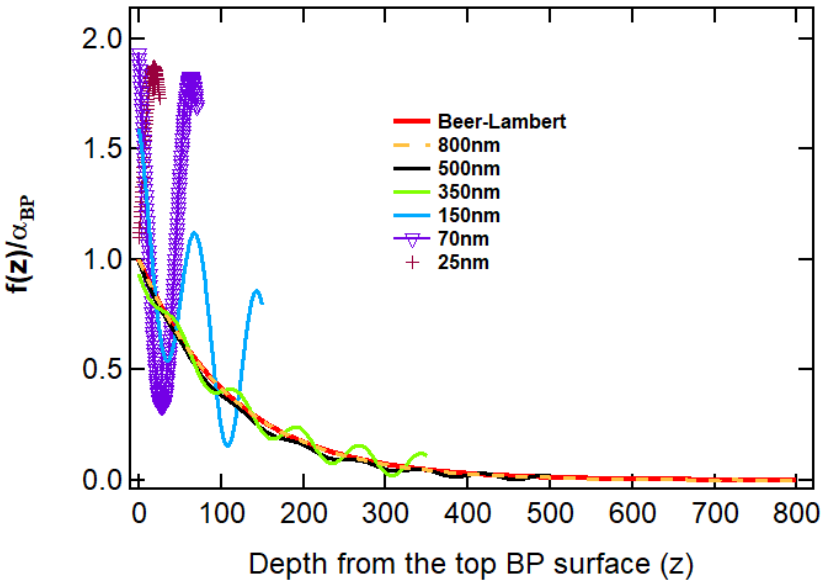

Figure 2.11 Calculated light attenuation function, $\boldsymbol{f(z)}$, for different values of the BP flake thickness as indicated in the legend. In the figure, *z*, is the distance from the top BP surface. All the calculations have been performed using the SiO_2 and Si complex refractive values reported in ref.[39] and using for BP a refractive index and attenuation coefficient calculated averaging the values at $\boldsymbol{\lambda}$=532nm along the zigzag and armchair directions: $\bar{\boldsymbol{n}}_{\boldsymbol{BP}}\sim\mathbf{3.6}$ and $\bar{\boldsymbol{k}}_{\boldsymbol{BP}}\sim\mathbf{0.4}$.

beam path. For a maximum output laser power of 180 mW the unattenuated incident power (i.e. without the ND filters) measured at the sample surface was 60 $\pm$ 0.5 mW.

Thickness of the investigated multilayer BP flakes

In order to elucidate the role played by the SiO_2/Si substrate on the laser heating and ablation of multilayer BP flakes, the experiments were carried out on flakes exfoliated in two different thickness ranges discriminated by the value of the light penetration depth: $\delta_{BP} = 1/\alpha_{BP}$, where α_{BP} is the absorption coefficient of BP. The value of the light penetration depth in BP is, in principle, different along the two in-plane crystallographic axis, i.e. the armchair (AC) and zig-zag (ZZ) direction, but a rough estimation for this quantity can be obtained using the experimental value of α_{BP} ≈0.01 nm^{-1} measured with an unpolarized incident radiation for a wavelength close to λ=532 nm.[52] We noticed that for BP flakes having thickness below $3\delta_{BP}$ ≈300 nm, hereafter named as *thin BP flakes*, the absorption of the light along the cross-plane direction of BP can be strongly modulated by optical interference effects due to multiple reflections at the top and bottom interface of the flake. For flakes with thickness above 300 nm, hereafter named as *thick BP flakes*, instead, these effects can be considered in a good approximation negligible and the absorption of the light along the cross-plane direction is mainly regulated by the well-known Beer-Lambert exponential attenuation law. This behavior can be clearly seen in Figure 2.11 which illustrates the calculated light attenuation function, $f(z)$, for BP flakes with different thickness. Here, *z* is the distance from the top BP surface and the analytic expression of $f(z)$ can be derived from equation 2.8 for the amplitude of the excitation electric field in BP in presence of multiple reflection effects:

$$f(z) \propto \alpha_{BP}|F_{ex}(z)|^2 \qquad (2.14)$$

where α_{BP} is the absorption coefficient of BP. As can be seen from figure 2.11, if the thickness of the sample becomes an integer multiple of $\frac{\lambda}{4n_1}$, where λ is the wavelength of the excitation (or scattered) light and n_1 the refractive index of BP, constructive or destructive interference between the light rays originating from multiple reflections at the top and at the bottom interfaces of the sample play a dominant role and introduce an oscillating modulation on $f(z)$. In the limit of BP thicknesses $d_1 \gg \frac{\lambda}{4n_1}$, instead, $f(z)$ follows the well-known Beer-Lambert light attenuation law: $|f(z)|^2 \rightarrow \alpha_{BP} e^{-\alpha_{BP} z}$.

The *thick BP flakes* were obtained typically with a liquid phase exfoliation (LPE) approach. Bulk BP crystals were sonicated (for 3-4 hours) in isopropyl alcohol solution and then the suspensions, after a 20 min centrifugation, were drop-casted on clean SiO_2/Si substrates. After drying the solvent, the sample were quickly inspected under the optical microscope so as to determine the BP flakes with bigger sizes where to carry out the subsequent AFM and Raman characterizations. The typical AFM-determined thickness of the thick BP flakes varied between 0.3 µm and 1.2 µm. *Thin BP flakes*, instead, were obtained via a tape-exfoliation approach (using a Nitto 3M™ tape) by multiple peelings of bulk BP crystals. The exfoliated flakes were then then directly transferred on clean SiO_2/Si substrates for the AFM and Raman characterizations. The typical thickness of the such thin BP flakes ranged between 10 nm and 120 nm.

Laser heating and ablation

Figure 2.12(a) illustrates the principle of the laser heating and Raman characterization experiments carried out on exfoliated thick and thin BP flakes. The Raman spectra measured in one of such experiments on a thick BP flake are reported in figure 2.12(b). We notice that at low incident optical powers the Raman spectra are characterized by the presence of only three peaks corresponding to the first order, $A_g^1(362\ cm^{-1})$, $B_{2g}(439\ cm^{-1})$ and $A_g^2(467\ cm^{-1})$ Raman bands of BP. Figure 2.12(b) shows also that increasing the incident laser power above a certain threshold, denoted by P_c, the Raman spectra drastically change. In particular, above P_c the BP Raman bands show a reduction in the intensity accompanied by the appearance of a fourth band at ~520 cm^{-1} due to the silicon substrate. Moreover, as illustrated by the optical microscope image in the inset of figure 2.12(b), the focused laser beam area on the surface of the BP flake (see the circled-area in red) shows a marked alteration in the reflectivity when illuminated by an incident optical power above the threshold P_c. This effect and the concomitant reduction in the intensity of the Raman bands can be interpreted as a result of a localized laser ablation of the top layers of the flake. Similarly to what reported in refs.,[68], [71] using a fixed light exposure time, we observed that the laser ablation occurs whenever the incident optical power reaches a threshold value, P_c. In our experiments, the laser ablation of thick BP-flakes, within the (0.3-1.2) µm thickness range, was observed to occur systematically between 14-16 mW whereas in the case of thin BP-flakes, with a thickness lying within the (10-120) nm range, the threshold power showed more pronounced variations. This fact is also demonstrated by the behavior of the Raman shifts, $\Delta\omega$, of the BP Raman bands when plotted as function of the incident laser power, P_{inc}. As can be noticed from figures 2.12(c) and 2.12(d), the threshold ablation power P_c correspond to the minimum of the experimentally determined $\Delta\omega$ vs. P_{inc} curves. In particular, figure 2.12(d) reports the $\Delta\omega$ vs. P_{inc} curves obtained for the A_g^2 mode

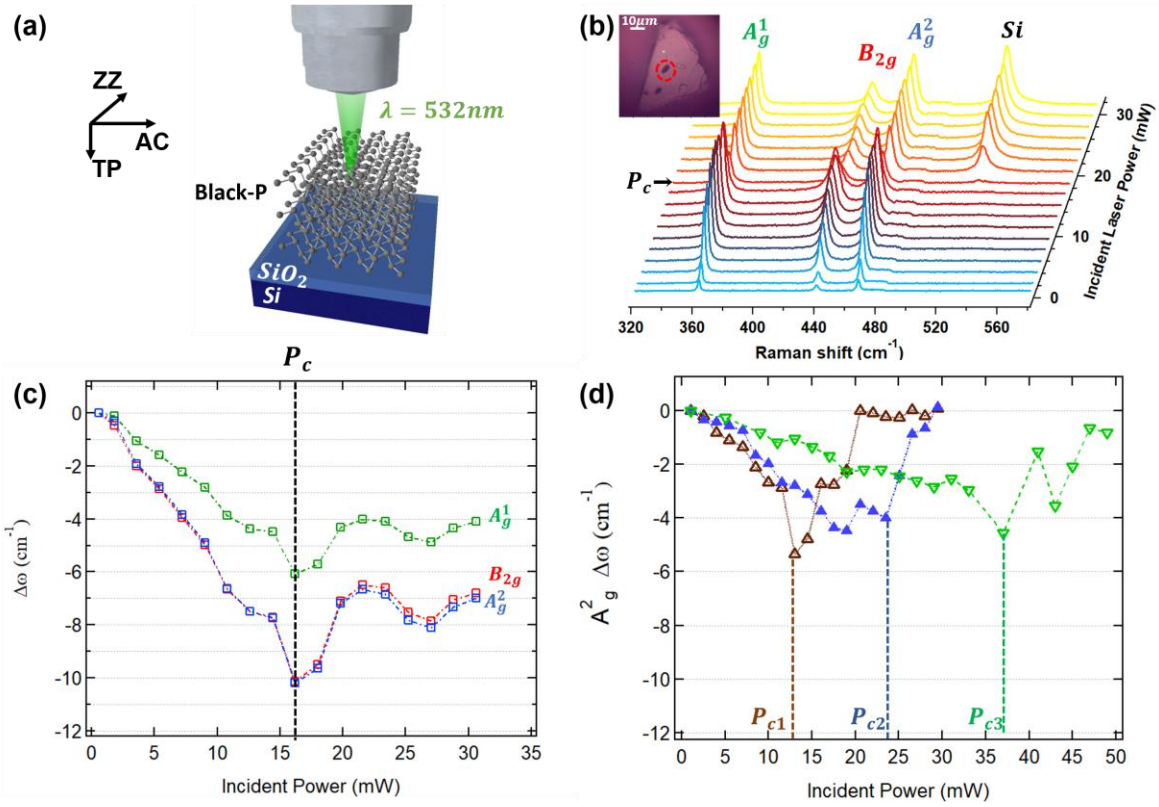

Figure 2.12 (a) Schematic illustration of a laser heating experiment carried out on a SiO2/Si supported BP crystal. The zigzag (ZZ), armchair (AC) and cross-plane (CP) direction of the BP crystal also indicated **(b)** Waterfall plot of all the Raman spectra acquired during a laser heating and ablation experiment on a thick LPE BP flake. Inset: optical microscope image of a thick LPE BP flake showing the laser ablated region (circled in red). **(c)** Raman shifts of the BP $\boldsymbol{A_g^1}$, $\boldsymbol{B_{2g}}$ and $\boldsymbol{A_g^2}$ Raman modes as function of the incident power calculated from the Raman spectra reported in (b). **(d)** Raman shift of the BP $\boldsymbol{A_g^2}$mode as function of the incident laser power for three different tape-exfoliated BP flakes. The values of the threshold ablation power ($\boldsymbol{P_c}$) are also indicated.

from three different tape exfoliated flakes. For such thin multilayer BP flakes, we clearly see that the positions of the minima have strong variation above 14 mW.

Raman band shifts before and after the ablation

Figures 2.12(c) and 2.12(d) help to reveal further differences in the laser heating and ablation of thick and thin multilayer BP flakes.

Firstly, we notice that by increasing the incident laser power the position of the BP Raman bands linearly red shifts towards lower wavenumbers. In particular, the slope, $\frac{\Delta\omega}{\Delta P_{inc}}$, of the $\Delta\omega$ vs P_{inc} curves of the A_g^1, B_{2g} and A_g^2 modes measured in the low-power regions (i.e. before P_c) are remarkably different. From figure 2.12(c) we see that for the B_{2g} and A_g^2 modes the $\frac{\Delta\omega}{\Delta P_{inc}}$ slope is roughly similar (≈-0.62 - -0.63 cm^{-1}/mW) whereas is much lower for the A_g^1 mode (≈-0.37 cm^{-1}/mW). This marked difference in the low-power behavior of the B_{2g}, A_g^2 and A_g^1 modes is caused by the nature of the atomic vibrations associated to these Raman modes and it occurs regardless of the flake thickness. Indeed, since the B_{2g} and A_g^2 modes are associated to in-plane atomic vibrations along the zig-zag and armchair direction of BP and the A_g^1 mode to

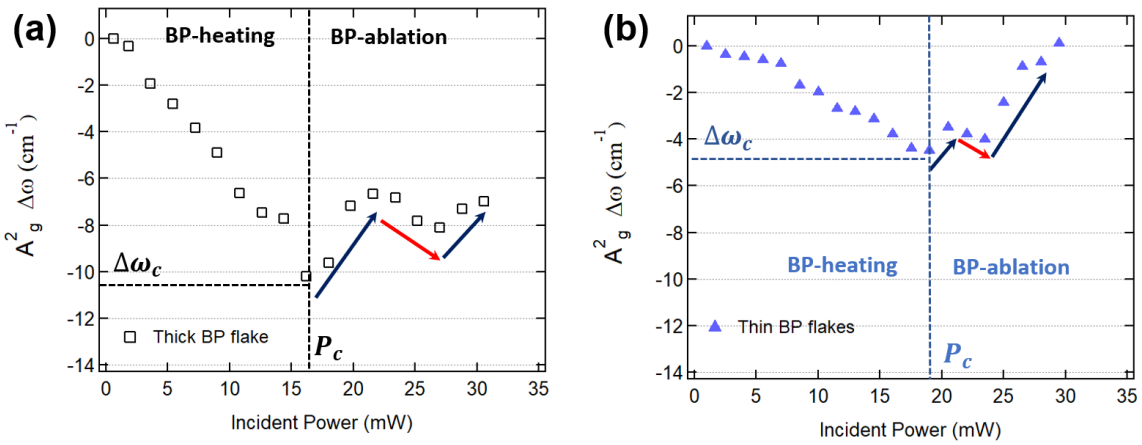

Figure 2.13 Raman shift of the BP A_g^2 mode as function of the incident laser power for **(a)** a *thick* LPE BP flake (square data points) and **(b)** a *thin* tape-exfoliated BP flake (triangular data points). Blue and red arrows indicate the ablation and heating regions, respectively. The threshold incident powers (P_c) and Raman shift values at the ablation ($\Delta\omega_c$) of the flakes are also indicated.

the out-of-plane atomic vibrations, the latter is more influenced by the effects of the weak vdW interactions between the puckered BP layers with respect to the other two Raman modes.

However, each time the behavior of the Raman shifts of multilayer thin and thick BP flakes was compared, we have always observed that the slopes $\frac{\Delta\omega}{\Delta P_{inc}}$ measured from thin BP flakes in the low power region (i.e. $P_{inc} < P_c$) were systematically lower than that measured from thick BP flakes. Such thickness dependence in the low-power behavior of the BP Raman modes is evidenced more clearly in figures 2.13(a) and 2.13(b) which compare the $\Delta\omega$ vs P_{inc} curves experimentally determined for the A_g^2 mode in a multilayer thick and thin BP flake, respectively. The value of the Raman shifts $\Delta\omega$ reported in these figures can be used to estimate the average local temperature increase ΔT in the flake caused by the laser optical heating using the following first-order equation:[82]–[84]

$$\Delta\omega(T) = \omega(T) - \omega_0 = \chi(T - T_0) = \chi\,\Delta T \qquad (2.15)$$

where ω_0 is the frequency of a Raman mode extrapolated in the limit of zero incident laser power ($P \to 0$), T_0 the ambient temperature and χ is the first-order Raman-temperature coefficient of the considered Raman mode. The slope of the $\Delta\omega$ vs P_{inc} curve of the A_g^2 mode measured in the low-power region from a thin BP flake (see figure 2.13(b)) suggests that the laser-induced temperature increase is lower when compared to that occurring in a thick BP flake (see figure 2.13(a)). In particular, we have used the value of the Raman shift, $\Delta\omega_c$, measured at P_c to estimate the temperature, T_c, at which the laser ablation of the flakes occurs. As indicated by the dashed lines in the figures 2.13(a) and 2.13(b), for the thick BP flake $\Delta\omega_c$ =-10.77 cm^{-1}, whereas for the thin BP flake $\Delta\omega_c$ =-5.06 cm^{-1}. Assuming an ambient temperature of $T_0 = 20\ °C$ and using the value of the first-order Raman temperature coefficient for the A_g^2 mode reported in ref.,[82] $\chi_{A_g^2}$=0.0276 cm^{-1} K^{-1}, the ablation temperature predicted from equation (2.15) for the thick BP flake is T_c~410 °C whereas for the thin BP flake is T_c~203 °C. Such discrepancy between the Raman-predicted ablation temperatures of a thick and thin BP flake did not change even when calculated using other possible experimental values reported in literature for the first order temperature coefficient of the A_g^2 mode.[35], [82], [85], [86] This

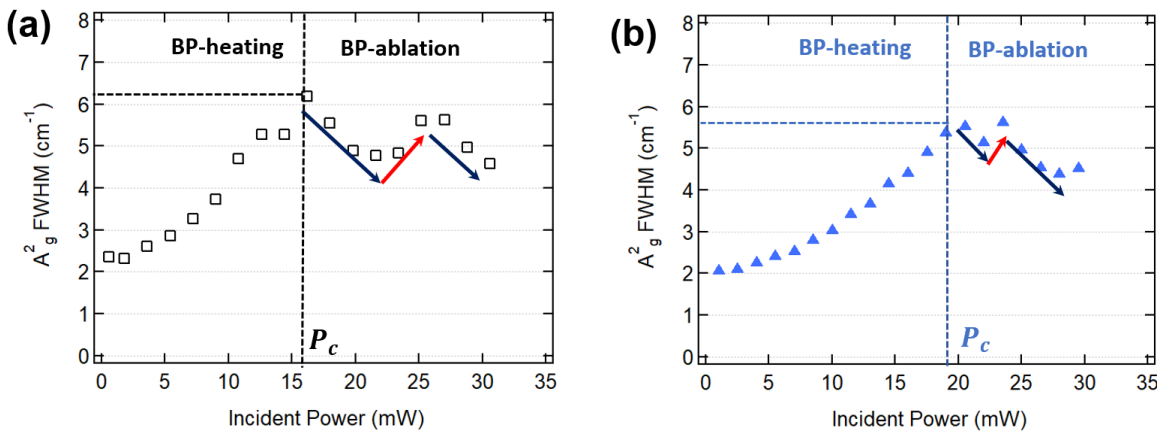

Figure 2.14 Full width half maximum (FWHM) values calculated for the A_g^2 for a **(a)** *thick* LPE BP flake and a **(b)** *thin* tape-exfoliated BP flake . The blue and red arrows indicate the ablation and laser heating regions, respectively. The black dashed line denotes a nearly identical FWHM value observed at the threshold ablation powers.

result is quite unexpected considering that the typical temperatures reported for the thermal sublimation of BP all lie within the 350-400°C range.[46], [87], [88]

The behavior of the Raman peak positions measured at the incident optical power above the threshold value, $P_{inc} > P_c$, shows also other unexpected results. From figure 2.13(a) and 2.13(b), we see that in both the thin and thick BP flake the A_g^2 peak positions blue shift proceeding towards higher-wavenumbers with a zigzag-like trend as highlighted by the red and blue arrows. We assigned the blue-arrow regions to the occurrence of laser ablation processes in the illuminated area of the BP flake whereas the red-arrow regions were ascribed to situations in which the thinned BP flakes were only heated by the laser light without ablation. In particular, at the onset of the regions indicated by red arrows in figures 2.13(a) and 2.13(b), the incident laser light did not produce an ablation despite the flake was illuminated by an optical power above the threshold value P_c. In the ablation regions (blue-arrow regions), instead, the shift in the positions of the A_g^2 mode suggests that the ablation temperature of the thinned flake decreases. Despite of being counterintuitive, this result was systematically observed in all the experiments performed on thick and thin BP flakes and leaves an open question regarding the Raman probed temperatures of exfoliated BP flakes.

Raman bandwidths before and after the ablation

Figure 2.14(a) and 2.14(b) show the behavior of the A_g^2 peak full width half maximum (FWHM) measured as function of the incident power in a thin and thick BP flake, respectively. We notice that in the low power region ($P_{inc} < P_c$) the FWHM increases by raising the incident optical power. Since the FWHM is a monotonic increasing function of the temperature,[82], [84], [89] the behavior of the FWHM corroborates the temperature increase within the Raman probed region also observed from the Raman shifts at $P_{inc} < P_c$. However, we notice that the value of the FWHM measured at the threshold ablation power P_c is not much different (less than 1 cm^{-1}) between the thin (~5.6 cm^{-1}) and thick (~6.2 cm^{-1}) BP flake (see the horizontal dashed lines in figures 2.14(a)-2.14(b)). Thus, in a marked contrast with the conclusions drawn from equation (2.15), this finding indicates that the ablation temperature derived from the

FWHM values at P_c may be nearly identical in both the thick and thin multilayer BP flake. Since the sublimation temperature of BP is not expected to depend sensitively on the flake thickness in the multilayer regime, we consider this result quite reasonable. However, it does not help to explain the anomalous behavior observed on the Raman shifts at P_c.

For an incident optical power increased above the threshold, P_{inc}>P_c, the behavior of the A_g^2 peak full width half maximum (FWHM) reproduces the zigzag-like sequence observed on the $\Delta\omega$ vs P_{inc} curves. However, the amplitude of the zigzag-like modulation in the FWHM vs P_{inc} curves is comparatively less pronounced than the amplitude of the zigzag-like modulation observed from the $\Delta\omega$ vs P_{inc} curves. This FWHM behavior proves that during the ablation of the flake (the blue arrow regions in the figure) the temperature of BP did not vary much from the values obtained at P_c casting again a doubt on the temperature predictions that can be derived from the Raman shifts of the BP Raman modes.

2.4.2 Substrate effects on the laser thinning and heat dissipation

The discrepancies observed between the Raman temperatures probed by the FWHM values and those probed by means of the Raman shifts in thick and thin multilayer BP flakes can be reconciled only understanding the physical mechanisms that link the laser heating to the Raman peak shifts and bandwidths. A better insight on such effects, in turn, can help to gain an improved comprehension of the cross-plane heat dissipation through multilayer BP flakes exfoliated on thermal insulating SiO_2/Si substrates

Numerical solution of the heat diffusion problem in supported BP flakes

Since the typical timescales of the laser illumination in our experiments were of the order of tenths of seconds, the temperature distribution $T(\boldsymbol{x})$ generated in the BP flakes by the optical absorption of the incoming radiation was calculated solving, with a finite element method, a stationary heat diffusion equation:[79], [90], [91]

$$\nabla \cdot (\boldsymbol{\kappa}(\boldsymbol{x})\nabla T) + \dot{Q}(\boldsymbol{x}) = 0 \qquad (2.16)$$

where $\boldsymbol{\kappa}(\boldsymbol{x})$ is position-dependent thermal conductivity tensor and $\dot{Q}(\boldsymbol{x})$ is the heat source term (W/m^3). The latter describes the heat generated by the laser optical absorption inside the volume of the material. In order to numerically solve the equation (2.16) we made some simplifying assumptions.

Firstly, as mentioned previously, BP is a strongly anisotropic material and therefore the values of the thermal conductivity along the AC, ZZ and TP directions are all different. However, in order to exploit the cylindrical symmetry of the heat source term $\dot{Q}(\boldsymbol{x})$ and, thus, reduce the dimensionality of equation (2.17), we modeled BP as an effective material characterized by an average in-plane thermal conductivity $\kappa_{eff} = \sqrt{\kappa_{AC}\kappa_{ZZ}}$~28.8 $\frac{W}{mK}$ and a cross-plane thermal conductivity κ_{TP}~4 $\frac{W}{mK}$. [9], [74], [92], [93] In this way it was possible to recover a solution of the 3D problem (2.16) by exploiting the azimuthal symmetry in cylindrical coordinates of a 2D heat equation solved in a (r, z) domain where r is the in-plane and z the cross-plane direction.

Secondly, the 2D-domain on which the heat equation was solved was partitioned in three regions in order to assign everywhere the values of the thermal conductivity $\boldsymbol{\kappa}(\boldsymbol{x})$ and model the effects of the finite thermal boundary conductance, G_{int}, at the interface between BP and

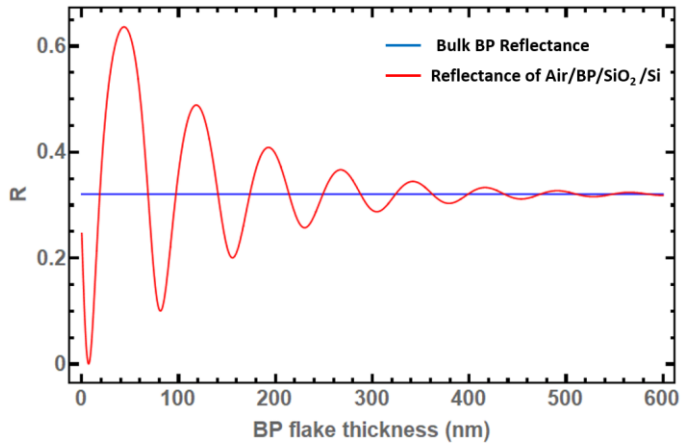

Figure 2.15 Normal incidence reflectance, R, of BP as function of the BP flake thickness calculated from the Fresnel formula for the reflectance in a two layer BP/SiO_2 system on top of a semi-infinite silicon substrate. For thicknesses above ≈300 nm the BP reflectance becomes nearly constant with a value close to the reflectance of bulk BP. The calculation of R has been performed using the SiO_2 and Si complex refractive values reported in ref.[39] and using for BP a refractive index and attenuation coefficient calculated averaging the values at $\boldsymbol{\lambda}$=532 nm along the zigzag and armchair directions: $\bar{\boldsymbol{n}}_{\boldsymbol{BP}}\sim\mathbf{3.6}$ and $\bar{\boldsymbol{k}}_{\boldsymbol{BP}}\sim\mathbf{0.4}$.

SiO_2. The latter quantity describes the efficiency of heat transfer between BP and SiO_2 and, generally, depends on the preparation conditions of the interfaces of these two materials as well as on the BP flake thickness.[75], [76] Therefore, to account in our model of the thermal effects caused by the finite value of thermal boundary conductance, we defined an interfacial region between a 50 nm thick SiO_2 region and a BP region with variable thickness. Such interfacial region was assumed with a thickness, d_{int}, negligibly small with respect to the thickness of the other two domains so to assign to this region a fictious thermal conductivity value, k_{int}, calculated from the value chosen for the thermal boundary conductance G_{int}, i.e.: $k_{int} = \frac{d_{int}}{1/G_{int}}$. The thermal conductivity value used in the SiO_2 domain, instead, was assumed to be: $\kappa_{SiO_2}\sim 0.9\ \frac{W}{mK}$, i.e lower than the thermal conductivity typically reported in literature for the bulk SiO_2 glass which is $\kappa_{SiO_2}\sim 1.4\ \frac{W}{mK}$. The deviation of the thermal conductivity of the SiO_2 film from the bulk value accounted for the effects due to the finite interfacial boundary conductance that exists at interface between the 50 nm -thick SiO_2 film and the silicon substrate (see e.g. references [94], [95]). Since silicon has a thermal conductivity ($\kappa_{Si}\sim 148\frac{W}{mK}$) typically two order of magnitude higher than that of SiO_2 and BP, the thermal effects due to a semi-infinite silicon substrate have been modeled by imposing a thermal bath boundary condition on bottom interface of the SiO_2 region, i.e. $T(r, z = 0)$=20 °C. Finally, the lateral extension of the BP, SiO_2 and interfacial regions has been assumed identical and equal to 7μm, i.e. wide enough to minimize unwanted geometric boundary effects on the calculated distribution of temperatures.

The heat source term $\dot{Q}(\boldsymbol{x})$ in equation (2.16) depends both on the laser beam intensity profile, $g(r, z)$, and on the attenuation of the laser light due to the absorption along the cross-plane direction, $f(z)$:[90]

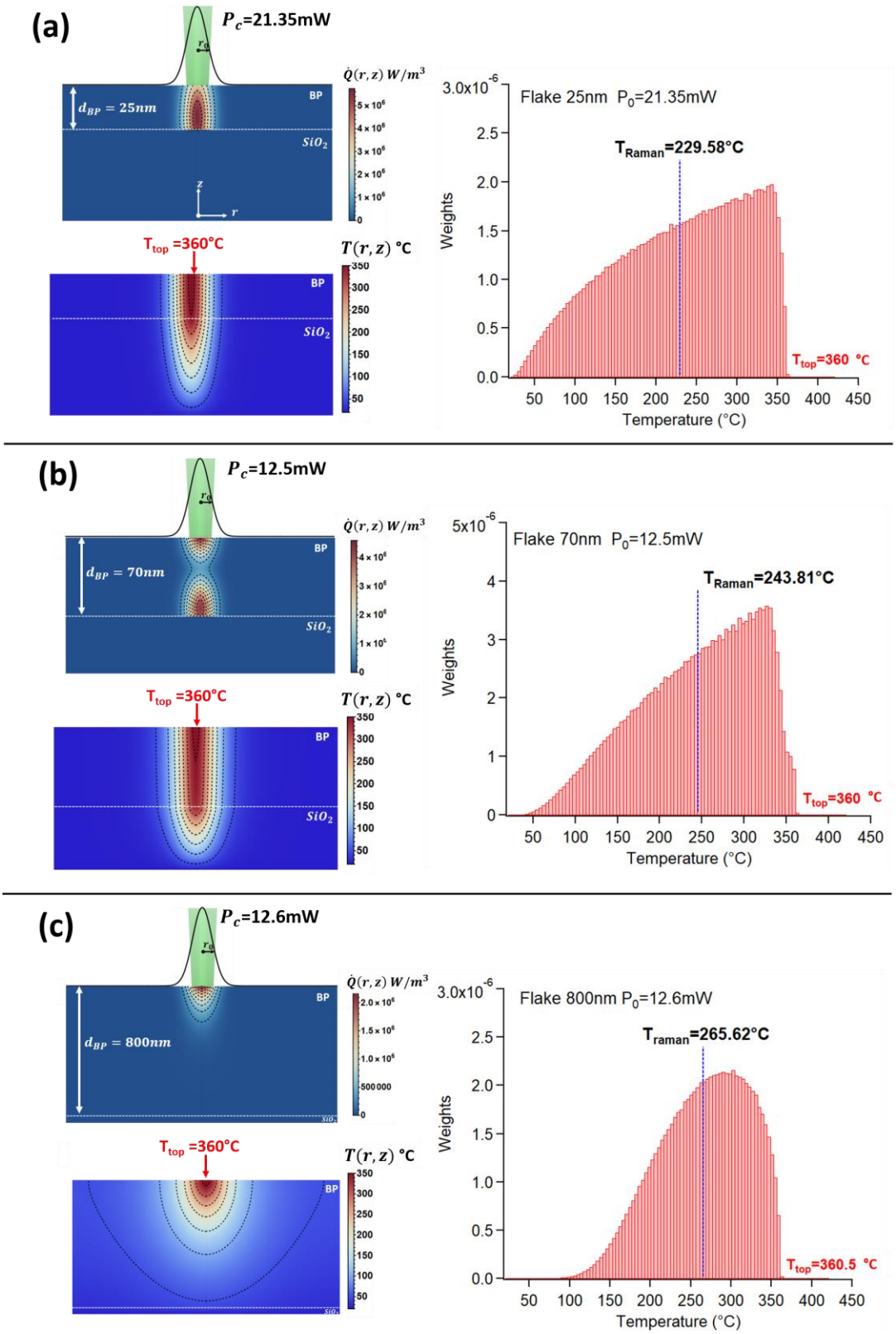

Figure 2.16 2D Plots of the heat source term $\dot{\boldsymbol{Q}}(\boldsymbol{x})$ and the temperature distribution $\boldsymbol{T}(\boldsymbol{x})$ calculated by numerically solving the stationary heat equation in BP flakes supported on SiO_2 (50 nm)/Si for three different values of the BP thickness. **(a)** 25 nm, **(b)** 70 nm, **(c)** 800 nm. For each thickness, the value of the incident power $\boldsymbol{P_c}$ for which the temperature at T(r=0, $\boldsymbol{z = z_{BP}}$) is ~360 °C (corresponding to the ablation temperature of BP) is also reported along with the temperature-histograms of the Raman probed temperatures in the BP region.

$$\dot{Q}(\boldsymbol{x}) = \frac{P_{inc}}{\pi r_0^2}(1-R)f(z)g(r,z) \tag{2.17}$$

where r_0 is the laser beam radius and R is the reflectance calculated on the top ($z = z_{BP}$) BP surface. Assuming a gaussian laser beam, the intensity profile function, $g(r,z)$, can be expressed as:

$$g(r,z) = \frac{r_0^2}{r_0^2 + N_A^2(z-z_{BP})^2} e^{-\frac{r^2}{r_0^2+N_A^2(z-z_{BP})^2}} \tag{2.18}$$

where N_A is the numerical aperture of the Raman microscope objective and z_{BP} the coordinate of the top surface of the BP-flake. The value of laser beam radius, r_0, used in both the equations (2.17) and (2.18) has been estimated from the formula for the diffraction limited laser spot size: $r_0 \cong 0.6\frac{\lambda}{N_A}$. The reflectance on the top BP interface, R, is generally a thickness dependent function and can be calculated from the Fresnel-formula for the reflectance in a 2 layer BP/SiO_2 system over a semi-infinite Si-substrate[90], see figure 2.15. The attenuation function $f(z)$ in the BP region is given by the equation (2.14) and, as we have already seen before, for BP flakes thinner than $\delta_{BP} \approx 300$ nm behaves like an exponentially attenuated oscillating function due to interferential modulation effects. Inside the SiO_2 region, instead, $f(z)$=0, because SiO_2 is optically transparent to the visible laser radiation and does not introduce any attenuation to the incoming laser light.

The plots of the heat source term $\dot{Q}(\boldsymbol{x})$ over the 2D integration domain of the heat-equation are reported in figures 2.16(a), (b) and (c) for three BP flakes having different thickness. We notice that in the case of a thick 800 nm BP flake (figure 2.16(c)), $\dot{Q}(\boldsymbol{x})$ is attenuated exponentially in the cross plane (z) direction whereas in the case of a thin 25nm and 70 nm BP flake (figures 2.16(a) and (b), respectively), the cross plane behavior of $\dot{Q}(\boldsymbol{x})$ is modulated by interferential oscillations caused by multiple reflections effects..

Origins of the oscillating behavior of the threshold laser ablation power

The second rows in figure 2.16(a), (b) and (c) plot the temperature distribution $T(r,z)$ obtained by numerically solving the heat equation (2.17) from the corresponding heat source terms. All the temperature distributions illustrated in figure 2.16 were calculated by choosing an appropriate P_{inc} value such that the temperature obtained on the top ($z = z_{BP}$) BP surface (along the r=0 axis of the laser beam) is ~360 °C. Such temperature can be considered as the ablation temperature of BP and, therefore, the corresponding P_{inc} value used in our calculations provides an estimation of the threshold power P_c experimentally observed at the ablation of the BP flakes. We notice, moreover, that the calculations of figure 2.16 were also performed assuming an ideal thermal coupling ($G_{int} \to \infty$) between the BP and SiO_2 interfaces.

Despite of this ideal approximation, we see that the numerical solution of our thermal model is able to take into account the trends experimentally observed in threshold ablation power of thick and thin BP flakes. In particular, we see that the threshold ablation power of a 25 nm thick BP flake is P_c=21.3 mW, i.e. higher than the threshold ablation power of an 800 nm thick BP flake which is P_c=12.6 mW.

The values of P_c determined by solving the heat diffusion equation in BP flakes with different thickness assuming both an ideal thermal coupling (blue line) condition and a more realistic situation with a finite value of the thermal boundary conductance ($G_{int} = 4.61\ MWm^{-2}K^{-1}$,

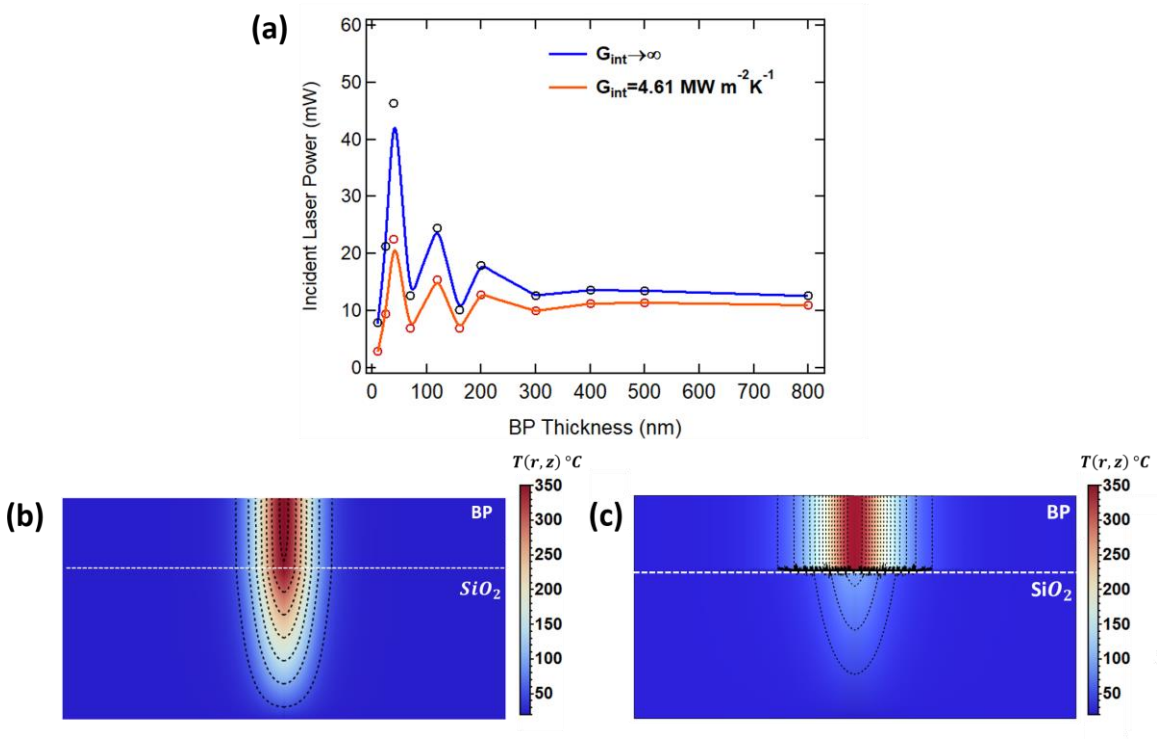

Figure 2.17 (a) Plot of the threshold ablation power $\boldsymbol{P_c}$ determined by solving the heat diffusion equation in SiO_2 (50 nm)/Si supported BP flakes with different thickness. The datapoints obtained from the calculations are indicated by circles whereas the continuous lines are interpolations carried out between the datapoints. For each thickness two situations have been considered: ideal thermal coupling ($\boldsymbol{G_{int}} \to \infty$) at the BP/$SiO_2$ interface (blue line) and a finite value ($\boldsymbol{G_{int} = 4.61\ MWm^{-2}K^{-1}}$) for the thermal boundary conductance at the BP/SiO_2 interface (orange line). The 2D plots of the temperature distribution calculated in these two situations for a 25 nm thick BP flake are illustrated in **(b)** for the ideal ($\boldsymbol{G_{int}} \to \infty$) case and in **(c)** for the case with a finite value of $\boldsymbol{G_{int}}$.

orange line) are reported in figure 2.17(a). In both the situations we see that the threshold ablation power is characterized by an oscillating behavior as function of the thickness, especially when the thickness of BP flakes becomes smaller than $3\delta_{BP} \approx 300$ nm. This oscillating behavior of P_c is a consequence of the interferential modulation of the absorbed light in BP and successfully explains the huge differences in the threshold ablation power experimentally observed in the thin BP flakes (see figure 2.12(d)).

Figure 2.17(a) highlights also that the finite value of the thermal boundary conductance produces always a lowering of the threshold ablation power, P_c, at a given BP thickness. This effect turns out to be more pronounced in thin rather than thick BP flakes and indicates that in the latter case the heat dissipation mechanism is governed mainly by the nature of the thermal coupling with the SiO_2 interface rather than by the intrinsic thermal properties of BP. This fact is also qualitatively demonstrated in figures 2.17(b) and 2.17(c) that compare the temperature distributions obtained in a 25 nm thick BP flake in the case of an ideal thermal coupling with the SiO_2 substrate and with a finite value of the boundary thermal conductance. In the latter situation the temperatures in each point of the BP region become higher due to a worse heat diffusion towards the underlying thermal bath and, therefore, the optical power required to bring at sublimation the top BP layers decreases.

However, in thin BP flakes the value of the thermal boundary conductance is expected to be higher than the value used in our calculations ($G_{int} = 4.61\ MWm^{-2}K^{-1}$) due to a more uniform contact with the supporting substrate.[75], [76] A low value of the thermal boundary conductance together with a huge (i.e. almost one order of magnitude) difference between the values of the thermal conductivities of BP and of silicon is responsible of the so-called heat-sink effect of the substrate. This means that, the Si-substrate is able to effectively dissipate the fraction of incident power not absorbed in BP, especially when the thickness of the latter becomes much lower than the light-penetration depth. As we will see in the following, this effect can lead to not only to a lowering of the threshold ablation power but also to a lowering of the Raman probed temperatures.

Origins of the anomalous behavior of the Raman shifts in thick and thin BP flakes

The temperature (and power) dependence of the BP Raman peaks is generally described as a result of three effects: [89], [96]

$$\Delta\omega(T) = \Delta\omega_A(T) + \Delta\omega_V(T) + \Delta\omega_M(T) \tag{2.19}$$

In equation (2.19), the first term $\Delta\omega_A(T)$ is the frequency shift caused by the decay of optical phonons due to the phonon-phonon anharmonic interaction. This term is given by the following expression:[84], [89]

$$\Delta\omega_A(T) = A\left(1 + \frac{2}{e^x - 1}\right) + B\left(1 + \frac{3}{e^y - 1} + \frac{3}{(e^y - 1)^2}\right) \tag{2.20}$$

where the A and B constants define the relative importance of three and four-phonon decay processes and, in principle, can be thickness dependent with $x = \frac{\hbar\omega_0}{2k_bT}$, $y = \frac{\hbar\omega_0}{3k_bT}$ and ω_0 the Raman mode frequency at T=0 °K. The second term, $\Delta\omega_V(T)$, comes from the BP lattice thermal expansion and, generally, is described using a Grüneisen constants model[89], [97]:

$$\Delta\omega_V(T) = \omega_0\left(e^{-\gamma_V\int_0^T \alpha_{V_{BP}}(T')dT'} - 1\right) \tag{2.21}$$

with γ_V the microscopic Grüneisen parameter and $\alpha_{V_{BP}}(T)$ the volumetric thermal expansion coefficient of BP. Finally, the third term in equation (2.19), $\Delta\omega_M(T)$, describes the effect of the mechanical strain caused by the thermal expansion coefficient mismatch between the BP flake and the underlying SiO_2/Si substrate. In particular, since SiO_2 has a positive thermal expansion coefficient in the 20 °C-400 °C temperature range that is two order of magnitudes lower[98], $\alpha_{V_{SiO_2}} = 0.49 \times 10^{-6}\ °C^{-1}$, than the value reported for BP[99], $\alpha_{V_{BP}} = 24.8 \times 10^{-6}\ °C^{-1}$, the former exerts on the BP flake a compressive strain during its laser heating process. Following Yoon et al [96] the Raman shift additionally produced by the compressive strain effect is given by:

$$\Delta\omega_M(T) = \beta\int_{T=20°C}^{T}\left(\alpha_{V_{SiO_2}}(T') - \alpha_{V_{BP}}(T')\right)dT' \tag{2.22}$$

where β is the biaxial strain coefficient of the considered Raman mode. In equation (2.22) the biaxial strain coefficient β can be expressed in terms of the Grüneisen parameter via the relation:[96], [100] $\beta = -2\omega_0\gamma_V$. The measured value of the Grüneisen parameter for the A_g^2 mode of BP is 0.13[101] and, therefore, the biaxial strain coefficient is negative. Since the thermal expansion coefficient mismatch between BP and SiO_2 is also negative in the 20 °C-400°C range, we conclude that the mechanical strain effect (2.22) contributes to the overall

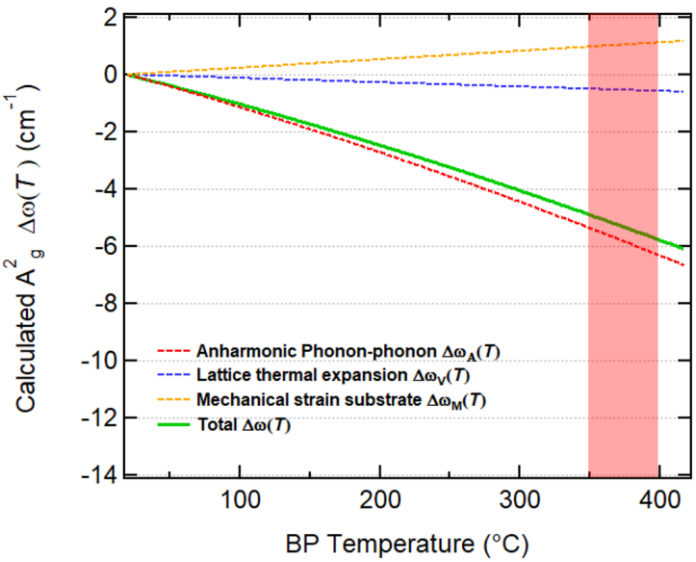

Figure 2.18 Calculated temperature dependence of the Raman shift of the $\boldsymbol{A_g^2}$ mode obtained as sum of the phonon-phonon anharmonic (red dashed line), lattice thermal expansion (blue dashed line) and mechanical strain of the substrate (yellow dashed line) contributions. The calculation has performed using equation (2.19) with the values of the parameters reported in ref. 89 for a 20nm BP flake. The vertical red band highlights the typical temperature range experimentally reported for the onset of the thermal sublimation in BP.

Raman shift in equation (2.19) with a positive sign, i.e. in an opposite way with respect to the other two terms $\Delta\omega_A(T)$ and $\Delta\omega_V(T)$. A more quantitative estimation of the order of magnitude of the $\Delta\omega_A(T)$, $\Delta\omega_V(T)$ and $\Delta\omega_M(T)$ terms to the overall Raman shift can be calculated at the ablation temperature of BP using the values of A, B, and ω_0 parameters reported in ref.[89] in the case of a 20 nm BP flake. Figure 2.18 reports the behavior of the $\Delta\omega_A(T)$, $\Delta\omega_V(T)$ and $\Delta\omega_M(T)$ terms calculated in this way in the 20-400 °C temperature range. We see that the phonon-phonon anharmonic effect, $\Delta\omega_A(T)$, brings the major contribution to the overall Raman shift varying from $-5.4\ cm^{-1}$ at T_C=350 °C to $-6.3\ cm^{-1}$ at $T_c = 400\ °C$. The intrinsic BP lattice thermal expansion, $\Delta\omega_V(T)$, instead, gives a contribution always of the order of -0.5 cm^{-1} in the 350-400 °C ablation temperature range whereas the mechanical strain effect, $\Delta\omega_M(T)$, contributes always with a positive shift of the order of $\sim 1\ cm^{-1}$. Overall, we see that when the three $\Delta\omega_A(T)$, $\Delta\omega_V(T)$ and $\Delta\omega_M(T)$ terms are accounted together, the total Raman shift from equation (2.19) lies in the $[-4.9\ cm^{-1}, -5.7\ cm^{-1}]$ range for ablation temperatures between 350 °C and 400 °C. This result agrees well with the Raman shift value, $\Delta\omega_c$ =-5.06 cm^{-1}, measured at the ablation in the case of thin BP flakes (see figure 2.13(b)). For thick BP flakes, instead, the measured Raman shift, $\Delta\omega_c$ =-10.77 cm^{-1}, does not match exactly the value predicted from equation (2.19), even when the contribution due to the mechanical strain of the substrate is excluded. The reason for this discrepancy can be probably ascribed to a more pronounced thickness dependence in the A, B parameters in equation (2.20). In this respect, we notice, for example, that using different values for the A, B and ω_0 constants, such as those measured in ref.[82], the calculated Raman shift becomes $\sim 10.7\ cm^{-1}$ for an ablation temperature of T_c=360 °C in good agreement with the experimental value measured at the ablation in thick BP flakes (figure 2.13(a)).

Not-uniform collection efficiency of the Raman scattering and substrate heat-sink effect

Apart from the above discussed physical effects, an additional cause that can influence the power and temperature dependence of the Raman peak shifts is related to the not-uniform collection efficiency of the Raman scattered radiation from the illuminated region within the material. This effect together with the heat sink effect due to the substrate, can generate an additional blue-shift on the Raman peaks of thin BP-flakes when compared to the Raman peak shift of the thick flakes.

In order to understand this, we firstly observe that the experimentally measured Raman peak shapes of, for example, the A_g^2 vibrational modes are actually the result of a convolution of many spectral (Gaussian-Lorentzian) contributions originating within the Raman scattering volume in the laser-illuminated region of the BP crystal. Each contribution, ideally, can be ascribed to a Raman scattering center located in a given (r, z) location of the BP crystal and characterized by a Raman spectrum in which the position of the A_g^2 mode reflects the local-temperature in that point. However, the contribution from each (r, z) scattering center to the final convolution of the spectral A_g^2 line-shape is not identical but must be weighted by a multiplicative factor that accounts for the efficiency of collection of the Raman scattered radiation from the considered (r, z) location. Indeed, the collection efficiency of the Raman radiation is not uniform within the whole volume of the BP crystal for two main reasons. The first one is due to the not-uniform shape of the (gaussian) laser beam intensity profile, $g(r, z)$. The second one is the modulation of the Raman scattered light caused by optical interference effects. The modulation in the Raman scattered light can be described, as illustrated in paragraph 2.2.1, via the product $|F_{ex}(z)F_{sc}(z)|^2$ where the functions $F_{ex}(z)$ and $F_{sc}(z)$ are defined at a given depth z *from the top BP surface* by equations 2.8. Therefore, the multiplicative factor that weights each Gaussian-Lorentzian contribution coming from a (r, z) point within the BP region is given by: $rg(r, z)|F_{ex}(z)F_{sc}(z)|^2$. Notice that the additional r factor has been added so to account for the cylindrical symmetry of the 3D problem around the laser beam axis at r=0.

One possibility to describe the experimentally measured Raman shifts, Δω, and temperatures is to consider the Raman probed temperatures as the result of a weighted average of the local temperatures $T(r, z)$ within the scattering volume of the BP crystal. In other words:

$$T_{Raman} = \frac{\int_{BP} T(r,z)g(r,z)|F_{ex}(z)F_{sc}(\mathrm{z})|^2 rdrdz}{\int_{BP} g(r,z)|F_{ex}(z)F_{sc}(z)|^2 rdrdz} \qquad (2.23)$$

The temperature histograms reported in figure 2.16(a), (b) and (c) for three different BP thicknesses have been calculated, as described above, weighting each $T(r, z)$ value in a given (r, z) location with the Raman collection efficiency weight: $rg(r, z)|F_{ex}(z)F_{sc}(z)|^2$. As can be seen from the reported average T_{Raman}, when the temperature of the top BP surface is at the sublimation temperature of BP (~360 °C) the average measured T_{Raman} value is always much lower. Moreover, in a thin BP flake (see the 25 nm and 70 nm case reported in figures 2.16(a) and 2.16(c)) the average T_{Raman} is even lower than the T_{Raman} value determined on a thick (800 nm) BP flake. These results provide an alternative explanation for the blue shifts observed on the Δω values during the ablation of the BP flakes (blue arrow regions in figures 2.13(a) and 2.13(b)) but have one strong disadvantage: they are not able to account for the huge differences observed in the Raman shift at the threshold ablation power between the thick and the thin BP

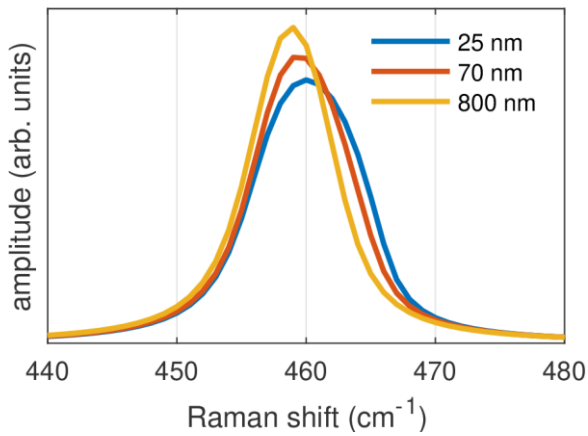

Figure 2.19 Calculated spectral line shapes of the A_g^2 Raman mode assuming a temperature of ~**360 °C** at the focal point on the top surface of three BP flakes with different thickness. The blue-shift of the Raman frequency towards high wavenumbers in thinner flakes can be clearly noticed. All the spectral line shapes were numerically obtained from a weighted sum of Gaussian-Lorentzian line shapes with weights determined from the temperature histograms reported in figure 2.16.

flakes. We remember, in fact, that the Raman probed ablation temperature in a thick BP flake is T_c~410° whereas in a thin BP flake is T_c~203°.

In order to find a more satisfying explanation for such discrepancy, we envisaged another method to estimate the Raman temperatures from the calculated $T(r,z)$ distributions. More in detail, we calculated the spectral line shape of the A_g^2 peak from a weighted sum of Gaussian Lorentzian contributions centered at the Raman frequencies determined using equation (2.15) and the values of the local temperature in each (r,z) point within the BP volume. Each Gaussian Lorentzian contribution has been weighted in the sum with the $rg(r,z)|F_{ex}(z)F_{sc}(z)|^2$ factor that accounts for the different Raman collection efficiency from each (r,z) location within the scattering volume. Moreover, the FWHM of each Gaussian-Lorentzian contribution has been also considered as a temperature dependent $\Gamma(T(r,z))$ quantity. The final spectral lines shapes of the A_g^2 mode obtained in this way are reported in figure 2.19. We notice that at the ablation, i.e. when the top BP surface is at ~360 °C, a 25 nm and 70 nm thick BP flake red shift towards lower wavenumber less than an 800 nm thick BP flake. This means that, even when the effects of equation (2.19) are not explicitly taken into account, the Raman temperature probed in thin BP flakes at the ablation is always lower than the Raman temperature probed in thick ones. The physical reason for such behavior can be traced in the heat-sink effect of the substrate that produces a more localized temperature distribution around the laser-spot radius in a thin BP flake (i.e. with a thickness less than $3\delta_{BP}$ ≈300 nm) rather than in the case of a thick BP flakes. Due to the existence of a more localized temperature distribution, even if the top layers are heated at the sublimation temperature with an incident power above P_c (blue-arrow regions in figure 2.13), the average temperature probed by means of the Raman shifts appears to be lower. However, from figure 2.19 we see also that difference between the Raman peak positions of thick and thin BP flakes at the ablation are small: $\sim 1\ cm^{-1}$. Therefore, we are led to conclude that the heat-sink effect of the substrate and the effect of the not-uniform Raman collection efficiency are not able to explain alone the experimentally observed difference in the Raman shift (and in the Raman

probed temperature) between thick and thin BP flakes. As we have seen, this shifts can be fully understood only by including the physical effects described by the equations (2.19)-(2.22).

Origins of the behavior of the Raman bandwidths in thick and thin BP flakes

The temperature dependence of the Raman peaks bandwidth (FWHMs) is not affected by the volumetric expansion of the BP lattice and by the mechanical strain effect with the supporting substrate but it depends only on the decay of optical phonons due to the phonon- phonon anharmonic interaction according to the following equation:[82], [84], [89]

$$\Gamma(T) = \Gamma_0 + \mathrm{C}\left(1 + \frac{2}{e^{\mathrm{x}} - 1}\right) + D\left(1 + \frac{3}{e^{y} - 1} + \frac{3}{(e^{y} - 1)^2}\right) \qquad (2.24)$$

where the constant Γ_0 is the temperature independent line-broadening. Using equation (2.24) and the values of C, D, Γ_0 and ω_0 constants reported in ref.[89] for a 20nm thick BP flake we were able to estimate the ablation temperature of BP from the FWHM values measured at P_c obtaining T_c~360 °C for the thin BP flake and T_c~420 °C for the thick BP flake. Both these values agree well with the values reported in literature for the thermal sublimation of BP, which typically lies in the 350-400 °C range,[46], [87], [88] and helped to resolve the contradiction in the ablation temperatures probed from the Δω values in thick and thin BP flakes.

For P_{inc}>P_c the slight decrease observed in the line broadening (blue arrow regions in figure 2.14(a) and 2.14(b)) suggests that the local temperature probed on a thinned BP flake can be slightly lower than the value determined at P_c. Since the temperature dependence of the FWHM only depends on the effects of the phonon-phonon anharmonic coupling and since the latter is not expected to have a strong thickness dependence in multilayer BP flakes, the slight decrease of the line broadening at P_{inc}>P_c can be ascribed as a consequence of the localized heat distribution and of the not-uniform Raman collection efficiency of the radiation from the thinned region of the BP flakes, discussed previously.

The ablation of the flakes and the consequent diminution in the FWHM values (as well as the corresponding blue shift of the $\Delta\omega$) stop each time the top BP layers are not able to reach the sublimation temperature anymore for any further increase of the incident laser power. This situation typically happens at the onset of the regions indicated by red arrows in figures 2.13 and 2.14 where the thickness of the flake reaches a value for which the absorption of the radiation is minimum due to the effects caused by the optical interferences.

Conclusions

In conclusion, we found out that the ablation of the BP flakes occurs always at a given threshold incident optical power and that such threshold is strongly affected by a not trivial interplay between thermal coupling and optical effects with the supporting substrate.

Moreover, we understood that a simple linear model for the temperature dependence of the Raman shifts (equation 2.15) may lead to discrepancies when used to probe the temperatures in multilayer BP flakes especially at high incident optical powers close to the ablation threshold of BP. In particular, to account the huge discrepancies in the Raman temperatures probed in thin and thick BP flakes it is necessary to include non-linear contributions due to the phonon-phonon an harmonic coupling, the thermal expansion of the BP lattice and the mechanical strain effect with the supporting substrate. Additionally, we also observed that the heat-sink effect of the substrate together with the not-uniform Raman collection efficiency from the flakes may

slightly alter the Raman shift values and the predicted temperatures at the ablation. In order to get a clear picture of the laser heating and ablation of BP, we considered the temperature/power dependence of the FWHM. The latter quantity is insensitive to the effects caused by the volumetric expansion of the lattice and by the mechanical strain with the supporting substrate and can help to disentangle the discrepancies in the temperatures estimated from the Raman shift values, especially at high incident optical powers.

Bibliography

[1] S. C. Dhanabalan, J. S. Ponraj, Z. Guo, S. Li, Q. Bao, and H. Zhang, "Emerging Trends in Phosphorene Fabrication towards Next Generation Devices," *Advanced Science*, vol. 4, no. 6, p. 1600305, Jun. 2017, doi: 10.1002/advs.201600305.

[2] X.-Y. Wang, A. Narita, and K. Müllen, "Precision synthesis versus bulk-scale fabrication of graphenes," *Nature Reviews Chemistry*, vol. 2, no. 1, p. 0100, Dec. 2017, doi: 10.1038/s41570-017-0100.

[3] M. Yi and Z. Shen, "A review on mechanical exfoliation for the scalable production of graphene," *J. Mater. Chem. A*, vol. 3, no. 22, pp. 11700–11715, 2015, doi: 10.1039/C5TA00252D.

[4] A. Castellanos-Gomez *et al.*, "Isolation and characterization of few-layer black phosphorus," *2D Materials*, vol. 1, no. 2, p. 025001, Jun. 2014, doi: 10.1088/2053-1583/1/2/025001.

[5] A. Castellanos-Gomez *et al.*, "Deterministic transfer of two-dimensional materials by all-dry viscoelastic stamping," *2D Mater.*, vol. 1, no. 1, p. 011002, Apr. 2014, doi: 10.1088/2053-1583/1/1/011002.

[6] J. O. Island, G. A. Steele, H. S. J. van der Zant, and A. Castellanos-Gomez, "Environmental instability of few-layer black phosphorus," *2D Materials*, vol. 2, no. 1, p. 011002, Jan. 2015, doi: 10.1088/2053-1583/2/1/011002.

[7] A. Favron *et al.*, "Photooxidation and quantum confinement effects in exfoliated black phosphorus," *Nature Materials*, vol. 14, no. 8, pp. 826–832, May 2015, doi: 10.1038/nmat4299.

[8] Y. Huang *et al.*, "Interaction of Black Phosphorus with Oxygen and Water," *Chemistry of Materials*, vol. 28, no. 22, pp. 8330–8339, Nov. 2016, doi: 10.1021/acs.chemmater.6b03592.

[9] Z. Luo *et al.*, "Anisotropic in-plane thermal conductivity observed in few-layer black phosphorus," *Nature Communications*, vol. 6, p. 8572, Oct. 2015, doi: 10.1038/ncomms9572.

[10] G. Wang *et al.*, "Introduction of Interfacial Charges to Black Phosphorus for a Family of Planar Devices," *Nano Lett.*, vol. 16, no. 11, pp. 6870–6878, Nov. 2016, doi: 10.1021/acs.nanolett.6b02704.

[11] Y. Saito and Y. Iwasa, "Ambipolar Insulator-to-Metal Transition in Black Phosphorus by Ionic-Liquid Gating," *ACS Nano*, vol. 9, no. 3, pp. 3192–3198, Mar. 2015, doi: 10.1021/acsnano.5b00497.

[12] V. Nicolosi, M. Chhowalla, M. G. Kanatzidis, M. S. Strano, and J. N. Coleman, "Liquid Exfoliation of Layered Materials," *Science*, vol. 340, no. 6139, pp. 1226419–1226419, Jun. 2013, doi: 10.1126/science.1226419.

[13] S. Lin, Y. Chui, Y. Li, and S. P. Lau, "Liquid-phase exfoliation of black phosphorus and its applications," *FlatChem*, vol. 2, pp. 15–37, Apr. 2017, doi: 10.1016/j.flatc.2017.03.001.

[14] J. R. Brent, N. Savjani, E. A. Lewis, S. J. Haigh, D. J. Lewis, and P. O'Brien, "Production of few-layer phosphorene by liquid exfoliation of black phosphorus," *Chem. Commun.*, vol. 50, no. 87, pp. 13338–13341, 2014, doi: 10.1039/C4CC05752J.

[15] D. Hanlon *et al.*, "Liquid exfoliation of solvent-stabilized few-layer black phosphorus for applications beyond electronics," *Nature Communications*, vol. 6, p. 8563, Oct. 2015, doi: 10.1038/ncomms9563.

[16] P. Yasaei *et al.*, "High-Quality Black Phosphorus Atomic Layers by Liquid-Phase Exfoliation," *Advanced Materials*, vol. 27, no. 11, pp. 1887–1892, Mar. 2015, doi: 10.1002/adma.201405150.

[17] A. H. Woomer, T. W. Farnsworth, J. Hu, R. A. Wells, C. L. Donley, and S. C. Warren, "Phosphorene: Synthesis, Scale-Up, and Quantitative Optical Spectroscopy," *ACS Nano*, vol. 9, no. 9, pp. 8869–8884, Sep. 2015, doi: 10.1021/acsnano.5b02599.

[18] J. Kang *et al.*, "Stable aqueous dispersions of optically and electronically active phosphorene," *Proceedings of the National Academy of Sciences*, vol. 113, no. 42, pp. 11688–11693, Oct. 2016, doi: 10.1073/pnas.1602215113.

[19] J. Kang *et al.*, "Solvent Exfoliation of Electronic-Grade, Two-Dimensional Black Phosphorus," *ACS Nano*, vol. 9, no. 4, pp. 3596–3604, Apr. 2015, doi: 10.1021/acsnano.5b01143.

[20] A. F. Routh, "Drying of thin colloidal films," *Rep. Prog. Phys.*, vol. 76, no. 4, p. 046603, Apr. 2013, doi: 10.1088/0034-4885/76/4/046603.

[21] B. Zhang *et al.*, "Exfoliated layers of black phosphorus as saturable absorber for ultrafast solid-state laser," *Optics Letters*, vol. 40, no. 16, p. 3691, Aug. 2015, doi: 10.1364/OL.40.003691.

[22] H. Kaur *et al.*, "Large Area Fabrication of Semiconducting Phosphorene by Langmuir-Blodgett Assembly," *Sci Rep*, vol. 6, no. 1, p. 34095, Dec. 2016, doi: 10.1038/srep34095.

[23] J. D. Wood *et al.*, "Effective Passivation of Exfoliated Black Phosphorus Transistors against Ambient Degradation," *Nano Letters*, vol. 14, no. 12, pp. 6964–6970, Dec. 2014, doi: 10.1021/nl5032293.

[24] H. Li *et al.*, "Rapid and Reliable Thickness Identification of Two-Dimensional Nanosheets Using Optical Microscopy," *ACS Nano*, vol. 7, no. 11, pp. 10344–10353, Nov. 2013, doi: 10.1021/nn4047474.

[25] P. Blake *et al.*, "Making graphene visible," *Applied Physics Letters*, vol. 91, no. 6, p. 063124, Aug. 2007, doi: 10.1063/1.2768624.

[26] G. Teo *et al.*, "Visibility study of graphene multilayer structures," *Journal of Applied Physics*, vol. 103, no. 12, p. 124302, Jun. 2008, doi: 10.1063/1.2938840.

[27] Z. H. Ni *et al.*, "Graphene Thickness Determination Using Reflection and Contrast Spectroscopy," *Nano Lett.*, vol. 7, no. 9, pp. 2758–2763, Sep. 2007, doi: 10.1021/nl071254m.

[28] J. Yang *et al.*, "Optical tuning of exciton and trion emissions in monolayer phosphorene," *Light: Science & Applications*, vol. 4, no. 7, pp. e312–e312, Jul. 2015, doi: 10.1038/lsa.2015.85.

[29] P. Y. Yu and M. Cardona, *Fundamentals of semiconductors: physics and materials properties*, 4. ed. Berlin: Springer, 2010.

[30] H. B. Ribeiro, M. A. Pimenta, and C. J. S. de Matos, "Raman spectroscopy in black phosphorus: Raman spectroscopy in black phosphorus," *J. Raman Spectrosc.*, vol. 49, no. 1, pp. 76–90, Jan. 2018, doi: 10.1002/jrs.5238.

[31] J. Ribeiro-Soares, R. M. Almeida, L. G. Cançado, M. S. Dresselhaus, and A. Jorio, "Group theory for structural analysis and lattice vibrations in phosphorene systems," *Phys. Rev. B*, vol. 91, no. 20, p. 205421, May 2015, doi: 10.1103/PhysRevB.91.205421.

[32] H. B. Ribeiro *et al.*, "Edge phonons in black phosphorus," *Nature Communications*, vol. 7, p. 12191, Jul. 2016, doi: 10.1038/ncomms12191.

[33] H. B. Ribeiro *et al.*, "Unusual Angular Dependence of the Raman Response in Black Phosphorus," *ACS Nano*, vol. 9, no. 4, pp. 4270–4276, Apr. 2015, doi: 10.1021/acsnano.5b00698.

[34] A.-L. Phaneuf-L'Heureux *et al.*, "Polarization-Resolved Raman Study of Bulk-like and Davydov-Induced Vibrational Modes of Exfoliated Black Phosphorus," *Nano Lett.*, vol. 16, no. 12, pp. 7761–7767, Dec. 2016, doi: 10.1021/acs.nanolett.6b03907.

[35] S. Zhang *et al.*, "Extraordinary Photoluminescence and Strong Temperature/Angle-Dependent Raman Responses in Few-Layer Phosphorene," *ACS Nano*, vol. 8, no. 9, pp. 9590–9596, Sep. 2014, doi: 10.1021/nn503893j.

[36] J. Wu, N. Mao, L. Xie, H. Xu, and J. Zhang, "Identifying the Crystalline Orientation of Black Phosphorus Using Angle-Resolved Polarized Raman Spectroscopy," *Angewandte Chemie International Edition*, vol. 54, no. 8, pp. 2366–2369, Feb. 2015, doi: 10.1002/anie.201410108.

[37] F. Xia, H. Wang, and Y. Jia, "Rediscovering black phosphorus as an anisotropic layered material for optoelectronics and electronics," *Nature Communications*, vol. 5, Jul. 2014, doi: 10.1038/ncomms5458.

[38] X. Ling *et al.*, "Anisotropic Electron-Photon and Electron-Phonon Interactions in Black Phosphorus," *Nano Letters*, vol. 16, no. 4, pp. 2260–2267, Apr. 2016, doi: 10.1021/acs.nanolett.5b04540.

[39] J. Kim *et al.*, "Anomalous polarization dependence of Raman scattering and crystallographic orientation of black phosphorus," *Nanoscale*, vol. 7, no. 44, pp. 18708–18715, 2015, doi: 10.1039/C5NR04349B.

[40] Y. Y. Wang, Z. H. Ni, Z. X. Shen, H. M. Wang, and Y. H. Wu, "Interference enhancement of Raman signal of graphene," *Appl. Phys. Lett.*, vol. 92, no. 4, p. 043121, Jan. 2008, doi: 10.1063/1.2838745.

[41] D. Yoon *et al.*, "Interference effect on Raman spectrum of graphene on SiO 2 / Si," *Phys. Rev. B*, vol. 80, no. 12, p. 125422, Sep. 2009, doi: 10.1103/PhysRevB.80.125422.

[42] S.-L. Li, H. Miyazaki, H. Song, H. Kuramochi, S. Nakaharai, and K. Tsukagoshi, "Quantitative Raman Spectrum and Reliable Thickness Identification for Atomic Layers on Insulating Substrates," *ACS Nano*, vol. 6, no. 8, pp. 7381–7388, Aug. 2012, doi: 10.1021/nn3025173.

[43] G. Faraone, E. Balduzzi, C. Martella, C. Grazianetti, A. Molle, and E. Bonera, "Thickness determination of anisotropic van der Waals crystals by Raman spectroscopy: the case of black phosphorus.," *Nanotechnology*, Jun. 2020, doi: 10.1088/1361-6528/ab9d3f.

[44] R. Hultgren, N. S. Gingrich, and B. E. Warren, "The Atomic Distribution in Red and Black Phosphorus and the Crystal Structure of Black Phosphorus," *The Journal of Chemical Physics*, vol. 3, no. 6, pp. 351–355, Jun. 1935, doi: 10.1063/1.1749671.

[45] W. Lu *et al.*, "Plasma-assisted fabrication of monolayer phosphorene and its Raman characterization," *Nano Research*, vol. 7, no. 6, pp. 853–859, Jun. 2014, doi: 10.1007/s12274-014-0446-7.

[46] W. Luo, R. Yang, J. Liu, Y. Zhao, W. Zhu, and G. (Maggie) Xia, "Thermal sublimation: a scalable and controllable thinning method for the fabrication of few-layer black phosphorus," *Nanotechnology*, vol. 28, no. 28, p. 285301, Jul. 2017, doi: 10.1088/1361-6528/aa76ae.

[47] X. Ling *et al.*, "Low-Frequency Interlayer Breathing Modes in Few-Layer Black Phosphorus," *Nano Letters*, vol. 15, no. 6, pp. 4080–4088, Jun. 2015, doi: 10.1021/acs.nanolett.5b01117.

[48] X. Luo *et al.*, "Large Frequency Change with Thickness in Interlayer Breathing Mode—Significant Interlayer Interactions in Few Layer Black Phosphorus," *Nano Lett.*, vol. 15, no. 6, pp. 3931–3938, Jun. 2015, doi: 10.1021/acs.nanolett.5b00775.

[49] W. Luo, Q. Song, G. Zhou, D. Tuschel, and G. Xia, "Study of Black Phosphorus Using Angle-Resolved Polarized Raman Spectroscopy with 442 nm Excitation," *arXiv:1610.03382 [cond-mat]*, Oct. 2016, Accessed: Jul. 04, 2020. [Online]. Available: http://arxiv.org/abs/1610.03382.

[50] Balduzzi, Emanuele, "Monitoring the thickness evolution of laser-exfoliated black phosphorus flake by Raman spectroscopy," Università degli studi di Milano Bicocca, 2019.

[51] N. Mao *et al.*, "Optical Anisotropy of Black Phosphorus in the Visible Regime," *J. Am. Chem. Soc.*, vol. 138, no. 1, pp. 300–305, Jan. 2016, doi: 10.1021/jacs.5b10685.

[52] D. Li *et al.*, "Polarization and Thickness Dependent Absorption Properties of Black Phosphorus: New Saturable Absorber for Ultrafast Pulse Generation," *Scientific Reports*, vol. 5, no. 1, Dec. 2015, doi: 10.1038/srep15899.

[53] E. Bonera, M. Fanciulli, and D. N. Batchelder, "Combining high resolution and tensorial analysis in Raman stress measurements of silicon," *Journal of Applied Physics*, vol. 94, no. 4, pp. 2729–2740, Aug. 2003, doi: 10.1063/1.1592872.

[54] A. N. Rudenko and M. I. Katsnelson, "Quasiparticle band structure and tight-binding model for single- and bilayer black phosphorus," *Phys. Rev. B*, vol. 89, no. 20, p. 201408, May 2014, doi: 10.1103/PhysRevB.89.201408.

[55] J. Pei *et al.*, "Producing air-stable monolayers of phosphorene and their defect engineering," *Nature Communications*, vol. 7, p. 10450, Jan. 2016, doi: 10.1038/ncomms10450.

[56] J. Jia *et al.*, "Plasma-Treated Thickness-Controlled Two-Dimensional Black Phosphorus and Its Electronic Transport Properties," *ACS Nano*, vol. 9, no. 9, pp. 8729–8736, Sep. 2015, doi: 10.1021/acsnano.5b04265.

[57] M. C. Robbins, S. Namgung, S.-H. Oh, and S. J. Koester, "Cyclical Thinning of Black Phosphorus with High Spatial Resolution for Heterostructure Devices," *ACS Appl. Mater. Interfaces*, vol. 9, no. 14, pp. 12654–12662, Apr. 2017, doi: 10.1021/acsami.6b14477.

[58] S. Fan *et al.*, "Rapid thermal thinning of black phosphorus," *J. Mater. Chem. C*, vol. 5, no. 40, pp. 10638–10644, 2017, doi: 10.1039/C7TC03462H.

[59] X. Liu *et al.*, "Scanning Probe Nanopatterning and Layer-by-Layer Thinning of Black Phosphorus," *Adv. Mater.*, vol. 29, no. 1, p. 1604121, Jan. 2017, doi: 10.1002/adma.201604121.

[60] P. Masih Das *et al.*, "Controlled Sculpture of Black Phosphorus Nanoribbons," *ACS Nano*, vol. 10, no. 6, pp. 5687–5695, Jun. 2016, doi: 10.1021/acsnano.6b02435.

[61] N. Clark *et al.*, "Scalable Patterning of Encapsulated Black Phosphorus," *Nano Lett.*, vol. 18, no. 9, pp. 5373–5381, Sep. 2018, doi: 10.1021/acs.nanolett.8b00946.

[62] G. H. Han *et al.*, "Laser Thinning for Monolayer Graphene Formation: Heat Sink and Interference Effect," *ACS Nano*, vol. 5, no. 1, pp. 263–268, Jan. 2011, doi: 10.1021/nn1026438.

[63] Z. Lin *et al.*, "Precise Control of the Number of Layers of Graphene by Picosecond Laser Thinning," *Sci Rep*, vol. 5, no. 1, p. 11662, Dec. 2015, doi: 10.1038/srep11662.

[64] A. Castellanos-Gomez, M. Barkelid, A. M. Goossens, V. E. Calado, H. S. J. van der Zant, and G. A. Steele, "Laser-Thinning of MoS_2: On Demand Generation of a Single-Layer Semiconductor," *Nano Letters*, vol. 12, no. 6, pp. 3187–3192, Jun. 2012, doi: 10.1021/nl301164v.

[65] P. S. Kollipara, J. Li, and Y. Zheng, "Optical Patterning of Two-Dimensional Materials," *Research*, vol. 2020, pp. 1–15, Jan. 2020, doi: 10.34133/2020/6581250.

[66] J. Aumanen, A. Johansson, J. Koivistoinen, P. Myllyperkiö, and M. Pettersson, "Patterning and tuning of electrical and optical properties of graphene by laser induced two-photon oxidation," *Nanoscale*, vol. 7, no. 7, pp. 2851–2855, 2015, doi: 10.1039/C4NR05207B.

[67] S. Cho *et al.*, "Phase patterning for ohmic homojunction contact in MoTe2," *Science*, vol. 349, no. 6248, pp. 625–628, Aug. 2015, doi: 10.1126/science.aab3175.

[68] J. Lu *et al.*, "Bandgap Engineering of Phosphorene by Laser Oxidation toward Functional 2D Materials," *ACS Nano*, vol. 9, no. 10, pp. 10411–10421, Oct. 2015, doi: 10.1021/acsnano.5b04623.

[69] G. Qiu *et al.*, "Ultrafast Laser-Shock-Induced Confined Metaphase Transformation for Direct Writing of Black Phosphorus Thin Films," *Adv. Mater.*, vol. 30, no. 10, p. 1704405, Mar. 2018, doi: 10.1002/adma.201704405.

[70] M. J. L. F. Rodrigues *et al.*, "Resonantly Increased Optical Frequency Conversion in Atomically Thin Black Phosphorus," *Adv. Mater.*, vol. 28, no. 48, pp. 10693–10700, Dec. 2016, doi: 10.1002/adma.201603119.

[71] A. Kundu, R. Rani, and K. S. Hazra, "Controlled nanofabrication of metal-free SERS substrate on few layered black phosphorus by low power focused laser irradiation," *Nanoscale*, vol. 11, no. 35, pp. 16245–16252, 2019, doi: 10.1039/C9NR02615K.

[72] M. Engel, M. Steiner, S.-J. Han, and P. Avouris, "Power Dissipation and Electrical Breakdown in Black Phosphorus," *Nano Lett.*, vol. 15, no. 10, pp. 6785–6788, Oct. 2015, doi: 10.1021/acs.nanolett.5b02622.

[73] F. Ahmed *et al.*, "High Electric Field Carrier Transport and Power Dissipation in Multilayer Black Phosphorus Field Effect Transistor with Dielectric Engineering," *Adv. Funct. Mater.*, vol. 27, no. 4, p. 1604025, Jan. 2017, doi: 10.1002/adfm.201604025.

[74] B. Sun *et al.*, "Temperature Dependence of Anisotropic Thermal-Conductivity Tensor of Bulk Black Phosphorus," *Adv. Mater.*, vol. 29, no. 3, p. 1603297, Jan. 2017, doi: 10.1002/adma.201603297.

[75] T. Wang, R. Wang, P. Yuan, S. Xu, J. Liu, and X. Wang, "Interfacial Thermal Conductance between Mechanically Exfoliated Black Phosphorus and SiO_x : Effect of Thickness and Temperature," *Advanced Materials Interfaces*, vol. 4, no. 16, p. 1700233, Aug. 2017, doi: 10.1002/admi.201700233.

[76] L. Zhang and G. Ouyang, "Size-dependent interface thermal conductance in black phosphorus/SiO_2 heterojunctions," *Journal of Physics D: Applied Physics*, vol. 52, no. 2, p. 025302, Jan. 2019, doi: 10.1088/1361-6463/aae9bd.

[77] T. Beechem, L. Yates, and S. Graham, "Invited Review Article: Error and uncertainty in Raman thermal conductivity measurements," *Rev. Sci. Instrum.*, vol. 86, no. 4, p. 041101, Apr. 2015, doi: 10.1063/1.4918623.

[78] A. A. Balandin *et al.*, "Superior Thermal Conductivity of Single-Layer Graphene," *Nano Lett.*, vol. 8, no. 3, pp. 902–907, Mar. 2008, doi: 10.1021/nl0731872.

[79] W. Cai *et al.*, "Thermal Transport in Suspended and Supported Monolayer Graphene Grown by Chemical Vapor Deposition," *Nano Lett.*, vol. 10, no. 5, pp. 1645–1651, May 2010, doi: 10.1021/nl9041966.

[80] S. Sahoo, A. P. S. Gaur, M. Ahmadi, M. J.-F. Guinel, and R. S. Katiyar, "Temperature-Dependent Raman Studies and Thermal Conductivity of Few-Layer MoS_2," *J. Phys. Chem. C*, vol. 117, no. 17, pp. 9042–9047, May 2013, doi: 10.1021/jp402509w.

[81] H. Zhou *et al.*, "High thermal conductivity of suspended few-layer hexagonal boron nitride sheets," *Nano Res.*, vol. 7, no. 8, pp. 1232–1240, Aug. 2014, doi: 10.1007/s12274-014-0486-z.

[82] A. Łapińska, A. Taube, J. Judek, and M. Zdrojek, "Temperature Evolution of Phonon Properties in Few-Layer Black Phosphorus," *J. Phys. Chem. C*, vol. 120, no. 9, pp. 5265–5270, Mar. 2016, doi: 10.1021/acs.jpcc.6b01468.

[83] E. S. Zouboulis and M. Grimsditch, "Raman scattering in diamond up to 1900 K," *Phys. Rev. B*, vol. 43, no. 15, pp. 12490–12493, May 1991, doi: 10.1103/PhysRevB.43.12490.

[84] M. Balkanski, R. F. Wallis, and E. Haro, "Anharmonic effects in light scattering due to optical phonons in silicon," *Phys. Rev. B*, vol. 28, no. 4, pp. 1928–1934, Aug. 1983, doi: 10.1103/PhysRevB.28.1928.

[85] L. Su and Y. Zhang, "Temperature coefficients of phonon frequencies and thermal conductivity in thin black phosphorus layers," *Appl. Phys. Lett.*, vol. 107, no. 7, p. 071905, Aug. 2015, doi: 10.1063/1.4928931.

[86] D. J. Late, "Temperature Dependent Phonon Shifts in Few-Layer Black Phosphorus," *ACS Appl. Mater. Interfaces*, vol. 7, no. 10, pp. 5857–5862, Mar. 2015, doi: 10.1021/am509056b.

[87] M. Fortin-Deschênes, P. L. Levesque, R. Martel, and O. Moutanabbir, "Dynamics and Mechanisms of Exfoliated Black Phosphorus Sublimation," *The Journal of Physical Chemistry Letters*, vol. 7, no. 9, pp. 1667–1674, May 2016, doi: 10.1021/acs.jpclett.6b00584.

[88] X. Liu, J. D. Wood, K.-S. Chen, E. Cho, and M. C. Hersam, "In Situ Thermal Decomposition of Exfoliated Two-Dimensional Black Phosphorus," *The Journal of Physical Chemistry Letters*, vol. 6, no. 5, pp. 773–778, Mar. 2015, doi: 10.1021/acs.jpclett.5b00043.

[89] D. Tristant, A. Cupo, X. Ling, and V. Meunier, "Phonon Anharmonicity in Few-Layer Black Phosphorus," *ACS Nano*, vol. 13, no. 9, pp. 10456–10468, Sep. 2019, doi: 10.1021/acsnano.9b04257.

[90] D. Bäuerle, *Laser Processing and Chemistry*. Berlin, Heidelberg: Springer Berlin Heidelberg, 2011.

[91] J. Judek, A. P. Gertych, M. Świniarski, A. Łapińska, A. Dużyńska, and M. Zdrojek, "High accuracy determination of the thermal properties of supported 2D materials," *Sci Rep*, vol. 5, no. 1, p. 12422, Dec. 2015, doi: 10.1038/srep12422.

[92] J. Zhu *et al.*, "Revealing the Origins of 3D Anisotropic Thermal Conductivities of Black Phosphorus," *Adv. Electron. Mater.*, vol. 2, no. 5, p. 1600040, May 2016, doi: 10.1002/aelm.201600040.

[93] G. Qin and M. Hu, "Thermal Transport in Phosphorene," *Small*, vol. 14, no. 12, p. 1702465, Mar. 2018, doi: 10.1002/smll.201702465.

[94] J. H. Kim, A. Feldman, and D. Novotny, "Application of the three omega thermal conductivity measurement method to a film on a substrate of finite thickness," *Journal of Applied Physics*, vol. 86, no. 7, pp. 3959–3963, Oct. 1999, doi: 10.1063/1.371314.

[95] T. Yamane, N. Nagai, S. Katayama, and M. Todoki, "Measurement of thermal conductivity of silicon dioxide thin films using a 3ω method," *J. Appl. Phys.*, vol. 91, no. 12, p. 9772, 2002, doi: 10.1063/1.1481958.

[96] D. Yoon, Y.-W. Son, and H. Cheong, "Negative Thermal Expansion Coefficient of Graphene Measured by Raman Spectroscopy," *Nano Lett.*, vol. 11, no. 8, pp. 3227–3231, Aug. 2011, doi: 10.1021/nl201488g.
[97] C. Postmus, J. R. Ferraro, and S. S. Mitra, "Pressure Dependence of Infrared Eigenfrequencies of KCl and KBr," *Phys. Rev.*, vol. 174, no. 3, pp. 983–987, Oct. 1968, doi: 10.1103/PhysRev.174.983.
[98] National Institute of Standards and Technology, "SRM 179; Fused-Silica." U.S. Department of Commerce, Gaithersburg, 1991.
[99] L. Henry *et al.*, "Anisotropic thermal expansion of black phosphorus from nanoscale dynamics of phosphorene layers," *Nanoscale*, vol. 12, no. 7, pp. 4491–4497, 2020, doi: 10.1039/C9NR09218H.
[100] T. M. G. Mohiuddin *et al.*, "Uniaxial strain in graphene by Raman spectroscopy: G peak splitting, Grüneisen parameters, and sample orientation," *Phys. Rev. B*, vol. 79, no. 20, p. 205433, May 2009, doi: 10.1103/PhysRevB.79.205433.
[101] G. Xiao *et al.*, "Compressed few-layer black phosphorus nanosheets from semiconducting to metallic transition with the highest symmetry," *Nanoscale*, vol. 9, no. 30, pp. 10741–10749, 2017, doi: 10.1039/C7NR03367B.

CHAPTER 3

Bottom-up synthesis of 2D phosphorus: epitaxial growth

3.1 Epitaxial techniques for the growth of 2D monoelemental lattices

The bottom up synthesis of 2D materials can be realized both with physical and chemical vapor deposition techniques. In physical vapor deposition (PVD) the source material is brought in a vapor phase, usually by thermal evaporation, and then condenses onto a target substrate to form a thin solid film. PVD processes require high vacuum or ultra-high vacuum (UHV) conditions so that the particles in the vapor phase can travel to the target substrate without colliding with the background gas. In chemical vapor deposition, instead, the target substrate is exposed to volatile precursors that chemically react or decompose on the substrate surface in a controlled atmosphere to grow a thin film. CVD processes usually requires substrates that are catalytically active to promote the material growths and the synthesis can be performed at pressures ranging from atmospheric to UHV. Both in PVD and CVD growth processes the interactions between the substrate and the deposited material assume a fundamental role that characterizes the final morphology of the deposited film. If these interactions are strong enough, the growth proceeds by forming an ordered crystalline layer in a direction normal to the substrate surface lattice and with a precise symmetry and commensurability relationship with respect to the latter. In this situation the growth process is termed as epitaxial.

In the following paragraph we will provide a brief description of the principal epitaxial growth techniques envisaged for the synthesis 2D monoelemental lattices with specific regard to the case of 2D Xenes. Subsequently, we will move our attention on the main object of the discussion of the present chapter, i.e. the epitaxial synthesis of 2D phosphorus and we will provide a more specific description of the experimental setup used for its epitaxial growth and “in-situ” characterization.

Methods for the epitaxial growth of Xenes

The epitaxial growth of Xenes can be realized according to three principal approaches: i) epitaxy by deposition, ii) epitaxy by segregation, and iii) epitaxy by intercalation.[1], [2] In the epitaxy by deposition the atoms evaporated from a source in UHV conditions condense and self-organize on a substrate. This is a non-equilibrium or kinetically driven process where the choice of an appropriate substrate as well as the fine tuning of the growth parameters (mostly the substrate temperature and the deposition flux) are the key-factors for the successful formation of a 2D epitaxial lattice. Generally, the choice of a substrate for the epitaxial growth of a 2D crystalline lattice is dictated by two factors. Firstly, the precursor material should not diffuse through the substrate since a high solubility of the former into the latter may induce the formation of compounds that become detrimental during the growth of a monoelemental overlayer. Secondly, the substrate surface lattice must have the appropriate symmetry and commensurability relationship with the lattice of the freestanding 2D material so to allow the growth of a 2D crystalline overlayer. The latter factor depends on the nature of the interaction between the precursor material and the substrate. If this interaction is strong enough, it may cause distortions to the lattice of the freestanding 2D monoelemental material giving rise to a multiphasic character to the synthesized Xene. A prototypical example in this respect is the case of Silicene on Ag(111)[3]–[5]. In contrast to the epitaxy by deposition, the epitaxy by

segregation requires the interdiffusion of the precursor atoms through a substrate deposited on an underlying precursor reservoir. The diffused atomic species subsequently self-organizes into a 2D epitaxial lattice according to the commensurability relationship with the substrate. Typical examples of Xenes grown by this approach are Silicene on ZrB_2[6] and germanene on Ag(111).[7] Finally, in the epitaxy by intercalation the atoms of the precursor material are evaporated from a source onto a matrix crystal that can be either permeable to the precursor atomic species or prone to react with them so to form a crystalline film in a Zintl phase. In the first case the precursor atoms once permeated below the crystalline matrix self-organize in a 2D epitaxial lattice according to the commensurability relation with the substrate. An example of this situation is silicene intercalated between graphene and a Ru(0001) substrate[8]. In the second case, instead, the precursor atoms are deposited on the surface of a heated matrix crystal so to form the planar cationic layers of a Zintl crystalline film. The deposited precursor atoms favor the extraction of the atomic species from the matrix towards the surface that thus self-organize in an anionic Xene sheet of the crystalline Zintl film. The latter situation is encountered, for example, in the case of the Zintl silicide phases (e.g. $SrSi_2$, $EuSi_2$, $GdSi_2$) obtained by thermal intercalation of atoms of strontium, europium or gadolinium evaporated onto a crystalline silicon (111) substrate.[9], [10]

Except for the epitaxy by segregation method, the epitaxy by deposition and by intercalation of 2D Xenes is commonly carried out by Molecular Beam Epitaxy (MBE). MBE is an evaporative PVD technique in UHV characterized by extremely low evaporation and deposition rates that allow the realization of kinetically controlled growth processes with atomic precision. When compared to other synthesis methodologies for the bottom-up synthesis of 2D materials, MBE is time consuming and does not offer a scalable production rate. However, this technique offers also strong advantages such as the possibility to attain epitaxial growths of 2D materials with an unprecedented control of their thickness, composition and crystalline quality even on large areas. (often only limited by the atomic terraces width of the substrates).

3.2 UHV system for Molecular beam epitaxy

The experimental system (Omicron NanoTechnology GmbH) used for the sample growths and in-situ characterizations is schematically depicted in figure 3.1. It consists of three interconnected chambers kept at a base pressure of $\sim 10^{-10} mbar$: a preparation chamber (in orange), an analysis chamber for X-Ray Photoelectron spectroscopy (XPS) (in blue) and a Scanning Probe Microscopy (SPM) chamber (in green). The XPS chamber is used for the determination of the atomic species in the as-prepared samples and for the analysis of their chemical state while the SPM chamber is used for the in-situ morphological characterization of the sample surfaces. The samples can be loaded into (or extracted out) the system through a fast-entry lock and can be transferred between each chamber thanks to suitable sample holders moved by means of magnetic manipulators. Both the preparation and the XPS/SPM chambers are equipped with precision-manipulators that allow the movement and the positioning of the samples within each chamber. The preparation chamber of the UHV system is also furnished with a RHEED (Reflection High Energy Electron Diffraction) apparatus that allows the evaluation of the crystalline quality of the thin films during their growth process.

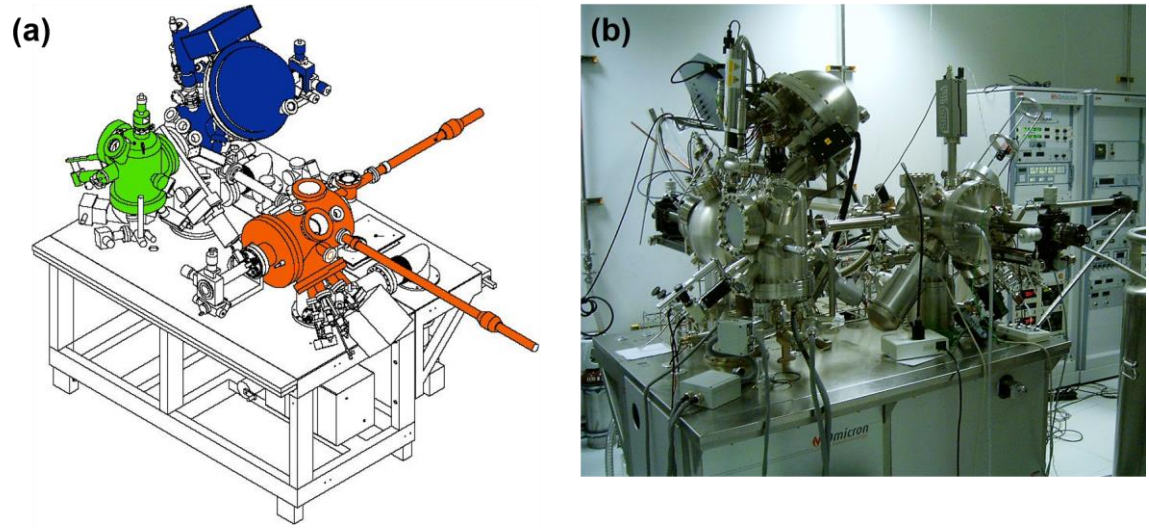

Figure 3.1 (a) Schematic depiction of the UHV system used for the MBE growth of 2D Xenes. The preparation, XPS analysis and SPM chambers are highlighted in orange, blue and green respectively. **(b)** Picture of the Omicron UHV system.

In order to ensure an optimal crystalline quality to the epitaxial films during their growth, the surfaces of the samples need to be previously prepared. The substrate preparation is typically carried out by repeated sputtering and annealing processes performed using an ion sputter gun mounted in the XPS chamber and the resistive heaters mounted on the sample holders of the precision-manipulators. The ion-sputtering removes all the organic contaminants from the surfaces of the samples with a directional beam of high-energy ions of an inert gas (Ar^+). Subsequently, the sputtered surfaces are restored back to their perfect crystalline periodicity by a thermal annealing treatment.

After the substrate preparation, the growth of the thin films is carried out in the preparation chamber employing different kinds of effusive sources for the UHV evaporation. Specifically, the synthesis of epitaxial-phosphorus samples was always performed by an electron-beam (e-beam) evaporator equipped with an anode-crucible containing black phosphorus crystals. Controlling the current through the e-beam emission filament and the accelerating voltage of the electrons towards the anode it was possible to accurately tune the evaporation rate of molecular P_4 (and P_2) species from the heated black phosphorus crystals. The UHV status of the system during the evaporation of the atomic or molecular species was cross-checked with a residual gas analyzer (RGA) attached to the preparation chamber. The aluminum thin-films, employed for the synthesis of the protective Al_2O_3 capping layers of the samples as we will see in Chapter 4, were evaporated by means of a Knudsen cell (k-cell). The voltage and the current provided to the k-cell were externally controlled so to achieve the appropriate evaporation temperature and, hence, partial pressure of the Al vapor. The Al deposition rate at given partial pressure was estimated performing a pre-calibration procedure by means of a quartz-microbalance mounted inside the preparation chamber. Finally, the synthesis of the silicene samples, discussed in chapter 5, was performed by resistive evaporation from an intrinsic silicon wafer brought at the sublimation temperature with an external power generator.

3.3 In situ characterization techniques

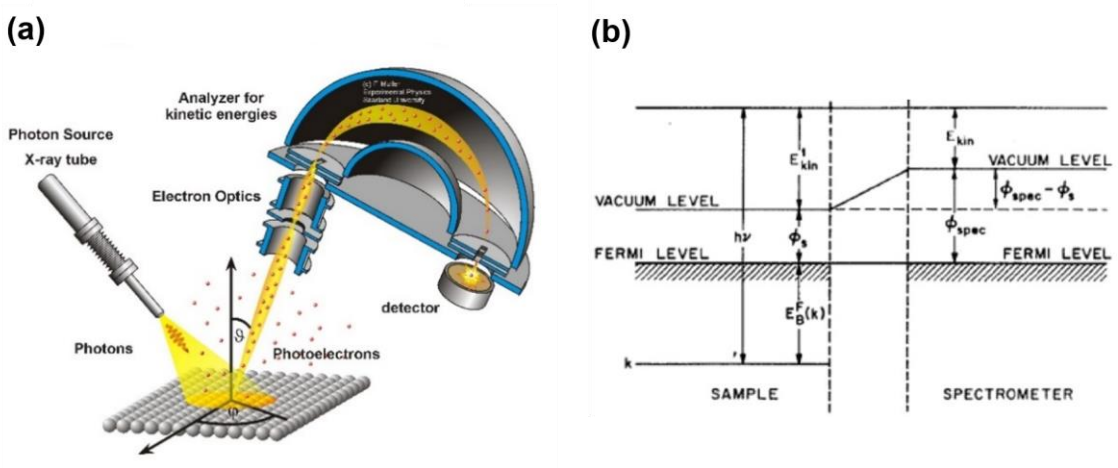

Figure 3.2 (a) Schematic depiction of an XPS experiment. (b) Energy levels diagram for the determination binding energy of the photoemitted electron. Note that the kinetic energy measured by the spectrometer $\boldsymbol{E_{kin}}$ is different from the kinetic energy referenced to the sample vacuum level $\boldsymbol{E^1_{kin}}$ due to the difference between the work function of the spectrometer $\boldsymbol{\phi_{spec}}$ and of the sample $\boldsymbol{\phi_s}$.

The growth of the silicene and of the epitaxial phosphorus samples with the UHV system described above offers two main advantages. Firstly, it ensures the thermodynamic stabilization of these 2D crystalline monoelemental lattices in a UHV environment by epitaxy on appropriate substrates. Secondly, it allows a direct access to their pristine interfaces by means of UHV characterization techniques. In particular, in the following paragraph we will review the physical phenomena at the basis of the XPS and SPM characterization methods that, combined with the results of theoretical calculations, play a fundamental role for the correct “in-situ” identification of Xenes.

3.3.1 X-Ray photoelectron spectroscopy

X-Ray photoelectron spectroscopy (XPS) is a photoemission spectroscopy technique (PES) that is able to identify the elemental composition as well as the chemical state of the atoms at the surface of a material. For this reason, it is also referred to as “electron spectroscopy for chemical analysis” (ESCA).

The physical principle of XPS is the photoelectric effect[11]. A photon, with energy in the soft-X ray range (<2 KeV), impinges on a sample photo-ionizing the core-energy level of the atoms in the material. The excited electrons travel through the sample towards the surface, escape in the vacuum and, finally, are collected by an analyzer that determines their kinetic energy (E_{kin}), as illustrated in figure 3.2(a). During their path towards the surface the electrons may lose energy due to inelastic scattering events occurring inside the material and, therefore, only a fraction of them effectively reach the energy analyzer. Thus, the escape depth of the emitted photoelectrons is restricted to only few nanometers below the sample surface making XPS a surface-sensitive technique. Since the intensity of the emitted photoelectrons is attenuated with the depth according to a Beer-Lambert law, the XPS sampling depth can be

roughly estimated as $\sim 3\lambda(E)\cos\vartheta$, where $\lambda(E_{kin})$ is the inelastic mean free path (IMFP) of the electrons emitted with a kinetic energy E_{kin} and ϑ is the electron take-off angle (measured from the surface normal as in figure 3.2(a)).

The final state of the system in any XPS photoemission experiment is characterized by the presence of a positive hole in a core energy level of an atom. The kinetic energy of the emitted photoelectron does not bring any direct information of the initial state of the unperturbed system and, additionally, it is influenced by the interaction between the photoionized system and the potential created by the core hole. Due to these complications, the determination of the final kinetic energy of the escaping electron is not always a trivial task. However, under the simplifying assumption that the interaction between the escaping electron and the system is instantaneous (sudden-approximation), it is possible to calculate the kinetic energy of the escaping photoelectron E_{kin} in terms of its core-level binding energy (E_B) as illustrated in the diagram of figure 3.2(b):

$$E_{kin} = h\nu - E_B - \phi_{spec} \qquad (3.1)$$

where $h\nu$ is the energy of the incoming X-Ray photons, ϕ_{spec} is the work-function of the spectrometer and E_B is core-level binding energy of the electron expressed, by convention, as a positive quantity (referenced to the fermi level of the system E_F). Equation (3.1) is fundamental for the interpretation of the XPS spectra. By fixing the work-function of the analyzer and the energy of the incoming photons, the kinetic energy of the electrons determines their binding energy and vice versa. Thus, an XPS spectrum is always given by the intensity (counts per second) as function of the binding energy of the emitted core electrons. Since the latter quantity varies between the chemical elements and, for a given element, is also influenced by nature of the chemical bonding with other atomic species in the same material, by studying the peaks-positions in the XPS spectra it is possible to quantify the atomic species present in a material and how these species are chemically bonded each other.

In the present work all the XPS measurements were carried out by means of a non-monochromatic X-Ray source equipped with a magnesium anode at an emission energy of 1253.6 eV (Mg-K_α X-Ray Line). The kinetic energy of the emitted photoelectrons was analyzed with a hemispherical energy analyzer working with a pass energy of 20 eV. The takeoff angle was set at $\vartheta = 53\ °C$ so that the emitted photoelectrons probed only the atomic species at the surfaces of the as-deposited epitaxial 2D materials.

3.3.2 Scanning Tunneling Microscopy (STM)

The surface morphology of the as-deposited samples was studied by Scanning Tunneling Microcopy (STM) performed inside the SPM chamber of the UHV system of figure 3.1. The SPM chamber is equipped with an Omicron Variable Temperature STM (VT-STM) that can perform STM measurements by varying the sample temperatures between 25 K and 1500 K. Additionally the same instrument can be used for Atomic Force Microscopy (AFM), Kelvin Probe Force Microscopy (KPFM) and Ballistic Emission Electron Microscopy (BEEM) measurements.

Scanning tunneling microscopy operation modes

The basic physical principle behind STM is the quantum mechanical tunneling of the electrons through the vacuum barrier separating the sample surface and a sharp conducting

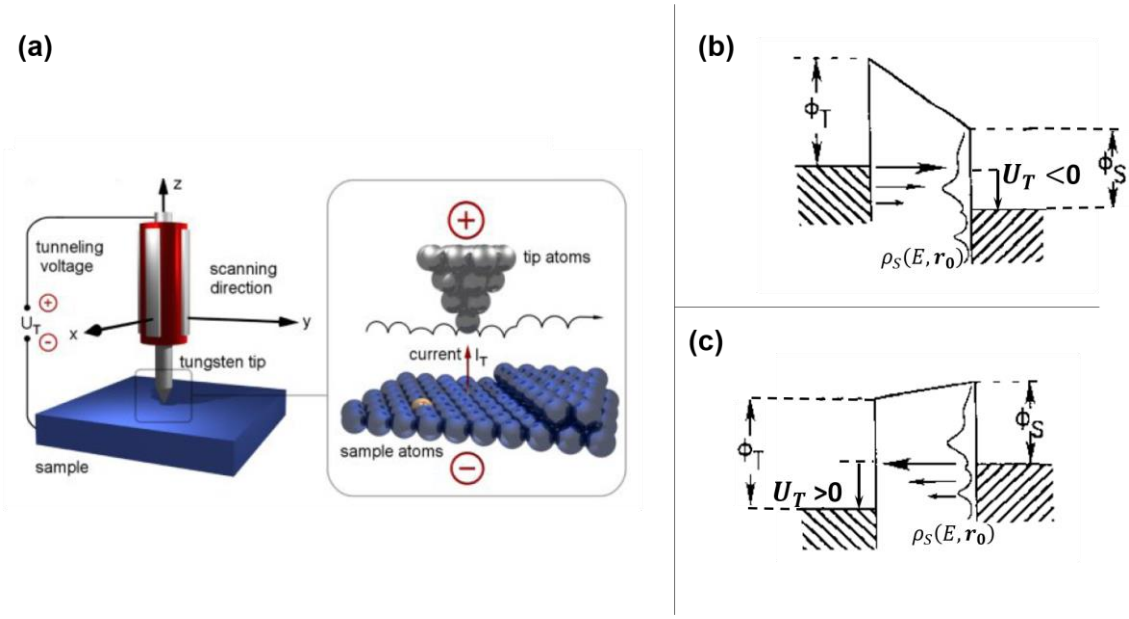

Figure 3.3 (a) Schematic diagram of the working principle of a Scanning Tunneling Microscope. **(b)** and **(c)** Energy level diagram of the sample-vacuum-tip junction under the influence of an external bias voltage. For positive sample bias (negative tip bias): the electrons tunnel from tip to the sample whereas negative sample bias (positive tip bias): electrons tunnel from sample to the tip. (b) and (c) adapted from reference [17]

tip[12], usually made of W or PtIr. The tip is brought close enough to the surface so that, under an applied voltage bias (U_T), a tunneling current (I_T) of the order 0.1-1nA can be measured, as illustrated in figure 3.3(a). The typical "close-enough" distance to have a quantum tunneling effect through the vacuum gap between the tip and the sample lies in the 4-7Å range. During an STM measurement the position of the tip is scanned in two lateral dimensions on the sample surface by means of piezoelectric drivers and the tunneling current is measured at each location. An image of the surface can be reconstructed according to two different modes of operation:

- In "constant current mode" a feedback circuit constantly adjust the tip height during the scan, to keep the tunneling current constant. Therefore, an image of the surface can be reproduced by measuring the variation of the tip position along the direction perpendicular to the surface. Operatively these variations in the tip position are deduced directly from voltages supplied to the piezoelectric drivers.
- In the "constant height mode" the height of the tip is kept constant over the surface, and the small features on it are reflected in changes of the tunneling current. In this case the feedback circuit is open (i.e. does not control the tunneling current) and the current defines the STM image.

The "constant height" mode of imaging is used only in some special circumstances, for example, when the surface of the sample is extremely flat and, in general, can be viewed as a particular case of the "constant current" imaging mode. In the latter case, in order to keep stable the tunneling current with tip-sample separations of the order of few angstroms, the STM apparatus requires a precise control of the position of the electrodes and a system to limit the effects of external vibrations to much less than an angstrom. In the Omicron VT-STM system this is accomplished by suspending the STM base plate by four springs that damp the external oscillations by means of an eddy currents damping mechanism consisting in a ring of copper

plates mounted on the STM base with each plate running through fixed magnets. The resonance frequency of the whole mechanical system is 2 Hz.

Basic theory of scanning tunneling microscopy

The imaging mechanism of an STM can be theoretically understood with the aid of the Bardeen's tunneling theory [13] and using the Tersoff and Hamman[14], [15] approximation to model the interaction between the tip electrode and the sample. According to the Bardeen theory, also known as *independent electrodes approximation*, the tunneling current can be expressed as:

$$I_T = \frac{2\pi e}{\hbar}\sum_{\nu\mu}\left|M_{\mu\nu}\right|^2 f_S(E_\mu)(1 - f_S(E_\nu + eU_T))\delta\left(E_\nu - E_\mu\right) \tag{3.2}$$

where $f_S(E_\mu) = 1/\left(1 + e^{\left(E_\mu - E_{FS}\right)/k_b T}\right)$ is the Fermi function of the sample, E_{FS} the equilibrium Fermi level, U_T the voltage drop across the barrier and $M_{\mu\nu}$ the matrix element of the tunneling Hamiltonian that couples the energy eigenstates of the sample, ψ_μ, to that of the tip, χ_ν, with energy E_μ and E_ν, respectively:

$$M_{\mu\nu} = -\frac{\hbar^2}{2m}\int_{S_0}\left(\overline{\chi_\nu}\,\boldsymbol{\nabla}\psi_\mu - \overline{\psi_\mu}\,\boldsymbol{\nabla}\chi_\nu\right)d\vec{\boldsymbol{S}} \tag{3.3}$$

with S_0 a surface lying entirely within the barrier region separating the tip and the sample half spaces. In the Tersoff and Hamman approximation the tip is considered as a sphere of radius R centered at $\boldsymbol{r_0}$ and the wavefunctions of the electrons in the vacuum barrier are described by evanescent waves with spherical symmetry (*s-waves*):

$$\chi_\nu(r) \equiv \chi_E(r) = A_\nu\frac{e^{-\kappa_T|r-r_0|}}{|r - r_0|} \tag{3.4}$$

with $\kappa_T = \sqrt{2m(\phi_T - E)/\hbar^2}$, ϕ_T the work function of the tip and A_ν a renormalization constant that depends on the tip radius and on the energy. Using equation (3.4) in equation (3.3) the matrix element $M_{\mu\nu}$ becomes:

$$M_{\mu\nu}(E) = -\frac{2\pi\hbar^2}{m}A_\nu\psi_\mu(\boldsymbol{r_0}) \tag{3.5}$$

So, in the Tersoff and Hamman approximation the tunneling matrix element is proportional to the sample wavefunction evaluated at the center-tip position. The sample wave functions can be generally described by Bloch waves in the $\boldsymbol{r}_\parallel = (x, y)$ plane, i.e. $\psi_\mu(\boldsymbol{r}) \equiv \psi_{\boldsymbol{k}_\parallel, E_{\boldsymbol{k}_\parallel}}(\boldsymbol{r}_\parallel, z)$ with $\boldsymbol{k}_\parallel$ the wavevector component parallel to the sample surface.

Recalling the definition of local density of states (LDOS) of the sample $\rho_S(E, \boldsymbol{r_0})$ and of the tip $\rho_T(E, \boldsymbol{r_0})$:

$$\begin{aligned}\rho_S(E, \boldsymbol{r_0}) &= \sum_\mu\left|\psi_\mu(\boldsymbol{r_0})\right|^2\delta\left(E_\mu - E\right)\\ \rho_T(E, \boldsymbol{r_0}) &= \rho_T(E) = \sum_\nu\delta(E_\nu - E)\end{aligned} \tag{3.6}$$

equation (3.2) can be rewritten as an integral:

$$\begin{aligned}I_T \propto \int_{-\infty}^{+\infty}\rho_T(\epsilon + E_{FS} - eU_T)\rho_S(\epsilon + E_{FS}, \boldsymbol{r_0})[f_S(E_{FS} + \epsilon - eU_T)\\ - f_S(E_{FS} + \epsilon)]\,|A(\epsilon + E_{FS} - eU_T)|^2 d\epsilon\end{aligned} \tag{3.7}$$

If the temperatures are low enough (or the bias voltages are small) so that: $eU_T \ll k_B T$ and if $eU_T \ll \phi_{S,T}$, only the Bloch states in an energy interval of width eU_T close to the equilibrium Fermi level of the sample E_{FS} contribute to the summations in the equation (3.6). Therefore, the integral in equation (3.7) becomes:

$$I_T \propto \int_0^{eU_T} \rho_T(\epsilon + E_{FS} - eU_T)\rho_S(\epsilon + E_{FS}, \boldsymbol{r_0})\, |A(\epsilon + E_{FS} - eU_T)|^2 d\epsilon \qquad (3.8)$$

and if we assume that the coefficient $A(\epsilon + E_{FS} - eU_T)$ does not vary much with the energy, we can write:

$$I_T \propto |A|^2 \int_0^{eU_T} \rho_T(\epsilon + E_{FS} - eU_T)\, \rho_S(\epsilon + E_{FS}, \boldsymbol{r_0}) d\epsilon \qquad (3.9)$$

The tunneling current is, thus, determined by a convolution between the local density of states of the tip and that of the sample. If in the energy interval $[0, eU_T]$ the LDOS of the tip can be considered uniform, we see that the tunneling current at low bias, namely $eU_T \ll E_{FS}$, becomes:

$$I_T \propto eU_T |A|^2 \rho_T(E_{FS}) \rho_S(E_{FS}, \boldsymbol{r_0}) \qquad (3.10)$$

i.e. it is proportional to the contours of constant LDOS at the Fermi level on the surface or, alternatively, it is proportional to the charge density of the surface Bloch waves with energy close to the Fermi level. This quantity can be easily obtained from first-principle calculations and allows to compare the results obtained from the STM surface topography with the theoretical atomic models proposed for the surfaces structures.

An explicit expression of the sample LDOS $\rho_S(E_{FS}, \boldsymbol{r_0})$ can be calculated in the case of a metallic surface with a 1D periodicity using the so-called *leading Bloch wave approximation*[16]. Under these assumptions it is possible to show that $\rho_S(E_{FS}, \boldsymbol{r_0}) \propto e^{-2\kappa s}\left[1 + Ce^{-\beta(s)} \cos^2\left(\frac{\pi}{a}x\right)\right]$, where s is the tip-sample separation distance, C a constant, $\beta(s)$ a function of the tip-sample separation, $\kappa = \sqrt{2m\phi_{eff}/\hbar^2}$ and ϕ_{eff} the effective local potential barrier height (in good approximation equal to the average of the tip and sample work functions) Therefore, the tunneling current at very small bias can be written as:

$$I_T \propto e\rho_T(E_{FS}) U_T e^{-2s\sqrt{\frac{2m\phi_{eff}}{\hbar^2}}} \left(1 + Ce^{-\beta(s)} \cos^2\left(\frac{\pi}{a}x\right)\right) \qquad (3.11)$$

It is interesting to note that the first term in equation (3.11) is identical to the expression of the tunneling current through a 1D square barrier of height ϕ_{eff}. If the tip-sample distance s is kept constant this term gives a constant contribution, whereas the second term in equation (3.11) describes the atomic corrugation on the sample surface with periodicity a.

The Tersoff-Hamman model (or s-wave tip model) can be considered valid for metallic surfaces if the corrugation amplitudes are larger than 0.3 nm[16]. However, in most of the STM experiments the actual achievable vertical resolution is often much smaller than 0.3 nm and varies between 0.005-0.05 nm. To quantitatively interpret and predict STM images having atomic resolutions the s-wave tip model needs to be generalized so to include the effects of tip atomic states with a symmetry different from an s-wave. For example, in case of W and PtIr tips, the density of states at Fermi level is mainly dominated by d-states rather than s states. These states are, therefore, the main responsible of the atomic resolution obtained in the STM images.

Scanning Tunneling Spectroscopy (STS)

At high sample-bias (but low temperatures) the results of the Bardeen tunneling theory can be qualitatively generalized using the WKB (Wentzel-Kramers-Brioullin) approximation for the tunneling current:[17]

$$I_T \propto \int_{E_{FS}}^{E_{FS}+eU_T} \rho_T(\epsilon - eU_T)\rho_S(\epsilon, \boldsymbol{r_0})T(\epsilon, eU_T, z)d\epsilon \qquad (3.12)$$

where $T(\epsilon, U_T, z)$ is the transmission factor of the tunnel barrier. The U_T dependence in $T(\epsilon, U_T, z)$ describes the deformation of the barrier in the limit high-voltages whereas at low voltages $T(\epsilon, U_T, z)$ is independent of U_T and has an exponentially decaying behavior with the vertical distance z and the energy ϵ. From equation (3.12) we see that only the states lying between E_{FS} and $E_{FS} + eU_T$ contribute to the tunneling current and since $T(\epsilon, eU_T, z)$ is an exponentially decreasing function with ϵ we conclude that for positive sample bias (negative tip bias, U_T<0) the electrons mainly tunnel from the tip towards the empty states of the sample at $E \approx E_{FS} - e|U_T|$ as illustrated in figure 3.3(b) while for negative sample bias (positive tip bias, U_T>0) the electrons mainly tunnel from the sample states near E_{FS} into the tip empty states at $E \approx E_{FS} - eU_T$, as illustrated in figure 3.3(c). Therefore, equation (3.12) suggests that by varying the energy window interval $[0, eU_T\ ]$ the contributions of different sample states to the tunneling current can be disentangled obtaining a spectroscopic information. This technique is known as Scanning Tunneling Spectroscopy (STS) and can be experimentally carried out following different approaches. For example:[17], [18]

- Recording and comparing the STM topography of the surface at different bias voltages it is possible to deduce information on the symmetry and energy of the electronic states.
- By fixing the tip-sample separation in a chosen location and ramping the tip-sample bias voltage the I_T-U_T curves can be measured. From the I_T-U_T curves the band gap of the sample at the location of the measurement can be determined. Furthermore, calculating dI_T/dU_T information on the sample LDOS can be deduced.
- By measuring the differential conductivity with a modulation technique (lock-in detection) it is possible to obtain dI_T/dU_T simultaneously with the constant current STM images. In this way it is possible to extract information on the sample states as function of both the energy and their spatial position.

In the latter two approaches the structures observed in dI_T/dU_T can be assigned to the features of the sample LDOS, $\rho_S(E, \boldsymbol{r_0})$. This can be qualitatively understood by taking the derivative of equation (3.12):

$$\frac{dI_T}{dU_T} \propto \rho_T(0)\rho_S(eU_T, \boldsymbol{r_0})T(eU_T, eU_T, z) + \int_{E_{FS}}^{E_{FS}+eU_T} \rho_T(\epsilon - eU_T)\rho_S(\epsilon, \boldsymbol{r_0})\frac{dT(\epsilon, eU_T, z)}{dU_T}d\epsilon \qquad (3.13)$$

The second term in (3.13) is caused by the voltage dependence of the tunneling factor $T(\epsilon, eU_T, z)$ and contributes to a smoothly varying background on which the spectroscopic information due to the first term (as function of U_T) is superimposed. Thus dI_T/dU_T is approximately proportional to the energy dependent LDOS of the sample. In some circumstances, normalizing the measured differential conductance, dI_T/dU_T, by the static (DC) conductivity I_T/U_T can minimize the effects of the voltage dependence of $T(\epsilon, eU_T, z)$ and the

influence of tip-sample spacing. These effects are typically more pronounced when the bias voltage becomes an appreciable fraction of the sample work function since in this case the U_T (and z) dependence in $T(\epsilon, eU_T, z)$ distort the spectrum. However, this normalization is both unnecessary and undesirable at small voltages because in this situation I_T/U_T reproduces well the sample density of states. Thus, the appropriate way to display the spectroscopy data obtained from STS measurements depends on the problem considered and a variety of approaches for collecting and displaying the STS spectra have been considered.[18]

3.4 Epitaxial synthesis of 2D Phosphorus

In Chapter 2 we have reviewed some of the main techniques for the top down synthesis of few layers and monolayer phosphorene flakes. Although, the mechanical exfoliation methods give a high crystalline quality of the synthesized samples such methods are time consuming, not scalable and lack of control on the thickness. Thinning techniques may help to improve the latter aspect but achieving a fine control on the thickness down to a single layer (2D α-P) is not simple and requires a previous optimization of the process parameters, as discussed in the case of the laser thinning of multilayer BP flakes. Furthermore, a common limitation of all the top down synthesis techniques is that the typical size of few-layer BP crystals is only of few micrometers and hence these approaches are not amenable for any wafer scale processing of 2D phosphorus.

Conversely, bottom-up techniques like, PVD or CVD, are able to achieve a high-yield synthesis of monolayer sheets with high control over the thickness and crystalline quality, as demonstrated in the case of graphene and MoS_2.[19], [20] However, in the case of phosphorene, the CVD growth is complicated by the requirements of high pressures and high temperatures processes using red phosphorus precursors and often results in nm-thick BP films with poor uniformity and crystalline quality[21]. A complementary approach in this respect relies on the high pressure, high temperature conversion of amorphous red phosphorus films deposited on substrates [22]–[24] but even in this case the converted BP crystalline size is limited. Therefore, up to now, no effective high throughput epitaxial method for the large area growth of monolayer phosphorene (2D α-P) has been demonstrated. A wafer scale synthesis process has been reported, instead, using pulsed laser deposition (PLD) but the resulting BP film had an amorphous nature[25]. The epitaxial growth of monolayer phosphorene (2D α-P) by PVD, instead, has never been investigated in literature even though there are many theoretical studies that have explored the role played by the substates in stabilizing the 2D α-P phase.[26], [27]

To date, the only 2D allotropic form of phosphorus that has been experimentally reported to grow by epitaxy is the 2D β-P (Blue-Phosphorene) phase. This allotrope has been synthesized for the first time in 2016 by Zhang et al [28] on (111) surface of gold substrates using molecular beam epitaxy. In the following paragraphs we will firstly illustrate the relevance of the substrate choice in the synthesis (and processing) of epitaxial 2D β-P. Then, by means of STM and XPS measurements, we will elucidate the details of its structure and the growth mechanism so to understand if epitaxial phosphorus (Epi-P) grown on Au(111) can be considered as a 2D Xene in the sense of the definition highlighted in paragraph 1.3.

3.4.1 Role of the substrate

The substrate choice is a pivotal factor into the design an appropriate device integration scheme for any epitaxial 2D material. On one hand, the substrate is the common denominator involved in all the aspects of the growth process: from the nucleation, to the modulation of the growth rate, to the lattice symmetry matching requirements as well as in the control of the crystalline phases of the 2D overlayer[29]. On the other, the substrate takes part in the design of any subsequent device fabrication step such as the choice of a suitable transfer methodology for delivering the epitaxial 2D material onto a new target substrate.[30]

From an interface engineering point of view, the simplest approach to achieve a large area epitaxy of a 2D single crystal consists in choosing a substrate with a surface symmetry identical to that of the freestanding 2D material and, moreover, with a suitable interaction strength that allows the stabilization of the 2D layer. In particular, considering the case of phosphorus, theoretical calculations have shown that a weak interaction with the substrate is not capable to support the self-assembly of P atoms or molecules into an ordered 2D crystalline phase[26]. Thus, aside from the lattice matching and symmetry requirements, the interaction between phosphorus and the substrate atoms plays a crucial role in the synthesis of its 2D crystalline allotropes. The growth of 2D β-P, for example, was proved to be energetically favored on GaN(001) substrates with an half-layer-by half layer growth mechanism[31] while the growth of a 2D α-P (phosphorene) phase requires substrates with a moderate interaction strength such as such as Al(111) or β-Sn(001)[27], [32].

Metallic substrates

Catalytic metallic surfaces have been commonly adopted in the growth of 2D materials including Xenes like silicene and borophene[5], [33]–[35] and they are, therefore, expected to stabilize also the formation of the 2D phosphorus allotropes. Qiu et al. have proved that the growth of the 2D β-P (blue-phosphorene) phase is energetically favored on the (111) surfaces of Au, Ag, Ni and Pt whereas the 2D γ-P phase is predicted to be most stable on Ru(0001) and Ni(111) surfaces.[27] Regarding the Au(111) substrates, the higher stability of the 2D β-P phase over the 2D α-P structure results from the high number of P atoms bonded to the gold atoms on the surface while in the case of 2D α-P only an half-layer of its crystalline structure is involved in such chemical bonding and, hence, its growth is not energetically favored[32].

Although theoretical calculations have provided guidelines for the selection of appropriate substrates for the growth of 2D phosphorus allotropes, the 2D β-P (blue-phosphorene) phase has been the only one experimentally synthesized by epitaxy up to now. In addition to Au(111) substrates, the synthesis of 2D β-P has been recently demonstrated also on thin Cu_3O_2 insulating layers grown on Cu(111) surfaces.[36] The presence of the thin Cu_3O_2 buffer layer reduces the interfacial interaction between P and Cu allowing the growth of the phosphorus 2D epitaxial layer. This is not possible, instead, in the case of phosphorus growths carried out on metallic Cu(111) surfaces[37], [38] characterized by a stronger interfacial interaction with the P atoms. These experimental evidences pinpoint again the importance of an appropriate substrate engineering for the growth of the 2D β-P phase.

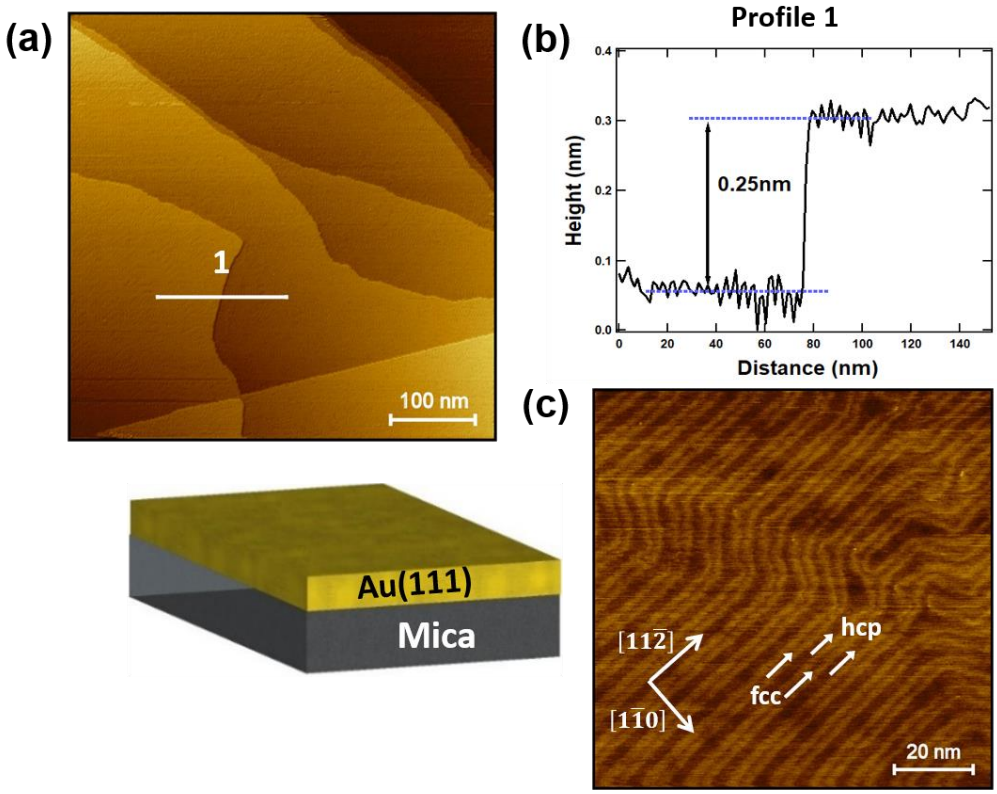

Figure 3.4 (a) STM (500x500) nm^2 topography of a clean Au(111) surface ($\boldsymbol{U_T}$=-0.67 V, $\boldsymbol{I_T}$=2 nA) . (b) Line profile along the direction indicated in (a). (c) STM (100x100) nm^2 image showing the "herringbone" $(\mathbf{22} \times \sqrt{\mathbf{3}})$ reconstruction of Au(111) ($\boldsymbol{U_T}$=-0.67 V, $\boldsymbol{I_T}$=2.3 nA)

Au(111)/Mica substrates

The case of epitaxial 2D β-P on Au(111) has been the subject of the majority of investigations in the past [28], [37], [39]–[44] and therefore, in the following, will be addressed in more detail also in relation to the problem of designing a device integration scheme that could be used as methodological standard in the case of other epitaxial Xenes grown on metallic substrates. In this respect, the first step towards the possible device integration of epitaxial phosphorene relies on the use of Au(111) thin (300 nm) film on mica substrates instead of expensive and hard-to-process Au(111) single crystals. As we will see in chapter 5, the layered nature of the mica allows the accessibility and the portability of the epitaxial membrane along the subsequent phases of the device integration path.

Figure 3.4 reports the STM images acquired on a clean Au(111) surface after several cycles of sputtering and annealing. The large scale (500x500) nm^2 topography reveals the atomically flat nature of the Au(111) substrate characterized by large terraces separated by monoatomic steps of 0.25 nm (see line profile in Figure 3.4(b)). The (100x100) nm^2 image in Figure 3.4(c) shows the typical strain-induced reconstruction of the Au(111) surface consisting in hexagonal close-packed (hcp) and face-centered cubic (fcc) regions separated by narrow bright areas of bridge sites forming the characteristic "herringbone" bands. The Au(111) surface reconstruction can be described by a $(22 \times \sqrt{3})$ unit cell commensurate with that of the (111) fcc lattice of gold. At each bending point ("elbow") of the herringbone modulation, the topmost Au layer exhibits a surface dislocation that may act as a nucleation site during the atomic depositions.[45]

3.4.2 MBE synthesis of epitaxial phosphorus on Au(111)

The MBE growth of phosphorus on Au(111) was operated with the UHV system of figure 3.1. Phosphorus was evaporated from an e-beam effusion cell containing black phosphorus as precursor. The residual gas analysis carried out during the deposition process revealed that the composition of the phosphorus vapor mainly consisted of P_4 molecular species.

Growth method

The exposure time of the Au(111) surface to the P_4 vapors and the vapor partial pressure both determined the final surface coverage of the deposited phosphorus thin film. Combined STM and XPS analysis proved that monolayer growth could be always achieved using a "standard" deposition time of 2 min 30 sec with P_4 partial pressures of 3.0×10^{-8} mbar. Monolayer coverage was also verified by varying the P_4 partial pressures below or above the 3.0×10^{-8} mbar values and, correspondingly, increasing or reducing the deposition times around the *standard value* of 2 min 30 sec (see table 3.1). However, in case of depositions carried out with partial pressures below a minimum value of 6×10^{-9} mbar or with exposure times shorter than 2 min 30 sec the final coverage observed on the Au(111) surface was always sub-monolayer.

The reorganization of the deposited phosphorus thin film in an ordered crystalline epilayer is mainly controlled by the temperature of the gold substrate. When the substrate was kept at room temperature (RT), P_4 molecules were found to condensate in an amorphous thin film, as illustrated by the large scale STM image in figure 3.5(a). The close-up STM image of figure 3.5(b) reveals the defective nature of the amorphous film characterized by coalesced phosphorus clusters separated by directional vacancies (black fractures in the image). A post deposition annealing carried out at temperatures between 230-270 °C leads to the reorganization of the amorphous film into a crystalline superstructure with hexagonal symmetry. Alternatively, the same hexagonal superstructure can be achieved by depositing P_4 directly on heated substrates between 230-270 °C. The overall crystalline quality of the resulting epitaxial film can be further improved by annealing the as-grown sample at the same growth temperature for about 20 minutes.

High quality and large area epitaxial growth

The hexagonal crystalline superstructure of epitaxial phosphorus on gold is characterized by flower-like domains consisting of a dark pore surrounded by six bright petals and can be clearly observed in the high resolution STM topography reported in figure 3.6(a). The distance between adjacent dark pores is $a = b =$1.44 nm, which is about five times the lattice constant of the (111) surface of gold (2.89 Å) or about four times the lattice constant of free standing β-P structure (3.33 Å). Therefore, the unit cell of the phosphorus hexagonal crystalline structure, outlined in figure 3.6(a), corresponds to a (5x5) supercell of Au(111) or to a (4x4) free standing β-P supercell. In the following the (5×5) phosphorus hexagonal superstructure on Au(111) will be identified with epitaxial 2D β-P (epitaxial-phosphorene). In the next paragraph we will examine if this identification can be considered appropriate after scrutinizing the different atomic models proposed for epitaxial phosphorus on gold. The growth of epitaxial phosphorus (or Epi-P) is uniform on the gold terraces and throughout the whole sample size (see the STM image in figure 3.6(b)) providing compelling directions for a possible wafer scale production of Epi-P on gold.

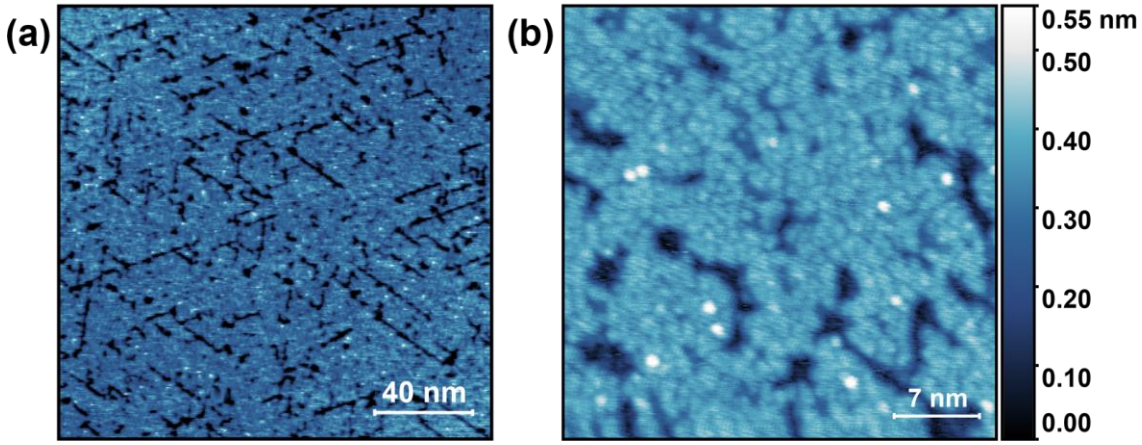

Figure 3.5 (a) Large scale STM (180x180) nm^2 and **(b)** close-up STM (35x35) nm^2 images ($\boldsymbol{U_T}$=1.3 V, $\boldsymbol{I_T}$=0.42 nA) of an amorphous phosphorus thin film obtained on Au(111) with the substrate kept at room temperature.

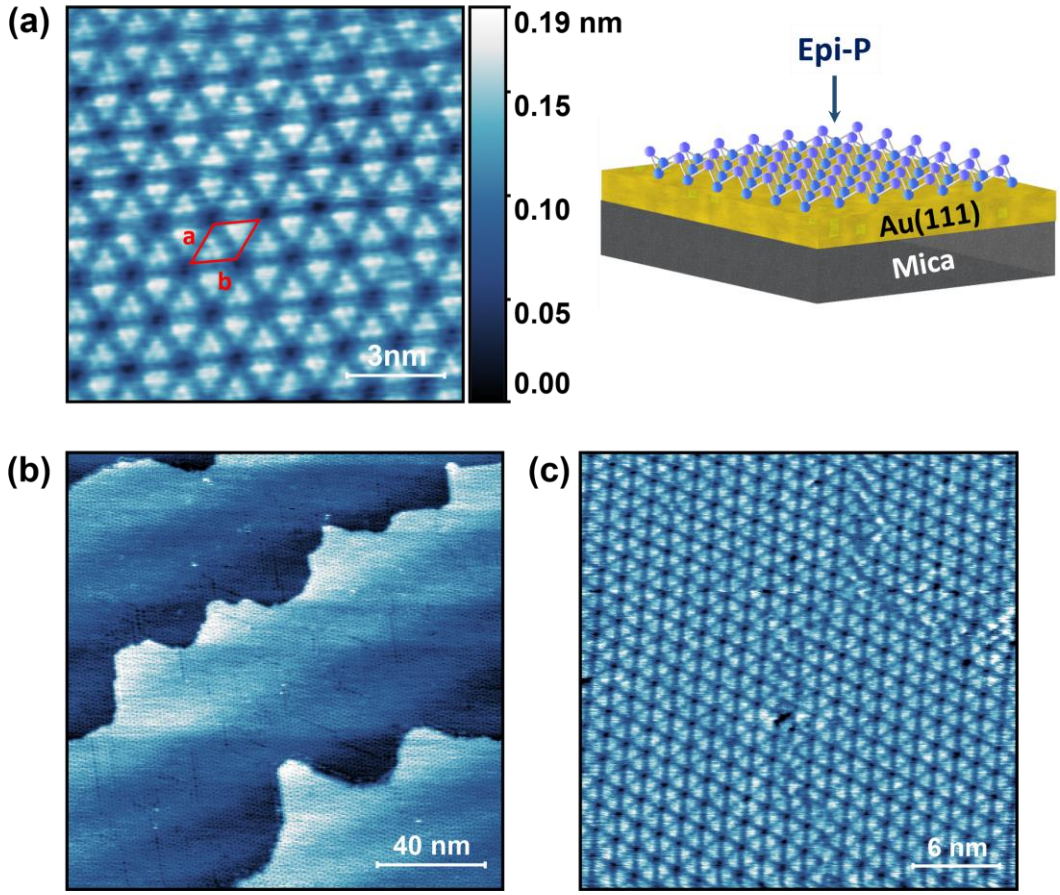

Figure 3.6 (a) High resolution (12x12) nm^2 STM topography ($\boldsymbol{U_T}$=1.3 V, $\boldsymbol{I_T}$=0.4 nA) of the phosphorus (5x5) hexagonal (flowerlike) superstructure obtained on Au(111) with the substrate heated in a the 230 °C-270 °C range. The red rhombus shows the superstructure unit cell. **(b)** Largescale (160x160) nm^2 and **(c)** close-up (30x30) nm^2 STM images ($\boldsymbol{U_T}$=1.4 V, $\boldsymbol{I_T}$=0.25 nA) showing a uniform and continuous layer covering the gold terraces. Phosphorus deposition parameters are for (a) 1 min at p=8x10^{-8} mbar with substrate temp of 263 °C for (b) and (c) are 5min at p=6x10^{-9} mbar with substrate temperature of 245 °C.

Moreover, at variance with the multiphasic nature of silicene on Ag(111)[26], [156], epitaxial phosphorus shows a single crystalline phase and a single crystalline orientation on the Au(111) surface (see figure 3.6(c)). This is a remarkable aspect that, in addition to the predicted high electron mobility [44], can reduce the issues related to the presence of grain boundaries in the case of silicene grown Ag(111) suspected to plague its carrier mobility when operated as a transistor channel.[46]

XPS analysis

In situ XPS measurements were carried out to probe the interfacial interaction between the Au(111) substrate and the epitaxial phosphorus layer and to verify its thermal stability after a prolonged (2 hours) low-temperature (280 °C) annealing. The XPS spectra of Au4f core levels, reported in figure 3.8(a) before and after the phosphorene growth and after 2h annealing at 280 °C, show a negligible shifts (<0.1 eV) that could be indicative of a weak charge transfer from the Au surface atoms to the P atoms of the Epi-P layer.

The P2p core levels showed in figure 3.8(b) have been fitted by two components placed at 129.4 (P 2p3/2) and 130.2 (P 2p1/2) eV by considering the 0.865 eV spin orbit split. The P2p core levels in epitaxial phosphorus are shifted to lower binding energy than those of black phosphorus (~130 eV) and red (~132 eV) phosphorus.[47], [48] This binding energy shift can be considered as a reliable marker for the identification of epitaxial phosphorus on gold. No substantial binding energy shift of the P2p peak was observed, instead, after the annealing at 280 °C indicating a good thermal stability of Epi-P to low a temperature process treatment.

Self-limited growth mechanism

The constant P 2*p*/Au 4*f* core levels ratio reported in Table 3.1 as function of the increasing deposition time for samples exposed to similar P_4 vapor partial pressures (sample 1, 2, 3) suggest that the growth of other epitaxial phosphorus layers beyond the first one could be inhibited by a self-limiting growth process where a key role is played by the catalytic activity of the gold (111) substrate. This is confirmed also by the STM image in figure 3.7 showing the morphology of the Au(111) surface obtained after a 5 min long (namely twice the time needed to achieve a standard monolayer coverage) phosphorus deposition. As confirmed by the presence of phosphorus clusters, the surface coverage is slightly above one monolayer but the hexagonal (5x5) superstructure is still well discernible, covering uniformly the whole substrate. Therefore, the intensity of the characteristic XPS P2p peak of epitaxial phosphorene located at 129.4 eV does not change much. The self-limited phosphorus growth on Au(111) has been reported in literature also by Xu et al [41] and by Zhuang et al [44] In the latter study the authors noticed that even a prolonged phosphorus deposition on the epitaxial phosphorus layer kept at room temperature does not introduce a substantial alteration in the hexagonal (5x5) superstructure on Au(111). The additional P_4 cluster fill the hollow sites of the flowerlike pattern due to a low reactivity and the absence of dangling bonds on the monolayer epitaxial phosphorus surface. As we will see in the next paragraph, these experimental observations can be well understood introducing an appropriate atomic model for the structure of epitaxial phosphorus on Au(111).

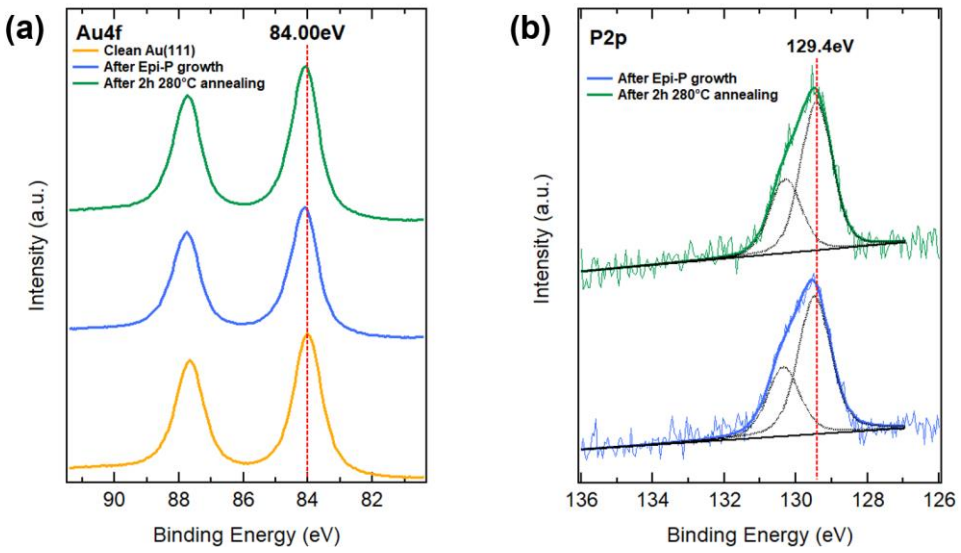

Figure 3.8 (a) XPS core level spectra of the (a) Au4f and (b) P2p before (yellow), after the epitaxial phosphorus growth (blue) and after a 2 hours annealing at 280 °C (green)

Table 3.1 Intensity ratio of the P2p(129.4 eV) and Au4f (84.0 eV) core levels as function of the deposition time.

Sample	Deposition time [min]	P_4 partial pressure (mbar)	P2*p*/Au4*f* ratio [a.u.]
Standard Reference Monolayer	2.5	3.0×10^{-8}	0.32
Monolayer (Fig. 3.6(a))	1	8×10^{-8}	0.30
1	5	1.0×10^{-7}	0.34
2	7	1.4×10^{-7}	0.29
3	10	3.0×10^{-7}	0.33

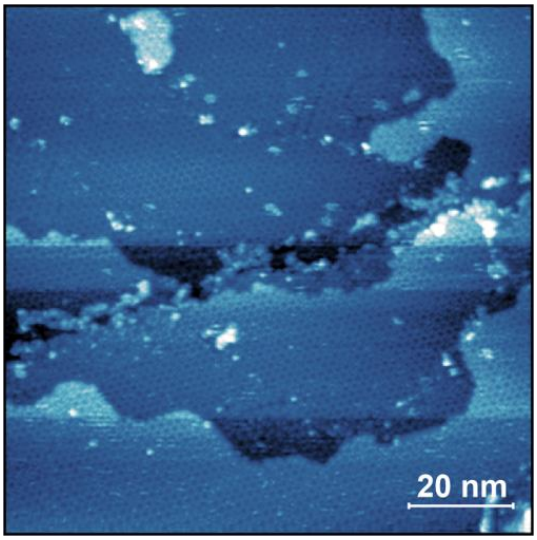

Figure 3.7 STM (100x100) nm^2 image ($\boldsymbol{U_T}$=1.2 V, $\boldsymbol{I_T}$=0.36 nA) of the Au(111) surface after a 5min long phosphorus deposition at 2.3×10^{-8} mbar showing the formation of phosphorus clusters on top of the (5x5) hexagonal superstructure and ruling out the formation of additional layers.

3.4.3 Atomic models and growth mechanism of epitaxial phosphorus on Au(111)

The morphology of the epitaxial phosphorus layer obtained from the analysis of the STM images has been explained according to a variety of atomic models. In the following we will review very briefly some of these models illustrating also how they are able to account for the salient features of the observed (5x5) phosphorus hexagonal superstructure on Au(111).

Disconnected epitaxial blue-phosphorene atomic models

All the initial atomic models for the (5x5) phosphorus hexagonal superstructure interpreted this structure in terms of an epilayer with the same buckled-lattice of the theoretically predicted free-standing blue-phosphorene 2D crystal.[28], [42], [44] Due to the large lattice mismatch existing between the free-standing blue-phosphorene (3.33Å) and the Au(111) surface (2.89 Å) the only way to accommodate the former on the latter is to break the blue-phosphorene structure in some points so to release the strain. The (4x4) Blue-P reconstruction on (5x5) Au(111) obtained in this way is characterized by an hexagonal or flowerlike pattern in which each "petal" of the pattern correspond to P_{16} blue-phosphorene islands matching one half of the (5x5) Au(111) unit cell.

However, a close inspection in the high-resolution STM image of figures 3.9(a) and 3.9(b) reveals that only few petals show six bright protrusions characteristic of the 6 top phosphorus atoms of a P_{16} blue-phosphorene island. Actually, most of the petals of the (5x5) phosphorus hexagonal superstructure are characterized by three bright protrusions. This observation is also confirmed by the blue STM line profile in Figure 3.9(a) that indicates two different heights, when crossing consecutive dark holes and therefore suggesting the presence of a second layer on top of the blue phosphorene P_{16} island. Indeed, the blue STM profile taken on the top layers shows that three additional phosphorus atoms are placed at 0.5 Å distance on top. Moreover, the green STM profile of Figure 3.9(a) also shows that the lateral distance of the on-top phosphorus atoms is on average 0.34 nm and they form a nearly regular triangular.

"Adatom-rich" atomic model

In order to account for these observations a second model for the (5x5) phosphorus hexagonal superstructure on Au(111) has been proposed.[43], [49]. In this atomic model two local configurations coexist together: beside diseperse P_{16} blue-phosphorene islands (green rhombus of figure 3.9(b)) there are also more common "adatom-rich" structures. In the "adatom-rich" structures three additional phosphorus atoms are accommodated on the top layer of the P_{16} island (yellow rhombus in figure 3.9(b)), so explaining the three bright protrusion observed in the high-resolution STM images. However, this model has been criticized by arguing that the number of protrusions in each petal of the (5x5) phosphorus hexagonal superstructure can be also strongly influenced by the STM tunneling parameters as well as by the tip preparation conditions. Theoretical simulations performed using a model based on a connected network of P_{16} blue-phosphorene islands have shown, instead, that the observed size (and asymmetry) of the central dark hollow site of the flowerlike pattern can be correctly reproduced. [50]

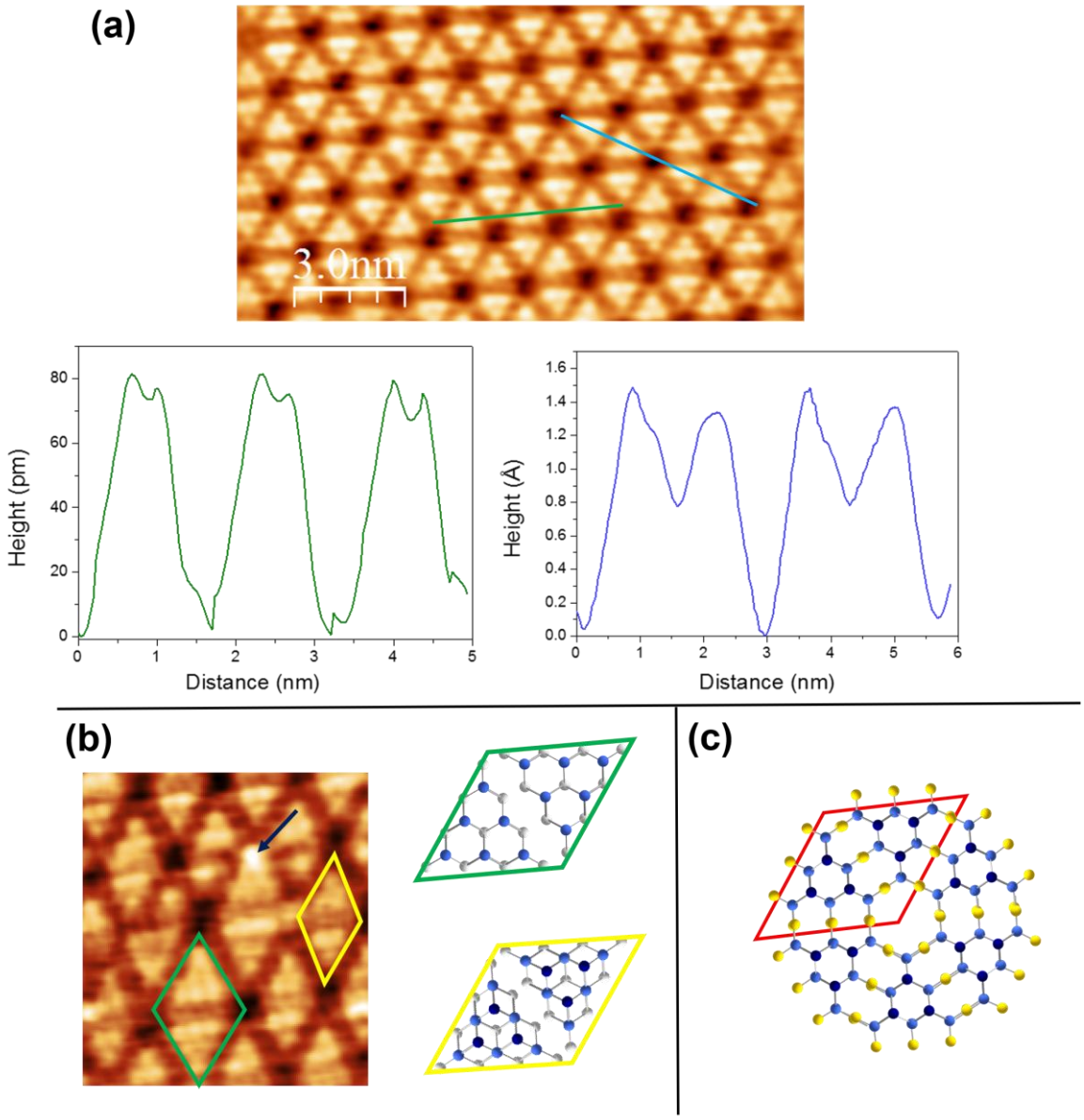

Figure 3.9 **(a)** High resolution STM (15x8) nm^2 image ($\boldsymbol{U_T}$=1.3 V, $\boldsymbol{I_T}$=0.4 nA) of the (5x5) hexagonal phosphorus reconstruction on gold obtained with the same deposition parameters of figure 3.6(a). The line profile along the blue and green direction are also shown. **(b)** Detail (8x6.5) nm^2 of the phosphorus hexagonal reconstruction showing the coexistence of two possible structures: P_{16} blue phosphorene islands (green rhombus) with 6 P atoms on-top and the "adatom-rich" (yellow rhombus) P_{16+3} structures with 3 P atoms on top. The blue arrow pinpoints an adsorbed P cluster into a hollow site. **(c)** Structural model for the Au-decorated phosphorus network. The unit cell is highlighted in red. In all the models the P atoms are represented by white, light-blue and dark-blue spheres according to the distance from the substrate. Au atoms are represented by yellow spheres.

Porous Au-phosphorus framework atomic model

Very recently, however, all the previous models for the phosphorus (5x5) hexagonal reconstruction have been questioned and critically re-examined by Tian et al.[39] and Zhao et al.[40]. According to these authors, the simulated STM images for both the P_{16} and the P_{16+3} ("adatom rich") atomic models are not able to account for all the rotational and mirror-like symmetries observed from the experimental STM data. Moreover, the "adatom-rich" model is not even stable from an energetic point of view due to the existence of some P atoms in each P_{16+3} island with a coordination number approaching five.

The most stable atomic model for the (5x5) phosphorus hexagonal reconstruction on Au(111) correspond actually to an Au-decorated "porous" network of P atoms rather than to a 2D epilayer. According to this model, there are two 9-atom blue-phosphorene fragments in each unit cell (see the red rhombus in figure 3.9(c)) and the neighboring P_9 monomers are connected with three bridging Au atoms from the substrate. In each P_9 monomer 6 P atoms are closer to the substrate whereas the remaining 3 P atoms are buckled-up and appear as bright trimers in the experimental STM images. The theoretical height difference between low and high-buckled P atoms is 1.13 Å which is slightly smaller than the buckling height in free standing β-P. [40]

Evidences in support of the porous Au-P framework model: growth mechanism

The Au-decorated phosphorus network model provides a more veritable picture that can even account for a series of experimental findings commonly observed in the STM images.

For example, the large scale STM image of figure 3.10(a) shows the typical "cavity-on-Au(111) terrace" morphology obtained after the deposition of one monolayer of phosphorus on Au(111). This surface morphology does not correspond to the formation of a second layer on top of the first one, as documented by the high-resolution STM image and by the line profile in figure 3.10(b), that shows a step height corresponding exactly to a monoatomic Au terrace of 0.25 nm. The formation of such cavities is caused by the growth mechanism of the (5x5) phosphorus hexagonal structure. As documented by Tian et al [39] and recently discussed by Zhang et al [51], the growth process can be understood in terms of a phosphorus driven Au etching pathway. Specifically, the Au atoms needed for the formation of the Au-decorated phosphorus network may come preferentially from two locations: the surface steps of the Au(111) substrates or the "elbow" sites of the Au herringbone reconstruction inside the Au terraces. The gold atoms on the step edges are less coordinated and, therefore, easily desorbed diffusing across the gold terraces until they coalesce into other Au layers or become part of the bridging sites between P_9 monomers. Consequently, the growth process significantly reshapes the Au terraces transforming the edges from straight lines into concave lines. This effect can be clearly noticed in the large scale STM image in figure 3.5(b). Moreover, Au atoms at the "elbow" sites of the herringbone reconstruction are easily displaced out from the gold surface and can either create a cavity or be substituted by other P atoms. The missing gold atoms at the "elbow" sites of the herringbone reconstruction, in turn, induce a structural transformation of the Au(111) surface in a "network of trigons". The modification of the Au(111) herringbone reconstruction in a "network of trigons" is highlighted with red arrows in the STM image of figure 3.10(c) showing also a (5x5) phosphorus hexagonal superstructure in a sub-monolayer coverage regime. At the "elbow" sites of each trigon there are missing gold atoms (not visible in the room-temperature STM image). Thus, in the proposed growth model for the (5x5)

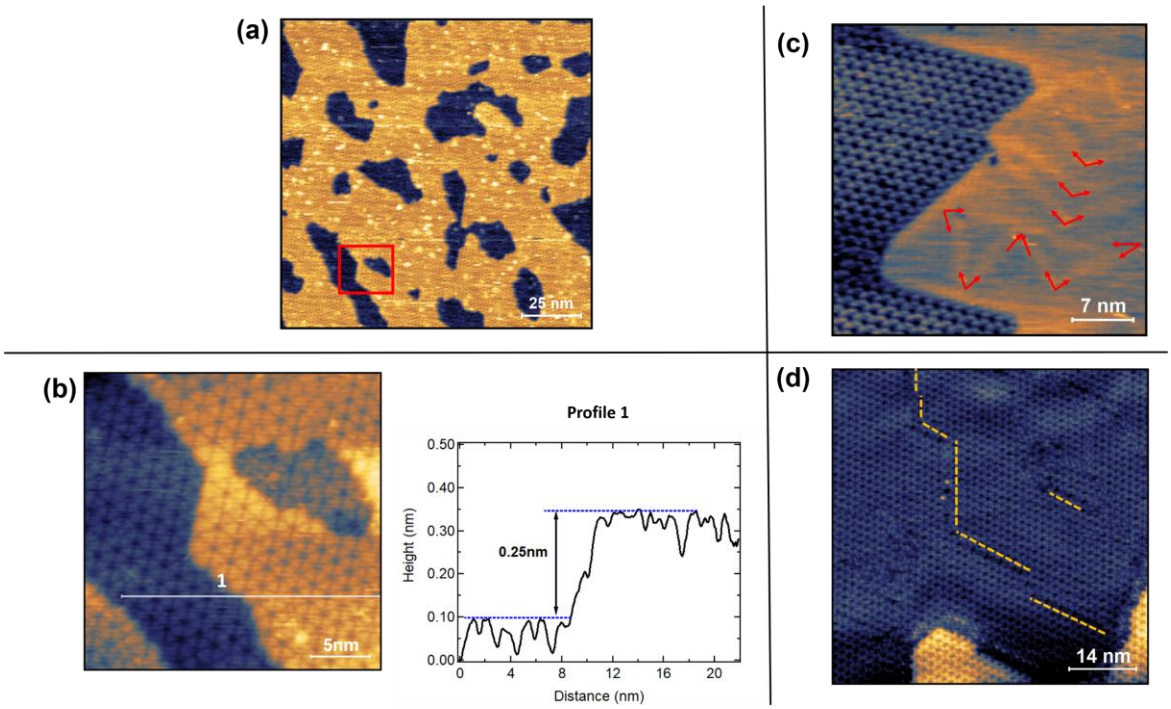

Figure 3.10 (a) Large scale STM image (130x130) nm^2 and **(b)** magnified (red box) STM image (25x25) nm^2 ($\boldsymbol{U_T}$=1.2 V, $\boldsymbol{I_T}$=0.3 nA) of the "cavity-on-terrace" morphology observed on the Au(111) terraces after the growth of the (5x5) phosphorus hexagonal superstructure. The line profile shows a height corresponding to a single Au monoatomic step. **(c)** STM image (35x35) nm^2 of the Au(111) surface ($\boldsymbol{U_T}$=-0.74 V, $\boldsymbol{I_T}$=1.1 nA) at sub-monolayer coverage showing the modification of the herringbone reconstruction in a "network of trigons" (red arrows) close to a (5x5) hexagonal P island. The deposition parameters for the sub-monolayer growth are: 2min 30sec exposure time at p=1.7x10^{-8} mbar **(d)** STM image (65x65) nm^2 showing the existence of dislocation lines and defects (indicated by the yellow dashed lines) in (5x5) phosphorus hexagonal superstructure.

phosphorus hexagonal superstructure, the nucleation occurs mainly in two locations: inside the gold terraces (at the elbow sites of the Au herringbone reconstruction) or at the Au(111) step edges.[51] The initial nuclei for the growth of the (5x5) hexagonal flowerlike structures have been investigated in the sub-monolayer growth regime by Xu et al.[41]. The formation of 1D phosphorus chains and of phosphorus patches with hexagonal symmetry (described by a $(\sqrt{3}\times\sqrt{3})R30°$ superstructures) is favored in the early stages of the growth process at sub-monolayer coverage regimes. These initial structures become the nuclei for the growth of the more stable (5x5) phosphorus hexagonal islands. The latter, upon further phosphors exposure grow rapidly consuming P atoms from the surrounding 1D P-chains and $(\sqrt{3}\times\sqrt{3})R30°$ patches and simultaneously etch the gold substrate along the step edges and the "elbow" sites of the herringbone reconstruction. Finally, when all the (5x5) phosphorus hexagonal islands coalesce together a continuous flowerlike pattern is created on the whole Au(111) sample. This pattern may be characterized by the presence of some defects such as dislocation lines. The latter occur along the joint boundaries between coalesced (5x5) phosphorus hexagonal islands and are clearly visible in the STM images as stripes with a darker color: see figure 3.10(d).

Evidences in support of the porous Au-P framework model: high-P coverage morphology

Another experimental observation that the Au-decorated phosphorus network model can account for is the change in the STM images upon further P exposure. In particular, Zhao et al

[40] have proven that P_4 molecules are mainly adsorbed on the top of the central pores of the (5x5) phosphorus hexagonal superstructure producing STM images characterized by very bright spots in-place of the dark hollow-sites of the flowerlike pattern. A P cluster adsorbed in the central pore of a phosphorus hexagonal structure can be noticed even in the STM image of figure 3.10(b) (indicated by the blue arrow). The possibility to host foreign atomic species in the hollow sites of the Au decorated phosphorus network offers compelling direction for the realization of functional interfaces built from ordered 2D nanostructures.

Evidences in support of the porous Au-P framework model: defective areas

Finally, the structures with 6-bright protrusions seldom observed in the STM images (see the green rhombus in the STM image of figure 3.9(b)), can be also understood in terms of the Au-decorated phosphorus network model as caused by defective areas consisting of P_{16} blue-P fragments instead of the more usual P_9 monomers. The presence of P_N blue-P fragments with N>9 concomitantly reduces the number and the size of the pores (dark hollow sites) observed in the (5x5) phosphorus hexagonal structure envisaging a possible method to control their density. For example, Zhou et al [52] have recently demonstrated that co-depositing the P-precursor with fullerene (C_{60}) molecules allows to fabricate a (5x5) phosphorus hexagonal superstructure on Au(111) characterized by a low density of pores and P_N fragments showing mostly 6 and 10 protrusions in the STM images.

Despite the Au-decorated phosphorus network model can explain many of the observed features in the STM images there is still an ongoing debate on the real atomic structure for the (5x5) hexagonal phosphorus superstructure on Au(111) that is also motivated by contrasting experimental evidences on its electronic structure, as we will briefly report in the following.

3.4.4 The 2D nature and the electronic structure of epitaxial phosphorus on gold.

According to the Au-decorated phosphorus network model, the (5x5) flowerlike superstructure observed on Au(111) cannot be identified as an epitaxial reconstruction of the freestanding 2D β-P (blue-phosphorene) lattice and, therefore, unlike the case of silicene on Ag(111) or of germanene on Au(111), cannot be considered as an epitaxial Xene in the sense of the definition given in Chapter 1. Rather, the (5x5) phosphorus superstructure on gold should be seen as a gold-phosphorus porous framework consisting of 2D β-P domains (or clusters) decorated by Au atoms. The stronger interaction between the P atoms and the Au atoms in this *porous* P-Au framework inhibits the formation of a continuous 2D epitaxial blue-phosphorene lattice giving to the entire system a metallic character, as reported by the band structure calculations performed in refs.[39], [40]

However, the metallicity predicted for the P-Au porous network is in marked contrast with the early experimental reports on the band structure of this system obtained from ARPES (Angle Resolved Photoelectron Spectroscopy) and from STS (Scanning Tunneling Spectroscopy) measurements. In particular, ARPES evidences have shown that this system is semiconducting[43], [44] and its band structure can be correctly reproduced by assuming an atomic model based on a 2D blue-phosphorene epilayer consisting of connected P_{16} islands.[42] Moreover, STS measurements [28], [50], [52] proved that the phosphorus flowerlike structure on Au(111) possesses a local semiconducting character with an experimental bandgap of $\sim 1eV$,

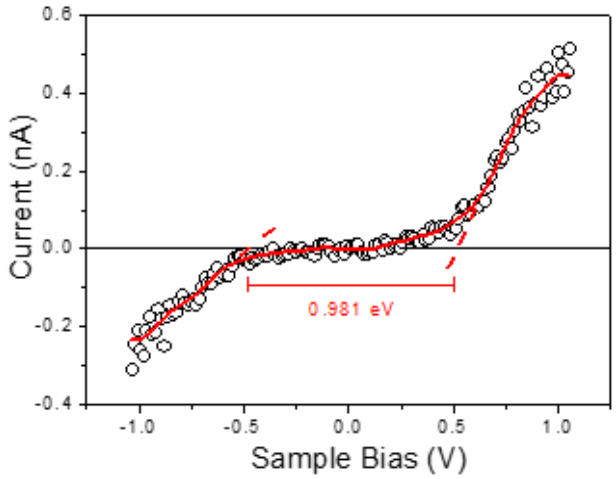

Figure 3.11 Average I(V) curve measured by STM from -1 to 1 V on epitaxial phosphorene grown on Au(111) showing a bandgap of 0.981 eV. Adapted from reference [49]

i.e. much lower than the 2.65 eV value calculated for freestanding 2D β-P. This semiconducting character is also clearly discernible in figure 3.11 that reports the average I(V) curves measured in different locations of the (5x5) phosphorus Au(111) superstructure during the STM imaging.

Conclusions

Although more research is needed to disentangle the true electronic structure and, therefore, the correct atomic model of the (5x5) phosphorus hexagonal epilayer on Au(111), its nature is undoubtedly 2D when considered from the point of view of the energy band dispersion [42]
In this respect and in close similarity with the case of 2D epitaxial Xenes, the electronic structure of the (5x5) hexagonal phosphorus epilayer on Au(111) could be eventually engineered through atomic manipulation and/or surface functionalization fostering at least two intriguing directions for forthcoming researches.

i. On one hand, the porous atomic structure of the (5x5) phosphorus hexagonal epilayer on Au(111) provides a way to weaken the interaction with the substrate by exploiting the intercalation process of foreign atomic species. Recent researches have proved that this is indeed possible using tellurium or silicon buffer layers[37], [51] or via intercalation of potassium atoms.[53]
ii. On the other, the long-range order of the porous phosphorus-Au network, either viewed as a P_2Au *Blue-P-Au alloy*[54] or as a disconnected β-P (blue-phosphorene) layer, offers a fascinating possibility to control with atomic accuracy the positioning of foreign molecules or atomic species at ordered sites so to create aligned nano-structures in two dimension or to tailor the features of the electronic band structure. Interesting attempts along this way contemplate the surface functionalization by fullerene or water adsorption[50], [52] or the design of kagome lattices with unusual flat band dispersion by adsorption of potassium atoms.[54]

Bibliography

[1] C. Grazianetti, C. Martella, and A. Molle, "The Xenes Generations: A Taxonomy of Epitaxial Single-Element 2D Materials," *physica status solidi (RRL) – Rapid Research Letters*, p. 1900439, Oct. 2019, doi: 10.1002/pssr.201900439.

[2] A. Molle, C. Grazianetti, L. Tao, D. Taneja, Md. H. Alam, and D. Akinwande, "Silicene, silicene derivatives, and their device applications," *Chemical Society Reviews*, vol. 47, no. 16, pp. 6370–6387, 2018, doi: 10.1039/C8CS00338F.

[3] C. Grazianetti, E. Cinquanta, and A. Molle, "Two-dimensional silicon: the advent of silicene," *2D Materials*, vol. 3, no. 1, p. 012001, Jan. 2016, doi: 10.1088/2053-1583/3/1/012001.

[4] R. Arafune *et al.*, "Structural transition of silicene on Ag(111)," *Surface Science*, vol. 608, pp. 297–300, Feb. 2013, doi: 10.1016/j.susc.2012.10.022.

[5] B. Feng *et al.*, "Evidence of Silicene in Honeycomb Structures of Silicon on Ag(111)," *Nano Letters*, vol. 12, no. 7, pp. 3507–3511, Jul. 2012, doi: 10.1021/nl301047g.

[6] A. Fleurence, R. Friedlein, T. Ozaki, H. Kawai, Y. Wang, and Y. Yamada-Takamura, "Experimental Evidence for Epitaxial Silicene on Diboride Thin Films," *Physical Review Letters*, vol. 108, no. 24, Jun. 2012, doi: 10.1103/PhysRevLett.108.245501.

[7] J. Yuhara *et al.*, "Germanene Epitaxial Growth by Segregation through Ag(111) Thin Films on Ge(111)," *ACS Nano*, vol. 12, no. 11, pp. 11632–11637, Nov. 2018, doi: 10.1021/acsnano.8b07006.

[8] G. Li *et al.*, "Stable Silicene in Graphene/Silicene Van der Waals Heterostructures," *Adv. Mater.*, vol. 30, no. 49, p. 1804650, Dec. 2018, doi: 10.1002/adma.201804650.

[9] A. M. Tokmachev *et al.*, "Topotactic synthesis of the overlooked multilayer silicene intercalation compound $SrSi_2$," *Nanoscale*, vol. 8, no. 36, pp. 16229–16235, 2016, doi: 10.1039/C6NR04573A.

[10] A. M. Tokmachev *et al.*, "Engineering of Magnetically Intercalated Silicene Compound: An Overlooked Polymorph of $EuSi_2$," *Adv. Funct. Mater.*, vol. 27, no. 18, p. 1606603, May 2017, doi: 10.1002/adfm.201606603.

[11] S. Hüfner, *Photoelectron spectroscopy principles and applications ; with 28 tables*. 2003.

[12] G. Binnig and H. Rohrer, "Scanning tunneling microscopy—from birth to adolescence," *Rev. Mod. Phys.*, vol. 59, no. 3, pp. 615–625, Jul. 1987, doi: 10.1103/RevModPhys.59.615.

[13] J. Bardeen, "Tunnelling from a Many-Particle Point of View," *Phys. Rev. Lett.*, vol. 6, no. 2, pp. 57–59, Jan. 1961, doi: 10.1103/PhysRevLett.6.57.

[14] J. Tersoff and D. R. Hamann, "Theory and Application for the Scanning Tunneling Microscope," *Phys. Rev. Lett.*, vol. 50, no. 25, pp. 1998–2001, Jun. 1983, doi: 10.1103/PhysRevLett.50.1998.

[15] J. Tersoff and D. R. Hamann, "Theory of the scanning tunneling microscope," *Phys. Rev. B*, vol. 31, no. 2, pp. 805–813, Jan. 1985, doi: 10.1103/PhysRevB.31.805.

[16] C. J. Chen, *Introduction to scanning tunneling microscopy*, 2nd ed. Oxford ; New York: Oxford University Press, 2008.

[17] R. J. Hamers, "Atomic-Resolution Surface Spectroscopy with the Scanning Tunneling Microscope," *Annu. Rev. Phys. Chem.*, vol. 40, no. 1, pp. 531–559, Oct. 1989, doi: 10.1146/annurev.pc.40.100189.002531.

[18] J. A. Stroscio and W. J. Kaiser, Eds., *Scanning tunneling microscopy*. Boston: Academic Press, 1993.

[19] X. Li *et al.*, "Large-Area Synthesis of High-Quality and Uniform Graphene Films on Copper Foils," *Science*, vol. 324, no. 5932, pp. 1312–1314, Jun. 2009, doi: 10.1126/science.1171245.

[20] J. Yu, J. Li, W. Zhang, and H. Chang, "Synthesis of high quality two-dimensional materials via chemical vapor deposition," *Chem. Sci.*, vol. 6, no. 12, pp. 6705–6716, 2015, doi: 10.1039/C5SC01941A.

[21] J. B. Smith, D. Hagaman, and H.-F. Ji, "Growth of 2D black phosphorus film from chemical vapor deposition," *Nanotechnology*, vol. 27, no. 21, p. 215602, May 2016, doi: 10.1088/0957-4484/27/21/215602.

[22] X. Li *et al.*, "Synthesis of thin-film black phosphorus on a flexible substrate," *2D Mater.*, vol. 2, no. 3, p. 031002, Aug. 2015, doi: 10.1088/2053-1583/2/3/031002.

[23] Q. Jiang, L. Xu, N. Chen, H. Zhang, L. Dai, and S. Wang, "Facile Synthesis of Black Phosphorus: an Efficient Electrocatalyst for the Oxygen Evolving Reaction," *Angew. Chem. Int. Ed.*, vol. 55, no. 44, pp. 13849–13853, Oct. 2016, doi: 10.1002/anie.201607393.

[24] C. Li *et al.*, "Synthesis of Crystalline Black Phosphorus Thin Film on Sapphire," *Adv. Mater.*, vol. 30, no. 6, p. 1703748, Feb. 2018, doi: 10.1002/adma.201703748.

[25] Z. Yang *et al.*, "Field-Effect Transistors Based on Amorphous Black Phosphorus Ultrathin Films by Pulsed Laser Deposition," *Advanced Materials*, vol. 27, no. 25, pp. 3748–3754, Jul. 2015, doi: 10.1002/adma.201500990.

[26] J. Gao, G. Zhang, and Y.-W. Zhang, "The Critical Role of Substrate in Stabilizing Phosphorene Nanoflake: A Theoretical Exploration," *Journal of the American Chemical Society*, vol. 138, no. 14, pp. 4763–4771, Apr. 2016, doi: 10.1021/jacs.5b12472.

[27] L. Qiu, J. C. Dong, and F. Ding, "Selective growth of two-dimensional phosphorene on catalyst surface," *Nanoscale*, vol. 10, no. 5, pp. 2255–2259, 2018, doi: 10.1039/C7NR08507A.

[28] J. L. Zhang *et al.*, "Epitaxial Growth of Single Layer Blue Phosphorus: A New Phase of Two-Dimensional Phosphorus," *Nano Letters*, vol. 16, no. 8, pp. 4903–4908, Aug. 2016, doi: 10.1021/acs.nanolett.6b01459.

[29] C. Liu, L. Wang, J. Qi, and K. Liu, "Designed Growth of Large-Size 2D Single Crystals," *Adv. Mater.*, vol. 32, no. 19, p. 2000046, May 2020, doi: 10.1002/adma.202000046.

[30] J. Kang, D. Shin, S. Bae, and B. H. Hong, "Graphene transfer: key for applications," *Nanoscale*, vol. 4, no. 18, p. 5527, 2012, doi: 10.1039/c2nr31317k.

[31] J. Zeng, P. Cui, and Z. Zhang, "Half Layer By Half Layer Growth of a Blue Phosphorene Monolayer on a GaN(001) Substrate," *Physical Review Letters*, vol. 118, no. 4, Jan. 2017, doi: 10.1103/PhysRevLett.118.046101.

[32] N. Han, N. Gao, and J. Zhao, "Initial Growth Mechanism of Blue Phosphorene on Au(111) Surface," *The Journal of Physical Chemistry C*, vol. 121, no. 33, pp. 17893–17899, Aug. 2017, doi: 10.1021/acs.jpcc.7b04209.

[33] P. Vogt *et al.*, "Silicene: Compelling Experimental Evidence for Graphenelike Two-Dimensional Silicon," *Physical Review Letters*, vol. 108, no. 15, Apr. 2012, doi: 10.1103/PhysRevLett.108.155501.

[34] A. J. Mannix *et al.*, "Synthesis of borophenes: Anisotropic, two-dimensional boron polymorphs," *Science*, vol. 350, no. 6267, pp. 1513–1516, Dec. 2015, doi: 10.1126/science.aad1080.

[35] B. Feng *et al.*, "Experimental realization of two-dimensional boron sheets," *Nature Chem*, vol. 8, no. 6, pp. 563–568, Jun. 2016, doi: 10.1038/nchem.2491.

[36] D. Zhou *et al.*, "Epitaxial Growth of Flat, Metallic Monolayer Phosphorene on Metal Oxide," *ACS Nano*, vol. 14, no. 2, pp. 2385–2394, Feb. 2020, doi: 10.1021/acsnano.9b09588.

[37] C. Gu *et al.*, "Growth of Quasi-Free-Standing Single-Layer Blue Phosphorus on Tellurium Monolayer Functionalized Au(111)," *ACS Nano*, vol. 11, no. 5, pp. 4943–4949, May 2017, doi: 10.1021/acsnano.7b01575.

[38] J. L. Zhang *et al.*, "Phosphorus Nanostripe Arrays on Cu(110): A Case Study to Understand the Substrate Effect on the Phosphorus thin Film Growth," *Advanced Materials Interfaces*, vol. 4, no. 14, p. 1601167, Jul. 2017, doi: 10.1002/admi.201601167.

[39] H. Tian *et al.*, "Two-Dimensional Metal-Phosphorus Network," *Matter*, vol. 2, no. 1, pp. 111–118, Jan. 2020, doi: 10.1016/j.matt.2019.08.001.

[40] S. Zhao, J. L. Zhang, W. Chen, and Z. Li, "Structure of Blue Phosphorus Grown on Au(111) Surface Revisited," *J. Phys. Chem. C*, vol. 124, no. 3, pp. 2024–2029, Jan. 2020, doi: 10.1021/acs.jpcc.9b10511.

[41] J.-P. Xu, J.-Q. Zhang, H. Tian, H. Xu, W. Ho, and M. Xie, "One-dimensional phosphorus chain and two-dimensional blue phosphorene grown on Au(111) by molecular-beam epitaxy," *Physical Review Materials*, vol. 1, no. 6, Nov. 2017, doi: 10.1103/PhysRevMaterials.1.061002.

[42] E. Golias, M. Krivenkov, A. Varykhalov, J. Sánchez-Barriga, and O. Rader, "Band Renormalization of Blue Phosphorus on Au(111)," *Nano Letters*, vol. 18, no. 11, pp. 6672–6678, Nov. 2018, doi: 10.1021/acs.nanolett.8b01305.

[43] W. Zhang *et al.*, "Epitaxial Synthesis of Blue Phosphorene," *Small*, vol. 14, no. 51, p. 1804066, Dec. 2018, doi: 10.1002/smll.201804066.

[44] J. Zhuang *et al.*, "Band Gap Modulated by Electronic Superlattice in Blue Phosphorene," *ACS Nano*, May 2018, doi: 10.1021/acsnano.8b02953.

[45] J. A. Meyer, I. D. Baikie, E. Kopatzki, and R. J. Behm, "Preferential island nucleation at the elbows of the Au(111) herringbone reconstruction through place exchange," *Surface Science*, vol. 365, no. 1, pp. L647–L651, Sep. 1996, doi: 10.1016/0039-6028(96)00852-7.

[46] L. Tao *et al.*, "Silicene field-effect transistors operating at room temperature," *Nature Nanotechnology*, vol. 10, no. 3, pp. 227–231, Feb. 2015, doi: 10.1038/nnano.2014.325.

[47] M. T. Edmonds *et al.*, "Creating a Stable Oxide at the Surface of Black Phosphorus," *ACS Applied Materials & Interfaces*, vol. 7, no. 27, pp. 14557–14562, Jul. 2015, doi: 10.1021/acsami.5b01297.

[48] A. I. Kovalev, D. L. Wainstein, D. I. Tetelbaum, W. Hornig, and Yu. N. Kucherehko, "Investigation of the electronic structure of the phosphorus-doped Si and SiO2:Si quantum dots by XPS and HREELS methods," *Surf. Interface Anal.*, vol. 36, no. 8, pp. 959–962, Aug. 2004, doi: 10.1002/sia.1811.

[49] C. Grazianetti, G. Faraone, C. Martella, E. Bonera, and A. Molle, "Embedding epitaxial (blue) phosphorene in between device-compatible functional layers," *Nanoscale*, vol. 11, no. 39, pp. 18232–18237, Oct. 2019, doi: 10.1039/C9NR06037E.

[50] N. Si *et al.*, "Imaging and Dynamics of Water Hexamer Confined in Nanopores," *ACS Nano*, vol. 13, no. 9, pp. 10622–10630, Sep. 2019, doi: 10.1021/acsnano.9b04835.

[51] J. L. Zhang *et al.*, "Synthesis of Monolayer Blue Phosphorus Enabled by Silicon Intercalation," *ACS Nano*, vol. 14, no. 3, pp. 3687–3695, Mar. 2020, doi: 10.1021/acsnano.0c00822.

[52] D. Zhou *et al.*, "Defect Generation and Surface Functionalization on Epitaxial Blue Phosphorene by C_{60} Adsorption," *J. Phys. Chem. C*, p. acs.jpcc.9b03344, May 2019, doi: 10.1021/acs.jpcc.9b03344.

[53] Y. Liu *et al.*, "Reversible Potassium Intercalation in Blue Phosphorene–Au Network Driven by an Electric Field," *J. Phys. Chem. Lett.*, vol. 11, no. 14, pp. 5584–5590, Jul. 2020, doi: 10.1021/acs.jpclett.0c01835.
[54] S. Sun *et al.*, "Designing Kagome Lattice from Potassium Atoms on Phosphorus–Gold Surface Alloy," *Nano Lett.*, vol. 20, no. 7, pp. 5583–5589, Jul. 2020, doi: 10.1021/acs.nanolett.0c02426.

CHAPTER 4

Oxidation and stabilization of 2D phosphorus

4.1 Oxidation of 2D phosphorus allotropes.

The high reactivity predicted and observed for 2D phosphorus allotropes in ambient conditions is inherently related to the buckling of their crystalline lattice and to the presence of lone pairs of electrons on the surface (see Chapter 1). This chemical instability is one of the major concerns during the processing of 2D phosphorus along the steps of any device integration scheme. In order to prevent these issues, a detailed understanding of the mechanisms governing the oxidation and the development of proper passivation and encapsulation strategies are mandatory tasks for any use of 2D phosphorus allotropes in operational device configurations. In the case of the 2D α-phase (i.e. single layer phosphorene) these two aspects have been the subject of extensive theoretical and experimental investigations that have allowed to get a better understanding of the role played by different oxidizing agents in its degradation and have also delineated the most effective encapsulation strategies to prevent it. However, in the case of the 2D β-P phase (blue phosphorene) there is still a paucity of research on both these aspects which in turn is responsible for a lack of progress towards the integration of this material in functional devices.

In this paragraph we will report on the oxidation mechanism and on the limited environmental stability of 2D β-P (blue phosphorene) considering specifically the case of 2D phosphorus grown by epitaxy on Au(111) substrates. The results obtained have been compared also with those already known in literature for few layers phosphorene (α-P) which will be briefly reviewed in the following section. Despite the fact that the atomic structure of 2D epitaxial phosphorus on Au(111) is still object of debate and an exact identification with epitaxial 2D β-P (blue phosphorene) may not be entirely appropriate, a better understanding of its chemical reactivity is demanded in order to guarantee development of suitable encapsulation strategies that allow the accessibility of this epitaxial material to “ex-situ” characterization and manipulation techniques.

4.1.1 Oxidation of few and monolayer phosphorene

Although black phosphorus (BP) is the most thermodynamically stable allotrope of phosphorus, few and single layer BP (or phosphorene) are not chemically inert and can be easily oxidized in air. This issue affects the performances of BP-based electronic devices degrading, for example, the field effect mobility and the On/Off ratio of FET transistors based on nm-thick BP channels. [1]–[3]

Experimental investigation of the air degradation of phosphorene.

Experimentally the deterioration of exfoliated BP flakes is observed soon after the preparation with the appearance of topographic bubble-like features on the surface of the samples with a density that increases with the time. The small protrusions developed on the surface of a tape-exfoliated BP flake can be clearly distinguished in the AFM image reported in figure 4.1(a) and have an apparent height that can exceed even the flake thickness (see the inset line profile). After some time, these bubbles start to coalesce together increasing their volume and becoming in this way visible under the optical microscope. This process is typically quicker for thinner samples (~1 hour after the exfoliation) and slower (~after 1-5 days) for samples thicker than

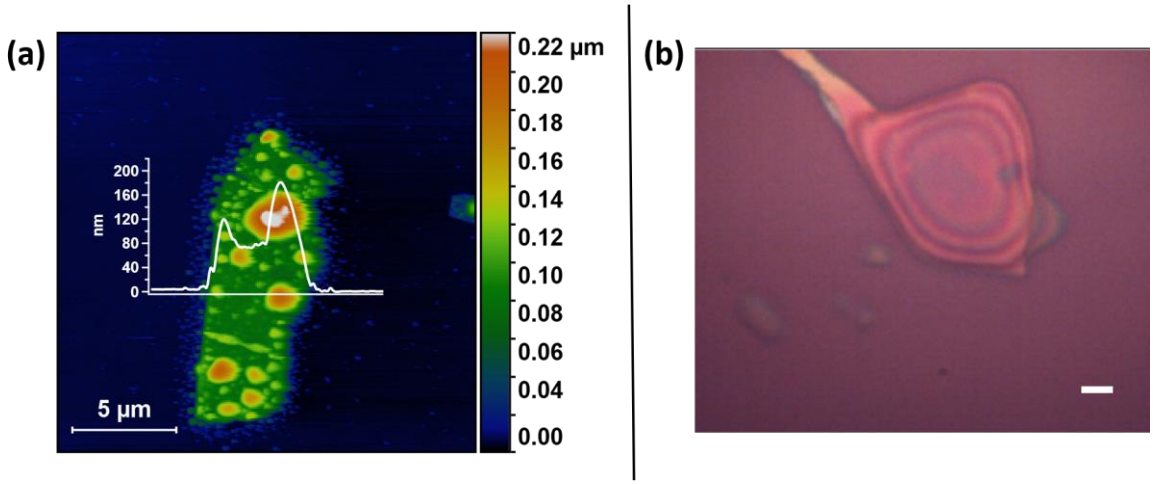

Figure 4.1 Degradation of BP flakes exposed to air. **(a)** AFM image (20x20) μm^2 of the surface of a tape-exfoliated BP flake after few days of air-exposure showing the formation of bubble-like protrusions. **(b)** Optical microscope image of a tape exfoliated BP flake after prolonged air exposure showing the formation of a single droplet-like feature on the flake surface.

20-30 nm.[4]–[6] Another commonly observed effect is the etching of the BP surface starting from the thinner edges of the sample and extending after many days of air exposure (>20 days) on larger areas of the sample surface. The latter typically become fully covered by a single droplet-like bubble as illustrated by the optical microscope image in Figure 4.1(b).

Contact angle measurements performed on water droplets in contact with the surface of exfoliated BP flakes have demonstrated that the pristine (freshly cleaved) BP surface is naturally hydrophobic and become hydrophilic only after the exposure to O_2 dissolved in water.[7] Therefore, these experiments have suggested that the bubble-like protrusions observed on the BP surface after air exposure could be caused by the condensation of H_2O droplets on the strongly oxidized (super-hydrophilic) regions of the flake surrounded, in the early stages of the degradation process, by more hydrophobic (less oxidized) zones. The air-degradation of BP involves also the production of acidic species such as phosphoric acid and other acids as demonstrated by the decrease in the pH of liquid solutions of suspended BP flakes prepared by liquid phase exfoliation. [8] Phosphoric acid species, however, are volatile and together with water adsorbates can be easily removed from the surface of air-degraded BP flakes by vacuum annealing treatments.[9] The etching dynamic of exfoliated BP flakes upon air exposure has been documented also with the aid of Raman spectroscopy by investigating the intensity modulation of the BP spectra acquired during successive stages of the degradation process. [10], [11], [6] Raman spectroscopy experiments have also proved that the light exposure plays an important role in the air degradation mechanism of BP expediting the oxidation reaction. [10] In particular, BP flakes under UV (248 nm) and blue illumination have shown the fastest degradation rates.[12]

Theory of the air degradation mechanism of phosphorene

The experimental picture t described above is that the air degradation mechanism of BP can be considered as a thickness-dependent photo-assisted oxidation reaction in which the main players are oxygen, water and light. The contribution of each of these factors has been actively debated in literature with many studies sometimes in disagreement with each other.

The most commonly accepted theory for the degradation of BP in air has been laid down in two theoretical works by Ziletti et al [13] and Zhou et al[14] and in the experimental study of Favron et al [10] According to these authors, the pristine (defect-free) surface of BP is unable to be chemically attacked by water molecules alone and the proposed mechanism for its degradation involves a multistep reaction pathway:

$$\begin{aligned} BP + h\nu &\leftrightharpoons BP^* && (a) \\ BP^* + O_2 &\rightarrow O_2^- + h^+ && (b) \\ O_2^- + h^+ + BP &\rightarrow P_xO_y && (c) \end{aligned} \qquad (4.1)$$

Initially the O_2 molecule is only physisorbed on the BP surface and the light illumination ($h\nu$) creates electron-hole pairs (a). A photogenerated electron can be transferred from the conduction band of BP to a physisorbed O_2 molecule generating a superoxide anion O_2^- and a positive hole h^+ in the valence band of BP(b). Normally the ground state of O_2^- is a triplet state but since the molecule is closer to the BP surface the interaction with the BP lone pairs lifts the ground-state degeneracy so that the singlet state becomes the most stable.[13] The oxidation reaction between the p-doped BP and the singlet O_2^- anion is energetically favored enabling the O_2^- dissociation and the chemisorption of oxygen atoms on the BP surface (c). The most stable configuration for the two chemisorbed oxygen atoms is given by the formation of dangling $P-O$ bonds tilted of 44.5°away from the BP surface in the direction of the electron's lone pairs. The dangling O atoms make the entire BP surface more hydrophilic favoring the formation of hydrogen bonds with adventitious water molecules. The water molecules draw the chemisorbed oxygen out the surface and concomitantly lift the connected P atoms leading to the dissolution of the top BP layers and, hence, to the observed ambient air etching process. The faster etching rate observed on thinner BP flakes exposed to air compared to thicker ones can be explained by the fact that the former have a wide energy bandgap lying in the visible region of the electromagnetic spectrum. Consequently, in thinner BP flakes the generation of excitons (i.e. bounded electron-hole pairs) under visible light illumination occurs with a higher rate and promotes the formation of many superoxide O_2^- anions that accelerate the degradation process.

The above-discussed model shows that the only prerequisite to trigger the BP oxidation is the exposure to light (with a proper wavelength). However, this assumption is still controversial and under debate. Other theoretical studies[15] have suggested a different degradation mechanism in which the oxidation of BP can occur spontaneously (i.e. not necessarily in presence of light) at room temperature and it is followed by the reaction of the oxides species (mainly P_3O_6 and P_4O_{10}) with water to produce phosphoric acids (H_3PO_4) and a defective phosphorene lattice at the surface of BP. Additionally, other experimental evidences have proven that it is also possible to oxidize BP with water and oxygen alone in a completely dark environment following a water-catalyzed (instead of a "light-exposure catalyzed") oxidation reaction.[16] According to this model the co-adsorption of water with oxygen on the BP surface promotes the electron transfer process to the oxygen molecule leading to the formation of surface oxides.

Investigation of the degradation of phosphorene after exposure to single oxidants

Clearly, all the previous explanations for the air degradation of BP are reasonable and it is likely that the global process is a result of the mutual effects of several competitive oxidation channels. In order to clarify and separate the contributions of each mechanism some

experimental studies have specifically addressed the effects of single oxidant species (oxygen or water) considered alone. In this respect, it has been shown that BP exposed to deoxygenated water can also be partially oxidized although at a much slower rate. [17]–[20] The oxidation of BP in water, although extremely unlikely on the pristine (defect-free) surface of BP, becomes possible in presence of defect sites such as steps edges or grain boundaries that are characterized by phosphorus atoms in unstable bonding configurations that can easily react with the water molecules.[20] The effects of the exposure of BP to pure molecular oxygen, instead, has been studied both in dark and light illumination conditions.[21] It has been observed that a prolonged exposure to molecular O_2 in dark condition leads to the formation of physisorbed oxygen only on the BP surface. In such conditions the probability for the oxygen dissociation and chemisorption is strongly suppressed. However, light illumination lowers the dissociation barrier leading to the formation of phosphorus suboxide species, PO_x, characterized by oxidation states P^{+x} with x=+3 or x<5.[19], [21] The formation of more stable phosphorus pentoxide compounds, P_4O_{10}, instead, seems to be kinetically hindered under pure oxygen exposure.[19] This stable oxide seems to form only with the concomitant presence of water, as documented by Edmonds et al [22] on bulk BP flakes and after a prolonged exposure to ambient-air conditions.

2D Phosphorus oxides

In general, the possibility to control the formation of a stable oxide on the surface of BP is a technologically relevant aspect since these oxides can be used as a protective encapsulation that prevents the further degradation of the sample. However, the degradation process in environmental conditions caused by the action of the water and oxygen on few layer phosphorene is generally too quick to allow the formation of stable oxide. The oxidation process of few layer phosphorene in pure O_2 environments, instead, has revealed promising potentialities in this respect. For example, Pei et al [23] have documented the fabrication of air-stable, i.e. chemically protected, mono and few layer phosphorene samples by forming P_xO_y oxides on their surface with plasma treatments in O_2 atmosphere.

Envisaging controllable oxidation processes for few layer and monolayer phosphorene (2D α-P) samples is a step further towards the chemical functionalization of this material opening, at the same time, a pathway for the realization of 2D phosphorus oxides. The oxidation studies presented in the next paragraph for the epitaxial phosphorus grown on gold (111) complete this picture providing also the preliminary insights into the chemical reactivity of the 2D β-P (blue phosphorene) phase which could be of general validity for all the 2D phosphorus allotropes.

4.1.2 Oxidation of epitaxial phosphorus on gold

Like silicene (but to a different extent), epitaxial phosphorus on Au(111) is unstable and quickly oxidizes when exposed to air. Its stability is elucidated in the comparative XPS study of Figure 4.3 where the P2p core level photoemission line is reported for a freshly grown sample (bottom) and after 10min of exposure to ambient air (top). As can be noticed from the permanence of the elementary P-P bonding component at 129.4 eV epitaxial phosphorus on gold partially survives after air exposure but the appearance of an extra component peaked at 134.0 eV suggests the presence of phosphorus atoms having higher oxidation states.

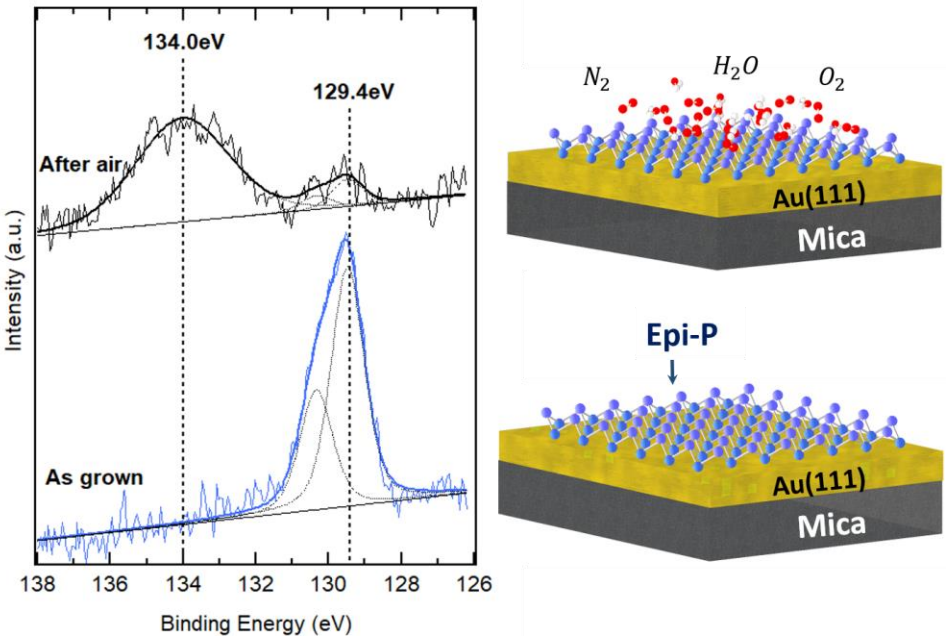

Figure 4.3 Comparison between the XPS P2p core level peaks of pristine (as-grown) epitaxial phosphorus and after 10 min exposure to ambient air.

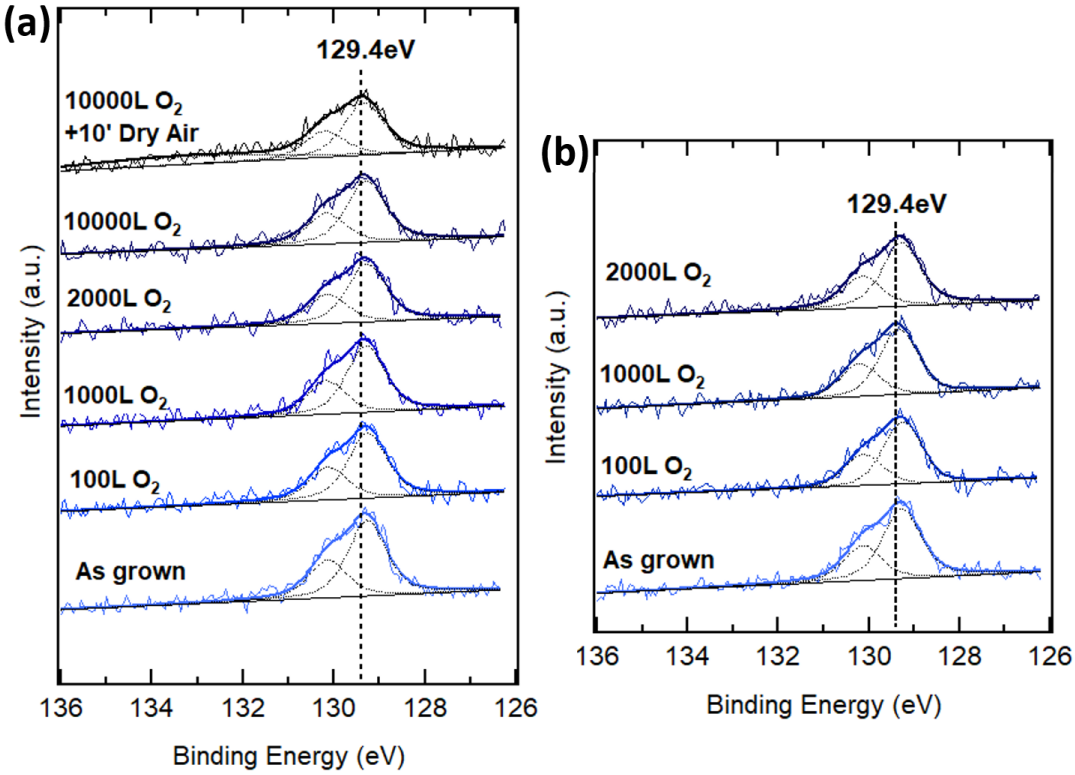

Figure 4.2. XPS investigation of the oxidation process of epitaxial phosphorus on gold. **(a)** P2p core level spectra obtained after O_2 exposure at partial pressure 1.3×10^{-6} mbar. The topmost P2p spectrum is obtained after 10' dry air exposure of the same sample. **(b)** P2p core level spectra after O_2 exposure at partial pressure 1.3×10^{-7} mbar.

The large FWHM of this higher binding energy component extending from 132 eV to 136 eV is a signature of the presence of P_2O_5, P_2O_3 oxides and P_2O_x suboxides with x<3[24] characterized by multiple $P-O$ and $P=O$ bonding states in analogy to what has already been reported in the case of air-exposed few layer phosphorene. [19], [20]

In-situ and Ex-situ XPS investigation of the oxidation of epitaxial phosphorus

Oxygen is known to play an important role in the preliminary stages of phosphorene (2D α-P) oxidation, but as seen in the previous paragraph it does not lead alone to the complete physical degradation of its puckered crystalline structure in ambient air. In order to unravel the oxidation mechanism of blue-phosphorene (2D β-P) in comparison to the one occurring in phosphorene (2D α-P), we have investigated the chemical reactivity of epitaxial phosphorus grown on gold to in-situ oxygen dosing and subsequently to ex-situ dry-air exposure.

Figure 4.2 shows the evolution of the core level P2p spectra with increasing oxygen dosage (expressed in Langmuir $1L = 1.3 \times 10^{-6}\ mbar \cdot s$) from 100 L to 2000 L. Two experiments were carried out: in the first one the O_2 partial pressure was set to 1.3×10^{-7} mbar, figure 4.2(b), whereas in the second one the O_2 partial pressure was set to 1.3×10^{-6} mbar, figure 4.2(a). The sample in the latter experiment was also exposed to an additional O_2 dosage of 10000 L followed by an ex situ dry air (i.e. O_2 + N_2 with low water vapor content) exposure of 10 min. Limited to our survey, we have noticed that as the oxygen dosage was increased no higher binding energy component appeared in the P2p XPS spectra indicating an exceptional endurance of epitaxial phosphorus to oxidation. This fact stands in marked contrast with the case of epitaxial silicene on Ag(111) that has been reported to be fully oxidized after an oxygen exposure of 100 L-600 L. [25]–[27] The higher chemical reactivity of silicene on Ag(111) compared to that of epitaxial phosphorus on Au(111) stems from the mixed sp^2/sp^3 hybridization of the Si atoms possessing unsaturated dangling bonds that quickly react with oxygen molecules. Interestingly our experiments have shown also that a subsequent short-term exposure of epitaxial phosphorus to dry air did not fully oxidize the pristine epitaxial layer. However, the appearance of a low-intensity peak in the binding energy range between 132 eV and 134 eV (see figure 4.2(a)) denoted the formation of oxide species characterized by phosphorus atoms in low oxidation states. It is likely that a pure Nitrogen atmosphere is effective in preventing the formation of such oxide species on the un-protected epitaxial phosphorus layer. However, we conclude that, compared to a short-term ambient air exposure, a short-term dry-air exposure is not able to induce the formation of stable P_2O_5 phosphorus oxides species on the surface of the epitaxial phosphorus.

STM investigation of the oxidation of epitaxial phosphorus

At a more fundamental level, the presence of phosphorus oxides after a short-term dry air exposure suggests that the interaction between the oxygen molecules and the epitaxial phosphorus layer occurs via a chemisorption process rather than via a physisorption process. The latter seems to be unlikely although possible at very low oxygen dosages (below 2000 L). An analogous conclusion about the nature of the interaction between oxygen and epitaxial phosphorus has been drawn recently in a paper by Zhang et al.[28] In their study, the authors exposed epitaxial phosphorus on gold to much higher oxygen dosages compared to those employed in our experiments and observed the appearance of a 134 eV phosphorus oxide peak

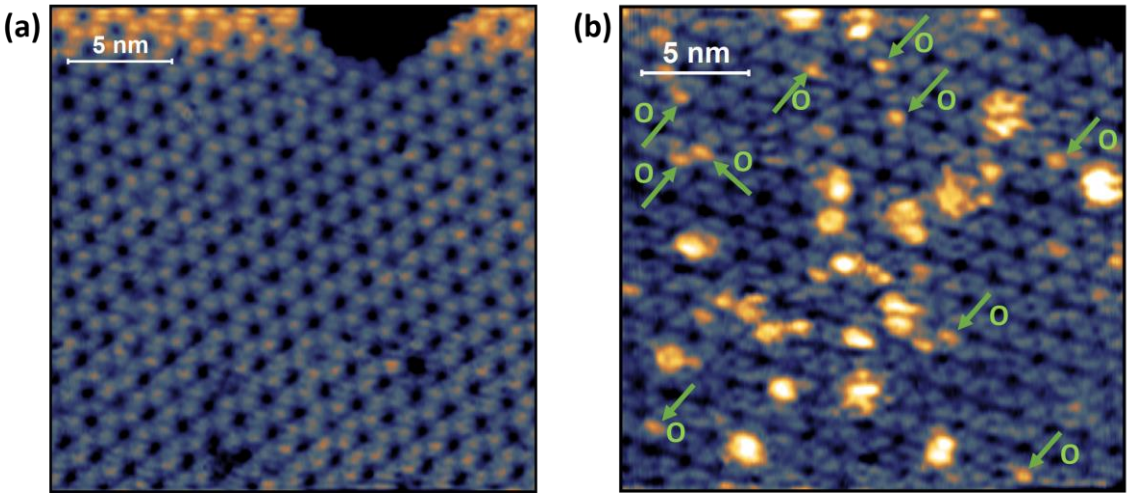

Figure 4.4. (a) STM image (23x23) nm^2 ($\boldsymbol{U_T}$=1.3 V, $\boldsymbol{I_T}$=0.34 nA) of the pristine surface of epitaxial phosphorus on gold before the oxidation. (b) STM image (23x23) nm^2 ($\boldsymbol{U_T}$=1.7 V, $\boldsymbol{I_T}$=0.23 nA) of the surface of the same sample after exposure to 2000 L O_2. Chemisorbed Oxygen atoms are indicated by green arrows. Phosphorus Deposition parameters: 5 min at 2.3x10^{-8} mbar, O_2 partial pressure:1.3 x10^{-7} mbar.

in the P2p XPS spectra. By a detailed in-situ STM and nc-AFM analysis the authors revealed that the chemisorbed oxygen atoms preferentially adsorb on top of one of the three buckled-up phosphorus atoms within each single petal (i.e. a P_9 island according to the atomic model presented in Chapter 3) of the flowerlike pattern of epitaxial phosphorus on gold. These findings agree well with the results of theoretical calculations that have investigated [13], [15] the interaction of oxygen with 2D α-P and 2D β-P. In the latter case, the calculations predicted that the most stable configuration for oxygen chemisorption to 2D β-P implies the formation of a dangling $P = O$ bond on the top sites of phosphorus atoms, i.e. along the direction of the lone electron pair, in agreement with the results of Zhang et al.[28] The interaction pathway between oxygen and epitaxial phosphorus is probably analogous to the one discussed previously for few layers phosphorene[14] and involves the triplet-to-singlet conversion of the approaching oxygen molecule with the subsequent dissociation of the oxygen atoms and formation of the chemical bonds. At higher oxygen dosages the authors also observed the formation of disordered bright protrusions on the whole surface of the epitaxial phosphorus layer possibly caused by oxygen atoms clustered together. The evolution towards such surface morphology can be clearly noticed in the STM images presented in figure 4.4, before (a) and after (b) 2000L of O_2 exposure. As can be seen in figure 4.4(b), besides the presence of bright protrusions, probably corresponding to oxygen atoms clusters, there are also small bright spots (denoted by green arrows) located at various position on the petals of the flowerlike phosphorus pattern. Following Zhang et al [28] we identify these spots with oxygen atoms adsorbed to the surface of epitaxial phosphorus on gold. Furthermore, we notice that the oxidation of epitaxial phosphorus on gold with elevated oxygen dosing (above 2000 L) does not permanently degrade the crystalline quality of the epitaxial layer in contrast to what has been reported in literature for epitaxial silicene on Ag(111). In the latter case, the oxidation completely destroys the crystalline epitaxial layer that acquires an amorphous appearance and, concomitantly, leaves some areas of the bare Ag(111) substrate exposed.[26], [29] Conversely, as firstly observed by Zhang et al [28], the oxidation process of epitaxial phosphorus in O_2 environment seems to be

reversible. A high temperature annealing help to fully recover the crystalline quality of the pristine epitaxial phosphorus layer.

All these experimental evidences reveal a peculiar oxidation chemistry of epitaxial phosphorus on gold which is different from that of silicene on Ag(111). Accurate investigations are, however, still needed to fully understand the oxidation mechanism and to resolve open questions such as the chemical reactivity with water, alone or in combination with oxygen, as well as the influence of the exposure to light which, in the case of few layer phosphorene (2D α-P), seems to catalyze a quicker oxidation reaction.

Bandgap engineering of epitaxial phosphorus oxides

From a scientific point of view a better control of the oxidation process of 2D epitaxial phosphorus on gold opens a pathway to achieve the on-demand modulation of its electronic properties. In this respect, the studies on the oxidation of epitaxial silicene on Ag(111) have shown the possibility to modulate the band structure of this material from semi-metallic to semiconducting (with an average bandgap of 0.18 eV)by controlling the oxygen dosing.[26] In the case of 2D phosphorus, theoretical calculations[30] have suggested that a fully oxidized form of 2D β-P (blue-phosphorene) phase can exhibit strain tunable quantum phase transitions in which the charge carriers could behave according to novel 2D quantum properties. However, preliminary scanning tunneling spectroscopy (STS) measurements performed on oxidized epitaxial phosphorus on gold by Zhang et al [28] indicate that the adsorption of oxygens atoms in a dangling configuration is not sufficient to lead to a significant modification of the band structure in this epitaxial material. Clearly this leaves an open framework where to carry out further research aiming to uncover the full scientific and technological potential of phosphorus oxides at the 2D level.

4.2 Stabilization of 2D phosphorus

As seen in the previous paragraph both exfoliated phosphorene and epitaxial phosphorus on gold quickly degrade upon exposure to ambient air if their surface is not protected with an encapsulating or passivating layer. Clearly, this fact poses a severe problem for all the potential applications of 2D phosphorus in the semiconductor technology and requires the development of “ad-hoc” protection strategies.

4.2.1 Stabilization strategies for few and monolayer phosphorene

In the case of few layer phosphorene, depending on the final application, different approaches for the encapsulation or passivation of the surface have been adopted.

For example, as seen in Chapter 1, the immediate protection from ambient air exposure of freshly exfoliated phosphorene flakes has been achieved by spin-coating in an inert atmosphere on the surface of the samples polymer films such as parylene, PMMA or polymer resists.[10], [31]–[33] Although such approaches are able to achieve a durable protection from the air-degradation, they are not always compatible with a direct integration of phosphorene into device architectures. In this respect, considering the specific integration of exfoliated phosphorene in

ultra-scaled 2D FET transistors, any stabilization strategy should be designed so to satisfy the following three requirements:

(i) Be an effective barrier for the diffusion of the oxidant chemical species (such as water and oxygen) towards the surface of the phosphorene layer;

(ii) Be transparent in the visible range of the electromagnetic spectrum so to allow the optical monitoring (for example, via optical microscopy or Raman spectroscopy) of the material integrity in all the subsequent phases of its device integration process;

(iii) Be thin enough to allow a maximum gate control on the underlying nm-thick layer.

Clearly, the evaluation of the effectiveness of any encapsulation method conceived along these points needs to be performed not only in terms of the intrinsic ability to stop any physical and chemical degradation of the surface but also in terms of a capability to provide a long-term stability to the electrical performances of the devices operated in ambient air conditions. In this regard, among the many approaches adopted in literature, those based on the encapsulation of phosphorene with insulating hBN layers or with Al_2O_3 oxides, have shown optimal results in the retention of the electrical characteristic of phosphorene FET transistors upon prolonged air exposure.

Van der Waals passivation and encapsulation of phosphorene

The stabilization of few layer phosphorene flakes by van der Waals passivation with hBN (or graphene) layers has been proposed for the first time by Doganov et al.[34] The authors transferred on exfoliated phosphorene flakes hBN or graphene layers in an inert atmosphere using a dry transfer-technique [35] and showing that these two atomically thin encapsulations act as an excellent barrier against oxygen and water molecules. Moreover, in the case of hBN the chemical inert, pinhole free and atomically flat interface allowed the reduction of the charge impurity scattering [35]–[37] with the underlying channel material giving, at the same time, an excellent gating action on it. In this respect, few layer phosphorene FET transistors fabricated with graphene contacts and hBN top-gate dielectrics have shown robust device performances over 2 months of air exposure.[38] However, besides being a promising route for the realization of full 2D heterostructures, the van der Waals encapsulation of phosphorene requires delicate manipulation and transfer techniques and, therefore, is hardly transferrable towards a large-scale fabrication technology.

Passivation and encapsulation via Al_2O_3 deposition

Conversely, the encapsulation of phosphorene via the Atomic Layer Deposition (ALD) of Al_2O_3 oxides[1], [3], [5], [39]–[41] offers the advantage of having a scalable approach also compatible with a FET device processing scheme. Moreover, the transparent nature of the Al_2O_3 oxides into the visible portion of the electromagnetic spectrum allows also an immediate assessment of the integrity of underlying phosphorene layers by means of optical and Raman spectroscopy techniques.

The ALD growth of Al_2O_3 capping layers involves typically the high-temperature reaction on the surface of the samples of two precursors: oxygenated water and the Trimethyaluminum (TMA). Clearly, due to the presence of oxygen and water, this encapsulation strategy requires a preliminary optimization in order to avoid an in-situ degradation of the phosphorene surface. In this regard, a possible strategy explored in literature [1] consists in the introduction in the ALD growth chamber of TMA pulses before those of H_2O so to minimize, in the initial cycles

of the ALD process, the adsorption of water on the phosphorene surface. Additionally, to protect the phosphorene crystals from the potential damage caused by the high temperature exposure to oxygenated H_2O, the first few nanometers of Al_2O_3 are grown at room temperature and then the remainder of the film is deposited with a standard Al_2O_3 growth recipe (at 150 °C-200 °C). Other methods developed to protect the phosphorene surface with Al_2O_3 thin films have exploited the in-situ growth of a few-nm thick metallic aluminum seeding layer followed by the oxidation in air or in O_2 environment.[3], [39]

In all these approaches, both the chemical and the electronic stability of the Al_2O_3 encapsulations is significantly influenced by the thickness of the oxide films. In this respect, different authors [3], [5] have reported that, although the deposition of a 1nm or 5nm thick Al_2O_3 capping layer is optimal for the realization of scaled 2D FET transistors, it is not able, however, to durably protect the underlying phosphorene channel from the degradation. For example, a detailed analysis performed by Gamage et al [5] has shown that the degradation of phosphorene flakes encapsulated with 1nm or 5nm thick Al_2O_3 films begins at the edges of the flakes and slowly grows inward oxidizing the flake surface below the oxide capping layer. Improved air-stability can be achieved only employing thicker (>20 nm) Al_2O_3 films grown conformally around the flake edges. However, Kim et al [3], proved that even in this case the fabricated phosphorene FET devices cannot retain the pristine electrical performances over an extended time-scale due to the slow diffusion of adsorbates through the Al_2O_3 capping. These authors, therefore, have proposed that an optimal strategy to achieve a long-term electronic and chemical stability of phosphorene consists in a double-layer encapsulation obtained by depositing a 25 nm Al_2O_3 capping dielectric and then an additional transparent hydrophobic fluoropolymer film that specifically prevents the penetration of water molecule towards the phosphorene channel surface.

4.2.2 Stabilization of epitaxial phosphorus on gold by Al_2O_3 encapsulation.

The success demonstrated by the Al_2O_3 encapsulation in minimizing the air degradation problem of few layer phosphorene samples suggests that a similar approach could be adopted even for the stabilization of epitaxial phosphorus on gold. Amorphous and optically transparent Al_2O_3 thin films have proved to achieve excellent results in preventing the oxidation also in case of epitaxial silicene samples grown on Ag(111) substrates. [25] On the other hand, the successful Al_2O_3 encapsulation of silicene has set a milestone along the device integration path of this epitaxial material and has allowed both the *ex-situ* manipulation and the optical characterization by Raman spectroscopy. [42] Motivated by these facts, it is interesting to explore if an analogous encapsulation strategy applied to epitaxial phosphorus on gold is still effective in protecting the as-grown material from the degradation caused by a prolonged air-exposure outside the UHV growth environment. Such study acquires a particular relevance in view of the subsequent *"ex-situ"* manipulation of epitaxial phosphorus which will be object of discussion in the Chapter 5.

In-situ growth of an Al_2O_3 encapsulating layer.

Thin Al_2O_3 capping layers were grown in UHV on top of epitaxial phosphorus/Au(111) substrates held at room temperature by a reactive co-deposition of Al and O_2. Specifically, Al

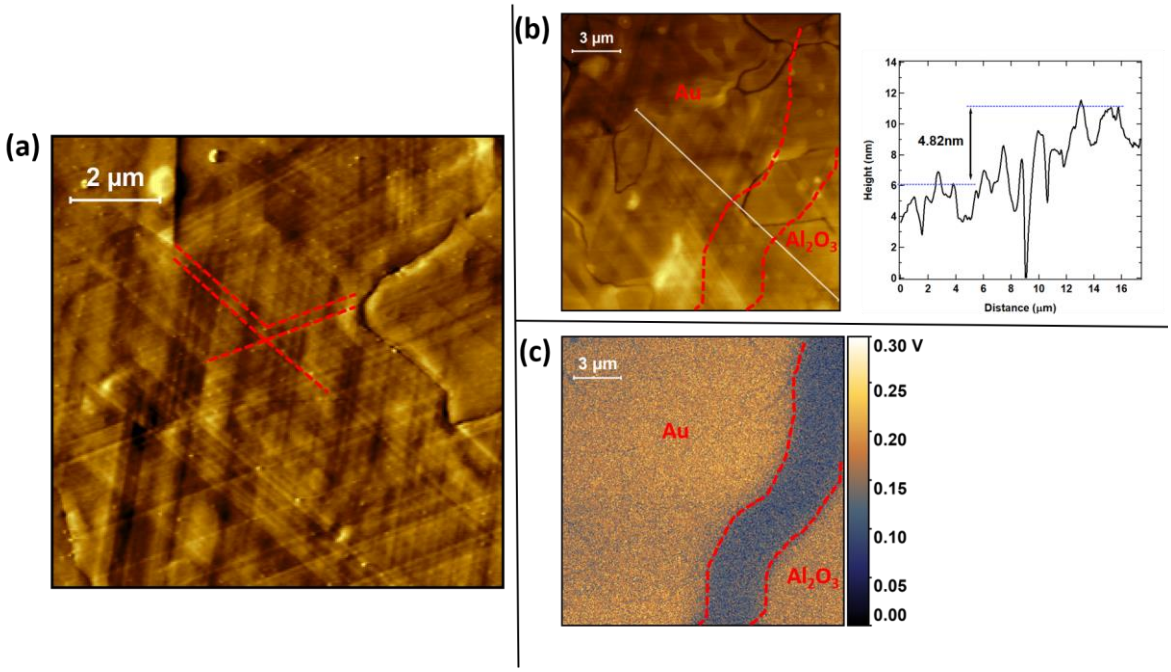

Figure 4.5 (a) Ex-situ AFM image (10x10) µm^2 with enhanced contrast of the surface of a Al_2O_3 capped Au(111)/mica "reference"-sample (i.e. without a phosphorus deposition). The hexagonal faceting of the fcc Au(111) planes is highlighted with red dashed lines**. (b)-(c)** AFM and Kelvin Probe Force (KPFM) images (17x18) µm^2 of the Au(111)/mica surface taken at the edge of the Al_2O_3 capped region. The deposition edge is indicated by red-dashed lines and has been obtained matching the corresponding KPFM image **(c)** taken on the same region. The line profile across the deposition edge gives the estimated Al_2O_3 thickness as reported in (b).

was evaporated in the growth chamber of the UHV system illustrated in figure 3.1 from a Knudsen-cell at a temperature of 890 °C and deposited on epitaxial phosphorus in an oxygen overpressure of 1.2×10^{-6} mbar to induce the formation of Al_2O_3. To minimize as much as possible the oxidation of epitaxial phosphorus, initially a 2.5-3 Å-thick aluminum capping was grown under exposure to an atomic Al-flux and only subsequently the oxygen was introduced in the UHV growth chamber by means of variable leak valve. The Al growth rate, determined with a quartz microbalance under pure Al flux conditions (i.e. at a pressure of 10^{-9} mbar in the UHV chamber), was $0.16\,\text{Å}/s$. This growth rate is not expected to remain the same in presence of oxygen, however it has been chosen low enough to promote the growth of a stoichiometric Al_2O_3 as successfully demonstrated in the case of silicene[25] and eventually to prevent damages to the underlying phosphorus layer caused by Al atoms imping at high-energy. The final thickness of the Al_2O_3 capping layer grown with a standard deposition time of 120 min was determined by an ex-situ AFM analysis carried out on a reference Al_2O_3 capped Au(111) sample, as described below.

Surface morphology and thickness of the Al_2O_3 capping layer

Figure 4.5 (a) illustrates a large scale (10x10) µm^2 image of the surface morphology of an Al_2O_3 capped Au(111)/mica sample measured ex-situ by AFM. It is well known from literature that the surface morphology of thin gold films grown on mica substrates are highly dependent on the evaporation parameters of gold.[43]–[45] In general, high-quality gold films deposited on mica show a large-scale surface morphology characterized by an hexagonal faceting of the (111) close-packed planes of gold with step edges meeting at an angle of 120°. Indeed, as

illustrated by the AFM image in figure 4.4(a), the deposition of a thin Al_2O_3 capping layer on Au(111)/mica does not alter this large-scale surface morphology (the fcc planes of gold are still clearly visible as highlighted by the red dashed lines) and suggests that the growth of the thin oxide film is conformal to the Au(111)/mica surface. However, the surface of the Al_2O_3 capped Au(111)/mica sample is additionally characterized by the presence of irregular ridges and furrows with a depth of the order of few nanometers (see figure 4.5(a) and (b)). The high conformality of the Al_2O_3 growth on this kind of surface makes difficult the ex-situ determination of the oxide thickness on the basis of an analysis carried out on AFM topographic images alone. Indeed, as shown in figure 4.5(b) the AFM topography taken in vicinity of the edge of the Al_2O_3 deposition does not show any clear height variation that help to locate the exact position of Al_2O_3 covered regions from the underlying Au(111) substrate. To overcome this difficulty, we employed scanning Kelvin probe force microscopy (KPFM) to locally map the variations in the contact potential difference between a metallic probe-tip and the underlying gold substrate. The presence of the thin Al_2O_3 layer is expected to modulate the electrostatic interaction between the metallic tip and the underlying gold substrate making thus visible the exact location of the edge of the deposition. This fact is clearly illustrated in the KPFM image in figure 4.5(c), where the edge of the deposition is at lower potential (blue-color) with respect to the surrounding Au(111) and Al_2O_3 capped regions. Once determined the exact location of the edge of the deposition from the KPFM image, the height of the Al_2O_3 capping layer with respect to the underlying gold substrate has been obtained from the line profile taken across the Au(111) and Al_2O_3 covered regions by matching the corresponding topographic AFM image as illustrated in figure 4.5(b). The measured height of a standard Al_2O_3 capping layer obtained after a 120 min deposition is approximately 5 nm.

Chemical stability of Al_2O_3 encapsulated epitaxial phosphorus samples

The effects of a 5 nm Al_2O_3 encapsulation on the chemical stability of epitaxial phosphorus deposited on Au(111)/mica substrates are elucidated in figure 4.7 by comparing for the same sample the P 2p photoemission line measured in-situ, prior and after the Al_2O_3 capping (figure 4.7(a)), and ex-situ after a prolonged exposure to ambient-air (>20 days) (figure 4.7(b)). The ex-situ XPS measurements were performed with a monochromatized X-Ray source using a collection geometry for the emitted photoelectrons with a take-off angle of 30° whereas the in-situ photoemission measurements were realized with the experimental system described in paragraph 3.3.1.The position of the P2p core level lines in figure 4.7 was assigned by correcting for the offsets caused by charging phenomena on the sample surface referencing the measured positions of the Au4f peaks of the gold substrate to the standard value of 84.0 eV. The reduced photoemission intensity and the broadening observed on the in-situ P2p line after the Al_2O_3 capping (violet, in figure 4.7(a)) is due to the additional scattering of the emitted photoelectrons inside the thickness of the Al_2O_3 capping layer grown on top of epitaxial phosphorus. Conversely, the high intensity observed for the ex-situ P2p line measured after air exposure (figure 4.7(b)) is due to a much higher emission intensity of the X-Ray monochromatized source with respect to the X-Ray source used for the in-situ measurements.

As evidenced in figure 4.7(b), the presence of a major P2p component at 129.4 eV (blue), assigned to the elemental P-P bonding of epitaxial phosphorus, and the appearance of a minor

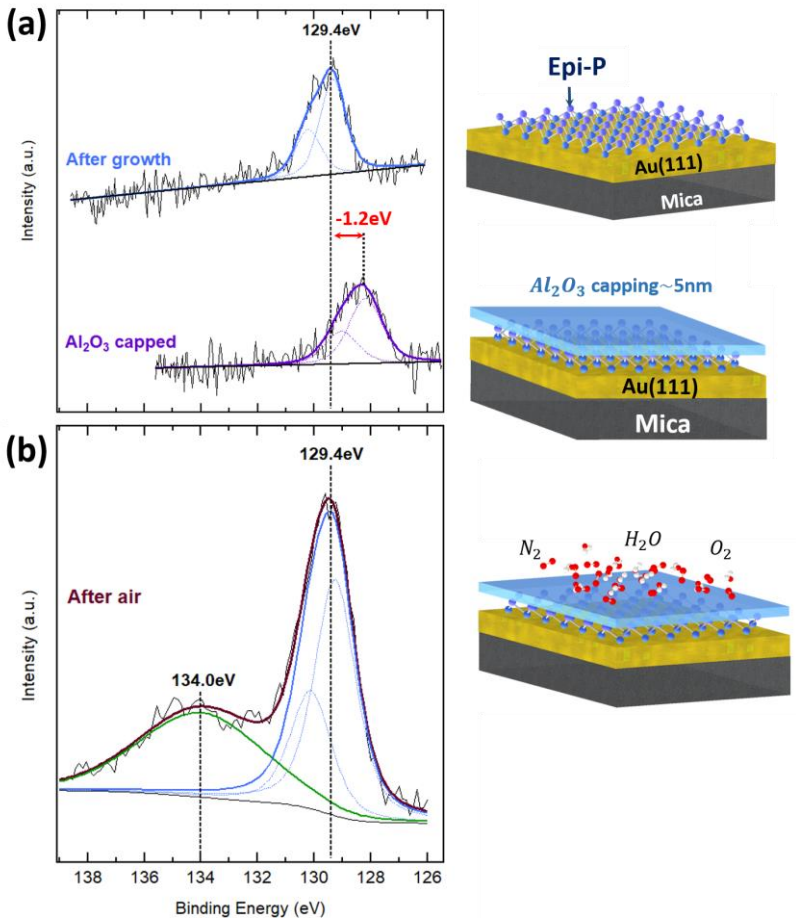

Figure 4.7 (a) XPS of the P2p core level taken before and after the encapsulation of epitaxial phosphorus with a 5 nm thick Al_2O_3 capping layer **(b)** P2p core level of the same Al_2O_3 capped epitaxial phosphorus sample measured "ex-situ" after a prolonged (>20 days) ambient air exposure. The P2p peak positions in each XPS experiment have been off-setted by referencing the Au4f core level positions to 84.0 eV.

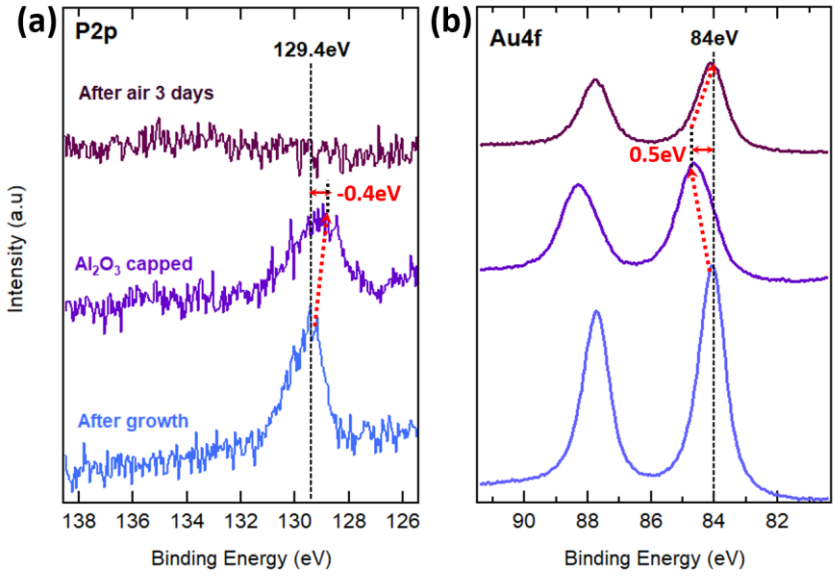

Figure 4.6 XPS of the P2p **(a)** and Au4f **(b)** core levels measured before, after the encapsulation with a 2.5 nm thick Al_2O_3 capping layer and after 3 days of ambient air exposure. No offsetting has been introduced on the P2p and Au4f peak position in this case. Red dashed arrows indicate the observed binding energy shifts.

higher binding energy component at 134.0 eV (green), related to phosphorus oxides, clearly demonstrate that a 5 nm Al_2O_3 capping is able to slow down significantly the oxidation process of epitaxial phosphorus on gold after a prolonged air-exposure. The presence of a minor (green) oxidized component in the air-exposed sample, however, indicates that Al_2O_3 capping layer could be partially permeable to external oxidants and, hence, may not be completely appropriate for a durable protection of epitaxial phosphorus on an extended time scale of several months. It is also possible, however, that such oxidized phosphorus species come from the edges of the Al_2O_3 deposition that, as demonstrated by the height profile reported in figure 4.5(b), are not uniform and characterized by a lower thickness. In this respect, we observe that an Al_2O_3 encapsulation with a thickness below 5 nm, is not suitable to durably protect the underlying epitaxial phosphorus layer from oxidation. This fact is clearly demonstrated by the P2p core-level spectra reported in figure 4.6(a) for a sample capped with a nominal 2.5 nm thick Al_2O_3 layer (i.e. grown using half of the standard deposition time). As can be seen from the disappearance of the elemental P-P bonding component at 129.4 eV, the underlying epitaxial phosphorus layer is almost completely oxidized just after 3 days of air exposure.

Electrostatics at the Al_2O_3 encapsulation layer interfaces

Unlike to the P2p spectra reported in figure 4.7(a), the binding energy axis of the P2p core level spectra reported in figure 4.6(a) has not corrected introducing an additional offset calculated by referencing the respective Au4f peaks to the standard 84.0 eV value (see figure 4.7(b)). Reporting the P2p and Au4f core level peaks as measured, allows us to get a better insight into another interesting feature that emerges from the XPS analysis of the Al_2O_3 capped epitaxial phosphorus samples. Indeed, comparing the P2p and Au4f lines in figure 4.6(a) and (b), before and after the Al_2O_3 encapsulation, we notice that the Au4f core levels are shifted to higher binding energy after the deposition of a thin (2.5 nm thick) oxide layer and, correspondingly, the P2p lines are shifted in the opposite direction, i.e. towards lower binding energies (as indicated by the red dashed arrows). Such peculiar binding energy shift of the P2p and Au4f peaks affects also the 5 nm capped sample reported in figure 4.7(a). In this case, however, the binding energy shift observed on the P2p core level after the Al_2O_3 capping (violet curve in figure 4.7(a)) is more noticeable (-1.2 eV) due to the extra offset introduced by referencing all the Au4f peaks of these spectra to the same 84.0 eV value. In any case (whether or not the binding energies are corrected by offsetting the Au4f peaks) we observe that on both the 2.5 nm and 5 nm Al_2O_3 capped samples charging phenomena occur at the interface between the Al_2O_3 capping and the underlying epitaxial phosphorus/Au(111) layer. We interpret the origin of such phenomena as a consequence of the formation of an interface dipole around the epitaxial phosphorus layer caused by a charge exchange occurring between the gold atoms and the electronic states in the Al_2O_3 capping layer.[46] Such picture is further motivated by the behavior of the Au4f core level spectra measured on a reference Al_2O_3(5 nm)/Au(111) sample before and after the Al_2O_3 capping and reported in figure 4.8. As demonstrate in figure 4.8, even in this case (i.e. without the presence of the epitaxial phosphorus layer at the interface between the Al_2O_3 and the Au(111) substrate) the Au4f peak of the capped sample is shifted to higher binding energies. Based on these facts, we speculate that the MBE growth of the Al_2O_3 oxide, although stoichiometric, may generate an excess of fixed positive charges in the oxide possibly caused by unsaturated chemical bonds between Al^{3+} and O^{2-} atoms at the interface with

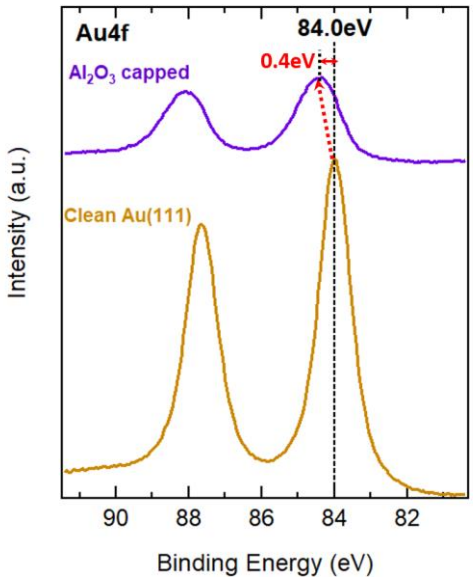

Figure 4.8 XPS of the Au4f core level taken before and after the deposition of a 5nm thick Al_2O_3 layer on a Au(111)/mica reference (i.e. without phosphorus deposition) sample. The red dashed arrow indicates the binding energy shift observed after the deposition of the capping layer.

gold. Such charge unbalance at the interface between the Al_2O_3 and the Au(111) substrate may draw electrons from the gold atoms making them "more positive" and, hence, increase the binding energy of the Au4f core levels. Correspondingly, the excess of negative charge in the Al_2O_3 capping layer in close proximity to the gold interface may affect the P2p core level positions measured in the Al_2O_3/Epitaxial-P/Au(111) samples giving to the epitaxial phosphorus layer a "more metallic" character. This picture is also corroborated by observing that the original binding energy shift of the Au4f core levels is restored whenever the Al_2O_3 capped epitaxial phosphorus samples are exposed to air as illustrated by the dashed arrows in in figure 4.6(b). In this case, the environmental reactivity may induce a partial (or complete) saturation of charge defects in the Al_2O_3 layer and thus *reset* the electrical unbalance at the interface.[24] We additionally point out that the existence of such interfacial charging phenomena observed from the XPS spectra of the Al_2O_3/Epitaxial-P/Au(111) samples is not consistent with a picture based on the formation of an aluminum-phosphorus-gold intermetallic at the interface between the Al_2O_3 capping and the epitaxial phosphorus layer for two main reasons.

(i) The Al deposition is performed always on the substrate held at room temperature. Therefore, intercalation of Al below the epitaxial phosphorus layer and Al-Au alloying are processes strongly inhibited at such low temperatures.

(ii) In analogy with the case of the Al_2O_3 encapsulation of silicene on Ag(111)[24], the strong interaction between the metallic Au substrate and the epitaxial phosphorus layer minimizes the chemisorption of Al adatoms if deposited in presence of highly reactive O_2 species. The latter will prefer to bind to the Al adatoms rather than interact with the epitaxial phosphorus layer, also in view of the low reactivity of the epitaxial layer to oxygen exposure documented in the "in-situ" oxidation studies.

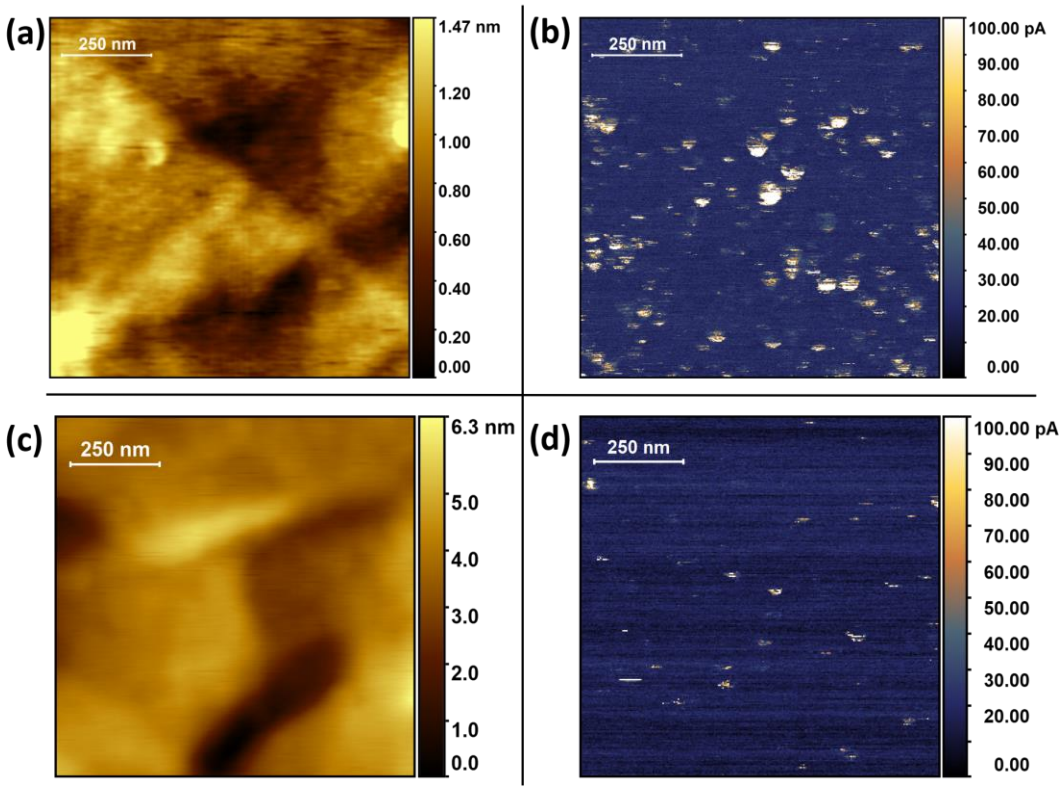

Figure 4.9 (a) AFM topography(1x1) µm^2 and **(b)** c-AFM (bias voltage 2.7 V) current map measured on an Al_2O_3 (5 nm) capped epitaxial phosphorus sample. **(c)-(d)** AFM (1x1) µm^2 and c-AFM (bias voltage 2.7 V) current map measured on an Al_2O_3 (5 nm) capped Au(111) reference sample.

Dielectric quality of the Al_2O_3 encapsulation

To conclude we want to briefly examine the dielectric quality of the thin Al_2O_3 encapsulating layer. This is a relevant aspect in all the applications in which a good gate oxide is required for the control of the charge flow in the underlying epitaxial material by means of an externally applied bias potential. Conductive AFM (c-AFM) reveals to be a particularly useful technique in this respect[47] and, in our case, has been applied to map the current leakage under a constant applied bias (2.7 V) through the thin 5nm thick Al_2O_3 capping layer both in an Al_2O_3/Epitaxial-P/Au(111) sample and in a "reference" Al_2O_3/Au(111) sample. The results of this analysis are reported in figure 4.9 (a)-(b) for the capped epitaxial phosphorus sample and (c)-(d) for the reference sample. From the current maps we notice that Al_2O_3 surface of both samples, although uniform in the topographic images in (a) and (c), is characterized by the appearance of isolated spots of high conductivity (bright regions) in the current images. These high conductivity regions have a typical size varying from 10 nm to 80 nm and the presence on both capped epitaxial phosphorus and reference samples suggests that they cannot be ascribed to an electric field induced interdiffusion of phosphorus atoms in the Al_2O_3 overlayer in the Al_2O_3/Epitaxial-P/Au(111) samples. It is likely, instead, that such high conductivity regions originate from an accumulation of metallic Aluminum species in highly reactive sites, such as local defects or grain boundaries, on the surface of either the epitaxial phosphorus or clean Au(111) substrate, during the deposition process. Overall, the net effect of such defective areas is to increase the current leakage in high-field conditions through the 5nm thick Al_2O_3 capping when employed as a gate oxide.

Conclusions

Although preliminary these results set the stage for further investigation on the dielectric integrity of the Al_2O_3 protective encapsulation and suggest that a possible strategy to overcome the dielectric reliability problems observed on the Al_2O_3 capped samples consists in the ex-situ thickening of the capping layer with the deposition of an additional high-quality Al_2O_3 film for example, by means of an optimized ALD process. Such approach, in turn, could help to minimize the oxidation problem observed on the capped epitaxial phosphorus samples on extended time scales (of the order of several months) and eventually provide to the Al_2O_3/Epitaxial-P/Au(111) membrane sufficient mechanical stability that, as we will see in the next chapter, is one of the major issues in the "ex-situ" manipulation of epitaxial phosphorus.

Bibliography

[1] J. D. Wood *et al.*, "Effective Passivation of Exfoliated Black Phosphorus Transistors against Ambient Degradation," *Nano Letters*, vol. 14, no. 12, pp. 6964–6970, Dec. 2014, doi: 10.1021/nl5032293.

[2] J. O. Island, G. A. Steele, H. S. J. van der Zant, and A. Castellanos-Gomez, "Environmental instability of few-layer black phosphorus," *2D Materials*, vol. 2, no. 1, p. 011002, Jan. 2015, doi: 10.1088/2053-1583/2/1/011002.

[3] J.-S. Kim *et al.*, "Toward air-stable multilayer phosphorene thin-films and transistors," *Scientific Reports*, vol. 5, no. 1, Aug. 2015, doi: 10.1038/srep08989.

[4] A. Castellanos-Gomez *et al.*, "Isolation and characterization of few-layer black phosphorus," *2D Materials*, vol. 1, no. 2, p. 025001, Jun. 2014, doi: 10.1088/2053-1583/1/2/025001.

[5] S. Gamage *et al.*, "Nanoscopy of Black Phosphorus Degradation," *Advanced Materials Interfaces*, vol. 3, no. 12, p. 1600121, Jun. 2016, doi: 10.1002/admi.201600121.

[6] F. Alsaffar *et al.*, "Raman Sensitive Degradation and Etching Dynamics of Exfoliated Black Phosphorus," *Scientific Reports*, vol. 7, p. 44540, Mar. 2017, doi: 10.1038/srep44540.

[7] Y. Huang *et al.*, "Interaction of Black Phosphorus with Oxygen and Water," *Chemistry of Materials*, vol. 28, no. 22, pp. 8330–8339, Nov. 2016, doi: 10.1021/acs.chemmater.6b03592.

[8] A. H. Woomer, T. W. Farnsworth, J. Hu, R. A. Wells, C. L. Donley, and S. C. Warren, "Phosphorene: Synthesis, Scale-Up, and Quantitative Optical Spectroscopy," *ACS Nano*, vol. 9, no. 9, pp. 8869–8884, Sep. 2015, doi: 10.1021/acsnano.5b02599.

[9] M. C. Robbins, S. Namgung, S.-H. Oh, and S. J. Koester, "Cyclical Thinning of Black Phosphorus with High Spatial Resolution for Heterostructure Devices," *ACS Appl. Mater. Interfaces*, vol. 9, no. 14, pp. 12654–12662, Apr. 2017, doi: 10.1021/acsami.6b14477.

[10] A. Favron *et al.*, "Photooxidation and quantum confinement effects in exfoliated black phosphorus," *Nature Materials*, vol. 14, no. 8, pp. 826–832, May 2015, doi: 10.1038/nmat4299.

[11] S. Walia *et al.*, "Defining the role of humidity in the ambient degradation of few-layer black phosphorus," *2D Mater.*, vol. 4, no. 1, p. 015025, Nov. 2016, doi: 10.1088/2053-1583/4/1/015025.

[12] T. Ahmed *et al.*, "Degradation of black phosphorus is contingent on UV–blue light exposure," *npj 2D Mater Appl*, vol. 1, no. 1, p. 18, Dec. 2017, doi: 10.1038/s41699-017-0023-5.

[13] A. Ziletti, A. Carvalho, D. K. Campbell, D. F. Coker, and A. H. Castro Neto, "Oxygen Defects in Phosphorene," *Physical Review Letters*, vol. 114, no. 4, Jan. 2015, doi: 10.1103/PhysRevLett.114.046801.

[14] Q. Zhou, Q. Chen, Y. Tong, and J. Wang, "Light-Induced Ambient Degradation of Few-Layer Black Phosphorus: Mechanism and Protection," *Angew. Chem. Int. Ed.*, vol. 55, no. 38, pp. 11437–11441, Sep. 2016, doi: 10.1002/anie.201605168.

[15] G. Wang, R. Pandey, and S. P. Karna, "Phosphorene oxide: stability and electronic properties of a novel two-dimensional material," *Nanoscale*, vol. 7, no. 2, pp. 524–531, 2015, doi: 10.1039/C4NR05384B.

[16] Z. Hu *et al.*, "Water-Catalyzed Oxidation of Few-Layer Black Phosphorous in a Dark Environment," *Angew. Chem. Int. Ed.*, vol. 56, no. 31, pp. 9131–9135, Jul. 2017, doi: 10.1002/anie.201705012.

[17] H. Wang *et al.*, "Ultrathin Black Phosphorus Nanosheets for Efficient Singlet Oxygen Generation," *Journal of the American Chemical Society*, vol. 137, no. 35, pp. 11376–11382, Sep. 2015, doi: 10.1021/jacs.5b06025.

[18] J. Kang *et al.*, "Stable aqueous dispersions of optically and electronically active phosphorene," *Proceedings of the National Academy of Sciences*, vol. 113, no. 42, pp. 11688–11693, Oct. 2016, doi: 10.1073/pnas.1602215113.

[19] W. Luo *et al.*, "Surface chemistry of black phosphorus under a controlled oxidative environment," *Nanotechnology*, vol. 27, no. 43, p. 434002, Oct. 2016, doi: 10.1088/0957-4484/27/43/434002.

[20] K. L. Kuntz *et al.*, "Control of Surface and Edge Oxidation on Phosphorene," *ACS Applied Materials & Interfaces*, vol. 9, no. 10, pp. 9126–9135, Mar. 2017, doi: 10.1021/acsami.6b16111.

[21] C. Han *et al.*, "Oxygen induced strong mobility modulation in few-layer black phosphorus," *2D Materials*, vol. 4, no. 2, p. 021007, Feb. 2017, doi: 10.1088/2053-1583/aa59ce.

[22] M. T. Edmonds *et al.*, "Creating a Stable Oxide at the Surface of Black Phosphorus," *ACS Applied Materials & Interfaces*, vol. 7, no. 27, pp. 14557–14562, Jul. 2015, doi: 10.1021/acsami.5b01297.

[23] J. Pei *et al.*, "Producing air-stable monolayers of phosphorene and their defect engineering," *Nature Communications*, vol. 7, p. 10450, Jan. 2016, doi: 10.1038/ncomms10450.

[24] A. Molle *et al.*, "Stability and universal encapsulation of epitaxial Xenes," *Faraday Discuss.*, p. 10.1039.C9FD00121B, 2020, doi: 10.1039/C9FD00121B.

[25] A. Molle *et al.*, "Hindering the Oxidation of Silicene with Non-Reactive Encapsulation," *Advanced Functional Materials*, vol. 23, no. 35, pp. 4340–4344, Sep. 2013, doi: 10.1002/adfm.201300354.

[26] Y. Du *et al.*, "Tuning the Band Gap in Silicene by Oxidation," *ACS Nano*, vol. 8, no. 10, pp. 10019–10025, Oct. 2014, doi: 10.1021/nn504451t.

[27] D. Solonenko, O. Selyshchev, D. R. T. Zahn, and P. Vogt, "Oxidation of Epitaxial Silicene on Ag(111)," *Phys. Status Solidi B*, vol. 256, no. 2, p. 1800432, Feb. 2019, doi: 10.1002/pssb.201800432.

[28] J. L. Zhang *et al.*, "Reversible Oxidation of Blue Phosphorus Monolayer on Au(111)," *Nano Letters*, vol. 19, no. 8, pp. 5340–5346, Aug. 2019, doi: 10.1021/acs.nanolett.9b01796.

[29] X. Xu *et al.*, "Effects of Oxygen Adsorption on the Surface State of Epitaxial Silicene on Ag(111)," *Sci Rep*, vol. 4, no. 1, p. 7543, May 2015, doi: 10.1038/srep07543.

[30] L. Zhu *et al.*, "Blue Phosphorene Oxide: Strain-Tunable Quantum Phase Transitions and Novel 2D Emergent Fermions," *Nano Lett.*, vol. 16, no. 10, pp. 6548–6554, Oct. 2016, doi: 10.1021/acs.nanolett.6b03208.

[31] Z. Luo *et al.*, "Anisotropic in-plane thermal conductivity observed in few-layer black phosphorus," *Nature Communications*, vol. 6, p. 8572, Oct. 2015, doi: 10.1038/ncomms9572.

[32] Y. Saito and Y. Iwasa, "Ambipolar Insulator-to-Metal Transition in Black Phosphorus by Ionic-Liquid Gating," *ACS Nano*, vol. 9, no. 3, pp. 3192–3198, Mar. 2015, doi: 10.1021/acsnano.5b00497.

[33] G. Wang *et al.*, "Introduction of Interfacial Charges to Black Phosphorus for a Family of Planar Devices," *Nano Lett.*, vol. 16, no. 11, pp. 6870–6878, Nov. 2016, doi: 10.1021/acs.nanolett.6b02704.

[34] R. A. Doganov *et al.*, "Transport properties of pristine few-layer black phosphorus by van der Waals passivation in an inert atmosphere," *Nat Commun*, vol. 6, no. 1, p. 6647, May 2015, doi: 10.1038/ncomms7647.

[35] C. R. Dean *et al.*, "Boron nitride substrates for high-quality graphene electronics," *Nature Nanotech*, vol. 5, no. 10, pp. 722–726, Oct. 2010, doi: 10.1038/nnano.2010.172.

[36] Y. Cao *et al.*, "Quality Heterostructures from Two-Dimensional Crystals Unstable in Air by Their Assembly in Inert Atmosphere," *Nano Letters*, vol. 15, no. 8, pp. 4914–4921, Aug. 2015, doi: 10.1021/acs.nanolett.5b00648.

[37] L. Li *et al.*, "Quantum Hall effect in black phosphorus two-dimensional electron system," *Nature Nanotechnology*, vol. 11, no. 7, pp. 593–597, Mar. 2016, doi: 10.1038/nnano.2016.42.

[38] A. Avsar *et al.*, "Air-Stable Transport in Graphene-Contacted, Fully Encapsulated Ultrathin Black Phosphorus-Based Field-Effect Transistors," *ACS Nano*, vol. 9, no. 4, pp. 4138–4145, Apr. 2015, doi: 10.1021/acsnano.5b00289.

[39] R. Galceran *et al.*, "Stabilizing ultra-thin black phosphorus with *in-situ* -grown 1 nm-Al_2O_3 barrier," *Appl. Phys. Lett.*, vol. 111, no. 24, p. 243101, Dec. 2017, doi: 10.1063/1.5008484.

[40] H. Zhu *et al.*, "Al_2O_3 on Black Phosphorus by Atomic Layer Deposition: An *in Situ* Interface Study," *ACS Applied Materials & Interfaces*, vol. 7, no. 23, pp. 13038–13043, Jun. 2015, doi: 10.1021/acsami.5b03192.

[41] J. Na *et al.*, "Few-Layer Black Phosphorus Field-Effect Transistors with Reduced Current Fluctuation," *ACS Nano*, vol. 8, no. 11, pp. 11753–11762, Nov. 2014, doi: 10.1021/nn5052376.

[42] A. Molle, C. Grazianetti, L. Tao, D. Taneja, Md. H. Alam, and D. Akinwande, "Silicene, silicene derivatives, and their device applications," *Chemical Society Reviews*, vol. 47, no. 16, pp. 6370–6387, 2018, doi: 10.1039/C8CS00338F.

[43] J. A. DeRose, T. Thundat, L. A. Nagahara, and S. M. Lindsay, "Gold grown epitaxially on mica: conditions for large area flat faces," *Surface Science*, vol. 256, no. 1–2, pp. 102–108, Oct. 1991, doi: 10.1016/0039-6028(91)91204-B.

[44] I. Ošťádal and P. Sobotík, "STM study of Au(111) growth on mica," *Czechoslovak Journal of Physics*, vol. 47, no. 4, pp. 445–449, 1997, doi: 10.1023/A:1021267308425.

[45] M. Levlin, A. Laakso, H. E.-M. Niemi, and P. Hautojärvi, "Evaporation of gold thin films on mica: effect of evaporation parameters," *Applied Surface Science*, vol. 115, no. 1, pp. 31–38, May 1997, doi: 10.1016/S0169-4332(96)00851-3.

[46] L. Kornblum, J. A. Rothschild, Y. Kauffmann, R. Brener, and M. Eizenberg, "Band offsets and Fermi level pinning at metal-Al 2 O 3 interfaces," *Phys. Rev. B*, vol. 84, no. 15, p. 155317, Oct. 2011, doi: 10.1103/PhysRevB.84.155317.

[47] K. Ganesan, S. Ilango, S. Mariyappan, M. F. Baroughi, M. Kamruddin, and A. K. Tyagi, "Conductive atomic force microscopy studies on dielectric breakdown behavior of ultrathin Al2O3 films," *Appl. Phys. Lett.*, vol. 98, no. 9, p. 092902, Feb. 2011, doi: 10.1063/1.3560307.

CHAPTER 5

Substrate transfer and device fabrication

5.1 Substrate transfer of 2D materials

In many cases, both the top down exfoliation and the bottom up epitaxial techniques do not allow the direct synthesis of 2D materials on a substrate appropriate for a device implementation. Thus, a crucial step along the device integration route of any 2D material is the development of a proper substrate transfer procedure. The optimization of such step is at least of equal importance to the optimization of the synthesis and stabilization phases since, most of the time, the degradation of the structural, chemical and electronic properties of 2D materials occurs during the transfer phase from a substrate to another.[1]

According to the employed synthesis technique different kinds of substrate transfer methods have been developed in literature.[2] Some of these methods allow the deterministic placement of a 2D crystalline layer in a pre-defined position whereas others lack of an accurate positional control but are able to achieve a transfer of 2D crystals on large areas. The former techniques are particularly suited to the case of mechanically exfoliated 2D materials,[3]–[6] the latter, instead, are suited to liquid phase exfoliated[7]–[10] and epitaxially grown 2D materials [11], [12] offering scalable approaches useful for industrial applications. In the following paragraph we will provide a general overview of some of the most common substrate transfer techniques developed for the manipulation of mechanically exfoliated and epitaxial graphene films. Most of these techniques can be obviously extended to the case of other mechanically exfoliated and epitaxially grown 2D materials, such as 2D TMDs and, eventually, can also be adapted to the substrate transfer of mechanically exfoliated phosphorene (α-P). In the latter case, however, the manipulation of the samples along each phase of the substrate transfer and device integration process must be performed in an inert atmosphere in order to avoid the degradation problems caused by the high chemical reactivity of this material.

Dry and wet substrate transfer methods for exfoliated and epitaxial 2D materials

Generally, the techniques employed for the transfer of mechanically exfoliated and epitaxially grown 2D material can be divided between *wet* and *dry* approaches. In a *wet* transfer approach one of the two surfaces of the 2D crystal comes into direct contact with a liquid solution which is, typically, an etchant used to free the 2D material from the supporting or growth substrate. In a *dry* transfer approach, instead, the surfaces of the 2D material are always protected from contacting liquids. Both *dry* and *wet* transfer processes require a carrier film that picks the 2D material by sticking to it and acts as a mechanical support during the transfer phase so to prevent unwanted tearing and/or folding of the 2D layer. For example, polymeric materials such as PMMA (polymethyl methacrylate) or PDMS (polydimethylsiloxane) have been commonly used as support membranes in the case of the substrate transfer of both exfoliated graphene flakes[3], [4], [6] and epitaxial graphene films grown on Cu or Ni substrates.[13]–[15] Two possible wet and dry substrate processes that use PMMA as polymer support for the transfer of mechanically exfoliated graphene flakes are schematically illustrated in figures 5.1(a) and 5.1(b), respectively. One of the greatest advantages of the substrate transfer processes realized with PMMA and PDMS consists in the optical transparency of these carrier membranes which allow for their use in combination with an optical microscope and a micromanipulator system so to achieve the deterministic placement of the 2D crystalline layers and eventually build 2D

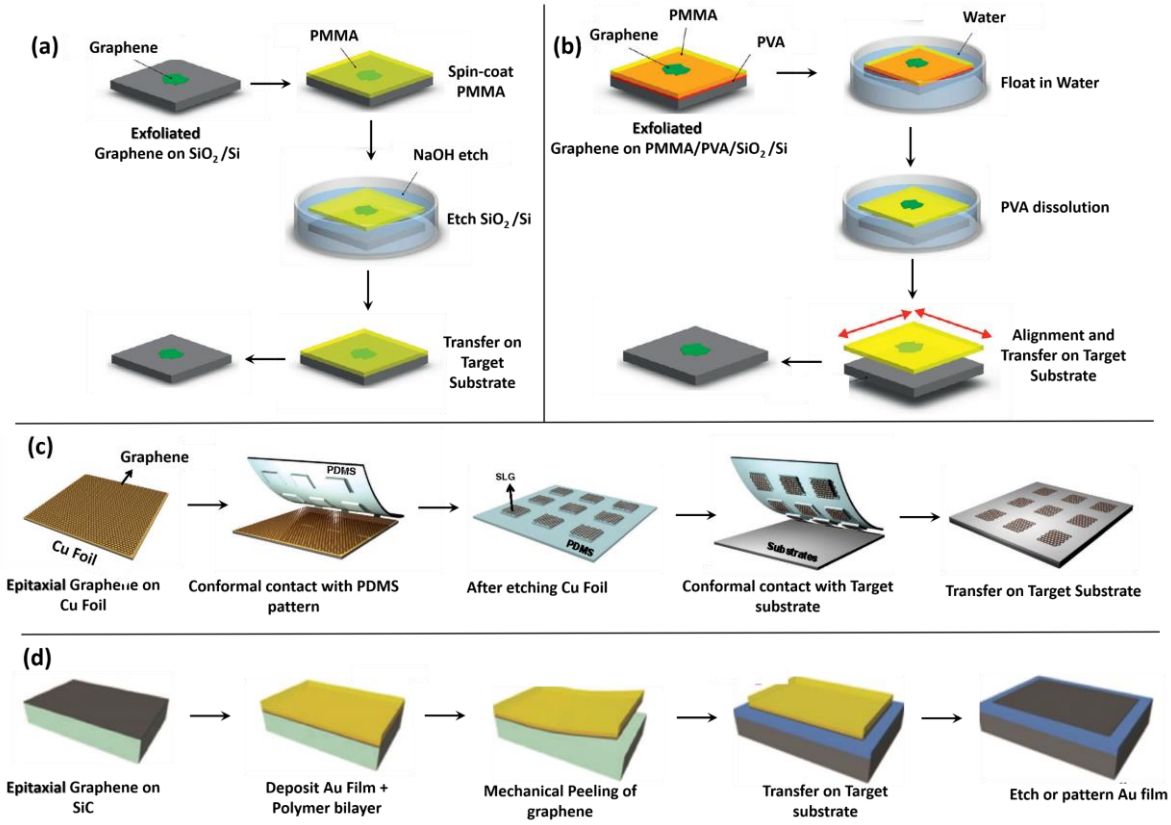

Figure 5.1 Some methods developed for the substrate transfer of mechanically exfoliated and epitaxial graphene**. (a)** Wet Transfer of graphene flakes exfoliated on SiO_2/Si by means of a PMMA polymer support and a subsequent SiO_2 etch in a NaOH bath. **(b)** Dry transfer of graphene flakes exfoliated on a PMMA polymer support. The PMMA support is spin-coated on a water soluble PVA layer that releases, after the dissolution, the PMMA\graphene membrane for "dry" transfer on a substrate. **(c)** Wet transfer of epitaxial graphene on a Cu substrate by means of Cu-etching followed by PDMS stamping on the target substrate**. (d)** Dry transfer of epitaxial graphene on a SiC substrate by mechanical peeling using an Au film + polymer bilayer. Figures (a) and (b) adapted from ref. [2] (c) adapted from ref. [15] and (d) adapted from ref. [20]

vertical heterostructures on a target substrate.[3], [6] Additionally, PDMS and PMMA can be molded or patterned in desired geometries by means of soft lithography and electron beam lithography (EBL) techniques, respectively. However, in the case of PDMS, the patterning processes can be easily carried out by stamping or bringing in contact the molded PDMS/2D material membrane with the acceptor substrate since, due to the relatively weak adhesion force between the 2D material and the PDMS stamp, the former can be easily released from the latter, as illustrated in the process reported in figure 5.1(c). In the case of PMMA, instead, once the polymer/2D material stack is brought in contact with the surface of the acceptor substrate, the PMMA layer is used as an EBL resist to pattern an etch mask with the desired geometries. After the etching, the polymer is dissolved and washed away with solvents (such as acetone). Obviously, due to the unremoved etching byproducts or polymer residues from the surface of the 2D materials, the optimization of the post-transfer cleaning procedures becomes often a mandatory step that helps to prevent the degradation of the electrical performances of the nanofabricated 2D devices.[2]

In the case of epitaxial 2D materials, the methods based on the mechanical peeling of the 2D layers from the growth substrate offer a valid alternative to achieve reliable substrate transfer

procedures that make no use of chemical etching steps and thus avoid the correlated contamination problems. Such *dry* transfer methods typically rely on a substance that glues the 2D epitaxial material and the carrier substrate used as mechanical support to peel the 2D crystal from the growth substrate. For example, the peeling of epitaxial graphene films grown on Cu substrates has been achieved using either specific linker molecules [16] or thin layers of epoxy glues[17] as adhesive layers to attach the supporting (flexible or rigid) substrates. Interestingly, the epoxy glue approach has been successfully readapted also in the case of the transfer of thin bismuth films grown on Si(111) by means of a modified mechanical peeling procedure based on the "double cantilever beam fracture" method.[18] Exfoliation transfer methods that make use of thermal releasing tapes[19] can be exploited as additional alternatives to those based on the use of epoxy and polymeric glues with the advantage to bypass the problems of the permanent chemical linking of the adhesive layer to the surface of the 2D crystal. However, all these approaches share a series of common drawbacks such as the fact to be too harsh, harming the structural integrity of the 2D crystals, or to unavoidably leave glue residues and contaminations that require additional cleaning steps. The use of glue substances can be circumvented using *dry* exfoliation transfer methods based on the mechanical peeling via bilayer metal+polymer films,[20], [21] as in the process shown in figure 5.1(d). In such approaches the 2D material sticks to the metal side of the bilayer metal+polymer film which is, in turn, used as a carrier membrane for the transfer on a target substrate. The transfer procedure is then completed by dissolving the polymer film and eventually etching or patterning the underlying metal with the required device geometries.

Large area transfer of epitaxial graphene

Clearly, most of the wet and dry substrate transfer methods mentioned above are appropriate only for a laboratory scale manipulation of 2D materials which aims to the fabrication of proof of concept devices. In order to extend the full scientific and technological potential of 2D materials to industrial and commercial applications it is necessary to develop both synthesis and transfer protocols with scalable approaches that allow for a large-scale handling. However, despite there are a lot of attempts along this way from the synthesis side, the research on substrate transfer methodologies that offer a scalable and large area approach is still scarce and it is built only on few successful demonstrations. One of these is, for example, the roll-to-roll transfer method developed for the large-scale continuous transfer of epitaxial graphene.[11]

Large area transfer of other epitaxial 2D materials and Xenes

In the case of other epitaxial 2D materials the development of large area transfer methods is still poor. Moreover, considering the case of epitaxial monoelemental 2D materials, i.e. the members of the family of Xenes, the development of substrate transfer methods has not even reached the stage of a laboratory scale implementation, despite the enormous potential that these 2D epitaxial materials offer for the next future nanoelectronics. Therefore, aiming at opening a pathway that could be of general validity for all the epitaxial Xenes, in the following paragraphs we will illustrate some preliminary attempts conceived along this direction considering, specifically, the case of epitaxial phosphorus on gold and epitaxial silicene on silver.

5.2 Substrate transfer methods for epitaxial 2D Xenes

Like epitaxial graphene grown on copper or on nickel, also in the case of epitaxial Xenes grown on metals the substrate is unwanted after the synthesis. Therefore, the substrate removal and the transfer of the 2D epitaxial crystal on a new target substrate are the next logical steps for the integration in device architectures. Unluckily, the strong interaction of epitaxial Xenes with the metallic substrate and the high chemical reactivity of their unprotected surfaces make any effort relying on already known wet and dry substrate transfer methods unsuccessful. Clearly, the ex-situ manipulation of epitaxial Xenes on metals requires the development of "ad-hoc" transfer methodologies that must take into account also the presence of encapsulating layers used for the stabilization of epitaxial Xenes outside the UHV growth environment.

Substrate transfer of epitaxial silicene with the SEDNE method

A first attempt along this way has been proposed in 2015 by Tao et al [22] for epitaxial silicene on Ag(111). In the proposed process, termed SEDNE (Silicon encapsulation and delamination with native electrodes), the silver substrate on which the epitaxial 2D lattice is grown is not etched away but rather, during the substrate transfer process, is used to protect from oxidation the epitaxial layer together with the in-situ grown Al_2O_3 encapsulation. Moreover, during the device fabrication process, the metallic substrate is employed also to define electrical contacts directly on the silicene epitaxial layer, without the need to carry any further metal deposition. From a device perspective, such approach offers the strong advantage of having no Fermi level misalignment or a chemically induced barrier at the interface between the metallic contacts and the 2D epitaxial layer owing to the intrinsic hybridization between Ag and silicene orbitals. [23] As a such the SEDNE process has been successfully used to fabricate the first silicene FET transistor.

Wet and dry methods for the substrate transfer of epitaxial Xenes

A central role in the development of the SEDNE process was played by the smart choice of the growth substrate, i.e. Ag(111) films deposited on mica crystals. The latter, thanks to their layered nature, can be easily cleaved by delamination techniques allowing a direct access to the underlying metallic substrate for the subsequent transfer and device fabrication steps.

In the following we will illustrate two novel Xene substrate transfer methods that still make use of metal/mica substrates but offer an additional improvement to the original SEDNE process and allow to extend it also to other epitaxial Xenes grown on metal/mica substrates. Specifically, we have considered a wet approach in which the mica is cleaved by means of a chemical bath and a dry approach in which the mica supporting substrate is mechanically delaminated. The former approach has been implemented in the case of Al_2O_3 encapsulated epitaxial phosphorus samples on Au(111)/mica substrates whereas the latter approach has been developed in the case of Al_2O_3 encapsulated epitaxial silicene samples on Ag(111)/mica substrates. Such approaches, although lack of a full optimization in all their steps, have a general validity paving the way for the establishment of methodological standards for the manipulation of other 2D epitaxial Xenes grown on metal/mica.

5.2.1 Wet substrate transfer method for epitaxial phosphorus on gold

Figure 5.2 schematically illustrates the various steps of the wet transfer approach used to transfer a thin Al_2O_3/Epitaxial-P/Au(111) membrane from the mica supporting substrate towards a device friendly substrate (such as SiO_2/Si). The mica crystal is delaminated from the Au(111) film via a chemical-aided cleavage process that is analogous to the template-stripping method used to prepare large area ultra-smooth metallic surfaces [24]–[26] and it involves three main passages:

(i) Initially, the Mica/Au(111)/Epitaxial-P/ Al_2O_3 sample is attached, using a thin layer of epoxy glue, onto a rigid target substrate with the Al_2O_3 side facing downwards.

(ii) The sample, attached on the rigid target substrate, is then dipped in a tetrahydrofuran (THF) bath for some time, typically, more than 30min. (best results, however, have been achieved with a 2-3 hours long bath)

(iii) After a deionized water rinsing, the entire mica crystal can be easily cleaved from the Au(111)/Epitaxial-P/Al_2O_3 membrane by gently lifting it with a razor blade at the points of weakest adhesion, i.e. typically along the edges of the mica crystal.

At variance with the SEDNE process, that uses a mechanical delamination method to separate the Al_2O_3 /Silicene/Ag(111) stack from the mica substrate, with some unavoidable residues of mica remaining in certain areas,[27] the use of a THF bath completely separates the mica crystal from the gold thin film allowing for a comparatively larger scale transfer. This is proven also by the Raman spectroscopic investigation of the delaminated surface of gold reported in figure 5.3(b). After the delamination, the Raman features of the mica substrate disappear leaving a Raman spectrum characterized only by the strong photoluminescent background of gold. However, with respect to the dry transfer methods relying on the mechanical delamination of mica, such as the aforementioned SEDNE process or the s-SEDNE method that will be illustrated in the next section, the use of a chemical bath leads to an unavoidable increase of the partial oxidation of the epitaxial phosphorus layer, as demonstrated by the ex-situ XPS investigation of the P2p core level reported in figure 5.3(a). The phosphorus oxide component (green) at 134.0 eV measured on the sample after the THF bath becomes comparatively higher than the identical 134.0 eV component measured on the air-exposed sample before the THF bath (compare with figure 4.6(b) in the previous chapter).

Optimization of the transfer procedure

Such issues advice for a careful process optimization of this substrate transfer procedure aiming to prevent the degradation of the epitaxial phosphorus layer and allow its subsequent integration into functional device architectures. For example, the use of a thicker Al_2O_3 oxide, grown ex-situ by ALD, could help to minimize the observed oxidation problem by slowing down the permeation of oxidant species through the thin Al_2O_3 capping layer. Moreover, as seen in the previous chapter; a thicker Al_2O_3 can boost the dielectric quality of the in-situ grown capping layer which is a fundamental aspect in all the device implementations that require the application of voltage bias to control the charge carriers flow in the epitaxial layer. Additionally, a thicker oxide can improve the mechanical stability of the thin Au(111)/Epitaxial-P/Al_2O_3 membrane during the mica delamination process. In this respect, it should be mentioned that another factor that plays a relevant role for the mechanical stability of the delaminated membrane is given by the quality of the surface of the Au(111) substrates.

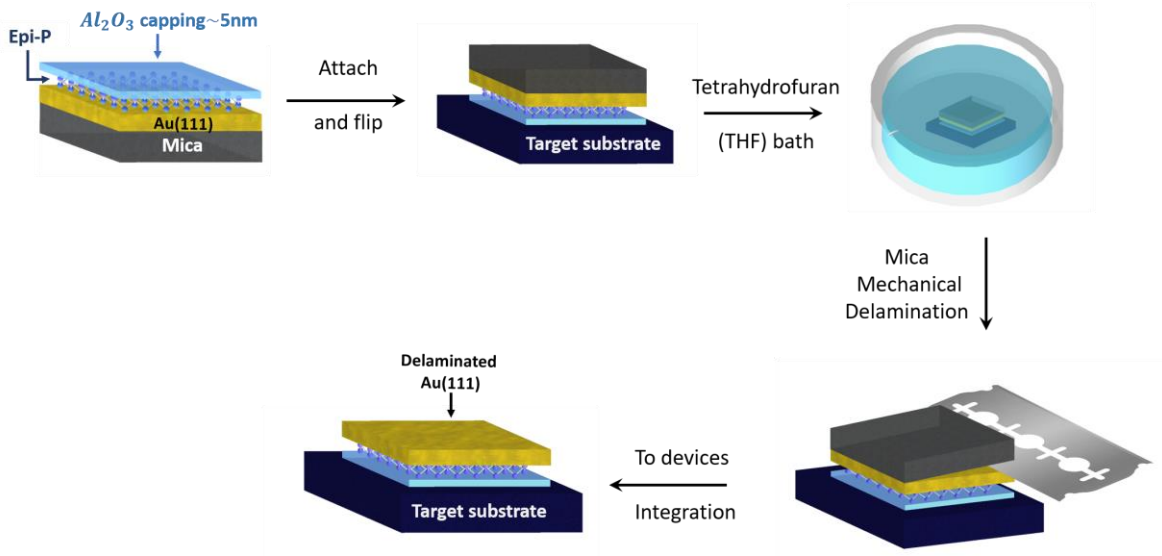

Figure 5.2 Wet substrate transfer procedure for epitaxial phosphorus on gold. Firstly, the Al_2O_3 capped epitaxial phosphorus sample on Au(111)/mica is overturned and attached on a device-friendly substrate. Then, the sample is immersed in a THF bath for ~30min in order to weaken the adhesion between mica and the Au(111) film. The mica crystal can be thus delaminated and the resulting Au(111)/Epitaxial-P/Al_2O_3 membrane is transferred on a new substrate. Figures adapted from reference [32]

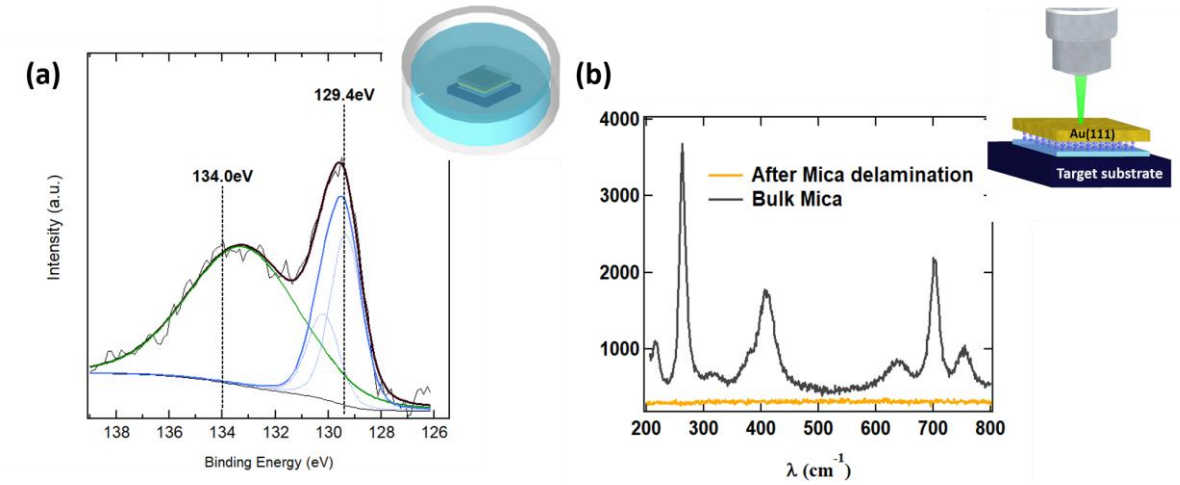

Figure 5.3 (a) XPS od the P2p core level taken on Al_2O_3 capped epitaxial phosphorus sample after the THF bath. **(b)** Raman spectrum of the THF-dipped sample before (gray) and after (yellow) the mica delamination showing the complete removal of the mica substrate. Figures adapted from reference [32]

Indeed, as shown in the previous chapter, the large scale topography of the Au(111) surface (see figure 4.5(a)) is characterized by the presence of ridges and furrows which can likely become the points of stress propagation during the delamination of mica and lead to a rupture and to an uncomplete transfer of the Au(111)/Epitaxial-P/Al_2O_3 membrane on the target substrate. A thicker oxide can prevent this problem giving a certain stiffness to the whole membrane during the manipulation.

The quality and the yield of the substrate transfer procedure can be also improved with a careful choice of the adhesive layer and of the solvent used for the chemical bath. In particular, thin epoxy films swell and partially dissolve once immersed in organic solvents; compromising the mechanical stability as well as the final smoothness of the template-stripped metallic surface. In this respect Wagner et al [24] have surveyed different commercial glues and developed appropriate protocols for their application as adhesion layer between the metallic surface and the supporting template. According to their study, the authors reported that THF solvents are best suited for the use with low viscosity epoxy glues (such as epo-tek 377®). Such process optimizations, although investigated for the template-stripping process of metals are still valid for the wet transfer procedure of Au(111)/mica substrates discussed above.

Finally, although the use of glues to attach the Au(111)/Epitaxial-P/Al_2O_3 membrane to the target substrates facilitates the mica cleavage process, this approach is clearly sub-optimal from the point of view of the device implementation since it may introduces a series of additional problems that span from the contaminations left by glue residues to the poor dielectric quality of the glue when used as gate material. Therefore, a significant process optimization could move in the direction of searching methodologies that avoid completely the use of adhesive layers to bond the Al_2O_3 surface to the target substrate. Possible approaches along this direction could be, for example, those based on the cold welding process [28] which makes use of an additional gold layer (which could be deposited on top of the Al_2O_3 capping layer) to bind the Au(111)/Epitaxial-P/Al_2O_3 membrane at elevated pressure and temperatures to a second gold layer evaporated on a target substrate. Or, another possible alternative, is offered by the low temperature direct bonding between Al_2O_3 surfaces of the Au(111)/Epitaxial-P/Al_2O_3 membrane and the surface of an Al_2O_3/Si target substrate.[29]

Generalization to the ex-situ manipulation of other Xenes: the UXEDO method

Despite the above-mentioned process optimizations require further experimental test for the validation into reliable device processing schemes, they can be potentially implemented even in the case of other Xenes epitaxially grown on metal/mica substrates, such as silicene on Ag(111) or germanene on Au(111). A hint along this direction is offered, for example, by the template stripping procedures already developed in literature for silver and other metals.[30], [31] Within this general framework, the wet substrate transfer process discussed above may provide an universal approach to Xene manipulation and, therefore, can be generally considered as an UXEDO (Universal Xene Encapsulation, Decoupling and Operation) methodology.[27], [32]

5.2.2 Dry substrate transfer method for epitaxial silicene on silver

In the following section we will report the principal steps of the dry substrate transfer procedure used to bring towards a device implementation both monolayer and multilayer silicene samples epitaxially grown on Ag(111)/mica substrates. This procedure, like the wet substrate transfer approach described before, has a certain degree of generality and can be eventually extended to the manipulation of other epitaxial Xenes on metal. At variance with the original SEDNE method,[22] however, the present procedure involves an initial deposition step of a thick Al_2O_3/Au gate stack on top of the ~5 nm thick Al_2O_3 capping layer. This step not only improves the mechanical strength the Ag(111)/silicene/Al_2O_3 membrane during all the phases of its manipulation, but it allows also a seamless dielectric gating action on silicene when integrated into a back-gated device configuration. The seamless growth of a gate stack on top of the in-situ grown Al_2O_3 capping layer, moreover, ameliorates the SEDNE process by simplifying the passages required for the transfer of the Ag(111)/silicene/Al_2O_3 membrane on a target substrate. Therefore, to distinguish such procedure from the original SEDNE method we will refer to it in the following as s-SEDNE (seamless-SEDNE) method.[33]

Growth and morphology of epitaxial silicene samples

The silicene samples processed with the s-SEDNE method were grown by molecular beam epitaxy with the UHV system shown in figure 3.1 (Chapter 3) onto Ag(111) (250 nm)/mica substrates previously prepared with several cycles of sputtering (Ar^+ ions at 1 KeV) and annealing (520 °C for 30 min). The thermal sublimation of silicon was achieved by resistively heating an intrinsic silicon wafer by means of an external power generator. Initially an STM investigation was performed on a set of test samples in order to determine the best conditions for the monolayer (ML) growth of silicene on Ag(111) and obtain a calibration of the silicon deposition rate. We verified that monolayer coverage was achieved with an output power of ~108 W and a deposition time of ~40 min corresponding to an estimated deposition rate of ~1.5-2 ML/h. During the silicon deposition the substrate temperature was kept within the 230 - 260°C range. As widely documented in literature,[34]–[36] the structure of silicene on Ag(111) is highly dependent on the substrate temperature and on the Ag(111) surface coverage and, in the monolayer regime, is characterized by the coexistence of different superstructures termed as silicene phases[1]. As can be clearly noticed from the STM image reported in figure 5.4(a), with the chosen temperature and deposition rate conditions, the morphology observed on epitaxial silicene on Ag(111) was characterized by the presence of domains corresponding to two different phases: a (3×3) silicene on (4×4) Ag(111) phase with an appearance similar to the flowerlike pattern of epitaxial phosphorus on gold (highlighted by a green dashed line in the figure) and a $(\sqrt{7} \times \sqrt{7})$ silicene on $(\sqrt{13} \times \sqrt{13})$ Ag(111) phase (highlighted by a blue dashed line). Once the conditions for the monolayer growth were optimized, the samples used for the subsequent s-SEDNE process were grown in a multilayer coverage regime, i.e. using a prolonged deposition time while keeping all the other deposition parameters constants. As reported in literature[37], [38] multilayer silicene grows with a terrace-growth mode in

[1] The nomenclature of the silicene phases in usually expressed following the Wood's notation, i.e. according to dimension of the epitaxial layer supercell. The dimension of the latter can be measured both with respect to the lattice vectors of the freestanding silicene lattice and to the lattice vectors of the (111) surface of silver.

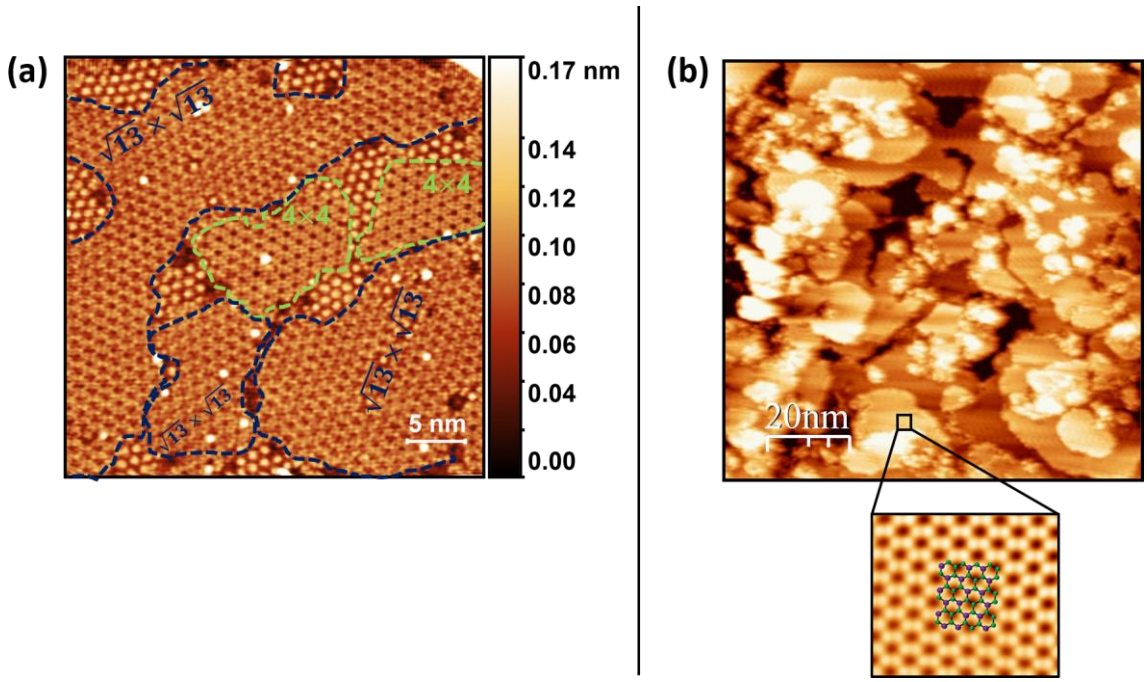

Figure 5.4 (a) STM image (35x35) nm^2 of monolayer silicene grown on Ag(111): the $(\mathbf{4} \times \mathbf{4})$ domains are highlighted with green contours whereas the $(\sqrt{\mathbf{13}} \times \sqrt{\mathbf{13}})$ domains with blue contours**. (b)** Large scale (100x100) nm^2 STM image of multilayer silicene (~5ML) on Ag(111). The inset report a high-resolution STM topography of the topmost layer of a multilayer silicene island with a superimposed ball and stick model of the $(\sqrt{\mathbf{3}} \times \sqrt{\mathbf{3}})$ surface reconstruction. Figure (c) adapted from references [33][38]

which each layer piles-up on top of a seeding layer of silicene at an height of ~0.2-0.3nm [37], [39] with the topmost layer characterized by a $\sqrt{3} \times \sqrt{3}$ surface reconstruction with respect to the free-standing silicene lattice. The typical large-scale surface morphology of a multilayer silicene sample is illustrated in figure 5.4(b) along with a zoomed high-resolution STM image of the $\sqrt{3} \times \sqrt{3}$ surface superstructure observed on top of a multilayer silicene island. The thickness of the multilayer silicene samples was estimated in terms of multiples of a single-layer (1L) silicene by comparing the deposition time used for the multilayer growth with the time needed for a monolayer growth. Specifically, the typical thickness of the processed multilayer silicene samples was ~9L with an equivalent nominal thickness of ~2.0-2.7 nm. To prevent the oxidation of the pristine surface of multilayer silicene during the exposition to ambient-air conditions, the as-grown samples were additionally protected with a ~5 nm thick Al_2O_3 encapsulating layer grown in-situ at room-temperature by reactive co-deposition of aluminium and oxygen and using the same growth protocol described in chapter 4 for the Al_2O_3 encapsulation of epitaxial phosphorus on gold.

Ex-situ Raman characterization of encapsulated silicene samples

The encapsulated multilayer silicene samples (9L thick) were then immediately inspected by ex-situ Raman spectroscopy using a Renishaw InVia spectrometer equipped with a 532 nm laser line. All the Raman measurements were performed in z-backscattering geometry using an incident laser power of 1mW and with a 50x (0.75NA) objective. Figure 5.5 reports the Raman spectrum measured in the 350-600 cm^{-1} range on an Al_2O_3 capped multilayer silicene sample.

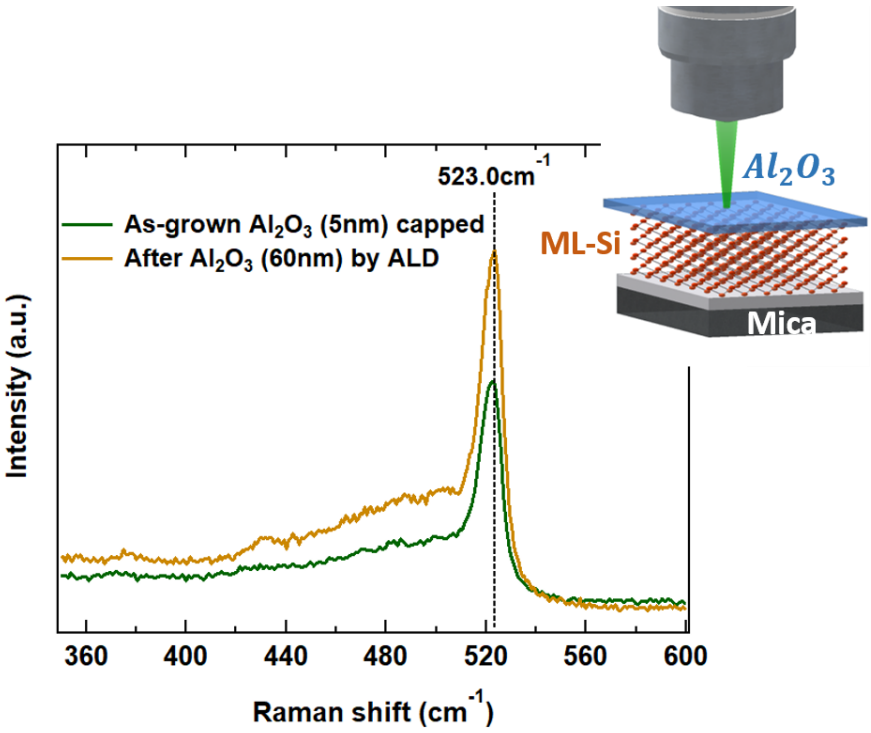

Figure 5.5 First-order Raman spectra of Al_2O_3 capped multilayer silicene before and after the ALD oxide growth. Adapted from reference [33]

Differently from crystalline silicon, which is characterized by a sharp first order Raman band at 520.5 cm^{-1} and, unlike monolayer silicene, whose Raman spectrum shows a first order (E_{2g}) peak at 514-516 cm^{-1},[40]–[43] multilayer silicene exhibits an intense first order band placed at $\sim$523.5 cm^{-1} along with a broad shoulder at lower frequency lying between 430 and 500 cm^{-1}. In agreement with the reports of the previous studies,[38], [44] the latter feature can be ascribed to the low symmetry activated Raman modes arising from the relaxation of the Raman selection rules caused by the reduced crystalline order within the epitaxial multilayer silicene sample.[38] The 523.5 cm^{-1} peak, instead, descends from the mixed sp^2/sp^3 character and, hence, from the shorter Si-Si bond length in each multilayer silicene island with respect to the typical bond length of bulk crystalline silicon. As such, the 523.5 cm^{-1} peak can be considered a signature of the crystalline nature of multilayer silicene and it can be used as an unambiguous marker for the validation of the stability of samples along all the subsequent processing steps.

Seamless gate stack fabrication

In order to fabricate a seamless gate stack, the Al_2O_3 capped samples were firstly thickened with an additional 60nm thick Al_2O_3 oxide grown by a standard ALD process using water and TMA precursors in an ALD reactor (Cambridge Nanotech Fiji F200) at a temperature of 200°C. Subsequently, an additional Ti (5nm)/70 (nm) Au electrode was evaporated on top of the Al_2O_3 oxide by e-beam evaporation (CHA Industries e-beam evaporator). The Raman spectrum of multilayer silicene taken soon after the ALD process and just before the evaporation of the metallic electrode, is shown in figure 5.5. The measured 523.5 cm^{-1} peak shows no substantial shift from the peak measured before the Al_2O_3 thickening, except for its higher intensity, indicating that the high-temperature ALD growth did not introduce alterations in the structure

of the epitaxial multilayer silicene films. The higher intensity of the 523.5 cm^{-1} peak in the ALD thickened sample, instead, can be probably ascribed to the interference enhancement of the Raman scattering intensity due to the multiple reflections in the thicker Al_2O_3 oxide.

Two tape delamination and transfer procedure

Like the SEDNE method, also the s-SEDNE method uses the pristine Ag(111) film underlying the mica supporting substrate to fabricate native device electrodes on the epitaxial (mono or multilayer) silicene film. However, to have access to the Ag film, the mica crystal should be firstly stripped off. Clearly, the success in the nanofabrication of silicene devices depends critically on this step since a sub-optimal delamination process can affect the outcome of all the subsequent patterning and etching phases of the device fabrication process. Unlike the wet UXEDO method considered above, the s-SEDNE method cleaves the mica by a dry approach that relies on the mechanical exfoliation with two tapes having different adhesive forces. As illustrated in figure 5.6(a), a piece of thermal-release tape (Semiconductor Equipment Corp. single side coated with releasing temperature of 120°C) is gently attached on the gate metal (Au) side of the Au/Al_2O_3/multilayer silicene/Ag/mica stack applying a uniform pressure to improve the adhesion between the two media. In this way the sample can be turned upside down to exfoliate a thick piece of mica substrate by means of the strong adhesive force exerted by another piece of thermal release tape (not shown in figure). This process leaves on the Ag(111) film only some residual mica layers. Such mica residues can be completely removed layer-by-layer with a tape assisted delamination that employs a low adhesion force tape (such as a 3M ™ Blue Nitto tape), as illustrated in figure 5.6(b). The complete removal of the mica layers requires multiple tape peelings and after each step the sample is checked under the Raman microscope to verify the presence of residual mica sheets, see figures 5.6(c) and 5.6(d). This peel-off process is critical to achieve a smooth and clean surface of silver, as under peel-off will have incomplete mica removal creating huge contact resistance in the device fabrication process and over peel-off will cause silver surface deformation due to the release of strain into the Au/Al_2O_3/multilayer silicene/Ag membrane. The effects of the strain release in the ~400nm thick Au/Al_2O_3/multilayer silicene/Ag membrane can be clearly seen in the optical microscope images reported in figures 5.6(b I) and 5.6(b II) and shows up as an increased number of wrinkles on the Ag surface after each peeling step. We found out that the optimal number of tape-peelings to remove the majority of the residual mica layers and, at the same time, avoid an excessive stress-induced wrinkling in the Ag film was between ~6 and 8. Best results, in terms of surface smoothness, could be achieved on Au/Al_2O_3/multilayer silicene/Ag membranes thickened with a gate-stack (oxide+metal) thicker than 200 nm. However, due to the statistical nature of the mechanical delamination process and depending on the preparation conditions of the Ag/mica interface, we have also observed that even using thicker gate-stacks a number of tape-peelings higher than 8 was sometimes required to expose the bare Ag surface. Nevertheless, despite the intrinsic randomness of the mica delamination process, flat and smooth mica-free surfaces of the order of 300–400 μm could be, in most of the cases, always obtained as demonstrated in the optical microscopy image of figure 5.6(c).

In order to transfer the encapsulated silicene onto a target substrate, the sample orientation must be changed so that the Au side can be attached to the target substrate. This is done by heating the material stack carrying thermal tape on a hot plate for more than 10s at 120 °C.

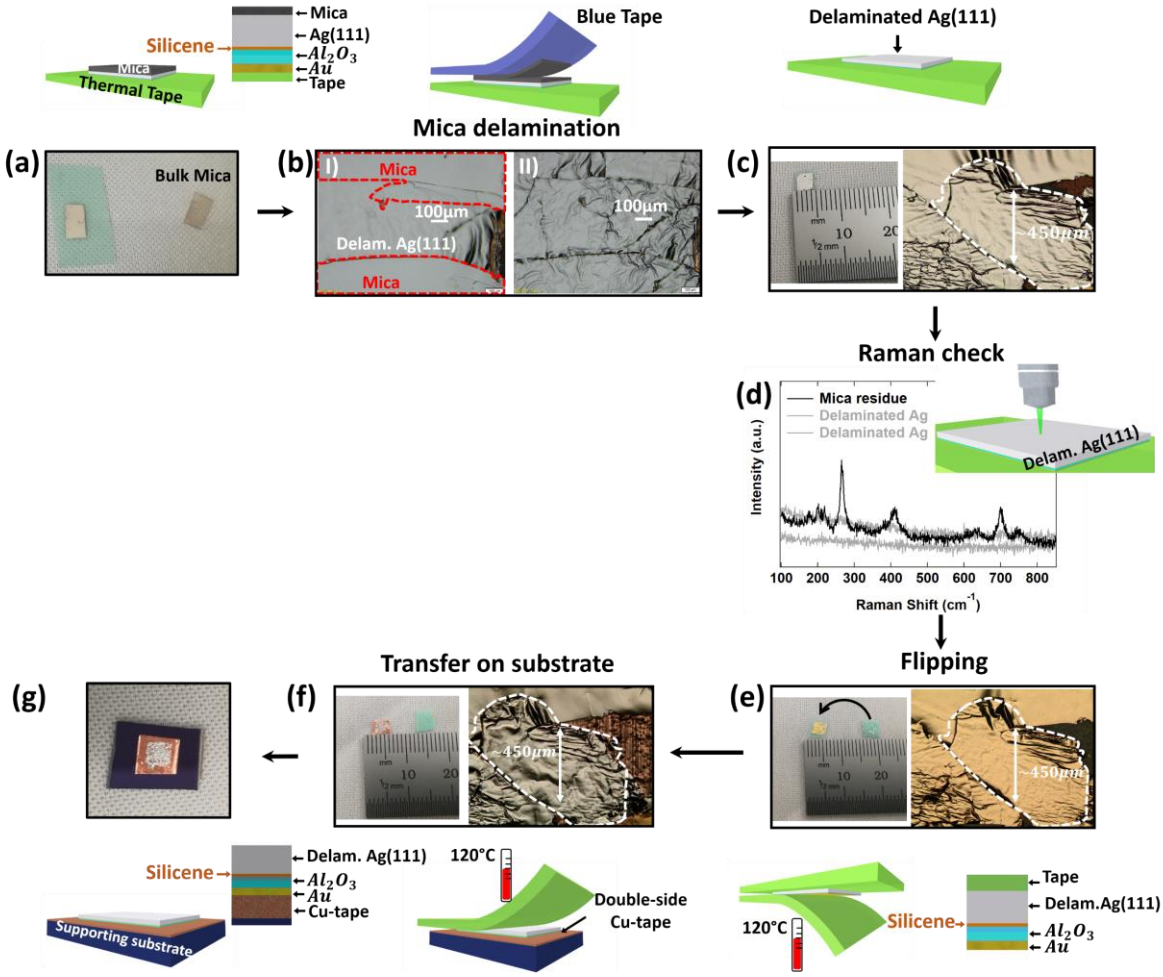

Figure 5.6 Two tape delamination and substrate transfer procedure for epitaxial silicene on silver. **(a)** After the deposition of a thicker Al_2O_3./Au gate stack the sample is attached Au face-down to a piece of thermal releasing tape. A big chunk of mica is removed by using another piece of thermal releasing tape (not shown). **(b)** Mechanical delamination of the residual mica layers with blue (Nitto) tape. The optical microscope images report the effects of the peelings on the Ag surface: **I)** after 4 peeling with some residual mica remaining, **II)** after 7 peelings with no residual mica but with a stress-induced wrinkling on the Ag surface. **(c)-(d)** After an optimal number of tape peelings large flat mica-free areas (with size of ~450 μm) can be observed on the Ag surface as confirmed by the optical microscopy image in c) and by Raman spectroscopy in d). **(e)** Sample flipping. The thermal release tape is heated to release the sample form the Au-side and picked-up with a new piece of thermal tape from the Ag side. **(f)-(g)** Transfer to a new substrate. The sample Au face down is released by heating and attached to a new supporting substrate with the aid of a conductive double-side copper tape. A back-gate device configuration is thus obtained. Figures adapted from reference [33]

Thus, the tape-glue loses its adhesion and another piece of fresh thermal tape, brought in contact with the Ag side of the Au/Al_2O_3/multilayer silicene/Ag membrane, can pick it up and lift it as shown in figure 5.6(e). The stack (Au face-down) is then attached on a double-sided conductive copper tape sitting on an arbitrary (rigid or flexible) substrate and the thermal tape is peeled-off gently by heating it for few seconds at 120 °C (Figure 5.6(f)). Due to the stronger adhesion of the copper tape, the Au/Al_2O_3/silicene/Ag stack is left on it with the delaminated Ag film facing up (Figure 5.6(g)). Thus, the multilayer silicene samples are left on a rigid (or eventually flexible) supporting substrate in a back-gate device configuration ready to be processed into the desired device architecture.

SEDNE vs s-SEDNE manipulation methods for epitaxial silicene

When compared to the original SEDNE method,[22], [38] the s-SEDNE method allows to circumvent some of the difficulties encountered in the former approach providing, at the same time, a much simpler procedure. For example, in the SEDNE method the complete delamination of the mica crystals was achieved by floating the samples in a buffer oxide etch (BOE) solution. This step was potentially unsafe and had a high-risk of irreparably damaging the thin delaminated Al_2O_3/silicene/Ag membranes because the latter had to be scooped on the target SiO_2/Si substrates directly from the acidic solution. Moreover, to form a firm and smooth contact with the surface of the supporting SiO_2/Si substrates, additional vacuum annealing steps were required. In this respect, although still preliminary, the s-SEDNE method provides a safer manipulation technique which makes no use of acid solutions and reduces the risk of irreversibly damaging the samples. Nevertheless, as we will see in the next paragraph, the device yield of this method remains still very low and necessarily calls for new ideas to optimize both the substrate transfer and mica delamination steps which remain the most critical aspects of this approach.

5.3 Fabrication of epitaxial phosphorus and silicene devices.

Both the wet and the dry substrate transfer methods described in the previous paragraphs result in a final configuration in which the bare surface of the metallic growth substrate of the Al_2O_3/epitaxial-Xene/metal sandwich is accessible and can be directly used for the subsequent fabrication of native device electrodes. The manufacturing of device electrodes on such metallic substrates generally involves two main steps:

i) the lithographic patterning of the electrode's geometries on a mask;
ii) the etching of the metallic substrate through the exposed areas of the patterned mask.

In this paragraph we will examine more in detail these two phases in the case of the realization of two common devices architectures: a back-gated FET transistor and a MIM (metal insulator metal) device.

Generally speaking, the fabrication of an operating FET transistor is a common test bench for the validation of any device integration scheme that aims to assess the electrical properties of a 2D material for digital and RF electronics applications. The integration into a MIM architecture, instead, has the objective to understand the potentialities of 2D materials within the broader class of memristive devices (memristors). [45], [46] A particular family of memristors is given

by devices that employ materials in which the resistance state can be externally tuned allowing the device to switch, for example, between two possible (high and low) resistance states. In this respect, the non-volatile resistive switching (NVRS) effect observed on certain 2D materials offer enormous potentialities for the fabrication of emergent non-volatile memories [47]–[49] and non-conventional (neuromorphic) computing architectures. [50], [51]

The back-gated FET devices considered in the following paragraph have been fabricated on Al_2O_3 capped multilayer silicene samples employing a processing scheme based on the s-SEDNE method. The successful integration of multilayer silicene in the ultrathin channel regions of FET transistors envisages a promising route for the use of any silicon allotrope with reduced dimensionality in next-generation ultra-scaled FET devices.[38]

The MIM devices, instead, have been realized in a vertical configuration on Al-capped epitaxial phosphorus/Au(111) samples following a device integration scheme in which the substrate transfer is carried out with a procedure similar to the dry substrate transfer technique conceived for silicene in the s-SEDNE method. The experimentally observed large band gap of the epitaxial phosphorus on gold [52]–[54] is expected to provide possible resistive switching mechanisms as suggested also by the studies carried out on exfoliated few layer phosphorene flakes [55]–[57] and on other atomically thin 2D materials.[58], [59]

Clearly, in both the proposed FET and MIM architectures the definition of the device active areas by etching is one of the most critical aspects. This is particularly true in the case of monolayer silicene on silver and epitaxial phosphorus on gold since both these materials, once exposed to air after the etching of the metallic substrate, are prone to an immediate degradation. As we will see in the following paragraphs, the successful fabrication of silicene and epitaxial phosphorus FET and MIM devices relies always on a preliminary optimization of the metal etching process.

5.3.1 Fabrication of a silicene back-gated FET

Figure 5.7 illustrates, schematically, the fabrication process of a multilayer silicene back-gated FET transistor. The fabrication process has been carried out on the delaminated (mica-free) silver surface of an Al_2O_3/multilayer silicene/Ag(111) membrane preliminary thickened with an Al_2O_3/Au gate stack and transferred on a rigid supporting substrate as required by the s-SEDNE approach.

EBL definition of the device geometry

The fabrication process begins with the definition, by means of electron beam lithography (EBL), of the device geometries into a PMMA resist. The geometric pattern consists of the following features: source and drain contact square pads, 50 µm wide, a thin channel region, typically 500 nm wide, and a surrounding isolation trench ~2.5 µm wide. The latter follows the profile of the contacting pads and isolates (after the etching) each device from the surrounding metallic film. The typical dimensions of a single device area are (200x50) µm, but further extreme downscaling is also possible by optimizing the lithographic step. The PMMA resist (950K A4) is spin-coated using a standard recipe (40 sec at 3000 rpm) and after the post-baking (2 min at 170 °C) results in a hardened transparent film with a typical thickness (measured on flat silver substrates) of 220 nm. A not much different value is expected for the PMMA thickness when spin-coated and cured on the delaminated Ag surfaces, although, as noted in the

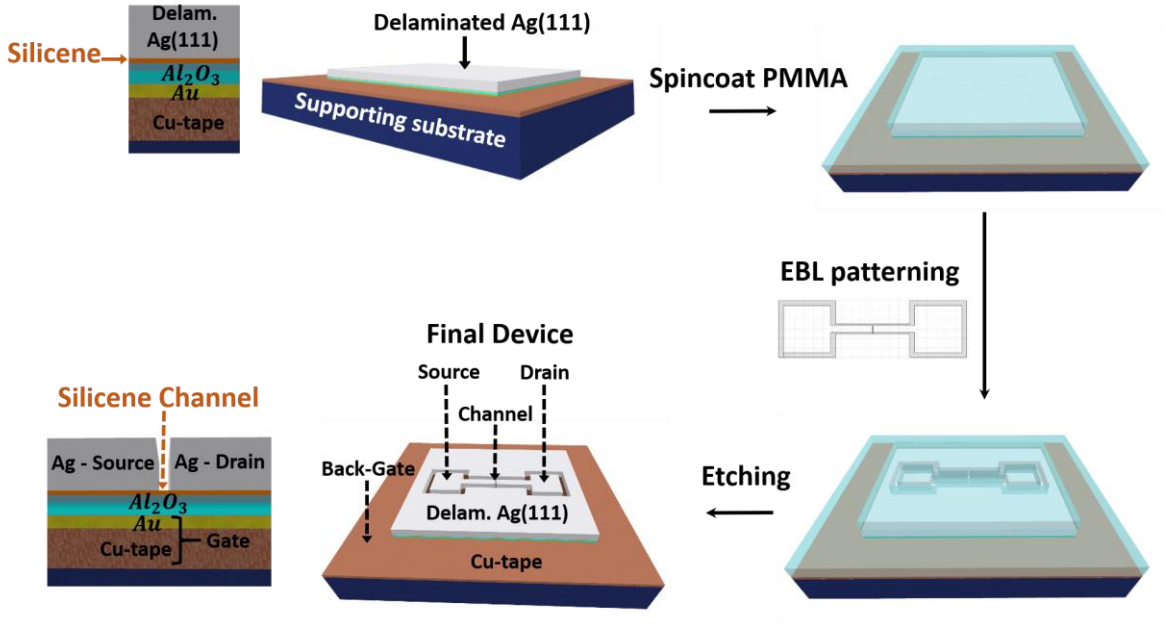

Figure 5.7 Fabrication of a back-gated FET multilayer silicene device with the s-SEDNE method**.** The source and drain contact pads, the device isolation trenches, and the channel region are patterned on a PMMA resist by EBL. After the lithography the resulting etch-mask is used to define the device structure on the delaminated silver surface of the samples by a wet-etching process. Figures adapted from reference [33]

previous paragraph, the presence of strain-induced surface wrinkles due to the mica delamination process may result in an uneven distribution of the resist. This unavoidable problem can be even accentuated by the soft and deformable nature of the polymeric tape-glue and may bring as consequence the possible over and under-exposure of the device geometries in the resist during the subsequent electron-beam writing phase. The EBL writing of the pattern (performed with a Raith Eline plus system) requires an initial alignment procedure that allows the precise positioning of the device pattern on the mica-free areas of the silver substrate. The EBL exposure parameters (such as the area step size, area dwell time and electron dose) needs to be carefully optimized before the writing so to achieve a good exposure of the PMMA resist especially in the thinnest channel regions (a typical electron dose employed was 360 $\mu C/cm^2$). After the exposure, the resist development is the final step of the lithography process. The sample is dipped into a developer (MIBK diluted in IPA at 1:3 ratio) for few seconds then rinsed in IPA and dried with N_2. The length of the developing and rinsing times is generally a function of the exposure parameters used during the EBL writing and strongly affects the good definition and resolution of the geometric features of the PMMA mask. For our typical lithographic processes, preliminary test carried out on flat silver substrates showed that well-defined patterns without overdevelopment and underdevelopment effects can be attained with a developing time of ~30 sec and a rinsing time in IPA of 2 min. Obviously, achieving a good definition of the PMMA mask on real multilayer silicene samples was far more difficult due to the above mentioned problems related to the poor uniformity of the resist and also to its scarce adhesion seldomly observed on some areas of the delaminated metallic surface. Taken all together the previous issues make manifest the challenging nature of the device patterning process on the delaminated silicene samples and account for the poor device yield resulting from the s-SEDNE method.

Optimization of the silver wet etching process

After the lithographic definition of the device mask in PMMA, the device geometric features need to be etched in the native Ag-film. This is accomplished with a chemical etching process that attacks the silver substrate through the exposed areas of the mask. To ensure a faithful replica of the device geometries on the metallic substrate without undesirable "undercut effects" caused by the isotropic nature of the wet etching, a preliminary optimization of the etching process is necessary. This optimization, generally, should involve all the aspects of the wet etching process such as, for example, the choice of the most appropriate etchant, the method of immersion of the samples in the etching bath, the calibration of the etching rate and the rinsing procedure used to wash away the etching by-products. Among these aspects the most critical for the fabrication of silicene devices are the choice of the etchant solution and the calibration of the etching rate. Therefore, the optimization of the chemical etching of delaminated silver surfaces has addressed specifically these two aspects.

We initially observed that commercial Ag etchants based on nitric acid strongly degrade silicene and, moreover, are too fast to allow for a reliable definition of the patterned features with a time-controlled etching process. Aqueous solutions of potassium iodide (KI)/Iodine (I_2), however, are better suited for this purpose as they offer selective etching of the Ag film without damaging the epitaxial silicene layer underlying it. However, commercially available KI/I_2 etchants have typical etching rates of ~1.2 μm min^{-1} at room-temperature and, therefore, are too fast to achieve a reliable time-controlled etching in a ~250 nm-thick Ag-film. As mentioned before, high etching-rates may cause a quick air-exposure of the epitaxial silicene layer underneath the metallic substrate affecting its structural integrity and, consequently, degrading its electric properties. This issue is particularly relevant in the case of the fabrication of monolayer silicene devices but seems to be less critical in the case of the multilayer silicene. In this case, the thick nature of the epitaxial layer may help to mitigate the air-instability problems since the oxidation of the topmost layers self-passivates and protects the material from any further degradation. [38], [44] However, even in this "more-stable" situation, a fast etching rate is still an undesirable aspect in the fabrication process of FET-devices, since it may result in an excessive "undercut" etching of the thin channel regions. On the other hand, a process with a too slow etching rate, obtained, for example, by diluting the iodide (KI)/Iodine (I2) solutions, may result in a not-complete removal of the silver residues from the thinnest channel regions and, therefore, imply the measurement of an unwanted I-V ohmic response during the test of the electrical characteristic of the FET devices.

In our preliminary etching experiments, we have observed that the dilution of commercial (KI)/Iodine (I_2) etchants may also cause the insurgence of another unexpected problem. As can be clearly seen in the AFM topography reported in 5.8(a), the etching of small 2-5 μm wide features with diluted commercial (KI)/Iodine (I_2) etchants led to the appearance of structures protruding from the etched Ag regions with heights ranging between ~0.3 μm and ~1 μm. To understand better the nature of such "bumpy" structures, we performed a Raman spectroscopic analysis. As can be seen from figure 5.8(b), the Raman spectrum taken on a silver etched region shows a broad-band located at 112 cm^{-1}. This spectral feature agrees well with the typical spectrum measured in backscattering configuration from bulk AgI crystalline salts.[60] Based on these results, we concluded that the "bumpy" structures observed in the etched areas were caused by the formation of AgI salts.

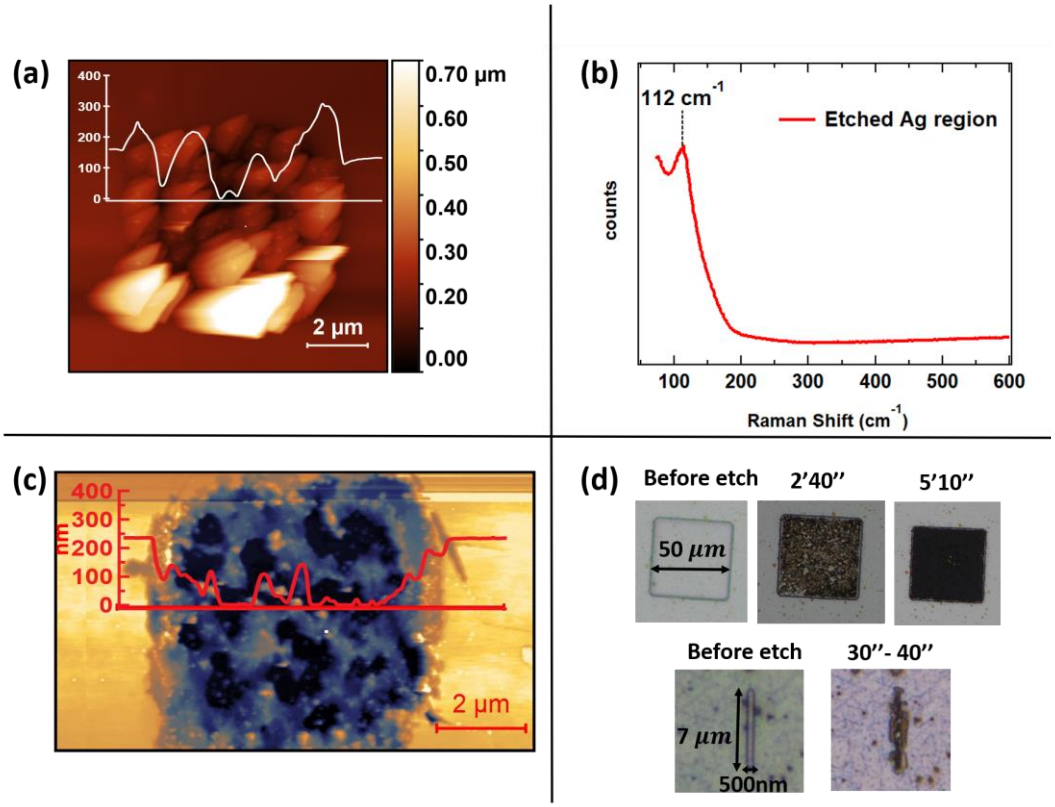

Figure 5.8 Investigation of the "salt-bump" formation problem and optimization of the silver etching process. **(a)** AFM (10x10)µm^2 image of a 5 µm square hole patterned in a 220 nm thick PMMA resist taken after a 2 sec etching with a 1: 8 H_2O diluted commercial KI\$I_2$ etchant. As shown by the superimposed line profile after the etching bath we observed structures protruding out the exposed Ag area. **(b)** The Raman spectra taken in the etched regions showed a band located to 112 cm^{-1} that we assigned to the formation of AgI salts. **(c)** AFM image (12x6) µm^2 of a partially etched 5 µm wide square hole employing an in-house prepared etchant with $[\boldsymbol{KI}]/[\boldsymbol{I_2}] \approx \mathbf{1700}$. No protruding structures were observed in this case, indicating a better dissolution of the AgI salts during the etching bath. **(d)** Optical microscope images of the etching of Ag-patterns with different size with the optimized in-house etchant with $[\boldsymbol{KI}]/[\boldsymbol{I_2}] \approx \mathbf{3400}$. Figures adapted from reference [33]

Table 5.1 Values of the experimentally determined etching-rates for different "in-house" KI\I_2 etchants prepared from KI and I_2 powders dissolved in 40ml DI-water. Adapted from reference [33]

Etchant	Mass % I_2	Mass % KI	Mass % H_2O	$\frac{[KI]}{[I_2]}$	Estimated etching Rate (>5μm features)
Etchant 1	0.65	6.93	92.42	**16**	~2.5$\mu m/min$
Etchant 2	0.05	47.04	52.91	**1767**	~1.5-1.3$\mu m/min$
Etchant 3	0.03	40.25	59.72	**3400**	~44-50nm/min
Etchant 4	0.02	41.83	58.15	**6000**	~16nm/min

These salts are generated from the by-products of the oxidation reactions occurring at the boundary layer with the silver surface. More in detail, the Ag dissolution in KI/I_2 solutions proceeds according to the following reaction: [61]

$$\begin{aligned} &I_{2(aq)} + I^- \leftrightharpoons I_3^- && (a) \\ &Ag + 2I^- \rightarrow AgI_2^- + e && (b) \\ &I_3^- + 2e \rightarrow 3I^- && (c) \end{aligned} \qquad (5.1)$$

Initially, iodine dissolves in water in presence of iodide generating tri-iodide ions, I_3^- (a) which oxidize silver to Ag^+. However, the dissolution of Ag at the metal-solution interface is thermodynamically allowed only by forming a stable metal-complex with a ligand already present in the solution. In this case the ligand is the iodide I^- ion which forms with the oxidized silver surface a soluble AgI_2^- complex according to the reaction (b). Finally, the electrons generated by the Ag oxidation are consumed by the reduction of the I_3^- oxidant (c). To ensure a progress and a good uniformity to the etching reaction, the oxidizing species should be continuously supplied at the boundary layer with the silver surface while the undesired AgI_2^- by-products must be evacuated.[62] In the etching of small features, however, the diffusion of the chemical species in and out of the boundary layer does not always occur in an efficient way due to the existence of uneven concentration gradients nearby tiny geometric structures. To prevent as much as possible this problem commercial iodide (KI)/Iodine (I_2) etchants usually employ surfactants that enhance the wettability of the surfaces and improve the uniformity of the etching process. Agitation can also help to favour a better diffusion of the etching by-products out of the etched areas and improve the etching uniformity. However, none of the previous strategies helped to reduce the accumulation of unwanted AgI_2^- metal-complexes during the etching of very small features in our test-experiments. The sub-optimal transfer of the reaction by-products in the bulk of the solution resulted, therefore, in the formation of the AgI complex salts in etched regions and, hence, was responsible of the observed "bumpy" structures in the AFM topographies.

To tackle this problem and, at the same time, obtain a slower etching rate, we decided to optimize the etching process by preparing "in-house" (KI)/Iodine (I_2) etchants dissolving raw KI and I_2 powders in DI water. It is well known [61] that the etching rate of KI/I_2 solutions it is extremely sensitive, besides to variations of the temperature, also to the concentration of the reagents. Higher concentrations of I_2 over KI, for example speed up the etching process but do not help to dissolve the etching by-products from the etched areas. The optimization of the silver etching process and the calibration of the etching rate of the home-made KI/I_2 etchants were performed using etch-masks patterned on flat silver substrates. These test-samples were dipped into the etchant bath at room-temperature with no agitation and, after some time, the etching was stopped by soaking them (for~5 min) in DI water rinse beakers. The etched samples were then inspected under the optical microscope and the topography of the etched regions measured by AFM. Table 5.1 reports the estimated etching rates obtained from combined optical and AFM analysis carried out on the test etch-mask immersed in different in-house KI/I_2 etchants prepared by varying the concentration of KI and I_2. As expected, we observed that aqueous solution with a low concentration of I_2 showed a lower etching rate. Moreover, the AFM analysis revealed that solutions at low concentration of I_2 with respect to the concentration of the KI salt did not produced protruding AgI compounds in the etching of small 5μm wide features (see the AFM topography in figure 5.8(c)). As documented in literature,[63] the

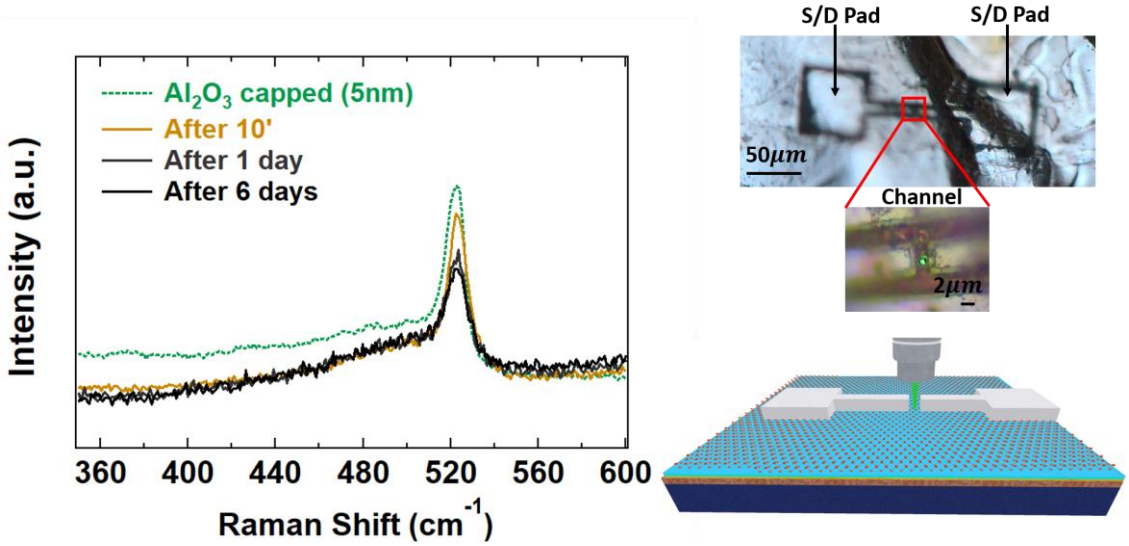

Figure 5.9 Raman spectra of multilayer silicene taken in the 1.2 μm wide channel region of the etched device structure showed in the optical microscope image. The spectra were measured after the etching process, i.e. after 10min, 1 day and 6 days of air-exposure. The Raman spectrum taken on the Al_2O_3 capped samples after the UHV growth (green line) is also shown for comparison. Figures adapted from reference [33]

increase of the concentration of KI improves the solubility of the AgI salts reducing, therefore, the accumulation of etching by-products in the etched regions.

Definition of the devices by wet etching

The optimized KI/I_2 etchants employed in the definition of the device patterns on the delaminated silver substrates were prepared with a typical concentration ratio [KI]/[I2] ≈ 3400. As can be observed from the optical microscope images reported in figure 5.8(d), with this optimized etchant we found that within 50 μm wide square regions the 250 nm thick Ag-substrate was completely etched in ≈5 min. Therefore, the resulting etching-rate was estimated to be of the order of 40–50 nm min^{-1} (see table 5.1). Thin trenches (see Figure 5.8(d)), however, were usually etched faster with an observed etching rate 8–9 times higher but did not show the formation of unwanted "salt-bumps" in the exposed areas.

The difference in the etching rate between large and small exposed areas can be detrimental in the nanofabrication of Xene devices. With our optimized "in-house" etchant the 500 nm wide device channels could be completely etched in 30-40 sec, as illustrated in figure 5.8(d). However, a 40 sec etching bath is not useful to remove the residual Ag from the 2.5 μm wide isolation trenches around the device contact pads. Successive etching baths can help to solve this problem but at expenses of introducing extensive undercutting along the already etched channel regions. We found out that the best strategy to carry out the etching of FET device patterns having channel width below 500 nm was to adopt a two-step patterning/etching process. In the first step only the isolation trenches of the source/drain contact-pads are EBL defined and etched by means of a fast-commercial KI/I_2 etchant. In the second step the thin channel regions between the source and drain contacts are EBL written and then carefully opened by etching with the slower home-made KI/I_2 etchant. Introducing a slow and time-controlled etching step after the EBL patterning of the device channels allowed us to gain a

precise definition of these regions that are crucial for the proper functioning of the silicene devices.

Stability of silicene after the etching

In order to check the survival of the exposed silicene against exposure to our home-made etchant, we defined the FET device structure, showed in Figure 5.9. The resulting ≈1.2 μm wide channel region allowed an easy access to the laser-probe used for the Raman spectroscopy as illustrated in the close-up optical microscope image in figure 5.9. The Raman spectra measured in this region after the etching process, i.e. after 10 minutes, 1 day and 6 days of ambient-air exposure, all matched well with the spectrum of the as-deposited Al_2O_3-capped silicene samples (compare with figure 5.5) thus validating the integrity of the epitaxial multilayer silicene layer after delamination, transfer, and FET device-fabrication process.

5.3.2 Fabrication of an epitaxial phosphorus MIM device

In the following paragraph we will illustrate the fabrication process followed for the realization of epitaxial phosphorus MIM devices envisaging also possible physical mechanisms that can mediate the nonvolatile resistive switching (NVRS) of this devices.

In-situ fabrication of the epitaxial phosphorus MIM structure

The MIM structures were realized on epitaxial phosphorus on Au(111)/mica samples protected by a ~9 nm thick metallic aluminium capping (see figure 5.10(a)) grown in-situ at room-temperature by means of the MBE system of chapter 3.

Thin aluminium films, once exposed to ambient air, are subjected to oxidation. The kinetic of the Al oxidation process is highly dependent on the preparation conditions of the surface, the temperature and the humidity of air and, therefore, the resulting Al oxide thickness is generally estimated to vary between 2 nm and 10 nm. [64], [65] However, the preliminary investigation carried out in Chapter 4 on the air stability of Al_2O_3 capped epitaxial phosphorus samples suggests that also an Al capping thicker than ~5 nm can be adequate in preventing a complete oxidation of the epitaxial phosphorus layer grown on Au(111). Thus, we reasonably expect that the innermost Al atomic planes in a ~9 nm thick MBE-grown Al film should be less prone to be oxidized preserving their metallic character even after a prolonged exposure to ambient air. Therefore, the synthesized epitaxial phosphorus layer turns out to be naturally sandwiched in a MIM structure consisting of a top Au(111) electrode and a bottom in-situ grown Al electrode.

Dry substrate transfer procedure

The main steps followed for the fabrication of the MIM devices are illustrated schematically in the figures 5.10(b)-(d). In order to give a better mechanical resistance to the Au(111)/Epitaxial-P/Al membrane during the subsequent mica delamination and substrate transfer phase the bottom Al electrode was thickened by evaporating an additional Ti\Au (~70 nm) film. Titanium (5 nm) was used to promote the adhesion of the evaporated 70 nm-thick Au film to the topmost oxidized surface of the Al capping. Like in the s-SEDNE method, the complete delamination of the mica was achieved following a dry-approach based on a two tapes exfoliation and transfer procedure. Once delaminated from the mica, the Au(111)/Epitaxial-P/Al/Ti/Au membrane was transferred and attached onto a rigid supporting substrate by means

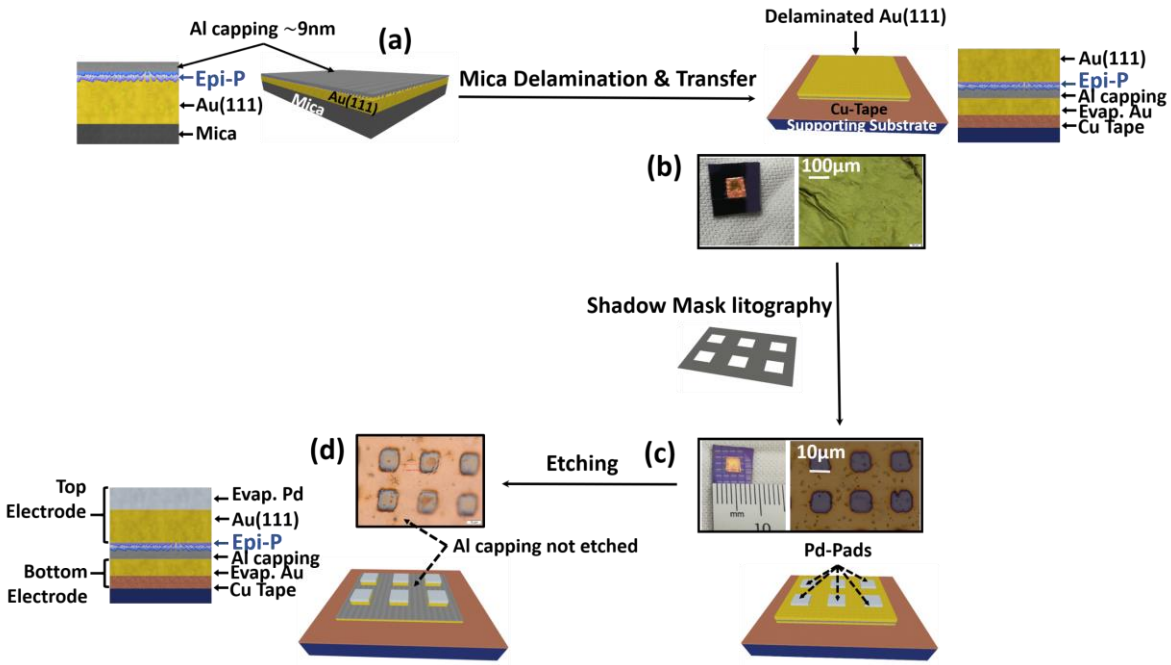

Figure 5.10 Fabrication of a MIM epitaxial phosphorus device**. (a)** Al encapsulated epitaxial phosphours samples are thickened with an additional Au\Ti deposition on top of the oxidized Al capping. **(b)** After the delamination of the mica substrate the Au(111)\Epitaxial-P\Al\Ti\Au membranes are transferred on a rigid supporting substrate. Conductive copper tape together with the Au\Ti evaporated film constitute the common bottom electrode of the MIM devices. **(c)-(d)** The MIM structures are defined by shadow mask lithography evaporating Pd top-electrodes and by subsequently etching the Au(111) exposed regions.

of a double-sided copper tape. The latter worked, in conjunction with the Au\Ti film, as the common bottom electrode of the MIM structures. Interestingly, unlike to what observed in the delamination and transfer of Al_2O_3/silicene/Ag(111) samples, we noticed that the delaminated Au/Ti/Al/Epitaxial-P/Au(111) membranes were characterized by a superior uniformity and surface smoothness with few strain-induced wrinkles on the Au(111) film as demonstrated by the optical microscope image reported in figure 5.10(b). The better results achieved in the delamination and transfer of the Au membranes compared to the case of the Ag ones may be ascribed to the weak adhesion of Au on mica. This fact facilitates the delamination procedure and reduces the strain released into the metallic film.

Definition of the MIM devices by wet etching

The MIM devices were defined, as illustrated in figure 5.10(c), by depositing square palladium pads on top of the delaminated gold surface by shadow mask lithography. The definition of the MIM structures into the native Au(111) substrate was then performed with the aid of a wet chemical etching step. Preliminary etching attempts showed that the exposed regions on the delaminated Au(111) substrate could be completely removed with a 6 min long bath in an undiluted commercial KI/I_2 etchant. The complete etching of the Au(111) substrate was confirmed by the change in the optical contrast (colour) in the exposed Au(111) areas surrounding the Pd-pads (compare the two optical microscope images reported in Figure 5.10(c) and 5.10(d)). It is likely that the $KI\backslash I_2$ etchant did not attack the oxidized Al layers in the etched areas acting as a protective encapsulation for the underlying evaporated Au/Ti bottom electrode. The thin AlO_x/Au/Ti film once exposed to air was responsible for the change in the optical

contrast observed in the optical microscope images. Besides this, we also observed some unwanted etching on the palladium pads, although at a much lower rate. This problem prevented us to achieve a good definition of the vertical MIM devices and clearly demands future process improvements to be solved.

In this respect, a nanofabrication and etching strategy like that already employed in the fabrication of silicene back-gated FETs could be beneficial. Top electrodes could be EBL patterned into a PMMA resist directly on the native Au(111) substrate defining and etching only thick isolation trenches around them. This solution, along with the use of a carefully optimized gold etchant, could have also the additional advantage of reducing the leakage of the electric field lines towards surrounding substrate regions during the electrical probe of the I-V characteristic on the vertical Au/Ti/Al/epitaxial-phosphorus/Au(111) MIM structures.

Proposed mechanisms for the resistive switching in epitaxial phosphorus MIMs

Despite the fabrication process described above is still preliminary and demands improvements the NVRS effect observed in solution-processed phosphorene nanosheets [55], [57], [66] and monolayer TMDs [58], [59], [67] suggests that also Au/Ti/Al/Epitaxial-P/Au(111) MIM devices could possess a similar behaviour. Here we propose two microscopic mechanisms that could provide a possible explanation for the NVRS in these systems.

The first mechanism can be inferred from the studies carried out on solution-processed BP resistive random-access memories (ReRAM). For these devices the trapping/de-trapping of the charge carriers and the rupture/formation of oxygen vacancy filaments through the degraded phosphorene nanosheets are believed to be at the origin of the non-volatile resistive switching.[55], [66] In the case of our vertical MIM structures, we hypothesize that the reversible oxidation of the encapsulated epitaxial phosphorus on gold [68] and the trapping/de-trapping mechanisms of the charge carriers at the Al/Epitaxial-P interface could provide an analogous microscopic mechanism for the non-volatile switching from a low resistance state (LRS) to an high resistance state (HRS). In particular, as we have seen in Chapter 4, both the oxidized Al capping and the semiconducting epitaxial phosphorus layer induce the formation of an interface dipole between the Al/epitaxial-P film and the Au(111) substrate. The internal electric field associated with the interface dipole could drive the MIM structure in a LRS without a preliminary soft-dielectric breakdown (electroforming process) as required in many conventional metal-oxide ReRAM.[69] The induced energy band bending at the Al/epitaxial-P/Au(111) interface may trap the charge carriers and create conductive paths between the top Au(111) and bottom Au/Ti electrodes. The MIM device can be driven from this LRS to an HRS by applying an external electric field with a polarity opposite to the direction of the internal electric field so to invert the band bending at the interface between the oxidized Al capping and Au(111) substrate. In this way the injection of the charge carriers between the two electrodes is prevented. Moreover, the device could be maintained in this HRS thanks to the formation of an interfacial phosphorus oxide layer caused by the electric field induced migration of oxygen ions through the (sub-stoichiometric) air-oxidized aluminium. If a sufficient voltage of opposite polarity is applied again, the reversible oxidation effect of the epitaxial phosphorus layer could, in principle, release the oxygen ions in the Al capping restoring, in this way, the original band bending condition that brings the device in a LRS state. The microscopic mechanism hypothesized above could work both in the in-situ Al_2O_3 and in the air-oxidized Al encapsulated

epitaxial phosphorus samples provided that the capping layer has a good dielectric quality (see the discussion at the end of Chapter 4).

A second possible mechanism that we hypothesize for the NVRS could be based on the dissociation-diffusion-adsorption (DDA) model used to explain the resistive switching in single layer TMD and hBN memristors [58], [59], [70], [67] In detail: under the effect of an external electric field a metal atom (or ion) can dissociate from the Al electrode and, then, diffuse and be adsorbed in a defective site (for example a vacancy) of the epitaxial phosphorus lattice. The adsorbed atom (ion) may act as a conductive point channel through the semiconducting epitaxial phosphorus layer driving the MIM device in a LRS. When an electric field of opposite polarity is applied the current through the conductive point channel can increase and provide enough energy to move the Al atom (or ion) away from the defective site so to bring the MIM device in a HRS. Despite the DDA model is well supported by STM/STS investigations in MoS_2 atomic sheets, [67] it may not be valid in the case of epitaxial phosphorus grown on Au(111) due to the porous nature of its atomic structure described in terms of an Au-P framework (see Chapter 3). However, if this fact can become an issue for the observation of the NVRS due to the disconnected nature of the Au-P framework, it does not prevent the observation of NVRS effects in epitaxial phosphorus on a more local (nanometer) scale. In fact, given the speculated semiconducting nature of blue-phosphorene, each disconnected blue-phosphorene islands of the Au-P framework structure, could show a NVRS effect mediated by point defects that can be eventually probed with the aid of local STM transport measurement.

In conclusion, the above-discussed mechanisms for the NVRS effect and the preliminary results achieved in the fabrication of epitaxial phosphorus MIM devices pave the way for forthcoming researches aiming to investigate memory or, more in general, memristive effects in any epitaxial phosphorus 2D polymorph.

Bibliography

[1] J. Kang, D. Shin, S. Bae, and B. H. Hong, “Graphene transfer: key for applications,” *Nanoscale*, vol. 4, no. 18, p. 5527, 2012, doi: 10.1039/c2nr31317k.

[2] F. Bonaccorso, A. Lombardo, T. Hasan, Z. Sun, L. Colombo, and A. C. Ferrari, “Production and processing of graphene and 2d crystals,” *Materials Today*, vol. 15, no. 12, pp. 564–589, Dec. 2012, doi: 10.1016/S1369-7021(13)70014-2.

[3] C. R. Dean *et al.*, “Boron nitride substrates for high-quality graphene electronics,” *Nature Nanotechnology*, vol. 5, no. 10, pp. 722–726, Oct. 2010, doi: 10.1038/nnano.2010.172.

[4] A. Reina *et al.*, “Transferring and Identification of Single- and Few-Layer Graphene on Arbitrary Substrates,” *J. Phys. Chem. C*, vol. 112, no. 46, pp. 17741–17744, Nov. 2008, doi: 10.1021/jp807380s.

[5] F. Bonaccorso, Z. Sun, T. Hasan, and A. C. Ferrari, “Graphene photonics and optoelectronics,” *Nature Photon*, vol. 4, no. 9, pp. 611–622, Sep. 2010, doi: 10.1038/nphoton.2010.186.

[6] A. S. Mayorov *et al.*, “Micrometer-Scale Ballistic Transport in Encapsulated Graphene at Room Temperature,” *Nano Letters*, vol. 11, no. 6, pp. 2396–2399, Jun. 2011, doi: 10.1021/nl200758b.

[7] H. Kaur *et al.*, “Large Area Fabrication of Semiconducting Phosphorene by Langmuir-Blodgett Assembly,” *Sci Rep*, vol. 6, no. 1, p. 34095, Dec. 2016, doi: 10.1038/srep34095.

[8] X. Li *et al.*, “Highly conducting graphene sheets and Langmuir–Blodgett films,” *Nature Nanotech*, vol. 3, no. 9, pp. 538–542, Sep. 2008, doi: 10.1038/nnano.2008.210.

[9] J. Li, M. C. Lemme, and M. Östling, “Inkjet Printing of 2D Layered Materials,” *ChemPhysChem*, vol. 15, no. 16, pp. 3427–3434, Nov. 2014, doi: 10.1002/cphc.201402103.

[10] Y. Hernandez *et al.*, "High-yield production of graphene by liquid-phase exfoliation of graphite," *Nature Nanotech*, vol. 3, no. 9, pp. 563–568, Sep. 2008, doi: 10.1038/nnano.2008.215.

[11] S. Bae *et al.*, "Roll-to-roll production of 30-inch graphene films for transparent electrodes," *Nature Nanotechnology*, vol. 5, no. 8, pp. 574–578, Aug. 2010, doi: 10.1038/nnano.2010.132.

[12] A. Shivayogimath *et al.*, "Do-It-Yourself Transfer of Large-Area Graphene Using an Office Laminator and Water," *Chem. Mater.*, vol. 31, no. 7, pp. 2328–2336, Apr. 2019, doi: 10.1021/acs.chemmater.8b04196.

[13] X. Li *et al.*, "Large-Area Synthesis of High-Quality and Uniform Graphene Films on Copper Foils," *Science*, vol. 324, no. 5932, pp. 1312–1314, Jun. 2009, doi: 10.1126/science.1171245.

[14] K. S. Kim *et al.*, "Large-scale pattern growth of graphene films for stretchable transparent electrodes," *Nature*, vol. 457, no. 7230, pp. 706–710, Feb. 2009, doi: 10.1038/nature07719.

[15] S. J. Kang *et al.*, "Inking Elastomeric Stamps with Micro-Patterned, Single Layer Graphene to Create High-Performance OFETs," *Adv. Mater.*, vol. 23, no. 31, pp. 3531–3535, Aug. 2011, doi: 10.1002/adma.201101570.

[16] E. H. Lock *et al.*, "High-Quality Uniform Dry Transfer of Graphene to Polymers," *Nano Lett.*, vol. 12, no. 1, pp. 102–107, Jan. 2012, doi: 10.1021/nl203058s.

[17] T. Yoon, W. C. Shin, T. Y. Kim, J. H. Mun, T.-S. Kim, and B. J. Cho, "Direct Measurement of Adhesion Energy of Monolayer Graphene As-Grown on Copper and Its Application to Renewable Transfer Process," *Nano Lett.*, vol. 12, no. 3, pp. 1448–1452, Mar. 2012, doi: 10.1021/nl204123h.

[18] E. S. Walker *et al.*, "Large-Area Dry Transfer of Single-Crystalline Epitaxial Bismuth Thin Films," *Nano Letters*, vol. 16, no. 11, pp. 6931–6938, Nov. 2016, doi: 10.1021/acs.nanolett.6b02931.

[19] J. D. Caldwell *et al.*, "Technique for the Dry Transfer of Epitaxial Graphene onto Arbitrary Substrates," *ACS Nano*, vol. 4, no. 2, pp. 1108–1114, Feb. 2010, doi: 10.1021/nn901585p.

[20] S. Unarunotai *et al.*, "Transfer of graphene layers grown on SiC wafers to other substrates and their integration into field effect transistors," *Appl. Phys. Lett.*, vol. 95, no. 20, p. 202101, Nov. 2009, doi: 10.1063/1.3263942.

[21] F. Liu *et al.*, "Disassembling 2D van der Waals crystals into macroscopic monolayers and reassembling into artificial lattices," *Science*, vol. 367, no. 6480, pp. 903–906, Feb. 2020, doi: 10.1126/science.aba1416.

[22] L. Tao *et al.*, "Silicene field-effect transistors operating at room temperature," *Nature Nanotechnology*, vol. 10, no. 3, pp. 227–231, Feb. 2015, doi: 10.1038/nnano.2014.325.

[23] D. Tsoutsou, E. Xenogiannopoulou, E. Golias, P. Tsipas, and A. Dimoulas, "Evidence for hybrid surface metallic band in (4 × 4) silicene on Ag(111)," *Applied Physics Letters*, vol. 103, no. 23, p. 231604, Dec. 2013, doi: 10.1063/1.4841335.

[24] P. Wagner, M. Hegner, H.-J. Guentherodt, and G. Semenza, "Formation and in Situ Modification of Monolayers Chemisorbed on Ultraflat Template-Stripped Gold Surfaces," *Langmuir*, vol. 11, no. 10, pp. 3867–3875, Oct. 1995, doi: 10.1021/la00010a043.

[25] M. Hegner, P. Wagner, and G. Semenza, "Ultralarge atomically flat template-stripped Au surfaces for scanning probe microscopy," *Surface Science*, vol. 291, no. 1–2, pp. 39–46, Jul. 1993, doi: 10.1016/0039-6028(93)91474-4.

[26] N. Vogel, J. Zieleniecki, and I. Köper, "As flat as it gets: ultrasmooth surfaces from template-stripping procedures," *Nanoscale*, vol. 4, no. 13, p. 3820, 2012, doi: 10.1039/c2nr30434a.

[27] A. Molle, C. Grazianetti, L. Tao, D. Taneja, Md. H. Alam, and D. Akinwande, "Silicene, silicene derivatives, and their device applications," *Chemical Society Reviews*, vol. 47, no. 16, pp. 6370–6387, 2018, doi: 10.1039/C8CS00338F.

[28] J. J. Blackstock, Z. Li, and G. Jung, "Template stripping using cold welding," *J. Vac. Sci. Technol. A*, vol. 22, no. 3, p. 602, 2004, doi: 10.1116/1.1710492.

[29] H. K. Sahoo, L. Ottaviano, Y. Zheng, O. Hansen, and K. Yvind, "Low temperature bonding of heterogeneous materials using Al_2O_3 as an intermediate layer," *Journal of Vacuum Science & Technology B, Nanotechnology and Microelectronics: Materials, Processing, Measurement, and Phenomena*, vol. 36, no. 1, p. 011202, Jan. 2018, doi: 10.1116/1.5005591.

[30] J. Diebel, H. Löwe, P. Samorí, and J. P. Rabe, "Fabrication of large-scale ultra-smooth metal surfaces by a replica technique," *Appl Phys A*, vol. 73, no. 3, pp. 273–279, Sep. 2001, doi: 10.1007/s003390100935.

[31] E. A. Weiss, G. K. Kaufman, J. K. Kriebel, Z. Li, R. Schalek, and G. M. Whitesides, "Si/SiO_2-Templated Formation of Ultraflat Metal Surfaces on Glass, Polymer, and Solder Supports: Their Use as Substrates for Self-Assembled Monolayers," *Langmuir*, vol. 23, no. 19, pp. 9686–9694, Sep. 2007, doi: 10.1021/la701919r.

[32] C. Grazianetti, G. Faraone, C. Martella, E. Bonera, and A. Molle, "Embedding epitaxial (blue) phosphorene in between device-compatible functional layers," *Nanoscale*, vol. 11, no. 39, pp. 18232–18237, 2019, doi: 10.1039/C9NR06037E.

[33] C. Martella *et al.*, "Disassembling Silicene from Native Substrate and Transferring onto an Arbitrary Target Substrate," *Adv. Funct. Mater.*, p. 2004546, Aug. 2020, doi: 10.1002/adfm.202004546.

[34] R. Arafune *et al.*, "Structural transition of silicene on Ag(111)," *Surface Science*, vol. 608, pp. 297–300, Feb. 2013, doi: 10.1016/j.susc.2012.10.022.

[35] P. Moras, T. O. Mentes, P. M. Sheverdyaeva, A. Locatelli, and C. Carbone, "Coexistence of multiple silicene phases in silicon grown on Ag(1 1 1)," *J. Phys.: Condens. Matter*, vol. 26, no. 18, p. 185001, May 2014, doi: 10.1088/0953-8984/26/18/185001.

[36] C. Grazianetti, D. Chiappe, E. Cinquanta, M. Fanciulli, and A. Molle, "Nucleation and temperature-driven phase transitions of silicene superstructures on Ag(1 1 1)," *Journal of Physics: Condensed Matter*, vol. 27, no. 25, p. 255005, Jun. 2015, doi: 10.1088/0953-8984/27/25/255005.

[37] P. Vogt *et al.*, "Synthesis and electrical conductivity of multilayer silicene," *Appl. Phys. Lett.*, vol. 104, no. 2, p. 021602, Jan. 2014, doi: 10.1063/1.4861857.

[38] C. Grazianetti *et al.*, "Silicon Nanosheets: Crossover between Multilayer Silicene and Diamond-like Growth Regime," *ACS Nano*, vol. 11, no. 3, pp. 3376–3382, Mar. 2017, doi: 10.1021/acsnano.7b00762.

[39] P. De Padova *et al.*, "Evidence of Dirac fermions in multilayer silicene," *Applied Physics Letters*, vol. 102, no. 16, p. 163106, Apr. 2013, doi: 10.1063/1.4802782.

[40] C. Grazianetti, E. Cinquanta, and A. Molle, "Two-dimensional silicon: the advent of silicene," *2D Materials*, vol. 3, no. 1, p. 012001, Jan. 2016, doi: 10.1088/2053-1583/3/1/012001.

[41] D. Solonenko *et al.*, "2D vibrational properties of epitaxial silicene on Ag(111)," *2D Materials*, vol. 4, no. 1, p. 015008, Oct. 2016, doi: 10.1088/2053-1583/4/1/015008.

[42] D. Solonenko, O. D. Gordan, G. Le Lay, D. R. T. Zahn, and P. Vogt, "Comprehensive Raman study of epitaxial silicene-related phases on Ag(111)," *Beilstein J. Nanotechnol.*, vol. 8, pp. 1357–1365, Jul. 2017, doi: 10.3762/bjnano.8.137.

[43] E. Cinquanta *et al.*, "Getting through the Nature of Silicene: An sp^2–sp^3 Two-Dimensional Silicon Nanosheet," *The Journal of Physical Chemistry C*, vol. 117, no. 32, pp. 16719–16724, Aug. 2013, doi: 10.1021/jp405642g.

[44] P. De Padova *et al.*, "24 h stability of thick multilayer silicene in air," *2D Materials*, vol. 1, no. 2, p. 021003, Aug. 2014, doi: 10.1088/2053-1583/1/2/021003.

[45] L. Chua, "Memristor, Hodgkin–Huxley, and Edge of Chaos," *Nanotechnology*, vol. 24, no. 38, p. 383001, Sep. 2013, doi: 10.1088/0957-4484/24/38/383001.

[46] L. Chua, "If it's pinched it's a memristor," *Semicond. Sci. Technol.*, vol. 29, no. 10, p. 104001, Oct. 2014, doi: 10.1088/0268-1242/29/10/104001.

[47] A. Chen, "A review of emerging non-volatile memory (NVM) technologies and applications," *Solid-State Electronics*, vol. 125, pp. 25–38, Nov. 2016, doi: 10.1016/j.sse.2016.07.006.

[48] F. Hui *et al.*, "Graphene and Related Materials for Resistive Random Access Memories," *Adv. Electron. Mater.*, vol. 3, no. 8, p. 1600195, Aug. 2017, doi: 10.1002/aelm.201600195.

[49] S. Bertolazzi *et al.*, "Nonvolatile Memories Based on Graphene and Related 2D Materials," *Adv. Mater.*, vol. 31, no. 10, p. 1806663, Mar. 2019, doi: 10.1002/adma.201806663.

[50] G. Cao *et al.*, "2D Material Based Synaptic Devices for Neuromorphic Computing," *Adv. Funct. Mater.*, p. 2005443, Oct. 2020, doi: 10.1002/adfm.202005443.

[51] W. Huh, D. Lee, and C. Lee, "Memristors Based on 2D Materials as an Artificial Synapse for Neuromorphic Electronics," *Adv. Mater.*, vol. 32, no. 51, p. 2002092, Dec. 2020, doi: 10.1002/adma.202002092.

[52] J. L. Zhang *et al.*, "Epitaxial Growth of Single Layer Blue Phosphorus: A New Phase of Two-Dimensional Phosphorus," *Nano Letters*, vol. 16, no. 8, pp. 4903–4908, Aug. 2016, doi: 10.1021/acs.nanolett.6b01459.

[53] E. Golias, M. Krivenkov, A. Varykhalov, J. Sánchez-Barriga, and O. Rader, "Band renormalization of blue phosphorus on Au(111)," *arXiv:1803.08862 [cond-mat]*, Mar. 2018, Accessed: May 19, 2018. [Online]. Available: http://arxiv.org/abs/1803.08862.

[54] W. Zhang *et al.*, "Epitaxial Synthesis of Blue Phosphorene," *Small*, vol. 14, no. 51, p. 1804066, Dec. 2018, doi: 10.1002/smll.201804066.

[55] C. Hao *et al.*, "Liquid-Exfoliated Black Phosphorous Nanosheet Thin Films for Flexible Resistive Random Access Memory Applications," *Adv. Funct. Mater.*, vol. 26, no. 12, pp. 2016–2024, Mar. 2016, doi: 10.1002/adfm.201504187.

[56] H. Tian *et al.*, "A Dynamically Reconfigurable Ambipolar Black Phosphorus Memory Device," *ACS Nano*, vol. 10, no. 11, pp. 10428–10435, Nov. 2016, doi: 10.1021/acsnano.6b06293.

[57] Y. Zhou *et al.*, "Black Phosphorus Based Multicolor Light-Modulated Transparent Memristor with Enhanced Resistive Switching Performance," *ACS Appl. Mater. Interfaces*, vol. 12, no. 22, pp. 25108–25114, Jun. 2020, doi: 10.1021/acsami.0c04493.

[58] R. Ge *et al.*, "Atomristor: Nonvolatile Resistance Switching in Atomic Sheets of Transition Metal Dichalcogenides," *Nano Letters*, vol. 18, no. 1, pp. 434–441, Jan. 2018, doi: 10.1021/acs.nanolett.7b04342.

[59] R. Ge *et al.*, "A Library of Atomically Thin 2D Materials Featuring the Conductive-Point Resistive Switching Phenomenon," *Adv. Mater.*, p. 2007792, Dec. 2020, doi: 10.1002/adma.202007792.

[60] G. L. Bottger and C. V. Damsgard, "Raman Scattering in Wurtzite-Type AgI Crystals," *The Journal of Chemical Physics*, vol. 57, no. 3, pp. 1215–1218, Aug. 1972, doi: 10.1063/1.1678379.

[61] T. A. Green, "Gold etching for microfabrication," *Gold Bull*, vol. 47, no. 3, pp. 205–216, Sep. 2014, doi: 10.1007/s13404-014-0143-z.
[62] L. Gabette, R. Segaud, S. Fadloun, X. Avale, and P. Besson, "Gold Wet Etch Optimization on 200mm Substrates for MEMS Applications," *ECS Trans.*, vol. 25, no. 5, pp. 337–344, Dec. 2019, doi: 10.1149/1.3202671.
[63] U. P. Shinde, H. S. Aher, and T. B. Pawar, "Solubility and Density of Silver Iodide in Water and DMF at Various Temperatures as Function of Potassium Iodide.," *IOSR JAP*, vol. 09, no. 04, pp. 64–67, Jul. 2017, doi: 10.9790/4861-0904016467.
[64] R. W. Revie and H. H. Uhlig, *Corrosion and Corrosion Control*. Hoboken, NJ, USA: John Wiley & Sons, Inc., 2008.
[65] Wm. H. Krueger and S. R. Pollack, "The initial oxidation of aluminum thin films at room temperature," *Surface Science*, vol. 30, no. 2, pp. 263–279, Apr. 1972, doi: 10.1016/0039-6028(72)90002-7.
[66] Y.-L. Hsieh, W.-H. Su, C.-C. Huang, and C.-Y. Su, "Solution-processed black phosphorus nanoflakes for integrating nonvolatile resistive random access memory and the mechanism unveiled," *Nanotechnology*, vol. 30, no. 44, p. 445702, Nov. 2019, doi: 10.1088/1361-6528/ab3606.
[67] S. M. Hus *et al.*, "Observation of single-defect memristor in an MoS2 atomic sheet," *Nat. Nanotechnol.*, Nov. 2020, doi: 10.1038/s41565-020-00789-w.
[68] J. L. Zhang *et al.*, "Reversible Oxidation of Blue Phosphorus Monolayer on Au(111)," *Nano Lett.*, vol. 19, no. 8, pp. 5340–5346, Aug. 2019, doi: 10.1021/acs.nanolett.9b01796.
[69] H.-S. P. Wong *et al.*, "Metal–Oxide RRAM," *Proc. IEEE*, vol. 100, no. 6, pp. 1951–1970, Jun. 2012, doi: 10.1109/JPROC.2012.2190369.
[70] X. Wu *et al.*, "Thinnest Nonvolatile Memory Based on Monolayer h-BN," *Adv. Mater.*, vol. 31, no. 15, p. 1806790, Apr. 2019, doi: 10.1002/adma.201806790.

CHAPTER 6

Conclusions and Perspectives

The interest in elemental 2D materials beyond graphene flourished over the past few years driven by both the scientific curiosity on their unique physical and chemical properties and by the disruptive impact that these materials can have in a wide range of technological areas such as nanoelectronics, sensing, spintronics, photonics, thermoelectrics, and energy systems.[1] However, any perspective technological implementation of such materials should always rely on the design of a feasible device integration scheme that, starting from the challenges involved in the material synthesis, can bring the 2D layer into a suitable device architecture that fully exploits the potential of its atomic and electronic structure.

Within this framework, the present thesis work has dealt with the investigation of the unresolved bottlenecks that prevent the establishment of a feasible path for the integration of 2D phosphorus allotropes in device architectures. In particular, we considered the case of 2D α-P (phosphorene) and 2D β-P (blue phosphorene) phases. These two phases are the most energetically stable among the 2D phosphorus allotropes and due to their peculiar optical, electronic, thermal and mechanical properties are among the possible 2D candidates for the realization of next generation electronic and optoelectronic ultra-scaled devices that can expand the potential of the post-graphene nanotechnology.

6.1 Results achieved and research perspectives for 2D α-P

The integration of the 2D α-P (phosphorene) phase in device architectures relies on a well consolidated path that has led to diverse technological applications in many areas. To date, the only way to obtain high crystalline quality 2D α-P samples is by means of top-down approaches based on the mechanical exfoliation of layered black phosphorus (BP) crystals. Such synthesis methods have two main bottlenecks:

- the lack of control on the thickness of the exfoliated crystallites (flakes) and,
- a not-scalable approach for the preparation of single layer and uniform 2D α-P crystals on large areas.

Among these two bottlenecks the latter can be considered almost intrinsic to the nature of the exfoliation methods and can be solved only shifting towards bottom up epitaxial growth techniques. The former bottleneck, instead, can be tackled by acting on two aspects:

i. investigating a quick method for the measurement of the thickness of few and multilayer BP flakes and,
ii. envisaging a controllable thickness reduction technique.

In this thesis work, the first aspect has been addressed by revisiting Raman spectroscopy as a metrological tool to estimate the thickness of multilayer black phosphorus flakes. These flakes are the most frequently obtained from any exfoliation procedure and our proposed Raman thickness determination method has provided a quick approach for the discrimination of the thickness of BP flakes in a range between 5nm and 100nm that is also able to take into account the intrinsic anisotropy of BP crystals.[2] Regarding the second aspect, we have specifically dealt with techniques based on the laser thinning of the exfoliated flakes. These approaches have the advantage of their versatility since they allow a localized material thinning and a simultaneous control of the thickness when coupled with an optical characterization technique such as the Raman spectroscopy. In order to improve the efficiency of these techniques we have

studied how the supporting SiO_2/Si substrates, on which the BP flakes are commonly prepared, influence the laser ablation process. In particular, we analysed in detail the laser heating and ablation in BP flakes exfoliated in two different thickness ranges, i.e. *thick* BP flakes in the 0.3-1.2μm range and *thin* BP flakes in the 10-120nm range, by means of Raman thermometry experiments and numerical calculation of the heat diffusion problem. We have understood that the laser heating and ablation of BP flakes can be affected by optical, thermal and even mechanical effects due to the substrate. Such effects can also influence the Raman measured temperatures when estimated from the shifts of the Raman peak positions. From this point of view, this study has opened two future **research perspectives** regarding:

(i) the optimization of the laser thinning technique by, for example, a careful substrate engineering or choice of the laser processing parameters so as to achieve the thinning of multilayer BP flakes toward the ultimate 2D α-P limit.

(ii) a better understanding of the temperature measurements by means of a Raman thermometry approach. This technique is commonly used in the investigations of the thermal properties of 2D materials and further researchers along this direction could move into the examination of the thermal properties of thin BP flakes supported on different substrates in order to gain a better insight into the mechanisms regulating the nanoscale heat dissipation in phosphorene devices.

6.2 Results achieved and research perspectives for 2D β-P

Compared to the 2D α-P (phosphorene) phase the 2D β-P polymorph (blue-phosphorene) presents challenges in all the steps of the device integration path: from the synthesis, that has to be necessarily carried out by epitaxy, to the oxidation and stabilization outside the UHV growth environment up to the design of proper manipulation schemes for the transfer on substrates suitable for the device fabrication.

Synthesis

Regarding the epitaxial synthesis, the choice of the substrate is the first challenge that has to be faced in order to ensure not only a large area and scalable growth but also the accessibility of the epitaxial material to any subsequent ex-situ processing. In this respect, the epitaxial growth of 2D β-P has been investigated on Au(111)/mica substrates rather than on bulk Au(111) crystals since the layered nature of mica allowed an easy manipulation of the epitaxial phosphorus/Au(111) membrane during the subsequent ex-situ processing phase. By means of a careful STM analysis we have seen that, despite its large area and crystalline growth, the atomic structure of epitaxial phosphorus on Au(111)/mica does not match exactly the crystal structure of an epitaxial 2D layer of β-P (blue phosphorene).[3] In particular, in this thesis work we have provided evidences in support of a model that describes epitaxial phosphorus on Au(111) as a gold-phosphorus *porous* framework where β-P domains are decorated by Au atoms . However, we have also noticed that such model is not able to explain the observed semiconducting character of epitaxial phosphorus on gold obtained via STS measurements (and ARPES). Clearly, such discrepancies between the electronic properties deduced from the atomic structure

and those directly measured on the as-grown material require further investigations to be fully understood. In this regard, we have envisaged two future **research perspectives**:

(i) The study of proper strategies to decouple the epitaxial 2D β-P layer from the Au(111) substrate in order to access to its intrinsic electronic properties

(ii) The realization of ordered nanostructures in two-dimension on the gold-phosphorus *porous* framework by means of surface functionalization with foreign molecules or atomic species.

Both these approaches have the advantage to achieve the on-demand tailoring of the electronic properties of epitaxial phosphorus/Au(111) and represent added values in the synthesis and processing of this epitaxial form of phosphorus.

Oxidation

The high chemical reactivity in environmental conditions is the next big challenge to face along the way for the device integration of 2D β-P. In order to achieve a better understanding of the oxidation mechanism of 2D β-P we have studied the oxidation of epitaxial phosphorus grown on Au(111). Despite there are still doubts regarding the correct identification of this epitaxial form of phosphorus with an epitaxial 2D layer of β-P (blue-phosphorene), the studies that we have carried out along this direction can be considered as the initial steps towards a better comprehension of the oxidation mechanism in blue phosphorene. In particular, by exposing the as-grown material to a controlled oxygen rich atmosphere, we found out that epitaxial phosphorus grown on Au(111) shows an exceptional endurance to oxidation compared to other epitaxial monoelemental 2D materials grown on metals such as, for example, Silicene on Ag(111).[3] Moreover, with the aid of STM measurements, we deduced that the degradation mechanism of epitaxial phosphorus on Au(111) is similar to that of 2D α-P (phosphorene) in which the first stages of the reaction involves the chemisorption of oxygen molecules on the pristine surface of the material. However, additional investigations are required in order to fully understand the air instability of epitaxial phosphorus and resolve open questions such as the chemical reactivity with water, alone or in combination with oxygen, as well as the influence of the exposure to light. Such kind of investigations can open also future **research perspectives** towards:

(i) The realization of a fully oxidized form of 2D β-P (blue-phosphorene) via a controlled oxidation process. From a scientific point of view, this surface functionalized form of blue phosphorene is highly attractive due to its theoretically predicted strain tunable quantum phase transitions in which the charge carriers behave according to novel 2D quantum properties.[4]

(ii) The implementation of epitaxial phosphorus on gold in gas sensors [5] or photocatalytic devices for solar water splitting reactions.[6] From a technological point of view the operating principle of these devices can exploit the peculiar interaction pathway of epitaxial phosphorus with water, oxygen and other molecular species.

Stabilization

For many technological applications in nanoelectronics such as, for example, field effect transistor [7] and memory devices the research of suitable strategies to stop or slow down as much as possible the interaction of epitaxial phosphorus with external oxidizing agents is a

highly desired objective. In this respect, we have investigated the effectiveness of a protection strategy based on the in-situ deposition of an Al_2O_3 capping layer on epitaxial phosphorus/Au(111) samples. With the aid of both in-situ and ex-situ XPS measurements, we have proved that an Al_2O_3 capping layer of ~5 nm can effectively preserve the integrity of epitaxial phosphorus grown on Au(111) and, at the same time, slow down the degradation process when the samples are exposed to air.[3], [8] However, such thin Al_2O_3 encapsulation is not able to fully prevent the degradation of epitaxial phosphorus on longer timescales, i.e. of the order of several months. In order to circumvent this roadblock, we have suggested that a possible strategy can rely on the ex-situ thickening of the Al_2O_3 capping with the deposition of an additional high-quality Al_2O_3 film grown via atomic layer deposition. This approach may help not only to minimize the oxidation problem observed on longer timescales but also reduce the dielectric reliability problems observed ex-situ by means of c-AFM measurements. Moreover, an additional advantage offered by a thicker Al_2O_3 capping could be in an improved mechanical stability of the Al_2O_3/Epitaxial-P/Au(111) membrane during the ex-situ manipulation phases. Further **research perspectives** on the Al_2O_3 stabilization of epitaxial phosphorus/Au(111) samples may be addressed towards two aspects:

(i) Researching the optimal thickness of the Al_2O_3 encapsulation or the optimal ex-situ strategy to fully stop the degradation process of epitaxial phosphorus on grown on Au(111).

(ii) A better understanding of the electrostatics and energy bands alignment at the interface between the MBE grown Al_2O_3 capping layer and the epitaxial-phosphorus/Au(111) substrate. Such investigation, as we have seen in Chapter 5, may provide preliminary insights into the possibility to control the charge carrier polarity at the Al_2O_3/epitaxial phosphorus interface which can be of relevance, besides for transistors, also for memory applications as suggested by the case of the Al_2O_3 encapsulated few layers phosphorene.[9]

Substrate transfer methods and devices fabrication

The lack of a proper methodology for the ex-situ manipulation is the last roadblock along any prospective device implementation of the 2D β-P allotropic form of phosphorus. With reference to the case of epitaxial phosphorus grown on Au(111)/mica substrates, any solution conceived to confront with this problem must include two steps:

- the delamination of the mica supporting substrate from the metallic Au(111) film, and
- the transfer of the delaminated Al_2O_3/Epitaxial-P/Au(111) membrane on a new target substrate on which the subsequent device fabrication needs to be performed.

In this respect, we have proposed two preliminary strategies that differ in terms of the method used for the delamination of mica from the thin metallic membrane:

i. a *wet* approach based on a chemical-aided cleavage process of mica and
ii. a *dry* approach based on a two-tape mechanical delamination of mica.[10]

Both these approaches are able to achieve the transfer of the delaminated Al_2O_3/Epitaxial-P/Au(111) membrane on a (rigid or flexible) target substrate and possess a certain degree of universality offering generalization to the case of other epitaxial monoelemental 2D materials (Xenes) grown on metal/mica. However, we observed that both the investigated approaches

require further optimization in order to solve some critical issues. In particular, the most relevant issues regard:

- the use of adhesives to attach the delaminated membrane on the target substrate, and
- the scarce uniformity of the delaminated metallic substrate after the delamination of the mica.

Both these problems may critically affect the subsequent device processing steps and reduce the device fabrication yield.

Nevertheless, both the proposed *wet* and *dry* manipulation procedures offer promising alternatives for the integration of epitaxial phosphorus grown on Au(111)/mica or, generally, any other epitaxial 2D Xene grown on metal/mica in device architectures. This possibility has been de facto explored examining the fabrication process of two possible device architectures: a FET device and a MIM device. Both these device architectures have been realized following the steps of the *dry* approach for the manipulation of epitaxial 2D Xenes on metal/mica substrates. In particular, the FET device architecture was implemented in the case of Al_2O_3 encapsulated multilayer silicene samples grown on Ag(111)/mica. The entire multilayer silicene device fabrication process (termed s-SEDNE), from the delamination of the mica substrate to the final fabrication of the transistor electrodes, can be viewed as an improvement of the original process conceived in literature for the fabrication of the silicene FET transistor.[11] The MIM device architecture, instead, has been realized on epitaxial phosphorus on gold samples opening the possibility to further **research perspectives** aiming to achieve:

(i) A better understanding of the electronic structure of epitaxial phosphorus grown on Au(111) when sandwiched between two metallic electrodes via the "ex-situ" electrical characterization of the material;

(ii) An experimental and theoretical study of resistive switching phenomena in AlO_x encapsulated epitaxial phosphorus/Au(111) membranes for future applications in ultra-scaled non-volatile memory devices.

Conclusion

In a general overview, the issues we analyzed and the solution provided along each step of the device integration process of the α-P and β-P 2D phosphorus polymorphs, despite being in many cases preliminary and requiring further researches for their optimization, acquire a particular relevance in any competitive assessment of the strength, weaknesses, opportunities and threats (in a so-called SWOT analysis) of any forthcoming 2D phosphorus technological application. Such kind of assessment is ultimately the first step for any meaningful road-mapping attempt aiming to foster the development of emergent technologies based on the family of 2D monoelemental materials beyond graphene.

Bibliography

[1] N. R. Glavin *et al.*, "Emerging Applications of Elemental 2D Materials," *Adv. Mater.*, vol. 32, no. 7, p. 1904302, Feb. 2020, doi: 10.1002/adma.201904302.

[2] G. Faraone, E. Balduzzi, C. Martella, C. Grazianetti, A. Molle, and E. Bonera, "Thickness determination of anisotropic van der Waals crystals by Raman spectroscopy: the case of black phosphorus.," *Nanotechnology*, Jun. 2020, doi: 10.1088/1361-6528/ab9d3f.

[3] C. Grazianetti, G. Faraone, C. Martella, E. Bonera, and A. Molle, "Embedding epitaxial (blue) phosphorene in between device-compatible functional layers," *Nanoscale*, vol. 11, no. 39, pp. 18232–18237, Oct. 2019, doi: 10.1039/C9NR06037E.

[4] L. Zhu *et al.*, "Blue Phosphorene Oxide: Strain-Tunable Quantum Phase Transitions and Novel 2D Emergent Fermions," *Nano Lett.*, vol. 16, no. 10, pp. 6548–6554, Oct. 2016, doi: 10.1021/acs.nanolett.6b03208.

[5] N. Liu and S. Zhou, "Gas adsorption on monolayer blue phosphorus: implications for environmental stability and gas sensors," *Nanotechnology*, vol. 28, no. 17, p. 175708, Apr. 2017, doi: 10.1088/1361-6528/aa6614.

[6] S. Zhou, N. Liu, and J. Zhao, "Phosphorus quantum dots as visible-light photocatalyst for water splitting," *Computational Materials Science*, vol. 130, pp. 56–63, Apr. 2017, doi: 10.1016/j.commatsci.2017.01.009.

[7] J. Wang *et al.*, "Performance of Monolayer Blue Phosphorene Double-Gate MOSFETs from the First Principles," *ACS Appl. Mater. Interfaces*, vol. 11, no. 23, pp. 20956–20964, Jun. 2019, doi: 10.1021/acsami.9b02192.

[8] A. Molle *et al.*, "Stability and universal encapsulation of epitaxial Xenes," *Faraday Discuss.*, p. 10.1039.C9FD00121B, 2020, doi: 10.1039/C9FD00121B.

[9] H. Tian *et al.*, "A Dynamically Reconfigurable Ambipolar Black Phosphorus Memory Device," *ACS Nano*, vol. 10, no. 11, pp. 10428–10435, Nov. 2016, doi: 10.1021/acsnano.6b06293.

[10] C. Martella *et al.*, "Disassembling Silicene from Native Substrate and Transferring onto an Arbitrary Target Substrate," *Adv. Funct. Mater.*, p. 2004546, Aug. 2020, doi: 10.1002/adfm.202004546.

[11] L. Tao *et al.*, "Silicene field-effect transistors operating at room temperature," *Nature Nanotechnology*, vol. 10, no. 3, pp. 227–231, Feb. 2015, doi: 10.1038/nnano.2014.325.

List of Publications

As of January 2021

- C. Martella, **G. Faraone**, M.H. Alam, D. Tanneja, L. Tao, G. Scavia, E. Bonera, C. Grazianetti, D. Akinwande and A. Molle, *"Disassembling silicene from native substrate and transferring onto arbitrary target substrate*", Advanced Functional Materials, 2004546, 2020

- **G. Faraone**, E. Balduzzi, C. Martella, C. Grazianetti, A: Molle and E.Bonera, "*Thickness determination of anisotropic van der Waals crystals by Raman spectroscopy: the case of black phosphorus*", Nanotechnology, Vol. 31, 415703, 2020

- A. Molle**, G. Faraone**, A. Lamperti, D. Chiappe, E. Cinquanta, C. Martella, E. Bonera, E. Scalise, C. Grazianetti, "*Stability and universal encapsulation of epitaxial Xenes*", Faraday Discussions, 2020

- Grazianetti, **G. Faraone,** C. Martella, E. Bonera, A.Molle, "*Embedding epitaxial (blue) phosphorene in beteween device-compatible functional layers*.", Nanoscale, 11, 18232-18237, 2019

Publications in preparation/submission:

- **G. Faraone**, R.Sipala, M.Mariani, C.Martella, C.Grazianetti, A.Molle, E.Bonera, "*Probing the laser ablation of Black Phosphorus by Raman Spectroscopy*" in submission on Journal of Physical Chemistry C, 2021

- D.Tanneja, Md. H. Alam, **G. Faraone**, L. Tao, D. Akinwande, "*Integration paths for Xenes*" Book Chapter in "Xenes: 2D synthetic materials beyond graphene"

Other publications not strictly related to the activity presented in the thesis:

- C. Lenardi, J. Mayer, **G. Faraone**, J. Cardoso, S. Marom, R. Modi, A. Podestà, S. Kadkhodazadeh, M. Di Vece, "*Nanoscale induced formation of silicide around gold nanoparticles encapsulated in a-Si*", Langmuir, 36, 4, 939-947, 2020

- **G. Faraone**, R. Modi, S. Marom, A. Podestà e M. Di Vece, "*Increasing the optical absorption in a-Si thin films by embedding gold nanoparticles*", Optical Materials, 75, 204-210, 2018

- Y. Yan, T. Santaniello, L.G. Bettini, C. Minnai, A. Bellacicca, R. Porotti, I. Denti, **G. Faraone**, M. Merlini, C. Lenardi e P. Milani, "*Electroactive ionic soft actuators with Monolitically Integrated gold nanocomposite Electrodes*", Advanced Materials, 29, 1606109, 2017

Acknowledgements

This thesis work provides only a glimpse on a three years long journey in which the experiences I had and the interactions with the people I met have contributed to shaping me both from a personal and professional point of view. Here, I want to express my gratitude to those people who, to various degrees, helped me along with the different steps of this journey and without whom I would not have been able to complete it until the end.

Firstly, I want to thank Dr. Alessandro Molle and Prof. Emiliano Bonera. They have been always present as supervisors and mentors helping me to learn a scientific/critical way of thinking and ask questions. I thank Alessandro for having provided me a solid organization on which carry out my research project, for motivating and pushing me out of my comfort zones. I thank Emiliano for having taught me the principles of the intriguing and vast field of Raman spectroscopy and for having welcomed me into the LASSEM group of the University of Milano Bicocca where I carried out an important part of my research project.

Special thanks also go to Dr. Carlo Grazianetti and Dr. Christian Martella. I want to thank Carlo for his enormous patience with me in teaching all the tricks of the epitaxial growths on the UHV MBE system at the CNR IMM laboratory and for putting me always on the right path on the epitaxial phosphorene project. I really want to thank Christian for the efforts that, more than one time, he patiently shared with me in the CNR cleanroom in the processing attempts on the epitaxial phosphorus/Au(111) samples and for all the instructive discussions we had on this topic.

I cannot forget to thank Prof. Deji Akinwande for having welcomed me in his research group at the Microelectronic Research Center (MRC) of the University of Texas-Austin during my visiting period in the United States. I will forever remember the Texan-period as a very formative experience where I met amazing people. In particular, although there are many to whom I would express my gratitude, I want especially to thank two of them: Dr. Deepyanti Tanneja for having taught me all the secrets of the MRC cleanrooms and for having followed me during all the phases of the fabrication of silicene devices and Dr. Hasibul Alam with whom I had insightful discussions during our morning coffee breaks on everything could push towards a device implementation our epitaxial phosphorus and silicene samples.

An enormous thank goes to all the people (researchers, technologists, postdocs, lab technicians, PhDs and student fellows) that have contributed to enrich my professional and personal experience at the CNR IMM laboratories in Agrate Brianza. I owe each one of them something. As head of the Agrate-Unit, I would particularly thank Dr. Grazia Tallarida for having welcomed me at the CNR IMM laboratories as an PhD student associate.

Finally, I am enormously grateful to the master students who helped me along with the different phases of the black phosphorus/phosphorene project at University of Milano-Bicocca under the supervision of Prof. Emiliano Bonera: Roberta Sipala, Emanuele Balduzzi, and Massimilano Mariani.

The list of people I want to thank doesn’t end here and it would require at least one more full page. However, I cannot fail to thank my whole family and friends for supporting and sustaining me in every moment of this journey.